The Henryk Niewodniczanski
Institute of Nuclear Physics
Polish Academy of Sciences

and

University of Lorraine

Msc. Sara El Houbbadi

Doctoral dissertation
Field of Study: Physics

Nanostructured copper-phosphonate functionalized mesoporous silica for nonlinear optical applications

Thesis written under the supervision of
dr hab. Magdalena Laskowska
and
dr hab. Alain Walcarius

Krakow, 2025

Acknowledgments

My deepest gratitude goes firstly to my supervisors, Dr. hab. Magdalena Laskowska and Dr. hab. Alain Walcarius for invaluable support during laboratory work and interpretation of research results.

I would like to express my gratitude to Dr. Mariela Brites-Helu and Dr. Agnieszka Karczmarska for assistance in performing the analysis using scanning electron microscopy, Dr. Maciej Zubko for transmission electron microscopy imaging, Dr. Lionel Richaudeau and the PhotoNS platform for the SAXS and GISAXS measurements, Dr. Jarosław Jędryka for NLO experiments, and Dr. Marek Doskocz for his assistance in the use of computational methods and DFT numerical simulations.

My profound gratitude goes also to Dr. Alexey Maximenko for his valuable guidance, expertise, and support during the XAS experiments.

I wish to express my warm and sincere thanks to my colleagues for their cooperation and assistance during the time I had the pleasure to work with them.

Last but not least, words fail to express my appreciation to my family, who have always provided me with the best support. Without their help, patience, and encouragement, this thesis would not be possible.

Acknowledgements

The National Science Centre funded this work as part of the **SONATA-19 (Grant-No: 2021/43/D/ST8/00737)** project entitled **"Novel bioactive composite coatings based on silica nanostructures for biological and environmental applications"** led by **Dr. hab. Magdalena Laskowska**. The materials studied in this work were created as part of this project, and the presented research contributes to their comprehensive characterization performed within the project's scope.

The work was done in collaboration with **SOLARIS National Synchrotron Radiation Centre**, where the X-ray absorption spectroscopy (XAS) study was conducted at **ASTRA beamline** (Absorption Spectroscopy beamline for Tender energy Range and Above) under the supervision of **Dr. Alexey Maximenko**. Research at the National Synchrotron Radiation Centre SOLARIS is supported by the Ministry of Science and Higher Education, Poland, under contract no. 1/SOL/2021/2.

The computational part of this work was performed at **Poznan Supercomputing and Networking Center - PCSS** under computational grant ID 579.

This thesis was carried out as part of a dual degree program between the Institute of Nuclear Physics, Polish Academy of Sciences (IFJ PAN), and the University of Lorraine, under the **Campus France Scholarship**.

I am grateful to **the Polish National Agency for Academic Exchange NAWA** for the financial support under the Programme **STER– Internationalisation of Doctoral Schools**, Project No. PPI/STE/2020/1/00020.

Streszczenie

W niniejszej pracy doktorskiej zbadano materiały oparte na strukturze krzemionki mezoporowatej SBA-15 funkcjonalizowanej grupami fosfonianu miedzi w różnych koncentracjach. Praca została poświęcona badaniom nad materiałem w postaci cienkich warstw jednak w celu wykonania dokładniejszej charakterystyki badany materiał został przygotowany również w postaci proszków. Taki podejście umożliwiło wykonanie szeroko zakrojonych badań i dokładnej charakterystyki otrzymanych nanokompozytów. W pracy ukazano również duży potencjał aplikacyjny opracowanych materiałów które mogą być w prosty sposób deponowane na różnorodnych powierzchniach za pomocą metody zanurzeniowej (ang. dip-coating).

W pierwszej części pracy przedstawiono charakterystykę otrzymanych materiałów potwierdzającą zgodność otrzymanych materiałów z założeniami syntezy. W szczególności potwierdzono skład pierwiastkowy wszystkich próbek za pomocą techniki EDS. Mapowanie z wykorzystaniem tej techniki ukazało jednorodność rozlokowania grup fosfonianu miedzi na powierzchni krzemionki. Kolejne wykorzystane techniki takie jak TEM, SAXS, GISAXS oraz izotermiczna sorpcja azotu pozwoliły na dokładne scharakteryzowanie uporządkowanej mezoporowatej struktury krzemionkowej pełniącej rolę nośnika grup funkcyjnych. Natomiast spektroskopia Ramana umożliwiła charakterystykę struktury molekularnej badanych układów.

W drugiej części pracy przedstawione zostały rezultaty badania za pomocą spektroskopii absorpcyjnej promieniowania rentgenowskiego (XAS) wykonanego na linii ASTRA w Narodowym Centrum Promieniowania Synchrotronowego SOLARIS. Zastosowane techniki XANES i EXAFS miały na celu umożliwienie przygotowania precyzyjnych modeli numerycznych odzwierciedlających strukturę molekularną badanych materiałów. Dlatego analiza ich wyników wsparta została symulacjami numerycznymi. Poprzez odpowiednie dobranie modeli numerycznych na podstawie wyników uzyskanych w tym badaniu możliwe było przeprowadzenie kolejnych etapów symulacji numerycznych mających na celu wyjaśnienie obserwowanych własności nieliniowo optycznych opracowanych materiałów.

Własności nieliniowo-optyczne obserwowane dla badanych w niniejszej pracy materiałów wykazują intrygującą zależność od koncentracji grup funkcyjnych i nie jest to zależność liniowa. Przeprowadzone badania wykazały, że za własności NLO odpowiedzialna jest nie tylko ilość grup fosfonianu miedzi ale również ich wzajemne oddziaływania, które świadczą o tym że materiał przedstawiony w niniejszej pracy można traktować jako materiał o dostrajalnych własnościach NLO.

Abstract

In this doctoral thesis, materials based on the mesoporous silica structure SBA-15 functionalized with copper phosphonate groups at various concentrations were investigated. Although the research focused on thin-film materials, in order to perform a more comprehensive characterization, the studied material was also prepared in powder form. This approach enabled extensive studies and a detailed characterization of the obtained nanocomposites. The thesis also demonstrates the high application potential of the developed materials, which can be easily deposited onto a variety of surfaces using the dip-coating method.

In the first part of the work, the characterization of the obtained materials confirmed their compliance with the synthesis assumptions. In particular, the elemental composition of all samples was confirmed using the EDS technique. Elemental mapping with this method revealed the homogeneous distribution of copper phosphonate groups on the silica surface. Further techniques such as TEM, SAXS, GISAXS, and nitrogen adsorption isotherms allowed for a detailed characterization of the ordered mesoporous silica structure serving as a carrier for the functional groups. Additionally, Raman spectroscopy enabled a preliminary characterization of the molecular structure of the studied systems.

The second part of the thesis presents the results of X-ray absorption spectroscopy (XAS) measurements performed at the ASTRA beamline of the National Synchrotron Radiation Centre SOLARIS. The applied XANES and EXAFS techniques aimed to provide the basis for developing precise numerical models reflecting the molecular structure of the studied materials. Therefore, the analysis of their results was supported by numerical simulations. By selecting appropriate numerical models based on the outcomes of these measurements, it was possible to carry out subsequent stages of simulations designed to explain the observed nonlinear optical (NLO) properties of the developed materials.

The nonlinear optical properties observed for the materials investigated in this work exhibit an intriguing dependence on the concentration of functional groups, which is not linear. The conducted studies showed that the NLO properties are determined not only by the amount of copper phosphonate groups but also by their mutual interactions. These findings indicate that the material presented in this thesis can be regarded as a system with tunable NLO properties.

Résumé

Dans cette thèse de doctorat, des matériaux à base de silice mésoporeuse de type SBA-15, fonctionnalisée par des groupements phosphonate de cuivre à différentes concentrations, ont été étudiés. La recherche s'est principalement concentrée sur des matériaux sous forme de couches minces, mais les matériaux étudiés ont également été préparés sous forme de poudres afin d'en réaliser une caractérisation plus complète. Cette approche a permis de mener des études approfondies et une caractérisation détaillée des nanocomposites obtenus. La thèse met également en évidence le fort potentiel d'application des matériaux développés, qui peuvent être facilement déposés sur diverses surfaces à l'aide de la méthode de revêtement par trempage (dip-coating). Dans la première partie du travail, la caractérisation des matériaux obtenus a confirmé leur conformité aux hypothèses de synthèse. En particulier, la composition élémentaire de tous les échantillons a été vérifiée par la technique EDS. La cartographie réalisée par cette méthode a montré une distribution homogène des entités phosphonate de cuivre à la surface de la silice. D'autres techniques, telles que le MET, le SAXS, le GISAXS et l'adsorption d'azote, ont permis de caractériser en détail la structure mésoporeuse ordonnée de la silice servant de support aux groupementss fonctionnels. De plus, la spectroscopie Raman a permis une première caractérisation de la structure moléculaire des systèmes étudiés. La deuxième partie de la thèse présente les résultats des mesures de spectroscopie d'absorption des rayons X (XAS) effectuées sur la ligne ASTRA du Centre National de Rayonnement Synchrotron SOLARIS. Les techniques XANES et EXAFS utilisées avaient pour objectif de fournir une base pour le développement de modèles numériques précis reflétant la structure moléculaire des matériaux étudiés. L'analyse de ces résultats a donc été complétée par des simulations numériques. Grâce à la sélection de modèles numériques appropriés, fondée sur les résultats de ces mesures, il a été possible de réaliser les étapes suivantes de simulations visant à expliquer les propriétés optiques non linéaires (NLO) observées pour les matériaux développés. Les propriétés NLO observées pour les matériaux étudiés dans ce travail présentent une dépendance intéressante vis-à-vis de la concentration en groupements fonctionnels, qui n'est pas linéaire. Les études menées ont montré que les propriétés NLO dépendent non seulement de la teneur en groupements phosphonate de cuivre, mais aussi de leurs interactions mutuelles. Ces résultats indiquent que les matériaux considérés dans cette thèse peuvent être considérés comme étant à propriétés NLO modulables.

Contents

List of acronyms

1 General introduction to the thesis and its objectives 1

2 Nanotechnology: From concept to a precisely tailored nanomaterials 4

2.1 Ordered Mesoporous Silica (OMS) 7

2.2 Mechanism of silica network formation 8

2.3 Structural directing agent and self-assembly mechanism 10

2.4 Functionalization pathways of ordered mesoporous silica 12

2.5 Overview of the adopted synthesis techniques 15

2.5.1 Sol-gel synthesis for mesoporous silica SBA-15 powders 15

2.5.2 Evaporation-induced self-assembly (EISA) for thin film formation 17

2.6 Potential applications of ordered mesoporous silica materials 18

3 Introduction to nonlinear optics and the spectrum of inorganic, organic, and hybrid materials for NLO applications 20

3.1 Introduction to nonlinear optics 20

3.2 Second order NLO effects: Second Harmonic Generation (SHG) 22

3.3 Third-order NLO effects: Third Harmonic Generation (THG) 24

3.4 Materials for NLO applications 25

3.4.1 Inorganic materials for nonlinear optics 26

3.4.2 Organic materials for nonlinear optics 30

3.4.3 Hybrid organic-inorganic materials for nonlinear optics: silica-based SHG materials 33

4 Synthesis of Ordered Mesoporous Silica SBA-15 functionalized with copper-phosphonate functional groups in powder and thin film form 39

4.1 Materials and reagents 40

4.2 Synthesis procedure of powdered SBA-15 with copper-phosphonate functional groups 40

4.3 Synthesis procedure of ordered mesoporous silica thin films with copper-phosphonate functional groups 43

5 Comprehensive characterization of structure and molecular composition obtained materials - confirmation of synthesis assumptions 45

5.1 Electron Microscopy 45
5.2 Energy-Dispersive X-Ray Spectrometry (EDS) 53
5.3 Nitrogen physisorption 60
5.4 Small-Angle X-ray Scattering (SAXS) and Grazing-Incidence Small-Angle X-ray Scattering (GISAXS) 67
5.5 Raman spectroscopy 73

6 Experimental study for resolving the copper phosphonate functional groups structure using X-Ray absorption fine structure spectroscopy (XAFS) 82

6.1 Introduction 82
6.2 Short introduction to X-Ray Absorption Near-Edge Spectroscopy (XANES) 83
6.3 Short introduction to Extended X-ray Absorption Fine Structure (EXAFS) 87
6.4 Copper K-edge XAFS transmission data analysis of SBA-$POO_2Cu20\%$. 88
6.4.1 XANES data analysis of SBA-$POO_2Cu20\%$ 88
6.4.2 EXAFS data analysis of SBA-$POO_2Cu20\%$ 90
6.5 Copper K-edge XANES data analysis of SBA-$POO_2Cu1.25\%$, 2.5%, 5%, and 10% powders and MSTF-$POO_2Cu2.5\%$, 5%, and 10% thin films . . . 94
6.6 Phosphorus K-edge XANES data analysis of SBA-$POO_2Cu1.25\%$, 2.5%, 5%, and 10% powders and MSTF-$POO_2Cu2.5\%$, 5%, and 10% thin films 100

7 Computational approach of resolving the copper phosphonate functional groups structure using XANES simulation 106

7.1 Introduction 106
7.2 Theoretical description of the absorption coefficient 107
7.2.1 FEFF10 theoretical overview 107
7.2.2 FEFF10 Software Graphical User Interface (GUI) 109
7.3 Geometry optimization of structural models using Gaussian16 111
7.3.1 Set (S1): Models representing the conformer at highest functional group concentration 112
7.3.2 Set (S2) and (S3): Models representing the conformer at lower functional group concentration, with and without copper 117
7.4 XANES analysis on the basis of numerical simulations 118

7.4.1 Verification of structural models: Extended second-shell EXAFS fitting based on simulation results 122
7.5 Analysis of Cu K-edge XANES spectra of SBA-POO_2Cu powders and MSTF-POO_2Cu thin films based on numerical models 124
7.6 Analysis of P K-edge XANES spectra of SBA-POO_2Cu powders and MSTF-POO_2Cu thin films based on numerical models 128

8 Characterization of nonlinear optical (NLO) properties 129
8.1 Experimental setup for SHG and THG measurements 129
8.2 Nonlinear optical properties of the copper-phosphonate functionalized mesoporous silica 131
8.3 Effect of intermolecular distances on nonlinear optical properties 137
8.3.1 Estimation of the average intermolecular distance between two adjacent functional groups 139
8.3.2 Effect of spatial arrangement of functional groups on nonlinear optical responses 143

9 General conclusions and future perspectives 149

Publications 152

Publications 155

Bibliography 169

Acronym	**Meaning**
AGS	Silver Gallium Sulfide ($AgGaS_2$)
APTES	3-Aminopropyltriethoxysilane
AzPTES	Azidopropyltriethoxysilane
BBO	Beta Barium Borate (β-BaB_2O_4)
BNTES	Butyronitrile Triethoxysilane
BrTMS	Bromotrimethylsilane
ClTMS	Chlorotrimethylsilane
CMC	Critical Micelle Concentration
COFs	Covalent Organic Frameworks
CPTES	Chloropropyltriethoxysilane
CTAB	Cetyltrimethylammonium Bromide
$Cu(acac)_2$	Copper(II) Acetylacetonate
DFG	Difference-Frequency Generation
DFT	Density Functional Theory
DMF	Dimethylformamide
EDS	Energy Dispersive X-ray Spectroscopy
EISA	Evaporation-Induced Self-Assembly
EXAFS	Extended X-ray Absorption Fine Structure
GPTMS	Glycidoxypropyltrimethoxysilane
HCl	Hydrochloric Acid
HOMO–LUMO	Highest Occupied Molecular Orbital – Lowest Unoccupied Molecular Orbital
ICT	Intramolecular Charge Transfer
ICPTES	Isocyanatopropyltriethoxysilane
KBBF	Potassium Beryllium Borate Fluoride ($KBe_2BO_3F_2$)
KDP	Potassium Dihydrogen Phosphate (KH_2PO_4)
KTP	Potassium Titanyl Phosphate ($KTiOPO_4$)
LB	Langmuir–Blodgett
LDT	Laser Damage Threshold
$LiNbO_3$ (LN)	Lithium Niobate

Acronym	**Meaning**
MLCT	Metal–Ligand Charge Transfer
MOFs	Metal–Organic Frameworks
MPTMS	Methacryloxypropyltrimethoxysilane
NaF	Sodium Fluoride
NCS	Noncentrosymmetric
NLO	Nonlinear Optics
OMS	Ordered Mesoporous Structures
P123	HO-$EO_{20}PO_{70}EO_{20}$H – poly(ethylene glycol)-block-poly(propylene glycol)-block-poly(ethylene glycol)
PMO	Periodic Mesoporous Organosilicas
PPTES	Phosphonate Propyl Diethyl Triethoxysilane
PZC	Point of Zero Charge
RH	Relative Humidity
SAXS	Small-Angle X-ray Scattering
SBA-15	Santa Barbara Amorphous-15 Mesoporous Silica
SDAs	Structure-Directing Agents
SEM	Scanning Electron Microscopy
SFG	Sum-Frequency Generation
SHG	Second Harmonic Generation
SDS	Sodium Dodecyl Sulfate (anionic surfactant)
SPIONs	Superparamagnetic Iron Oxide Nanoparticles
TEM	Transmission Electron Microscopy
TEOS	Tetraethyl Orthosilicate
THF	Tetrahydrofuran
THG	Third Harmonic Generation
TMOS	Tetramethyl Orthosilicate
VTES	Vinyltriethoxysilane
XAFS	X-ray Absorption Fine Structure
XANES	X-ray Absorption Near Edge Structure

1 General introduction to the thesis and its objectives

Silica is one of the most abundant materials on Earth, occurring naturally as quartz and sand, and at the same time one of the most widely used functional materials due to its chemical stability and versatile structural properties. It can be prepared in various forms, such as mesoporous structures (e.g., SBA-15, MCM-41), nanoparticles, thin films or aerogels, with tunable pore size, surface area, and morphology. These features make it highly versatile for applications in catalysis, adsorption, filtration, and drug delivery. Its surface silanol groups allow for easy functionalization by post-synthesis grafting or in one step by co-condensation of the silica precursors, both approaches using organosilane reagents, the introduction of organic groups, metal chelators, or biomolecule anchors. This adaptability supports a wide range of uses, including pollutant removal, biosensing, and catalysis, where silica acts as a stable and recoverable support. Moreover, established synthesis methods like sol-gel and Stöber processes provide excellent control over structural features and ensure reproducibility, making silica-based materials reliable for both research and industrial applications.

An important aspect of mesoporous silica-based systems is that their functionalization can be precisely controlled during synthesis, which makes it possible to systematically study how the concentration of functional groups (in this case, propyl–copper phosphonate) influences the resulting material properties. Previous studies conducted in our group have demonstrated that variations in functional group concentration significantly affect both second harmonic generation (SHG) and third harmonic generation (THG). Moreover, these investigations revealed that the optimal concentration of these groups depends directly on the type of porosity. We hypothesize that the spatial distribution of functional groups within the mesopores, particularly the spacing between groups at different concentrations, governs intermolecular interactions and, in turn, affects the nonlinear optical response.

Building on this understanding, the current dissertation aims to deepen our insight into mesoporous hybrid systems' structural and electronic properties. **The main objective of this work is to investigate and elucidate how the molecular and electronic configuration of propyl–copper phosphonate functional groups within silica type SBA-15 influences the nonlinear optical properties of the resulting**

composite material.

In this thesis, it is demonstrated that both forms of investigated nanocomposite (powders and thin films) have similar mesopores organisation and molecular structure, exhibiting thus the same optical properties. In addition, thin-film architectures provide the advantage of easy integration into photonic and optoelectronic devices. Their uniformity, stability, and compatibility with surface patterning techniques make them particularly attractive for applications in miniaturized sensors, nonlinear optical coatings, and lab-on-a-chip platforms.

To investigate the structure-related properties of the studied materials, X-ray absorption spectroscopy (XAS) supported by DFT simulations was employed. These techniques provided important insights into the copper coordination environment and the nature of the propyl-copper phosphonate groups, thereby supporting the evaluation of the proposed hypothesis.

The **specific objectives** of this thesis are summarized as follows:

1. **Preparation of copper-phosphonate functionalized mesoporous silica**
   To investigate the optical properties of the designed material, a co-condensation approach was employed to synthesize mesoporous silica functionalized with varying concentrations of propyl-copper phosphonate groups. The resulting nanocomposites, combining the silica framework with the functional groups, were prepared in two distinct morphologies: bulk powders and thin films. These two systems served as model platforms for evaluating the relationship between structure and properties.

2. **Structural and spectroscopic characterization**
   To verify that the obtained material is consistent with the synthesis assumptions, namely that the silica structure corresponds to the SBA-15 type and that the matrices contain the intended concentrations of functional groups, a series of tests was carried out. The techniques applied for this purpose included transmission electron microscopy (TEM), scanning electron microscopy (SEM), energy-dispersive X-ray spectroscopy (EDS), small-angle X-ray scattering (SAXS) or grazing-incidence small-angle X-ray scattering (GISAXS), isothermal nitrogen sorption, and Raman spectroscopy.

3. **Advanced experimental structural analysis via XAFS**
   To investigate the electronic structure and local atomic environment of the anchored functional groups, X-ray Absorption Fine Structure (XAFS) is the most suitable method. This analysis appears to be very effective in identifying the molecular structure of the functional groups and the copper environment responsible for the observed physicochemical properties of the investigated materials.

4. **Theoretical modeling and XANES simulation**
   In order to identify the numerical model of the functional group and its local environment that best represents the investigated material, XANES results will be employed. A series of numerical models will be used to generate theoretical XANES spectra, which will then be fitted to the experimental data. On this basis, the models that best correspond to the experiment will be selected. The finalized models will also serve as a foundation for calculating the HOMO–LUMO electronic structure and for performing hyperpolarizability analysis, helping to interpret and explain the mechanisms underlying the observed physical responses.

5. **Nonlinear optical properties characterization**
   The nonlinear optical properties, specifically Second Harmonic Generation (SHG) and Third Harmonic Generation (THG) responses, will be measured and analyzed to investigate how optical nonlinearity varies with functional group concentration and material morphology. The results of these studies and numerical simulations should make it possible to determine the influence of the molecular structure on the NLO properties of the investigated materials.

The thesis is divided into eight chapters. Chapters 1 and 2 provide literature background. The first chapter introduces the general concept of nanomaterials, highlighting advances in materials science, particularly the design of porous materials with tailored structural and physicochemical properties. Particular attention is devoted to the detailed discussion of ordered mesoporous silica (OMS). Chapter 2 examines the main families of nonlinear optical (NLO) materials, including organic, inorganic, and hybrid systems, with a focus on functionalized silica-based hybrids. The following chapters present the characterization of the obtained materials, confirming their compliance with the synthesis assumptions; the results of X-ray absorption spectroscopy (XAS) measurements, analyzed with the support of numerical simulations; and the characterization of nonlinear properties, along with an analysis of structure–property relationships.

2 Nanotechnology: From concept to a precisely tailored nanomaterials

Richard Feynman once said, "There's Plenty of Room at the Bottom" [1]. When he delivered this visionary statement in 1959, he likely foresaw that it would later serve as the philosophical foundation for a whole field of nanomaterials or nanotechnology. This field focuses on the ability to tailor and manipulate the properties of matter using either bottom-up or top-down approaches to control material dimensions. By reducing dimensionality from 3D bulk materials to 2D thin films, to 1D nanowires or nanotubes, and finally to 0D quantum dots, scientists have discovered that novel physicochemical properties emerge, driven by quantum confinement, surface effects, and other nanoscale phenomena. In the context of this dissertation, ordered mesoporous materials such as SBA-15 are a three-dimensional nanostructured material with highly ordered, nanometric mesopores arranged in a unidirectional hexagonal lattice. These materials are bulk solids with 1D pore arrays on the nanometric scale.

What truly intrigued me about Feynman's ideology is its creative openness. He believed that even if something appeared impossible, it could still be done with the right tools and mindset.

The constant use of "what if?" characterizes Feynman's and so many great scientists' way of thinking. This simple, conditional question is the foundation for discovery. What if we could write on an atomic scale? Imagine if we could manipulate matter one atom at a time? What if we simply peeled graphite with Scotch tape [2]? What if we could probe surfaces with a fine needle [3]? This type of thinking is what drives innovation in nanotechnology.

H. W. Kroto,J. R. Heath,S. C. O'Brien,R. F. Curl and R. E Smalley discovered fullerenes in 1985 [4], ushering in the golden era of nanotechnology. Iijima's discovery of carbon nanotubes in 1991 marked a watershed moment in the field [5]. Another revolutionary breakthrough came from the work of A. K. Geim and K. S. Novoselov, who famously isolated a single layer of graphene using ordinary Scotch tape, an experiment that reshaped the landscape of 2D materials [6]. Progress was made in the development of semiconductor nanocrystals for nanoelectronics, as well as perovskite nanocrystals for

high-efficiency solar cells, light-emitting diodes (LEDs), and optoelectronic devices. In parallel, biomedical applications expanded through the use of gold and silver nanoparticles in cancer treatment. The field has also grown to encompass nonlinear optical (NLO) nanostructures intended for ultrafast optics and next-generation photonic technologies, and of course, the field of catalysis with all its forms: photocatalysis, electrocatalysis, thermocatalysis [7] and plasmonic catalysis [8]. Last and not least, porous materials also have received great interest whether crystalline like zeolites, which were first described as natural hydrated crystalline mineral by A.Cronstedt in 1756 [9], Later, in the 1950s, scientists synthesized the first laboratory-made zeolites, specifically Zeolite A and Zeolite Y, for use in the oil refining industry. Since then, research on zeolites has flourished due to their promising performance in diverse applications, especially in gas separation and heterogeneous catalysis [10]. In 1992, researchers at Mobil Corporation demonstrated for the first time the templating of silicate and aluminosilicate frameworks around surfactant micelles, resulting in the formation of ordered mesoporous materials. These new materials, called MCM Mobil Composition of Matter (MCM) [11], represent a significant advancement from microporous to mesoporous structures with tunable pore sizes in the 2-10 nm range. The most well-known types in this class include MCM-41 (hexagonal structure, space group symmetry P6mm, with a unidirectional pore system), MCM-48 (cubic structure, space group symmetry la3d, with three-dimensional pore network), and MCM-50 (lamellar structure, lacking space group symmetry, consisting of silica layers stabilized by double layers of surfactant) [12]. The soft-templating method using surfactants has been applied to both pure silica and aluminosilicate systems. Researchers have rapidly modified these syntheses to include aluminium and other heteroatoms such as Ti, Zr, and Fe allowing tailoring of catalytic and structural properties. The development did not stop there. In 1998, the Santa Barbara Amorphous (SBA) family of materials was introduced. This group includes SBA-2 (hexagonal close-packed array) [13], SBA-12 (three-dimensional hexagonal network) [14], SBA-14 (cubic structure), SBA-15 (two-dimensional hexagonal symmetry), and SBA-16 (cubic cage-like structure). Among them, SBA-15 is the most extensively studied, owing to its highly ordered structural and textural features as well as its excellent thermal stability [12, 15].

Since my research focuses on mesoporous silica nanostructures, I would like to emphasize that ordered mesoporous silica materials represent an excellent example of how nanotechnology has advanced to the point where materials can be precisely tailored with specific architectures and functionalities. Researchers have demonstrated that these materials enable precise control over pore size, shape, and ordering at the nanoscale, while also allowing the integration of multiple levels of nanostructuring within a single system. One particularly intriguing aspect is that, when these materials are prepared as thin

films, they combine features of 2D nanostructured materials with a periodic mesoporous arrangement on the order of 2 to several nanometers. This results in a hierarchical structure with varying degrees of nanoscale organisation (both across the surface and within the volume).

The following sections will describe the studied ordered mesoporous silica systems, with a particular focus on SBA-15. I will discuss their structural characteristics, key properties, synthesis strategies (including formation mechanisms), and functionalization methods used to prepare these materials.

2.1 Ordered Mesoporous Silica (OMS)

The International Union of Pure and Applied Chemistry (IUPAC) defines mesoporous materials as those with pore sizes ranging from 2 to 50 nm [16]. This classification distinguishes them from microporous materials (pore diameter < 2 nm) and macroporous materials (pore diameter > 50 nm) (see Figure 2.1).

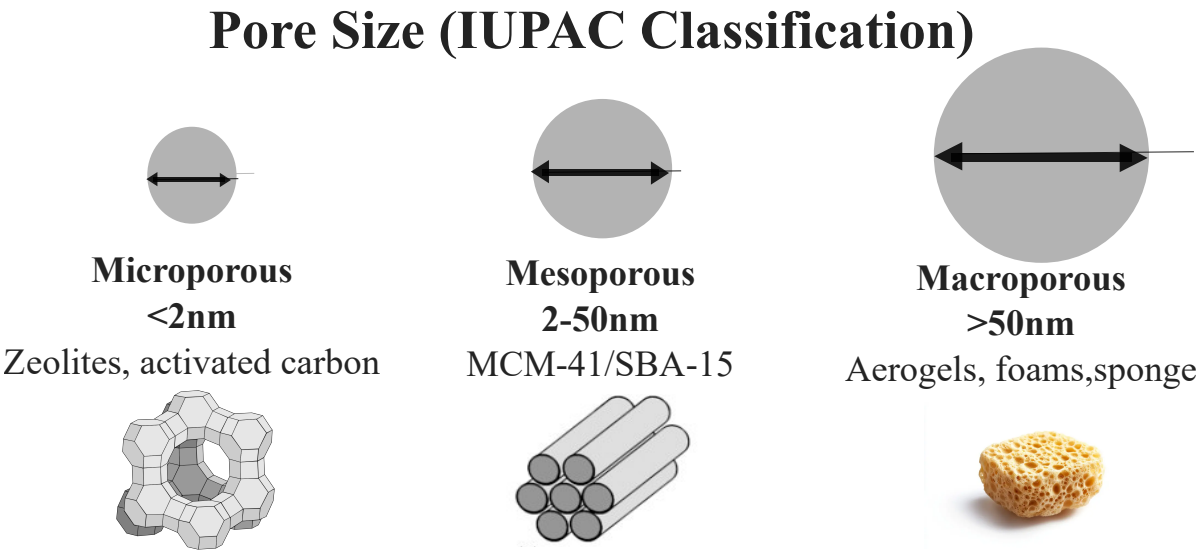


Fig. 2.1. Criteria for classifying porous materials based on pore size.

The year 1992 marked the first report of ordered mesoporous silica (OMS) nanostructures, published by the Mobil Research and Development Corporation. Using a liquid crystal templating (LCT) approach, they synthesized a new class of materials known as Mobil Crystalline Materials (MCM), including the well-known MCM-41 and MCM-48 [17]. Six years later, in 1998, the Santa Barbara research group introduced a new type of amorphous mesoporous silica called SBA-15. This material had a highly ordered porous structure and was synthesised using a triblock copolymer (Pluronic P123) as the structure-directing agent in an acidic sol-gel process [18].

By observing the structural parameters that distinguish SBA-15 from MCM-41, as listed in Figure 2.2, we can appreciate how the synthesis of mesoporous materials has become increasingly precise, leading to enhanced structural robustness and thermal stability. Both materials have hexagonally ordered pore structures, but they differ in several key characteristics: SBA-15 has thicker silica walls, larger pore sizes, and clearly defined cylindrical pores, whereas MCM-41 has thinner walls and smaller pores. Structurally, MCM-41 is considered a hexagonal one-dimensional (1D) system (noninterconnected pores), while SBA-15 has a hexagonal two-dimensional (2D) arrangement (interconnected pores) that is more structurally stable [19–21].

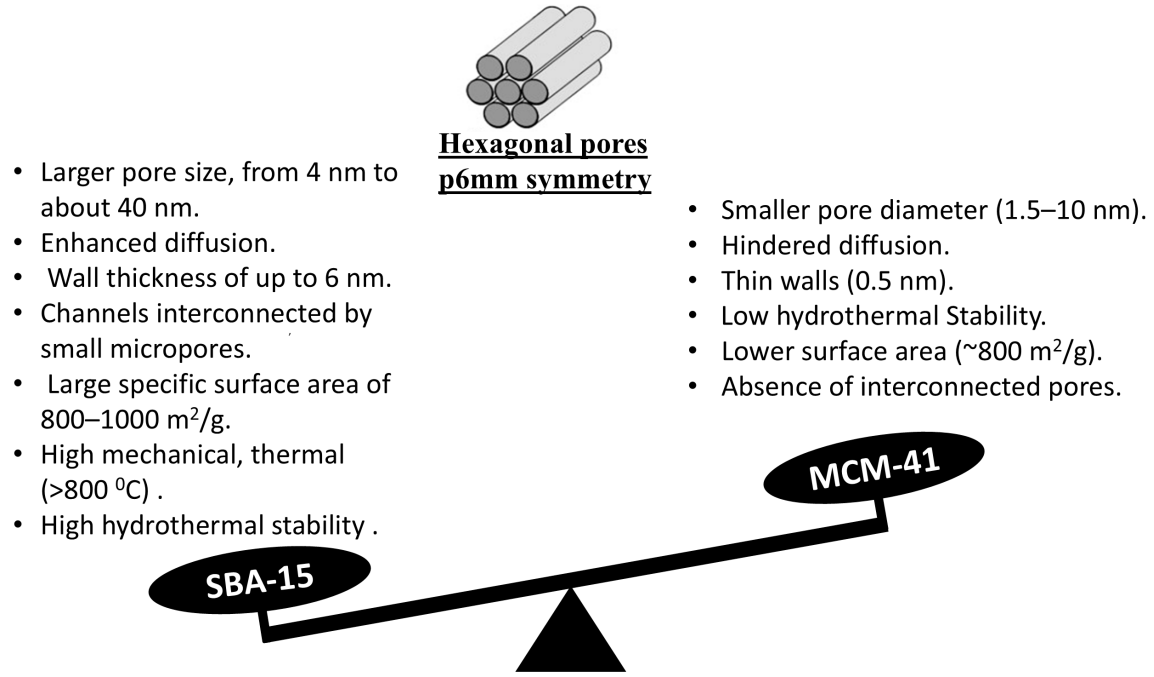


Fig. 2.2. Comparison of the properties of SBA-15 and MCM-41 mesoporous silica materials.

The morphology and structural arrangement of pores in OMS materials can be precisely tuned by varying synthesis parameters such as surfactant type and concentration, silica precursor, pH, temperature, and ageing time [22–25]. This control allows for tailoring of pore size, wall thickness, and pore connectivity, enabling the design of materials with properties optimized for specific applications.

When discussing ordered mesoporous silica (OMS) as a subclass of mesoporous materials, three key aspects must be considered: the formation of the silica matrix, the mechanism of porosity generation, and, most importantly, the structural ordering of the pores. Furthermore, the physicochemical properties of OMS can be further enhanced through appropriate functionalization.

So how do we get these OMS?

2.2 Mechanism of silica network formation

Regardless of the method used to form mesoporous silica nanostructures, the formation of a hydrolysed sol is a common step. This fundamental process involves the controlled hydrolysis of silica precursors such as tetraethyl orthosilicate (TEOS, $Si(OC_2H_5)_4$) or tetramethyl orthosilicate ($Si(OCH_3)_4$, TMOS) in the presence of water. Then the hydrolysis is followed by a condensation step, which can be induced under specific conditions depending on the chosen synthesis method.

Figure 2.3 illustrates the chemical reaction of the hydrolysis and condensation of TEOS molecules which act as building blocks to assemble the silica matrix during the condensation. The hydrolysis of tetraethyl orthosilicate begins with its reaction with water, resulting in the formation of silanol groups (Si–OH) and ethanol, as shown in the following equation [26]:

$$Si(OC_2H_5)_4 \ + H_2O \rightarrow \text{Si-OH} + C_2H_5OH$$

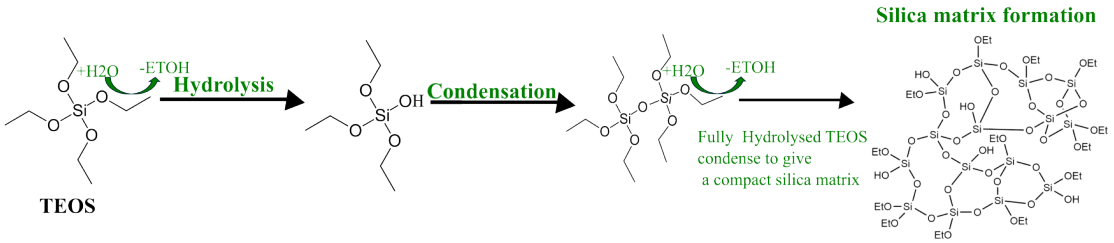


Fig. 2.3. Hydrolysis and condensation of TOES molecules.

Firstly, the hydrolysis reaction involves the orthosilicate precursor (TEOS) reacting with water through a nucleophilic attack of the oxygen atom in water on the silicon atom, producing silanol groups (Si–OH) and ethanol (C_2H_5OH). Adding a cosolvent, such as alcohols, dioxane, THF, or acetone, serves as a homogenising agent. It facilitates the mixing of hydrophobic silica precursors—particularly those containing bulky organic or alkoxy ligands (such as organosilanes)—with water, resulting in a more uniform reaction medium and enhanced hydrolysis efficiency [27]. Following hydrolysis, the silanol groups undergo a condensation reaction, linking together to form siloxane (Si–O–Si) bonds while releasing water [26]:

$$\equiv \text{Si-OH} + \ \equiv \text{Si-OH} \ \rightarrow \equiv \text{Si-O-Si} \equiv \ + H_2O$$

Secondly, silanol groups condense with each other to form siloxane bonds (Si-O-Si), releasing water molecules (H_2O). In practice, not all Si-OH (silanol) groups condense during the formation of the silica network. Due to steric hindrance or incomplete reaction kinetics, some of these Si-OH groups remain uncondensed, resulting in a silica surface rich in reactive silanol functionalities.

The rate and mechanism of hydrolysis and condensation in sol-gel derived silica systems are highly dependent on pH. These two processes, hydrolysis and condensation, work best in different pH ranges. Under acidic conditions, hydrolysis occurs quickly, whereas condensation takes longer. This promotes the development of linear or weakly branched polymeric silica structures. Under basic conditions, however, hydrolysis slows

while condensation accelerates, resulting in rapid nucleation and the formation of highly branched or colloidal silica particles [28, 29].

The surface charge of silica changes with pH due to the protonation and deprotonation of surface silanol groups (–SiOH). The pH at which the net surface charge of silica particles is zero is known as the point of zero charge (PZC), which typically lies between 1.5 and 4 [30]. At pH values above the PZC, silica surfaces have a negative charge (basic medium), which promotes electrostatic stabilization and particle repulsion. Below the PZC (acidic medium), the surface is positively charged, which may promote aggregation.

Now that we have established how the silica network forms, the next important question is: how is the ordered porosity introduced into the material ?

2.3 Structural directing agent and self-assembly mechanism

The mesoporosity of ordered mesoporous silica (OMS) is primarily achieved through the use of structure-directing agents (SDAs) or surfactants, which are the templates that guide the formation of the porous framework through the soft templating method. A surfactant is an organic molecule with a hydrophilic 'head' and a hydrophobic 'tail' that self-assembles into micelles in solution. These assemblies serve as templates around which silica condenses, eventually forming the mesoporous structure. SDAs can be classified according to their molecular structure and charge. They are broadly classified into ionic surfactants, such as cationic (e.g., CTAB) or anionic types (e.g., SDS), and non-ionic surfactants (e.g., Pluronic block copolymers P123) (see Figure 2.4).

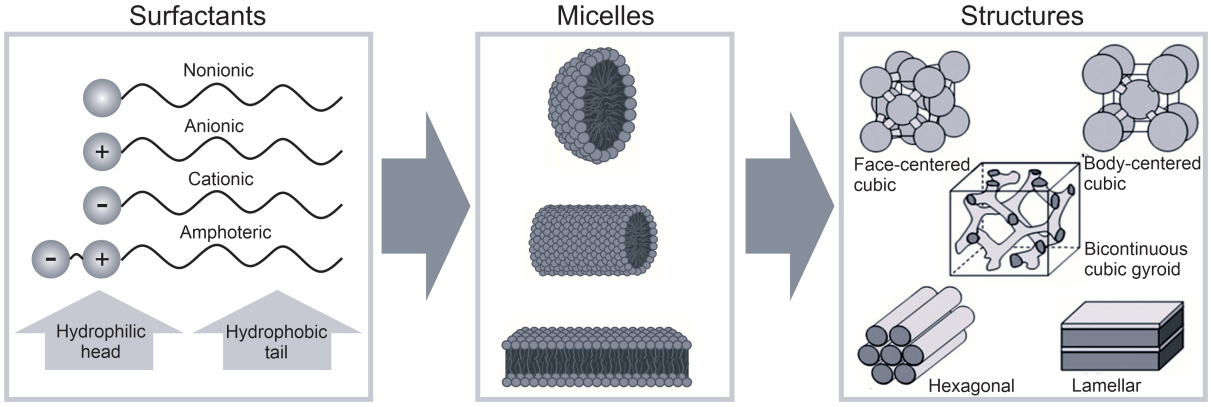


Fig. 2.4. Diagram showing types of surfactants, micelle shapes and mesostructures.

In soft templating, a template is strictly an organic molecule, whereas in hard templating, it can be inorganic, with an inorganic matrix (silica) growing around it, similar to a mold, so that when the template is removed, the final material retains the original template's shape and structure.

As depicted in Figure 2.4 the key factor in various pore shapes and structure is the self-assembly of the SDAs into micelles. Each micelle morphology tends to organize into a unique mesophase. For example, spherical micelles typically form cubic arrangements, cylindrical micelles tend to self-organize in hexagonal order, and lamellar micelles produce layered (lamellar) structures [31]. This tendency is crucial in defining the final pore spatial architecture, hence a wide spectrum of OMS systems. Concisely, a silica precursor and an organic surfactant together form the backbone of the soft templating process used to synthesize OMS.

Surfactants behave differently in polar and non-polar solvents due to their dual nature: they contain both hydrophilic (water-attracting) and hydrophobic (water-repelling) parts (Figure 2.5A).

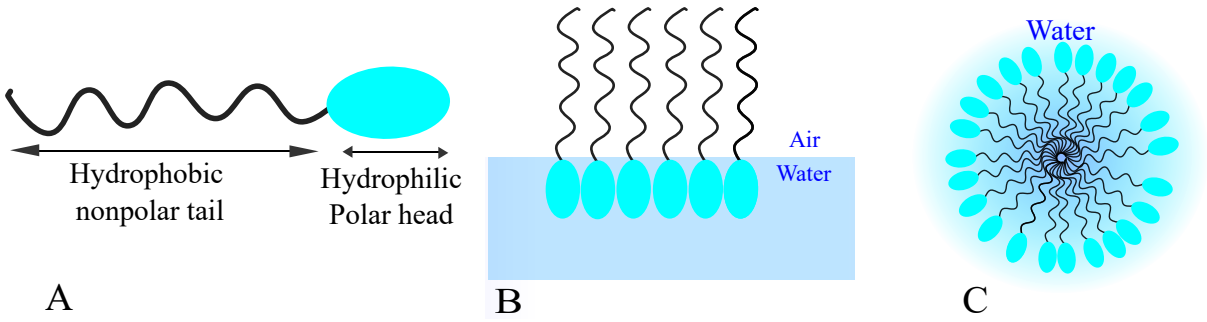


Fig. 2.5. Surfactant molecule and its behavior in aqueous media.

In aqueous solutions, amphiphilic surfactant molecules tend to arrange themselves at the water surface, with the hydrophilic head interacting with water and the hydrophobic tail extending away from it (Figure 2.5B). At low concentrations, surfactants primarily occupy the surface. However, as the surface becomes saturated, additional surfactant molecules begin to assemble into spherical micelles structures with hydrophobic tails shielded from water in the core and hydrophilic heads facing outwards (Figure 2.5C). Micelle formation begins at a concentration known as the Critical Micelle Concentration (CMC). Structure-directing agents (SDAs) have different CMC values based on their molecular structure and interactions with water [32]. By adjusting the surfactant concentration relative to the CMC, one can tune the shape and organisation of the micelles. In aqueous media, when the concentration of amphiphiles changes from low to high, a transition from spherical to rod-shaped micelle results, whereas higher concentration leads to the lamellar phase [32]. These micelles are formed by relatively weak non-covalent interactions, such as van der Waals forces and hydrogen bonds. Because of these weak interactions, the micelles can be easily removed, usually by washing or calcination, after the silica framework has aged and solidified.

Depending on the surface charge of the silica, which is affected by the pH of the reac-

tion medium, cationic or anionic surfactants can be strategically chosen for the synthesis of mesoporous silica. This decision has a significant impact on the self-assembly mechanism and the nature of the interaction between the inorganic silica species (I) and the surfactant (S). The interaction between the surfactant and the silica determines the orientation pathway of the structure, which has a direct impact on the architecture, ordering and uniformity of the pores in the material.

The literature describes various types of interactions, which can be classified into the following pathways (See Table 2.1):

Tab. 2.1. Different interaction mechanisms between the inorganic species (I), the head group of the surfactants (S), and the mediating ion M.

Pathway	**Surfactant Type**	**Silica Charge Condition**
S^+I^-	Cationic (CTAB)	Anionic silica (high pH),
S^-I^+	Anionic	Cationic silica (very low pH)
$S^+M^-I^+$	Cationic + Mediator (NO_3^-,Cl^-)	Cationic silica (very low pH)
S^0I^0	Neutral (P123)	Neutral silica (near PZC)

In all the synthetic routes mentioned in Table (2.1), electrostatic interactions between the surfactant (S) and the inorganic silica species (I) dominate the self-assembly process. However, in the S^0I^0 route, where the surfactant and silica species are electrically neutral (using P123 near the zero charge point of silica), assembly relies primarily on hydrogen bonding and van der Waals interactions, rather than electrostatics.

2.4 Functionalization pathways of ordered mesoporous silica

To enhance the versatility and functionality of mesoporous silica materials for specific applications in advanced technologies, functionalization strategies are commonly employed [33]. In general, functionalization of mesoporous materials allows for the precise tuning of surface properties, such as hydrophilicity, hydrophobicity, and the ability to bind specific guest molecules. It also enables modification of surface reactivity, protection against chemical attack, and adjustment of the bulk properties of the material. Additionally, functionalization can enhance the structural stability of these materials, particularly improving their resistance to hydrolysis.

Generally, there are two approaches to surface functionalization of mesoporous silica materials : post-grafting and direct synthesis, also known as one-pot cocondensation (see Figure 2.6).

Grafting was the first method used to functionalize the surfaces of different materials. It usually involves the formation of reactive species, such as radicals or ions, to initiate covalent bonding between organic molecules and surfaces. Several grafting methods exist, including free-radical grafting, ionic grafting, photochemical grafting, plasma radiation-induced grafting, and enzymatic grafting. Grafting is a post-synthetic method used with ordered mesoporous silicas (OMS). To expose the surface silanol (Si-OH) groups, mesoporous silica must first be synthesized, followed by surfactant removal (via calcination or solvent extraction). These groups then act as anchor points for the grafting of functional organosilanes or other molecules. The most obvious benefit of the post-grafting method is the excellent preservation of the mesostructure after functionalization. Furthermore, a wide range of functional groups can be grafted onto the surface. However, this method may result in a non-homogeneous distribution of organic groups within the pores. In some cases, excessive or uneven grafting may cause partial or complete pore blockage, reducing the accessibility and performance of the material in applications such as catalysis or adsorption.

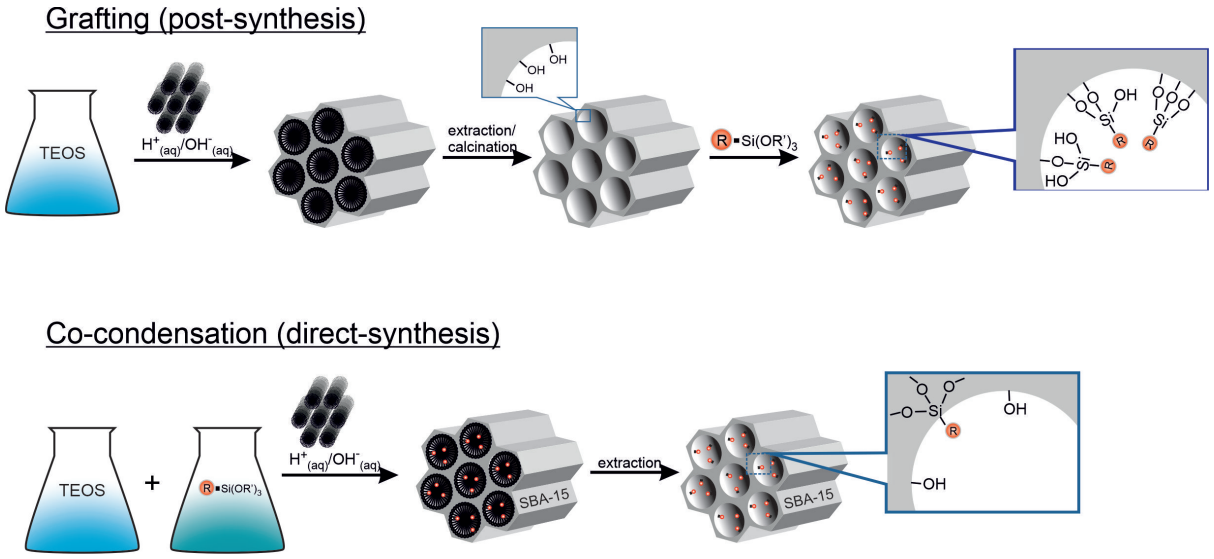


Fig. 2.6. Mesoporous silica functionalization pathways.

The second functionalization method is co-condensation, also known as the one-pot functionalization technique. This method introduces functional groups in a straightforward manner by including an organosilane precursor alongside the primary silica source (typically TEOS) at the start of the synthesis. Organosilanes with desired functional moieties are hydrolyzed and condensed with TEOS in the presence of water and a structure-directing agent. Co-condensation offers several numerous advantages, including direct anchoring of functional groups onto the silica framework, which allows for subsequent coordination of metal ions or selective interaction with target molecules. The uniform

distribution of functionalities improves the material's chemical reactivity as well as its hydrothermal stability. Furthermore, by adjusting the molar ratio of TEOS to the organosilane precursor, the concentration of functional groups embedded in the mesoporous matrix can be precisely controlled. This enables tuned intermolecular spacing, resulting in materials with diverse and tunable interaction mechanisms.

Combining surfactant-assisted self-assembly with co-condensation functionalization allows for precise tailoring of mesoporous silica materials to specific applications. Examples of the common organosilanes and their corresponding functional groups are summarized in Table 2.2.

Tab. 2.2. Different co-precursors and their corresponding functional groups.

Co-Precursor	**Functional Group**
Phosphonate propyl diethyl triethoxysilane (PPTES)	Phosphonic acid
3-Aminopropyltriethoxysilane (APTES)	Amine
Vinyltriethoxysilane (VTES)	Vinyl
Methacryloxypropyltrimethoxysilane (MPTMS)	Methacrylic
Chloropropyltriethoxysilane (CPTES)	Alkyl
Glycidoxypropyltrimethoxysilane (GPTMS)	Epoxide
Octyltriethoxysilane (OTES)	Octyl
Phenyltriethoxysilane (PTES)	Phenyl
Butyronitrile triethoxysilane (BNTES)	Nitrile
Azidopropyltriethoxysilane (AzPTES)	Azide
Isocyanatopropyltriethoxysilane (ICPTES)	Isocyanate

Periodic Mesoporous Organosilicas (PMOs) are a type of functionalized Ordered Mesoporous Silica in which organic groups are incorporated into the silica framework [34]. Incorporating other functional groups within the silica walls can be achieved using a different class of auxiliary precursors - not organosilanes, but silylated precursors [35] which contain multiple silane groups. These can provide a robust silica framework while still allowing for functionalization. This type of functionalization ensures good stability of the

immobilized molecules, such as cyclam, for instance, [36, 37]. On the other hand, as the number of silane arms increases, the degree of ordering in the final hybrid material tends to decrease.

The synthesis of this class of mesoporous hybrid materials via the sol-gel process can be categorized into three main approaches [38]: the soft templating method, the hard templating method, and a template-free approach.

2.5 Overview of the adopted synthesis techniques

In the realm of mesoporous silica synthesis, the Sol-Gel method is widely adopted. It is an approach based on a soft templating method in which surfactants or block copolymers are used to control the formation of mesoporous structures [29]. The term "sol-gel" is widely used in materials science and chemistry, as it describes a versatile and commonly employed process for synthesizing various materials, including mesoporous silica. The sol-gel process involves the transformation of a liquid sol (a colloidal suspension of particles) into a solid gel phase through a series of steps: hydrolysis, condensation, gelation, aging, drying, thermal treatment, and template removal [39].

The sol-gel method is a versatile approach that enables mesoporous silica to be fabricated in a variety of forms, including powders [40], fibers [41, 42], coatings, and thin films [29, 43]. Among these, thin films are particularly interesting for applications such as sensors [44, 45], optics [46], and catalysis because of their surface accessibility, potential for integration, and ability to coat surfaces with complex geometry. However, their characterization can be more difficult than that of powders, due to their limited mass and interaction with the substrate ((e.g., adhesion).

Current thin-film deposition techniques, such as dip-coating and spin-coating, allow precise control of layer thickness and uniformity, while remaining relatively simple and scalable. Despite these advantages, researchers continue to explore and refine other synthesis methods to better control the structural order, porosity and functional properties of mesoporous silica nanostructures, with the aim of optimizing them for increasingly demanding applications.

2.5.1 Sol-gel synthesis for mesoporous silica SBA-15 powders

As mentioned earlier, SBA-15 mesoporous silica is typically synthesized using the non-ionic triblock copolymer P123 as a structure-directing agent and tetraethyl orthosilicate (TEOS) as the silica precursor, all in an acidic environment. The formation of the mesostructure under these conditions is primarily driven by hydrogen bonding interactions, also known as the $S^0H^+M^-I^+$ mechanism (H^+ indicates the acidic environment,

M^- represents negatively charged silicate species) [33].

Several factors strongly influence the formation and quality of the SBA-15 structure, including :

- **Reaction temperature**: Thermal conditions affect micelle formation, silica condensation kinetics, and ultimately pore size and ordering [47].
- **EO/PO ratio of P123**: The hydrophilic/hydrophobic balance of the surfactant controls micelle geometry and phase behavior [48].
- **Acid concentration and pH**: These parameters influence the rate of silica hydrolysis and condensation, affecting particle morphology and mesophase development [49, 50].
- **Aging time and stirring conditions**: Both impact the degree of mesostructural ordering [51].
- **Surfactant/SiO_2 ratio**: The molar ratio between the structure-directing agent and the silica source determines final morphology and textural properties (e.g., pore volume and surface area) [52].
- **Counterions of the acid used**: Anions such as Cl^-, NO_3^-, or SO_4^{2-} can interact with the EO blocks of P123, modifying micelle packing and influencing the resulting mesostructure [52].
- **Use of polar organic solvents**: Solvents like DMF (dimethylformamide) can swell the hydrophobic core of P123 micelles, leading to increased pore size and altering wall thickness [52].

Controlled synthesis conditions are essential for producing high-quality SBA-15 mesoporous silica with a high surface area, well-ordered hexagonal mesostructure, uniform pore size (typically 5-10 nm), and thick pore walls. A temperature range of 35°C (for micelle formation and TEOS hydrolysis) to 80°C (for aging) is typically preferred to stabilize micelle organization and guide the self-assembly process [53]. A standard procedure involves adding **TEOS** to a solution of **P123 surfactant dissolved in HCl** while stirring continuously at 35-40°C. After stirring for 20-24 hours, the mixture is aged at **80-120°C for 24-48 hours** to promote silica condensation and wall thickening. Following gelation, a white solid silica precipitate forms, which is recovered through filtration or centrifugation (though if done too harshly, this can deform the ordered structure). The precipitate is thoroughly washed with distilled water, then dried overnight at room temperature, followed by **oven drying at 80°C for 5-6 hours** to remove residual moisture. Finally, **template removal** is achieved via **calcination**, typically by heating the sample at a controlled rate (e.g., 1°C/min) up to **550°C** and maintaining this temperature for **4-6 hours**, effectively removing the organic surfactant and exposing the mesoporous structure [29].

2.5.2 Evaporation-induced self-assembly (EISA) for thin film formation

Dip-coating and spin-coating are techniques primarily used for thin film fabrication, leveraging the process of evaporation-induced self-assembly (EISA). A schematic representation of this process is shown in Figure 2.7. EISA has proven to be a versatile method for constructing various film structures beyond silica. This technique involves preparing a solution rich in a volatile solvent, such as ethanol, methanol, or propanol. Using cationic surfactants results in two-dimensional hexagonal structures with pores aligned parallel to the substrate, forming a delicate silica framework with wall thicknesses around 10 Å. On the other hand, non-ionic surfactant templates lead to thicker walls, resulting in more robust structures [54, 55]. For dip-coating film, ordered mesophase structures form only after the surfactant concentration increases as the solvent evaporates. The thickness of the films is determined by the solvent's evaporation rate and solution viscosity. By increasing the ethanol content in the dipping solution, the solution viscosity decreases, which promotes the formation of a 2D hexagonal mesophase and results in thinner but highly aligned films. On the other hand, rapid solvent evaporation and fast TEOS condensation favor shorter ordering times. The withdrawal speed of substrate from the dipping solution can also affect the final film thickness. Moreover, a fine control over the humidity of the dip-coating chamber should be taken into consideration.

Grosso et al. [56, 57] proposed a model for the self-assembly mechanism and structural formation of dip-coated films. This model was developed using an in situ high-flux synchrotron Small-Angle X-ray Scattering (SAXS) study, which enables the observation of the rapid condensation processes occurring in less than 30 seconds. This technique provides detailed insights into the fast dynamics of film formation, which occurs in three regimes:

1. Formation of micelles at the film/air interface: Initially, micelles form at the interface between the film and the air.

2. Morphological transformation of micelles: These micelles undergo a morphological transformation to form both hexagonal and cubic 3D structures when the final film thickness is almost defined.

3. Intermediate 3D hexagonal phase: An intermediate 3D hexagonal phase is crucial for developing the specific Pm3n cubic structure.

The study elucidated the importance of the CTAB/TEOS ratio in obtaining different porosity arrangements: hexagonal (P63/mmc), cubic (Pm3n), and columnar hexagonal (p6m). In a similar study on dip-coated films using cationic surfactants, Cagnol et al. [58] showed that the quantity of water present in the film during mesostructuration depends

on the relative humidity (RH) during deposition. Changing the RH or the solvent vapor pressure just after evaporation induces a changes in film composition and potential modification of the mesostructure. This demonstrates a modulable steady state, during which the mesostructure can be altered by external influences. Therefore, precise control over the external RH is crucial for obtaining a highly ordered structure. Increased relative humidity slows down solvent evaporation, giving the micelles to organize properly.

However, in this work, the non-ionic surfactant P123 was used to prepare the mesoporous silica film with a structure similar to that of SBA-15 silica, the principles and physicochemical descriptions mentioned above still apply to them as well. For Pluronic P123, special attention should be paid to the volume percentage of surfactant to achieve a hexagonal arrangement of the micelles that can be compared with SBA-15 particles. For Pluronic P123-silica films, lamellar phases were observed for P123 concentrations between 63 and 75 vol%, 2D hexagonal phases between 40 and 55 vol%, and cubic phases between 30 and 36 vol%, closely paralleling the phases found for P123 in water [59]. Additionally, we aim to functionalize the porous silica matrix with organometallic moieties to alter the physicochemical properties of the hybrid material. As explained above, a common method to achieve this involves the incorporation of organic species by co-condensation of a tetraalkoxysilane with molecules containing a hydrolyzable silica group (organosilanes). The introduction of two different functional anchoring units is also possible.

Importantly, the addition of the organic species can induce phase changes in the deposited film beyond those expected from the templating surfactant alone. This is due to changes in micelle packing caused by the organosilane acting as a co-surfactant. Therefore, after a certain concentration of functional organic units, the desired porosity arrangement may be lost. Despite these limitations, this method is very useful and can be effectively used to create functionalized thin films.

2.6 Potential applications of ordered mesoporous silica materials

First, ordered mesoporous silica materials, with their various structural types, have received a lot of attention in the biomedical field, especially as nanocarriers for drug delivery. Their popularity stems from their tunable pore size, large surface area, and ease of surface functionalization, which enable the immobilization and controlled release of a diverse range of therapeutic agents. Numerous drugs have been successfully loaded into mesoporous silica carriers and released in response to specific stimuli, such as pH, temperature, or redox conditions.

In addition to drug delivery, these materials are now used for biosensing, disease diagnosis and treatment [60], and tissue engineering. Their versatility and biocompat-

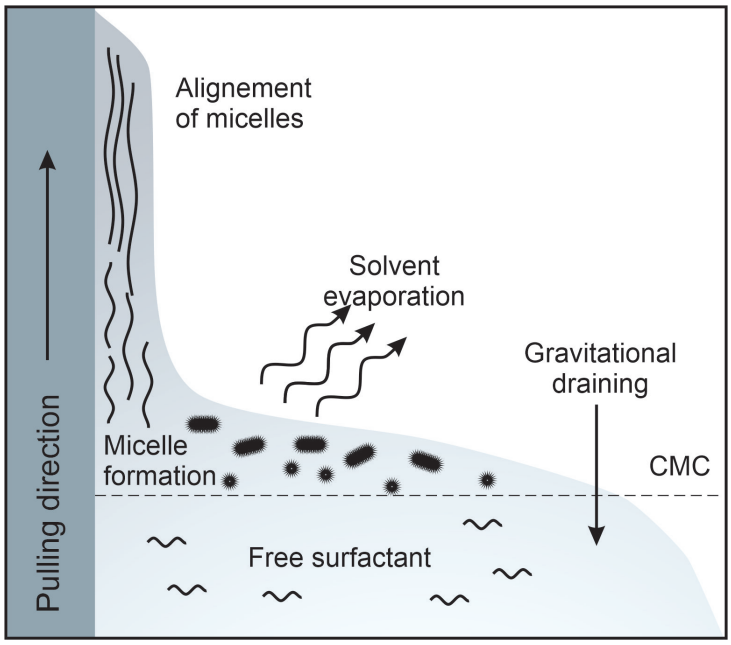


Fig. 2.7. Scheme of the evaporation-induced self-assembly (EISA) process.

ibility have keep them at the forefront of the development of cutting-edge biomedical technologies [61, 62].

Second, mesoporous silica materials have sparked considerable interest in the field of catalysis, owing to their large specific surface area, uniform and tunable pore sizes, and narrow pore size distributions. These properties make them ideal supports for the immobilization of single atoms or metal nanoparticles [63], allowing them to function as effective heterogeneous catalysts [64]. As a result, they have been extensively studied for catalytic applications in the production of fuels, bulk chemicals, fine chemicals, and pharmaceuticals.

Third, mesoporous silica materials have been widely used for environmental remediation and toxic element recovery. These materials can be functionalized with a wide range of organic and inorganic ligands or chelating agents that have a high affinity for capturing toxic elements like heavy metals (lead, mercury, arsenic) in soil or water [65].

Last but not least, the optoelectronic sector has benefited from the development of these ordered materials in a way that took advantage of the ordered and confining environment that these stablizing scaffold offer to integrate other optically active molecular moieties that can be useful for manipulating light propagation [66, 67].

3 Introduction to nonlinear optics and the spectrum of inorganic, organic, and hybrid materials for NLO applications

Because my dissertation is specifically concerned with investigating the nonlinear optical (NLO) properties of copper-phosphonate functionalized silica matrices, it is necessary to review the relevant literature. The system under investigation is made of an inorganic silica matrix with organometallic groups. As a result, it is worthwhile to investigate the individual properties of various NLO materials, as well as the potential benefits of combining inorganic matrices with organometallic functional groups in the form of hybrid materials. Before proceeding with that, a brief introduction to Nonlinear optics will be presented.

3.1 Introduction to nonlinear optics

It is fascinating to see the tremendous progress made in the field of nonlinear light-matter interactions, which dates back to 1845, when Sir John Herschel first documented the fluorescence in a quinine solution [68]. This phenomenon was later demonstrated by George Gabriel Stokes in 1852, who used a clever yet a simple experiment involving blue church glass (transmitting UV) and wine glass (blocking UV) to show that the emitted light was red-shifted, laying the foundation for our modern understanding of Stokes shift in fluorescence [69]. Later, in 1928, C.V. Raman and K.S. Krishnan discovered the Raman effect, revealing another type of inelastic light scattering in which incident photons exchange energy with molecular vibrations. Although fluorescence and Raman scattering are linear with respect to the electric field, these processes involve a nonlinear interaction in terms of energy exchange [70, 71].

The field of nonlinear optics was conceptually initiated in 1875, when John Kerr discovered that an intense electric field could induce birefringence in certain materials. Since then, there has been a growing interest in how matter responds to intense electromagnetic fields. In the late 1920s, scientists began to consider more complex interactions between light and matter, but these were mostly theoretical or limited to specific radio

waves. However, such effects were not experimentally observed until the 1950s, and even then, not with a large spectrum of light. The invention of the laser in 1960 marked a breakthrough that significantly launched the field of nonlinear optics. A key milestone was Franken's demonstration of second-harmonic generation in 1961, which is widely regarded as the formal beginning of the field [72].

Understanding the nature of light-matter interaction, especially concerning nonlinear responses, begins with understanding the fundamental structure of matter. Matter is composed of molecules, which are built from atoms consisting of a central nucleus (protons and neutrons) surrounded by electrons. The behavior of these charged particles is governed primarily by electromagnetic forces, particularly the Coulomb interaction. This force holds electrons to specific regions around the nucleus, resulting in electron orbitals or energy levels. Quantum mechanics provides a detailed description of electron behaviour within atoms. The concept of electron transitions between different energy levels within an atom caused by photon (electromagnetic wave) absorption or emission is fundamental to quantum theory. The potential energy experienced by an electron within an atom is determined by the interaction between the electron and the positively charged nucleus, as well as the interactions between electrons themselves (electron-electron repulsion). This potential energy landscape significantly affects the electronic structure of the atom and, consequently, its response to external stimuli, such as electromagnetic radiation. In more complex systems, such as molecules or solid-state materials, the interaction between electrons and their surroundings becomes even more complicated. Molecular geometry, chemical bonding, crystal structure, and intermolecular interactions all influence the electronic properties and light-matter interactions in these systems.

Nonlinear optical materials exhibit optical nonlinearities, meaning their response to an applied electric field is not directly proportional to that field strength. This nonlinearity arises from the interaction of light with the electrons and/or atomic/molecular vibrational modes within the material. Normally, laser light is considered sufficiently intense to induce changes in the optical properties of a material system. So now, why do we need to use intense radiation to observe this NLO effect? To answer this question holistically, one should recall the notion of dipole moment per unit volume, or polarization P(r) of a system that depends upon the strength E(t) of the applied field.

Applying an electric field to a material causes polarization within it. In linear regime, the polarization is directly proportional to the electric field, and the linear electric susceptibility χ coefficient connects these two quantities.

$$\vec{P}(t) = \epsilon_0 \left(\chi \vec{E}(t) \right) \tag{3.1}$$

Where ϵ_0 is the electric permittivity of free space.

In nonlinear optics, the optical response described by Eq.3.1 is expanded as a series in terms of the field strength E(t) as [73]:

$$\vec{P}_{\mathrm{NL}}(t) = \epsilon_0 \left(\chi^{(1)} \vec{E(t)} + \chi^{(2)} \vec{E(t)}^{\,2} + \chi^{(3)} \vec{E(t)}^{\,3} + \ldots \right) \tag{3.2}$$

$$\vec{P}_{\mathrm{NL}}(t) = \vec{P}^{(1)}(t) + \vec{P}^{(2)}(t) + \vec{P}^{(3)}(t) + \ldots \tag{3.3}$$

The quantities $\chi^{(2)}$ and $\chi^{(3)}$ are known as the second and third order nonlinear optical susceptibilities, respectively. These nonlinear susceptibilities describe a variety of nonlinear optical phenomena, including second harmonic generation, sum frequency generation (SFG), difference frequency generation (DFG), third harmonic generation, the Kerr effect, and others [73]. The general concept of frequency conversion of an NLO active medium is presented in Figure 3.1.

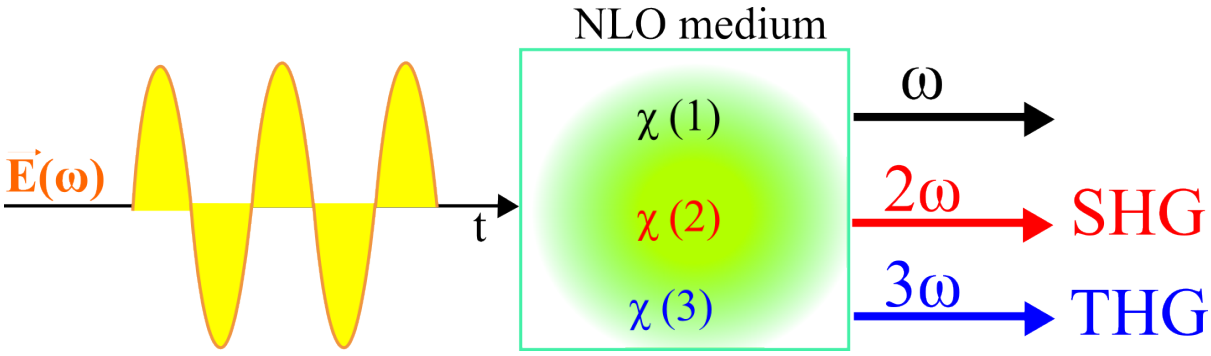


Fig. 3.1. Frequency-conversion of Nonlinear Optical medium

3.2 Second order NLO effects: Second Harmonic Generation (SHG)

Second order nonlinear optics includes phenomena resulting from the interaction of light and matter at intensities where the material's response is not directly proportional to the light's electric field. This nonlinearity enables several important processes, including sum-frequency generation (SFG) and difference-frequency generation (DFG).

This section focuses on the phenomenon of frequency doubling, also known as second harmonic generation (SHG) from a fundamental point of view. The SHG process effectively converts light at a given wavelength into light at half that wavelength, and it has a wide range of applications, including the creation of laser light at wavelengths that cannot be achieved directly through laser action. Second-order nonlinear optical interactions are primarily found in *non-centrosymmetric* crystals, which lack inversion symmetry. Consequently, media with centrosymmetric structures, such as isotropic liquids, gases, and amorphous solids like glass, do not exhibit SHG under conventional

phase-matching conditions [73]. Despite this, second-harmonic generation can still occur in amorphous materials. This phenomenon is frequently linked to structural asymmetries or local deviations from perfect inversion symmetry within the material. A good example is the materials studied in this thesis.

Second Harmonic Generation (SGH) is a process through which two identical photons interact with a nonlinear material to produce new photon that has twice the frequency of the original photons. This can be more rigorously described by the second order polarization $P^{(2)}(t)$ induced by an applied electric field.

Given a monochromatic electric field expressed as [73, 74] :

$$E(t) = E \cdot e^{-i\omega t} + E^* \cdot e^{i\omega t}, \tag{3.4}$$

According to equation 3.3, the second order polarization is given by [73]:

$$\vec{P}^{(2)}(t) = \epsilon_0 \chi^{(2)} \vec{E}(t)^2 = \epsilon_0 \chi^{(2)} \left[2|E|^2 + E^2 e^{-i2\omega t} + \text{c.c.}\right] \tag{3.5}$$

where "c.c." denotes the complex conjugate of the preceding 2ω term.

As we can see, two terms arise from the second polarization, the first term is constant and causes a phenomenon known as optical rectification, in which a static electric field (DC) is created across the nonlinear material [75], while the second term generates an electromagnetic wave with frequency 2ω or second harmonic.

In a classical approach, the nonlinear optical (NLO) response of a medium can be studied by examining the behavior of electrons within that medium.

In a non-centrosymmetric medium, the potential energy function felt by an electron is given by [73]:

$$U(x) = -\int F_{\text{restoring}}\, dx = \int \left(m\omega_0^2 x + max^2\right) dx = \frac{1}{2} m\omega_0^2 x^2 + \frac{1}{3} max^3. \tag{3.6}$$

A physical meaning that can be derived from the above equation is that the potential energy experienced by electrons in an asymmetrical nonlinear medium is different from its symmetric counterpart.

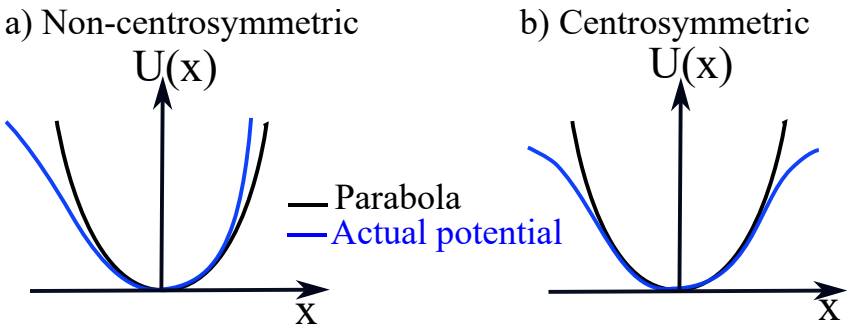


Fig. 3.2. a) Potential well for a non-centrosymmetric medium (b) Potential well for a centrosymmetric medium.

This means that the potential energy landscape is modified due to the nonlinear and asymmetrical properties of the medium, leading to different behaviour of the electrons. This explains why non centrosymmetry is a criterion for SHG responses. The potential energy function U(x) = U(-x) in a medium with centrosymmetric properties. This symmetry implies that only even powers of x could appear in the potential function U(x). However, for a noncentrosymmetric media, the potential U(x) must contain odd and even terms as described in equation 3.6 [76].

3.3 Third-order NLO effects: Third Harmonic Generation (THG)

As for third-order nonlinear optical (NLO) effects, the general reasoning is similar to that of second-order effects, but with some fundamental differences. The third-order NLO polarization is described by the following expression [74]:

$$P^{(3)}(t) = \varepsilon_0 \chi^{(3)} E(t)^3, \tag{3.7}$$

where $\chi^{(3)}$ is the third order nonlinear susceptibility.

In centrosymmetric systems, the second order polarization $P^{(2)}$ cancels out due to symmetry restrictions. Therefore, third-order effects represent the first non-vanishing contribution to the nonlinear response in such materials.

Among the various third-order nonlinear phenomena, the most commonly discussed are the Kerr effect and third harmonic generation (THG). Particular attention is given to THG in my work, which, similarly to second harmonic generation (SHG), involves the absorption of multiple photons. In this case, three photons of frequency ω are simultaneously absorbed to generate one photon at frequency 3ω.This frequency tripling is an important mechanism for generating ultraviolet light from infrared or visible laser sources and is widely applied in ultrafast optics and spectroscopy [77, 78]. Furthermore,

THG has found applications in imaging, particularly third-harmonic microscopy, which is a powerful label-free technique for imaging biological samples [79, 80]. THG is particularly useful for visualizing structural interfaces because it is inherently sensitive to optical discontinuities.

Unlike SHG, THG is allowed in all media irrespective of inversion symmetry, although its efficiency strongly depends on phase matching and material properties. In practice, the achievable conversion is limited by the damage threshold of the material under high-intensity excitation

3.4 Materials for NLO applications

Numerous studies have explored nonlinear optical (NLO) materials for applications such as frequency conversion, optical switching, and signal processing. Rather than repeating earlier work, this section aims to explore the spectrum of NLO materials and to identify the current frontier in second and third harmonic generation research, especially with respect to functionalized mesoporous silica hybrid materials.

Ultrafast laser technology advancements were pushing the boundaries of SHG and THG by generating shorter pulses with higher peak powers, allowing for more precise control and understanding of nonlinear optical processes.

For a material to exhibit NLO effects, such as second harmonic generation (SHG), a material must have certain properties, most notably non-centrosymmetry for SHG and a strong interaction with light at the appropriate frequencies. While many materials can exhibit NLO behavior under certain conditions, the efficacy and practicality of these effects vary greatly. The field of nonlinear optics is characterized by intense research activity, but the objectives are broader and more nuanced than simply discovering efficient materials with low fabrication costs but rather a set of requirements for instance a research of materials with wavelength flexibility or broad transparency windows [81–83], thermal stability and high optical damage threshold [84], or phase matching capability [85].

The incentive of research in the field of nonlinear optical (NLO) materials is always to find materials with a combination of properties that make them suitable for a variety of applications. These applications frequently have specific requirements and an ideal NLO candidate would be a material that provides a versatile platform for a variety of photonic technologies.

The pursuit of advanced nonlinear optical (NLO) materials has resulted in a large and diverse body of research, reflecting an interdisciplinary effort to synthesize new materials, understand their properties, and tailor them to specific applications. This research covers various types of materials, including inorganic, organic, and hybrid materials, each

with its own advantages and challenges. This chapter intend to explore these materials categories and their significance.

3.4.1 Inorganic materials for nonlinear optics

Inorganic materials have long been the most efficient and widely used class of nonlinear optical (NLO) materials in industrial applications due to their high thermal stability and mechanical strength. However, they generally lack the structural and chemical flexibility and ease of synthesis found in organic systems. Despite these limitations, inorganic materials often compensate with their higher nonlinear coefficients. Classic examples include Beta Barium Borate (BBO), Lithium Niobate ($LiNbO_3$), and Potassium Titanyl Phosphate (KTP), which continue to serve as benchmark materials in both fundamental studies and commercial applications.

As illustrated in Figure 3.3, inorganic NLO materials, which are often crystalline, can be classified in various ways. One common classification is based on their crystallinity, distinguishing between monocrystalline and polycrystalline NLO materials. Another commonly used classification organizes them according to their optical transparency range: ultraviolet (UV), visible (Vis), and infrared (IR). Each category includes subclasses such as oxides, chalcogenides, and pnictides, with the latter showing particular promise for IR applications [86].

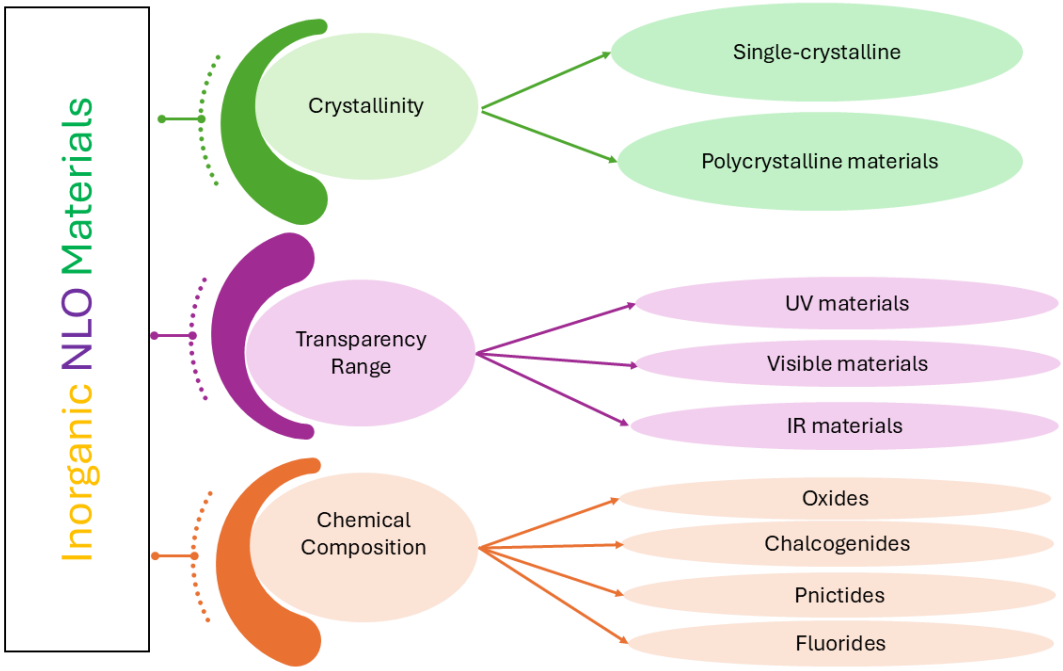


Fig. 3.3. Main Families of Nonlinear Optical Inorganic Materials.

Given the diversity of this class of materials, the present review will focus on repre-

sentative examples of inorganic materials exhibiting strong second- and third-harmonic generation responses.

Each category of the inorganic NLO materials shown in Figure 3.3 has distinct structural, electronic, and optical properties that define their nonlinear optical performance. The key differences stem from the following: Crystal structure, which determines phase-matching ability and anisotropy. The electronic band structure affects transparency and nonlinear susceptibility. Bonding nature, whether it is covalent or ionic, influences the nonlinear coefficient and the chemical composition, which determines thermal and chemical stability.

Monocrystal NLO materials and poly-crystalline SHG materials

In crystalline inorganic materials exhibiting second harmonic generation (SHG), the presence of a noncentrosymmetric (NCS) periodic structure is essential, as SHG is forbidden in centrosymmetric media. In contrast, third harmonic generation (THG) does not impose symmetry constraints, allowing both centrosymmetric and noncentrosymmetric materials to be active. Numerous NCS crystals with exceptionally high SHG efficiency have been extensively investigated. Benchmark compounds such as $KBe_2BO_3F_2$ (KBBF), β-BaB_2O_4 (BBO), KH_2PO_4 (KDP), $KTiOPO_4$ (KTP), $LiNbO_3$ (LN), and $AgGaS_2$ (AGS) are among the most studied and widely implemented in solid-state optical devices due to their strong nonlinear optical responses and broad transparency windows [87].

UV-Vis nonlinear optical materials

UV-Vis nonlinear optical (NLO) materials are characterized by their transparency in the ultraviolet (UV) and visible (Vis) spectral ranges. Some of these materials can also generate UV-Vis light through nonlinear frequency conversion, such as second-harmonic generation (SHG) and third-harmonic generation (THG). Still, their classification primarily refers to their ability to transmit light without absorption in these ranges. These materials are widely used in laser frequency conversion, high-resolution lithography, ultrafast spectroscopy, and biomedical imaging [88, 89].

For these systems to function effectively as UV-Vis NLO materials, several key properties are required. First, a wide band gap ensures transparency from deep-UV to the visible spectrum, preventing absorption losses. Second, a high second-order nonlinear coefficient ($\chi^{(2)}$) is necessary for efficient frequency conversion. A benchmark SHG coefficient is $d_{ij} > 0.39$ pm/V, as observed in KH_2PO_4 (KDP). Third, a high laser damage threshold (LDT) is critical for high-power laser applications, with a typical requirement of at least 5 GW/cm^2 for a single nanosecond pulse at 1064 nm. Additionally, phase matching capability is essential for efficient SHG and THG, often requiring precise angle or temperature tuning [88].

Several classes of materials are recognized for their UV-Vis NLO properties including:

Borates, such as β-BaB_2O_4 (BBO) and LiB_3O_5 (LBO), are known for their high transparency ranges (190 nm – 3.5 μm for BBO and 160 nm – 2.6 μm for LBO), strong nonlinear coefficients, and excellent phase-matching properties. They are widely used for frequency conversion in the UV and deep-UV regions.

Fluorides, including LiF and CaF_2, offer exceptional transparency in the deep-UV and vacuum ultraviolet (VUV) regions. These materials are commonly used in UV optics and high-energy laser systems.

Oxides, such as $KTiOPO_4$ (KTP) and KH_2PO_4 (KDP), exhibit good nonlinear efficiency and stability. KTP is widely used for generating green laser light (532 nm via SHG from 1064 nm), while KDP remains a standard NLO material in high-power laser fusion applications.

Despite the strong performance of these materials, several challenges remain in the development of UV-Vis NLO materials. Many materials with high nonlinear coefficients suffer from low laser damage thresholds, while others require precise phase-matching conditions that limit their operational flexibility. Additionally, some borates and oxides exhibit hygroscopic properties (humidity sensitive), affecting their long-term stability [88, 90].

Recent studies, including a viewpoint paper by Halasyamani et al., highlight the fundamental requirements for new deep-UV NLO materials [91]. These studies emphasize the need for materials that simultaneously exhibit high nonlinearity, wide transparency, high damage resistance, and environmental stability, paving the way for next-generation NLO materials.

Infrared and mid-infrared nonlinear optical materials

Infrared (IR) nonlinear optical (NLO) materials are essential for various photonic applications, including parametric down-conversion, mid-IR spectroscopy, thermal imaging, remote sensing, and ultrafast mid-IR photonics. These materials facilitate frequency conversion processes such as second harmonic generation (SHG), difference frequency generation (DFG), and optical parametric oscillation (OPO), enabling coherent light sources in the mid- and far-infrared (MIR and FIR) spectral ranges (3 μm to 1 mm). The availability of efficient mid-IR NLO materials is critical for laser-based chemical sensing, biomedical diagnostics.

Similarly to other systems to achieve high performance, IR and mid-IR NLO materials must satisfy several stringent criteria, including:

- **Wide transparency window**: A broad bandgap energy ($E_g > 3.5$ eV) ensures minimal linear absorption and prevents two-photon absorption at commonly used near-IR pump wavelengths (e.g., 1.064 μm, 1.55 μm).
- **High second- and third-order nonlinearity**: Strong nonlinear susceptibility ($\chi^{(2)}$

and $\chi^{(3)}$) is necessary for efficient frequency conversion, with high nonlinear coefficients (e.g., $d_{ij} > 20$ pm/V) facilitating SHG and DFG.

- **High laser damage threshold (LDT)**: The material must withstand high laser intensities without optical breakdown, particularly for pulsed applications.
- **Phase-matching capability**: The ability to phase-match fundamental and generated wavelengths is crucial to avoid destructive interference and maximize conversion efficiency.
- **Low optical losses**: Materials must have minimal free-carrier absorption and low scattering losses to ensure efficient mid-IR operation.
- **Thermal and mechanical stability**: High thermal conductivity and low thermal expansion coefficients are needed for stable performance under high-power operation.

The most promising IR NLO materials can be broadly categorized into **chalcogenides** and **pnictides**.

Chalcogenides family exhibits Strong Nonlinearity and Broad IR Transparency Chalcogenide NLO materials—comprising sulfides, selenides, and tellurides—are known for their strong covalent bonding, high nonlinear coefficients, and broad mid-IR transparency (up to 20 μm). These materials typically crystallize in layered or tetrahedral structures, which influence their electronic band structures and phase-matching capabilities,some know system include:

- **Zinc Germanium Phosphide ($ZnGeP_2$)**:As one of the most efficient mid-IR NLO materials, used in OPO systems and frequency conversion up to 12 μm. Exhibits a large nonlinear coefficient ($d_{36} = 75$ pm/V).Transparent from 0.74 to 12 μm with good LDT.
- **Gallium Selenide (GaSe)**: Show high SHG and THG efficiency with a nonlinear coefficient of $d_{22} = 54$ pm/V. Broad transparency range (0.62 – 18 μm). A layered structure leads to high birefringence but mechanical fragility.
- **Silver Gallium Sulfide ($AgGaS_2$) and Silver Gallium Selenide ($AgGaSe_2$)**:Another widely used material for mid-IR parametric down-conversion.Transparency range: $AgGaS_2$ (0.53 – 12 μm), $AgGaSe_2$ (0.73 – 18 μm).

Pnictides: are characterized by a high Damage Threshold and Efficient Phase Matching Pnictide-based NLO materials (nitrides, phosphides, arsenides, and antimonides) exhibit direct bandgap properties and are widely used in semiconductor-based nonlinear optics. They are particularly attractive for mid-IR photonic integration due to their compatibility with existing semiconductor fabrication techniques. Some of the known systems include:

- **Gallium Arsenide (GaAs)**: with a large nonlinear coefficient ($d_{14} = 94$ pm/V), making it one of the most efficient mid-IR NLO materials. Used in orientation-patterned

GaAs (OP-GaAs) for quasi-phase-matched frequency conversion. Transparency range: 0.9 – 17 μm.

- **Indium Phosphide (InP)**: Strong nonlinear response and high phase-matching capability in the IR range. Suitable for integration in semiconductor photonic circuits. Transparency range: 0.92 – 12 μm.

Despite their promising characteristics, IR and mid-IR NLO materials face significant challenges: Two-Photon and Free-Carrier Absorption especilly at high intensities,Thermal stability.

Recent advances in material design, including engineered domain structures, nanostructured mid-IR nonlinear devices, and alternative crystal growth techniques, aim to address these limitations. Novel materials with optimized band gaps, improved nonlinear coefficients, and higher damage thresholds are under active investigation to push the frontier of IR nonlinear photonics.

Recent reports can be used to provide a more systematic overview of solid-state NLO materials [86, 88].

3.4.2 Organic materials for nonlinear optics

Similarly, an organic compound must exhibit a noncentrosymmetric molecular structure to be an effective second-harmonic generation (SHG) material. The absence of inversion symmetry enables a non-zero second-order nonlinear susceptibility $\chi^{(2)}$, which facilitates the frequency doubling of incident light. Various classes of organic materials fulfill this criterion, including push-pull chromophores, conjugated polymers and oligomers, charge-transfer complexes, chiral organic crystals, and Langmuir-Blodgett (LB) films. More recently, research attention has extended to covalent organic frameworks (COFs) and metal-organic frameworks (MOFs), which offer structural tunability and modular design for SHG applications.

The discovery that SHG in organic systems arises predominantly from intramolecular charge-transfer interactions—particularly across donor–acceptor (D–A) motifs—has significantly advanced the development of efficient organic NLO materials. This charge-transfer mechanism not only boosts the nonlinear optical response but also offers distinct advantages over their inorganic counterparts. Organic materials typically exhibit faster optical responses due to electronic (rather than ionic or lattice-based) polarization mechanisms, making them highly suitable for high-speed optical modulation and ultrafast photonic applications. Additionally, they often present higher SHG efficiencies, easier tunability through molecular engineering, and cost-effective processing.

When moving from a bulk material to a molecular system, the nonlinear optical (NLO) properties change significantly due to differences in electronic structure, coherence, and

interaction mechanisms. In molecular systems, especially asymmetric molecules, large dipole-induced hyperpolarizabilities (β) enable strong second-order NLO responses, In bulk centrosymmetric materials, second-order nonlinear effects (χ^2) are forbidden in the dipole approximation. Still, they may appear due to quadrupole or surface effects because the inversion symmetry must be broken at the surface [92].

To achieve large nonlinear optical responses of molecular systems, the key idea is to create molecules with a highly conjugated π-electron system that is planar, as this facilitates efficient electron delocalization. By capping this conjugated system with electron-donor (D) and electron-acceptor (A) groups, a strong intramolecular charge transfer (ICT) is induced. This design strategy has been successfully applied to a wide range of NLO materials, including: polymer thin films [93].

The Main Push-Pull Systems for NLO Applications can be described as follows:

- **Classic D-π-A Systems:** In general, push-pull (D-π-A) systems, the donor (D), acceptor (A), and the π-bridge can be tuned in many ways to enhance nonlinear optical (NLO) properties. The choice of the acceptor strongly influences charge transfer (CT), while the donor enhances electron density and facilitates charge transfer. The π-bridge plays a key role in modulating NLO properties by influencing charge delocalization. By playing with the D, A, and the bridge type, we can have different types of push-pull chromophores with tunable NLO properties, see Table 3.1 and Figure 3.4.

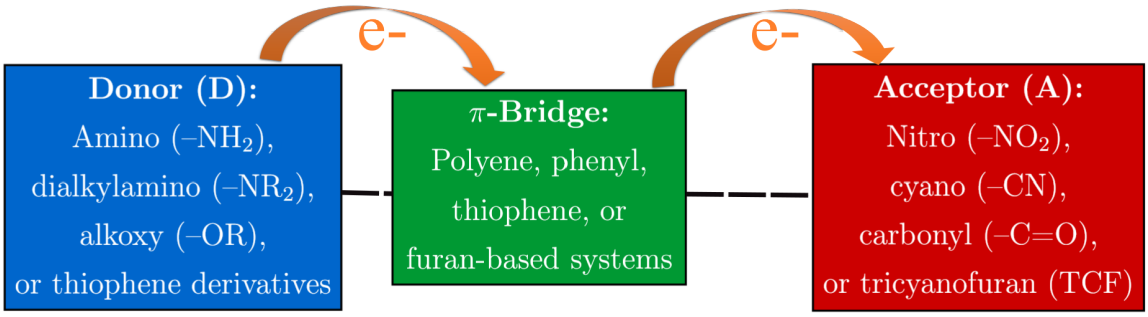


Fig. 3.4. Schematic Representation of Classic Push-Pull Systems for NLO with examples of A and D organic groups.

Tab. 3.1. Examples of push-pull systems for NLO applications.

Donor (D)	-Bridge	Acceptor (A)	Example
Triphenylamine (TPA) [94]	Azo (-N=N-)	Tricyanofuran(TCF) [95]	DR1-based dyes
Carbazole [96]	Polyene (-CH=CH-)	Benzothiazole [97]	Carbazole-BT systems [98]
Indoline [99]	Thiophene-vinylene	DCM [100]	Indoline-DCM chromophores
Phenothiazine [101]	Benzothiadiazole (BTD)	CF_3-TCF	Strong SHG materials
Thiophene [102]	Benzothiadiazole	TCF	TCF-thiophene derivatives

- **Extended Conjugation System:** Extended π–conjugation in D-π–A molecules has been proposed to enhance nonlinear optical (NLO) properties by decreasing the HOMO-LUMO energy gap and transition energies. This enhances charge transfer and polarizability, leading to high-performance NLO compounds. Examples of such extended π-conjugated systems include p-nitroaniline (pNA) derivatives, hemicyanine dyes, styryl dyes. [103, 104]
- **Multi-Branched (Octupolar) System:** Herein, a branched molecular architecture symmetrically arranged around a central bridge is adopted, which allows a multidirectional charge transfer between the branches. This geometry is mainly suited for third-order NLO effects due to the centrosymmetric arrangement of the molecular system that leads to a small dipole moment [105–107].
- **Zwitterionic System: Molecules with separated positive and negative charges:** Zwitterionic materials, which contain both positively and negatively charged groups but remain overall neutral, often exhibit high molecular dipole moments, which contribute to large hyperpolarizabilities, additionally [108, 109]. Some zwitterionic materials can form well-ordered films, enhancing macroscopic nonlinear optical effects [110, 111].
- **Organic optical Crystals:** Optical crystals based on organic salts with large chromophores are an emerging class of materials with high potential in nonlinear optics (NLO), but they are still not as extensively studied as their inorganic counterparts. Among these,DAST (4-N,N-dimethylamino-4′-N′-methyl-stilbazolium tosylate) and its derivatives stand out as one of the most important organic NLO crystals [112]. about 75% of all nonchiral organic chromophores crystallize in centrosymmetric space groups and thus display no second-order optical nonlinearity (SHG) [113], however a well-established strategy to achieve non-centrosymmetric alignment in organic nonlinear optical (NLO) crystals is designing D–π–A cationic chromophores paired with structurally distinct anions.
- **Conjugated Polymers and Oligomers:** Contrary to polydisperse polymer systems, oligomers are short-chain molecules with a more defined electronic structure, leading to sharper and more predictable NLO responses. They serve as models to study the electronic structure of conjugated polymers by extrapolating oligomeric properties to infinite chain lengths [114, 115].

  Oligomers such as: Oligothiophenes [116], Oligoacenes [117] are characterized by defined electronic states, making them ideal for theoretical and experimental studies.

  Conjugated Polymers such as: Polyacetylene, Polythiophene, Poly(p-phenylene vinylene) (PPV) with Extended π-electron delocalization enhance charge transfer and second-order NLO effects [118, 119].
- **Covalent Organic Frameworks (COFs):** COFs are fully crystalline porous organic

materials composed entirely of covalently linked organic building blocks. They exhibit lower density due to their composition of light elements such C, H, N, O, S. This class emerged as a hybrid of organic moieties to overcome challenges associated with the mechanical robustness of small organic molecules and oligomers, which are prone to dissociation in harsh environments and aggregation at higher densities which hinder their applicability. The framework concept stabilises these organic molecules, increasing the number density of chromophores in a rigid structure while preventing aggregation. Another key advantage of COFs is their porosity, which offers two significant benefits: first, the pores provide a facile pathway for functionalization, enabling fine-tuning of the NLO response without altering the framework structure; second, the porous nature allows for NLO switching properties by facilitating the movement of molecular fragments [120]. A discussion on COFs exhibiting second-order and third-order NLO responses has been reviewed by P.Biswal and coworkers [120].

- **Metal-Organic Frameworks (MOFs):** MOFs are hybrid crystalline porous materials made of metal nodes connected by organic linkers. Unlike COFs, which rely on covalent bonds, MOFs contain metal centers, which have a significant impact on their electronic and optical properties. Although the organic ligands primarily determine the NLO behavior in MOFs, the metal centers contribute to charge delocalisation and improve the overall stability of the framework. The structure of the organic ligands determines the pore size and morphology of MOFs, allowing for precise control of guest-host interactions. One significant advantage of MOFs in NLO applications is their ability to immobilise and disperse organic chromophores within their framework, resulting in high-density packing while minimizing non-radiative losses. Furthermore, the confined environment within MOF channels stabilizes highly polarizable organic species, which improves their NLO performance. MOFs' properties make them promising candidates for advanced NLO applications, particularly third-order nonlinear optics and frequency conversion processes. Several reviews have provided a comprehensive overview of strategies to prepare MOFs with NLO properties [121–124].

3.4.3 Hybrid organic-inorganic materials for nonlinear optics: silica-based SHG materials

Combining organic and inorganic materials into a single hybrid system has emerged as a powerful strategy for overcoming the limitations inherent in each component type and producing materials with enhanced and, in some cases, completely new functionalities. These hybrid materials, which combine the best of both worlds, have demonstrated significant potential in various applications, including nonlinear optics. Over the last decade, there has been significant progress in the field of nonlinear optical (NLO) materials, particu-

larly in developing organic-inorganic hybrid materials designed to improve NLO effects such as second harmonic generation (SHG). Several noteworthy developments include metal chalcogenides, metal halides, metal iodates, organic dye-doped silica, silica-based cross-linked chromophores [125–127].

Because my dissertation focuses on functionalized silica-based hybrid materials, in which the surface of the silica matrix is modified with nonlinearly active optical chromophores, the use of silica must be justified by its distinct benefits. These include high thermal and chemical stability, wide optical transparency, and compatibility with microelectronic technologies, making it an ideal platform for incorporating nonlinear optical functionalities. Furthermore, its biocompatibility, flexibility in synthesis and functionalization routes, and ability to be processed as thin films [128] make it a good substrate for the development of advanced NLO materials. In this context, I can cite the work of Shengxiang Ji et al., who used the in situ poling and sol-gel processing of 1,4-phenylene bis(4-trimethoxylsilylethylbenzoate) (PMSE) and Disperse Red 1 (DR1), to synthesise a new thermal-resistant second-order nonlinear optical film [129] On the same path, Shiwei Wang et.al. prepared a stable nonlinear optical (NLO) film containing "T" type alkoxysilane dye by the spin coating technique [127]. Moreover, Silica's ability to be structured at the nanoscale makes it an excellent host material for accommodating guest NLO molecules and enhancing specific functions, especially with the development of synthetic routes like sol-gel processing, templating, and etching to create nanoporous silica materials with controlled pore sizes and structures, now it's possible to exploit the periodic ordered and organised porosity to improve the optical response of the NLO guest chromophores that can be attached, with huge quantity on the surface of the pores or inside the structure due to high specific surface that the porosity bring along [130, 131].

Grafting, co-condensation, and the use of bis-silylated organic precursors (functionalization into the silica walls) are the three most common methods for incorporating functionalities into nanoscale silica matrices. Each method has distinct advantages and can be tailored to achieve the specific properties and functionalities required for different applications [33].

Mesoporous silica is used to host a variety of inorganic, organo-transition-metal oxides, organic, metals, and carbon guests [132, 133]. Although mesoporous silica does not have an intrinsic nonlinear optical (NLO) response, its well-defined and tunable pore structure provides a useful platform for confining polar chromophores. This confinement can promote intermolecular interactions and change the electronic environment of the chromophores, potentially inducing asymmetry in their molecular structure and thus improving their NLO properties. For instance, coordination metal and organometallic complexes are promising candidates for nonlinear optical (NLO) applications, owing to their

chromophoric nature and donor-acceptor configurations. The nonlinear optical response of these molecules is caused by the electrons' push-pull mechanism. This mechanism involves the transfer of electronic charge from electron-donating groups (donors) to electron-accepting groups (acceptors), which results in the polarization of the electron cloud and the generation of nonlinear optical effects [134]. Depending on the metal's oxidation state and the nature of the coordinated ligands, the metal center in an organometallic chromophore can act as an electron donor or acceptor.

1. **Silica-based hybrid materials for nonlinear optics (NLO):**

   In the scope of this dissertation, the discussion of hybrid organic–inorganic nonlinear optical (NLO) materials for second harmonic generation (SHG) will be limited to a specific class of materials based on ordered mesoporous silica as the host matrix. Given the wide variety of hybrid materials developed for NLO applications, this focus serves to narrow the scope of interest. In particular, I reviewed systems that exploited the ordered structure and confinement effects provided by mesoporous silica frameworks to enhance or control the NLO response.

   Starting from the Periodic Mesoporous Organosilicas (PMOs) as a promising class of hybrid organic-inorganic materials with nonlinear optical (NLO) applications. These materials are typically produced using sol-gel processes that involve the co-condensation of silica precursors with organosilane or bridged organosilica precursors. The resulting frameworks combine inorganic silica, organic chromophoric units, and mesoporosity to form a single, synergistic structure. Such periodic mesoporous organo- (bridged) Silicas (PMO) have a large surface area, tunable pore sizes, and spatially stabilized chromophores that are embedded in the silica walls or anchored to the pore surface [135].

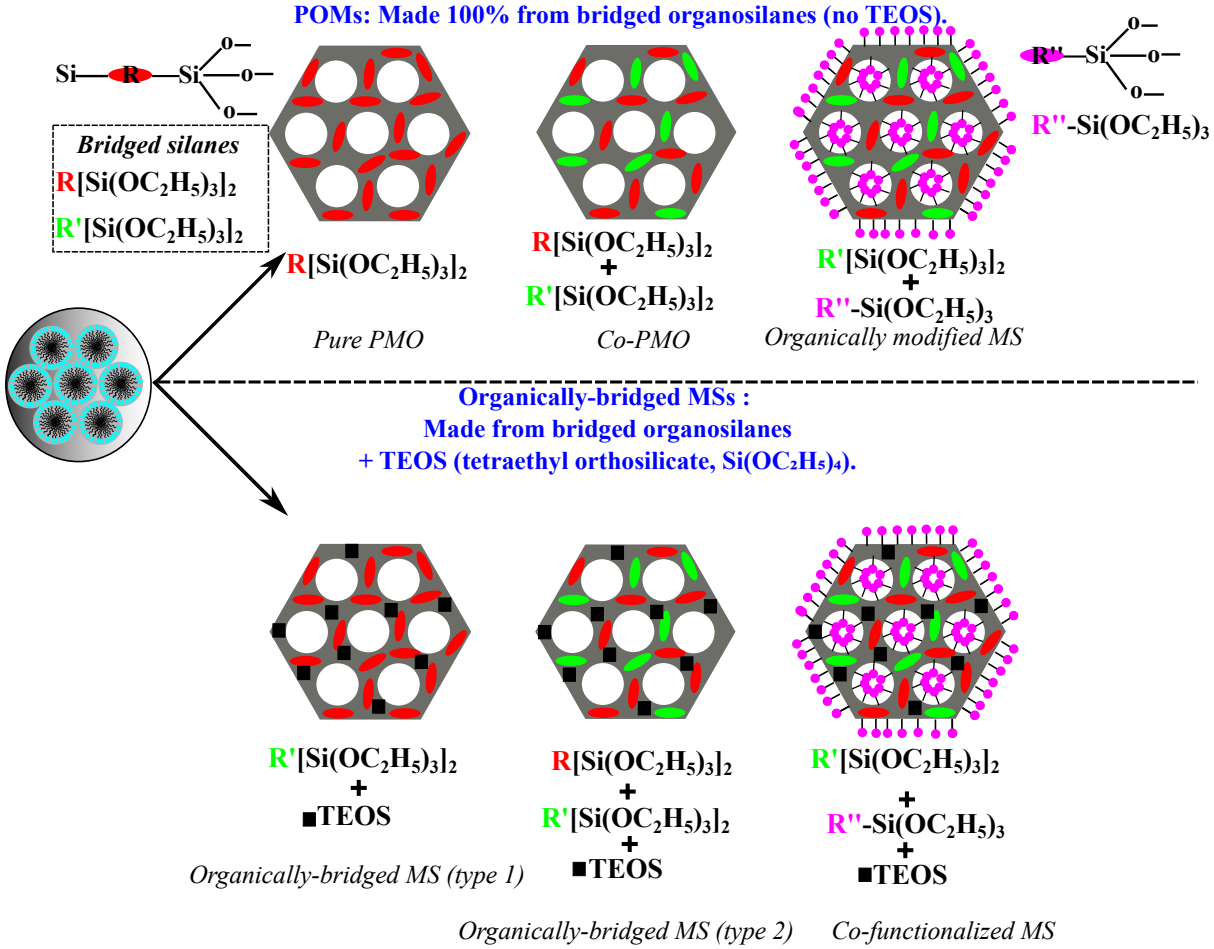


Fig. 3.5. Schematic overview of mesoporous organosilica materials with organo-bridged framework (organo-bridged PMOs and organo-bridged MS) [136].

The development of hybrid materials through the incorporation of active nonlinear optical (NLO) chromophores into mesostructured silica frameworks offers several strategic advantages. First, the rigid silica network effectively reduces chromophore aggregation while enhancing the thermal and mechanical stability of the system. Second, the high surface area and uniform porosity of the mesostructure facilitate controlled orientation and spacing of the NLO-active units—key factors in achieving optimal dipole alignment and improving second-order nonlinear optical responses. In particular, one-pot co-condensation strategies allow precise control over the chromophore loading, distribution, and microenvironment. This enables a systematic investigation of intra- and intermolecular interactions and their direct impact on NLO performance.

These hybrid materials, composed of both organic and inorganic components, offer a versatile platform for tailoring NLO behavior through compositional and structural modifications. By engineering the connectivity, morphology, and chemical

functionality of each domain, it becomes possible to tune optical properties for specific applications. While this area of research is relatively well-established, critical challenges persist, particularly in reducing optical losses within the inorganic matrix, improving the photochemical stability of the hybrid system, and enhancing the optical efficiencies of the organic moieties [137]. These issues underscore the need for innovative materials design and precise synthetic control.

In this context, ordered mesoporous silica (MS) materials—such as SBA-1, SBA-15, SBA-16, MCM-48, and MCM-41—have gained significant attention. Their highly ordered pore architectures, tunable pore sizes, and thick silica walls make them attractive candidates for advanced functionalization strategies. These structural features offer multiple degrees of freedom for tailoring surface chemistry and hosting functional species, rendering them ideal platforms for both passive and active optical applications.

A variety of functionalization techniques have been developed, with particular emphasis on SBA-15-based materials. Surface modification often targets the uniform dispersion of active units—such as chromophores or metal complexes—spatially separated by passive spacers. This is typically achieved through a multi-step synthetic approach following the concept of a "2D solid solvent," where the mesoporous matrix acts as a dynamic platform for attaching desired functionalities [138, 139].

For example, our group has explored SBA-15 functionalized with propyl-phosphonate or propyl-carboxylic acid groups. The relative concentrations of these functionalities can be finely tuned by adjusting the ratio of conventional silica precursors to organosilane-functionalized precursors. Such precise control enables specific applications: phosphonic acid units are well-suited for binding divalent metal ions, while carboxylic acid groups are more appropriate for monovalent ions.

Similarly, other types of lanthanide ions have been linked to modified meta-aminobenzoic acid in MCM-41 to enhance luminescence properties [140]. Various metal nanocrystals have also been successfully grown within the mesoporous channels of silica, including semiconductor materials such as PbS [141], CdS, CdSe [142], and GaN [143], as well as noble metals like gold (Au) [144]. In addition to metal-based species, a variety of organic chromophores such as azo dyes [145]—and other nonlinear optical molecules have also been incorporated into mesoporous silica frameworks [125, 146]. Functionalization, therefore, plays a crucial role in enhancing the performance of mesoporous silica-based systems. It extends their applicability across various domains—including catalysis, sensing, adsorption, and nanocarrier technologies—by allowing for tailored interactions at the molecular level [147, 148].

Despite these advances, the potential of mesoporous silica as a nonlinear optical material remains underexplored. With careful functionalization and rational design strategies, ordered mesoporous silica offers untapped opportunities in NLO applications. Further research is warranted to optimize these materials for high-performance photonic devices and to better understand the structure–property relationships that govern their optical behaviour.

2. **Coordination metal and Organometallic Complexes chromophores materials for nonlinear optics (NLO):**

   The main difference between coordination complexes and organometallic complexes lies in the type of bonding between the metal and its ligand. For organometallic complexes, the metal center is directly bonded to at least one carbon atom; on the other hand, coordination complexes do not possess metal-carbon bonds in their primary coordination sphere.

   Metal-ligand charge transfer (MLCT) transitions are the source of the nonlinear optical (NLO) properties of organometallic compounds. The vast tunability of these systems, whether by varying the metal center, oxidation state, coordination environment, or ligand structure, enables a massive spectrum of potential SHG-active compounds.

   - Metal choice: Transition metals like Ru, Os, Pt, and Ir are often used due to their strong MLCT transitions.
   - Ligand design: Electron-donating and withdrawing groups can tune the electronic structure. Chelating ligands (bipyridines, phenanthro- lines, terpyridines, Schiff bases) help stabilize the complex and enhance charge transfer.
   - Delocalization and symmetry: Extended π-systems, such as those in stilbazoles or alkynyl ligands, can improve polarizability, while asymmetric coordination environments can enhance SHG.

4 Synthesis of Ordered Mesoporous Silica SBA-15 functionalized with copper-phosphonate functional groups in powder and thin film form

The first stage of the research consists of the synthesis of functionalized mesoporous silica materials. This was achieved via a co-condensation approach to incorporate anchored propyl-diethyl phosphonate groups directly onto the silica inner pore surface with varying concentrations. Following this, the initial materials were silylated to deactivate residual silanol groups, effectively converting them into passive spacers. This step was essential to prevent unwanted interactions during the subsequent coordination of copper transition metal ions to the anchored functionalities. The synthesis of functionalized SBA-15 powders was carried out using a modified sol-gel method, while their thin film analogues were prepared through a modified dip-coating technique. Both material forms—powder and thin films—were synthesized with varying concentrations of the functional groups to evaluate structure–property relationships across different loading levels.

4.1 Materials and reagents

In all experimental syntheses, the highest purity reagents available were used. Tetraethyl orthosilicate (TEOS), Pluronic P123 ($EO_{20}PO_{70}EO_{20}$), chlorotrimethylsilane (ClTMS), copper(II) acetylacetonate ($Cu(acac)_2$), diethylphosphonate propyl triethoxysilane (PPTES), and bromotrimethylsilane (BrTMS) were purchased from Sigma-Aldrich (USA). Sodium fluoride (NaF) was purchased from Merck Ltd., tetrahydrofuran (THF), hydrochloric acid (HCl) from Chempur Ltd., and toluene ($C_6H_5CH_3$) from Poch Inc.

All solvents were dried and distilled prior to use to ensure anhydrous conditions.

Before dip-coating, standard glass substrates were thoroughly cleaned with distilled water and then ethanol in an ultrasonic bath, which was repeated several times to ensure surface cleanliness and the removal of organic or particulate contaminants. The dip-coating process was carried out in a custom humidity-controlled chamber with a humidifier, a thermometer, and a humidity sensor. This setup maintained a stable and appropriate drying environment for the dip-coated films.

4.2 Synthesis procedure of powdered SBA-15 with copper-phosphonate functional groups

The synthesis of SBA-15 silica containing propyl-copper-phosphonate units (SBA-POO_2Cu) involves a carefully controlled process to ensure the precise concentration of functional groups. The synthesis was conducted under an argon atmosphere, high-purity reagents were employed, including triblock copolymer Pluronic P123, tetraethyl orthosilicate (TEOS), bromotrimethylsilane (BrTMS), chlorotrimethylsilane (ClTMS), copper acetylacetonate ($Cu(acac)_2$) and phosphonate-propyl- diethyltriethoxysilane (PPTES). In the first stage, TEOS and PPTES were added to the 360 ml of 3.83 mM Pluronic P123 aqueous solution. The amounts and proportions of these reagents depend on the expected concentration of the functional groups in the silica matrix and are shown for all the samples tested in the Table 4.1.

Tab. 4.1. Molar composition of TEOS and PPTES for different concentrations of functional groups.

Concentration	20%	10%	5%	2.5%	1.25%
TEOS [mmol]	71.8	80.8	85.3	87.6	88.9
PPTES [mmol]	18.0	9.0	4.5	2.3	1.13

The pH of the aqueous solution was set at 1.5 using HCl. After stirring for two hours, 10mM of NaF was added to this mixture to induce hydrolysis and polycondensation. The materials were then immediately heated to 60°C in a hot oil bath and stirred at this temperature for 48 h under a reflux condenser. The resulting materials were filtered and washed with ethanol. The surfactant was removed by ethanol extraction in a Soxhlet apparatus for eight hours. The materials obtained contained the phosphonic ester units which were transformed to copper phosphonate units in three next steps silylation, hydrolysis, and copper functionalization. The subsequent stages of synthesis are shown in Figure 4.1.

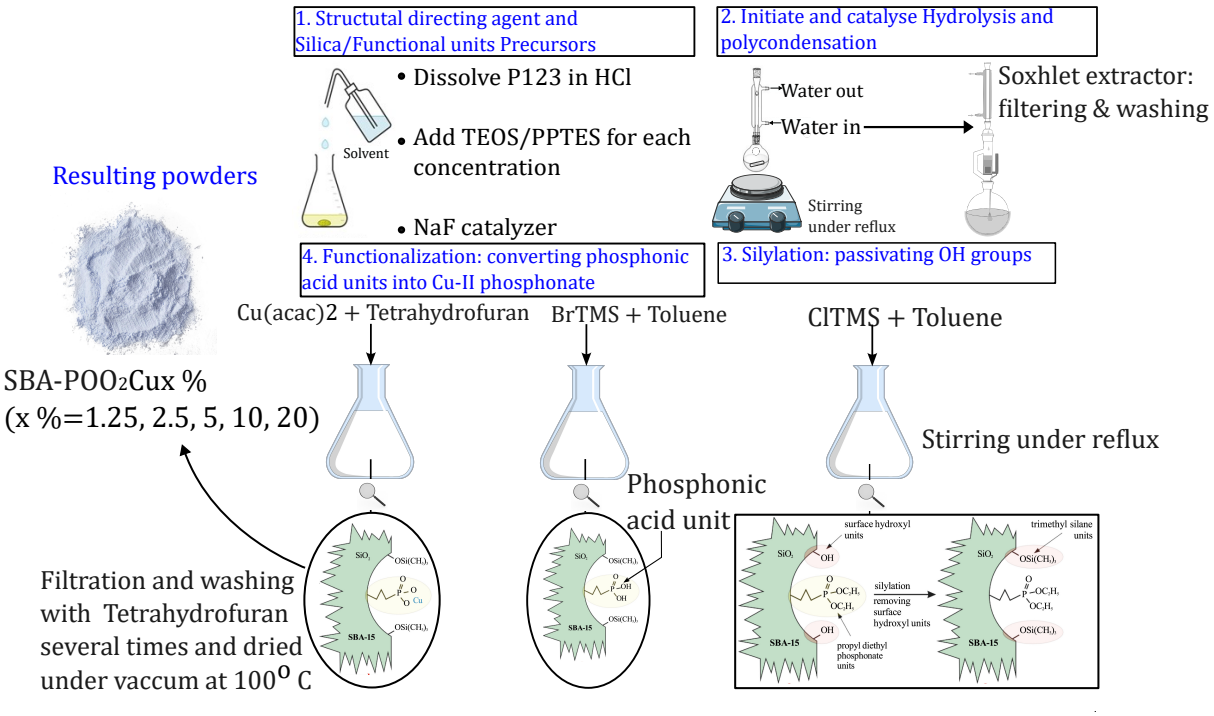


Fig. 4.1. Schematic illustration of the synthesis procedure SBA-POO_2Cu powders.

The silylation procedure was applied to protect the phosphonic acid groups from the side reactions during hydrolysis [149]. In this procedure resulting powder was treated with a 221 mM chlorotrimethylsilane (ClTMS) toluene solution. For each gram of silica powder 50 ml of the solution was used. The samples were refluxed for 12 h, and then washed with toluene and dried.

Next, the selective two-step hydrolysis was performed to convert ester units into phosphonic acid groups [150]. The samples were stirred in 15.4 M bromotrimethylsilane (BrTMS) toluene solution under a reflux condenser for 24 h. About 50 ml of toluene solution was used per one gram of dry silica powder. Next, the samples ware washed with toluene, dried, and placed under a reflux condenser again, this time with methanol

for 5 h. After that the resulting powder was filtered and dried.

The last step was the introduction of copper ions to the silica matrix. In this procedure, 2 mM $Cu(acac)_2$ tetrahydrofuran solution was used. About 50 ml of the solution was used per gram of dry silica powder. The samples were mixed with the solution and placed under a reflux condenser overnight. The resulting solid samples denoted SBA-PO_2CuX%, were recovered by filtration and washed several times with THF to remove excess copper salts. Then the samples were dried under vacuum in 100°C.

X% in the sample name represents the different concentration of the propyl-copper phosphonate functional groups. For the purposes of the studies presented here, five different molar concentrations ranging from 1.25% to 20% were prepared. By the concentration of functionalization we mean the proportion of SiO_2 and OSiR groups. Where R denotes the propyl-copper-phosphonate units. The molar concentration given in the sample names refers to the ratio between SiO_2 and OSiR groups and is as follows :

- SBA-PO_2Cu20% refers to silica SBA-15 with 20 mol% of propyl-copper-phosphonate groups, where the ratio between the functional precursor OSiR and SiO_2 used during the synthesis was 1:4.

4.3 Synthesis procedure of ordered mesoporous silica thin films with copper-phosphonate functional groups

In the first step of the procedure, the solution of ethanol, water, and HCl was prepared by mixing water and ethanol in a weight ratio of (2,5:2) and adding HCl to obtain 1,25 pH. To 5ml of this solution TEOS and PPTES were added in molar proportions given in Table 4.1. The solution was kept stirring for 2 h. At the same time, a second solution consisting of a 3 mM ethanol solution of P123 was prepared in a separate container. The second solution was kept stirring also for 2 h. After mixing the two solutions for two hours, they were combined by adding 70 ml of the second solution to the first solution. The sol obtained was stirred for a further 3 hours followed by the addition of 4 grams of aqueous hydrochloric acid solution at pH=1.25. After aging the sol for 2 h dip-coating deposition of the thin film started. The sol preparation steps and following deposition procedure are shown in Figure 4.2.

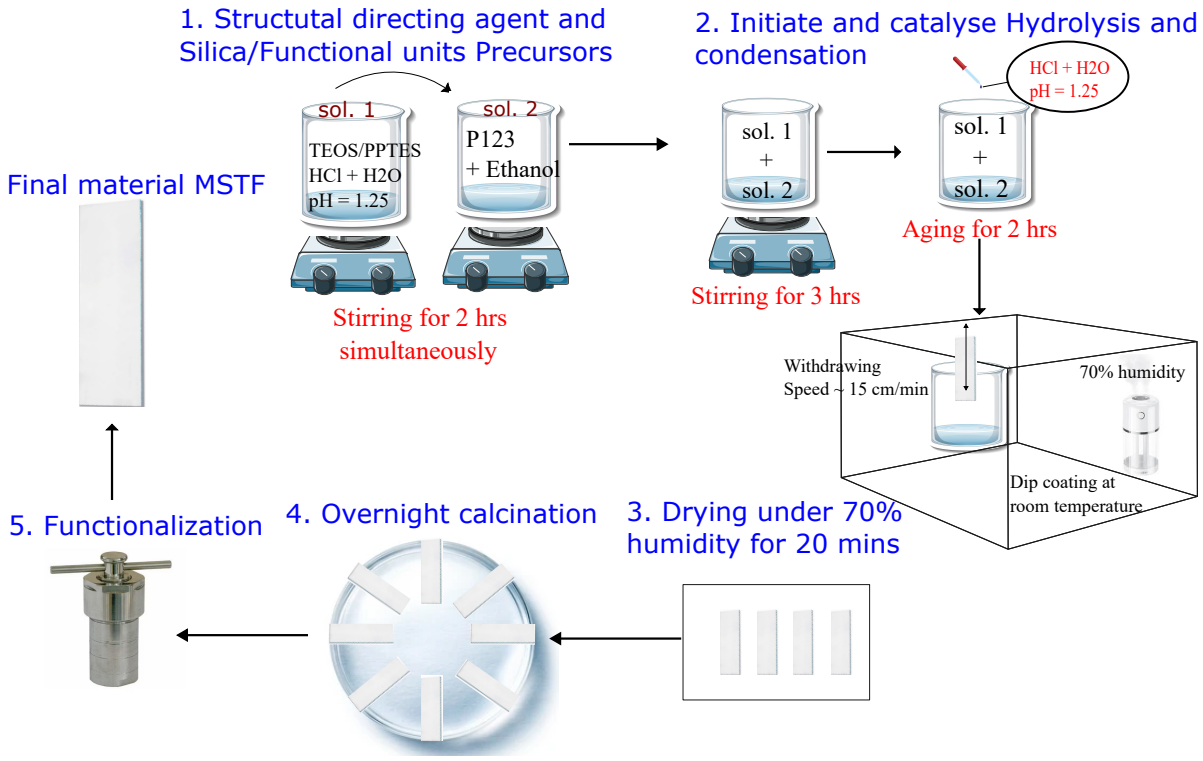


Fig. 4.2. Schematic illustration of the preparation procedure MSTF-POO_2Cu thin films.

To obtain thin films of good quality, the relevant parameters of the dipping procedure were selected, and the closed-chamber dip-coater was used. The glass substrates were dipped into the sol solution and withdrawn at a constant speed of 15 cm per minute

in a closed chamber with a relative humidity of 70% and a temperature of 22°C. Next, the substrates were left for 20 minutes in the chamber for proper thin film formation. All thin films obtained were aged overnight at 100°C and after that, the surfactant was removed by ethanol extraction. At this stage of the preparation procedure, thin films containing phosphonic ester groups were prepared. To obtain mesoporous silica thin films with copper phosphonate groups a three-step procedure as described for powdered samples was applied.

5 Comprehensive characterization of structure and molecular composition obtained materials - confirmation of synthesis assumptions

This chapter will provide a comprehensive characterization of the synthesized mesoporous silica materials, with a focus on structural integrity, porosity, morphology, and chemical composition. The mesoporous architecture is first evaluated using transmission electron microscopy (TEM) to confirm the presence of ordered pore systems. Scanning electron microscopy (SEM) complements this analysis by providing information about the morphology of powder grains and the surface topography of thin films. Textural properties, such as pore volume and specific surface area, will be determined through nitrogen physisorption measurements. Small-angle X-ray scattering (SAXS) and grazing-incidence SAXS (GISAXS) are used to determine the degree of spatial ordering within the pore structure. Energy-Dispersive X-ray Spectroscopy (EDS) is used to investigate the elemental composition and uniform distribution of the samples, both qualitatively and quantitatively. Finally, Raman spectroscopy is used to confirm that the molecular architecture obtained matches the structure envisioned during the synthesis planning.

5.1 Electron Microscopy

Electron microscopy (EM) exploits the short de Broglie wavelength of high-energy electrons to achieve nanoscale to atomic resolution. The high resolving power of electron microscopes stems from the wave–particle duality of electrons, described by the de Broglie relation:

$$\lambda = \frac{h}{p} \tag{5.1}$$

where λ is the de Broglie wavelength, h is Planck's constant and p is the momentum of the particle.

Since momentum is the product of mass and velocity, the relation can be rewritten as:

$$\lambda = \frac{h}{mv} \tag{5.2}$$

where m is the mass and v is the velocity of the particle.

The accelerating voltage (or electron potential) determines the velocity of electrons and thus their kinetic energy and momentum.

$$eV = \frac{1}{2}mv^2 \tag{5.3}$$

hence

$$v = \sqrt{\frac{2eV}{m}} \tag{5.4}$$

where e is the elementary charge (1.602×10^{-19} C), m is the mass of the electron (9.109×10^{-31} kg), and V is the accelerating voltage in volts.

The accelerating voltage increases the electron's velocity and momentum, resulting in a shorter de Broglie wavelength. This explains why electron microscopes can achieve such high spatial resolution.

In Transmission Electron Microscopy (TEM), electrons are typically accelerated at 100–300 kV, resulting in wavelengths of about 0.002–0.005 nm and enabling sub-nanometer resolution. Scanning Electron Microscopy (SEM) operates at lower voltages, usually 1–30 kV, giving electron wavelengths around 0.1–0.5 nm and providing surface resolution down to a few nanometers. The choice of the accelerating voltage is carefully selected, depending on the type of the sample under investigation [151].

Both techniques require high-vacuum environments to minimise electron scattering by air molecules and ensure stable beam propagation. This greatly exceeds conventional light microscopy's resolution limits, allowing for detailed imaging of nanoscale structures

Electron Microscopy techniques, including TEM and SEM, were employed to investigate both the internal structure and surface morphology of the synthesized porous silica-based hybrid materials. TEM is a high-resolution technique ideal for imaging nanostructures and internal features, such as the pore arrangement in SBA-15, where pore sizes are typically less than 7 nm. It operates by transmitting a beam of electrons through an ultrathin sample. Contrast in TEM images arises from differences in electron density and sample thickness—denser or thicker regions scatter more electrons and appear darker. The use of electromagnetic lenses and a fluorescent screen enables highly magnified visualization of internal features critical to understanding the geometry and distribution of pores (See Figure 5.1).

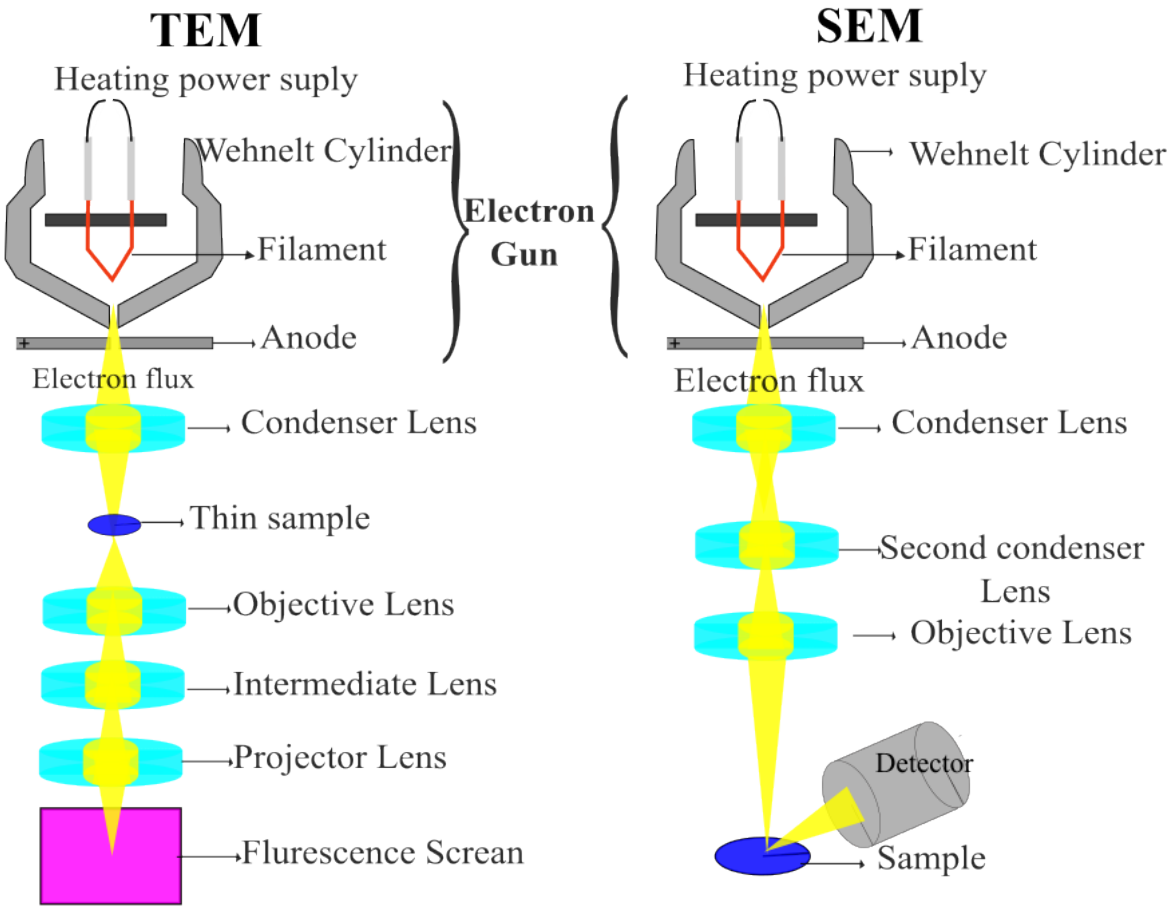


Fig. 5.1. Schematic diagram of Transmission Electron Microscope and Scanning Electron Microscope.

In contrast, SEM provides high-resolution, 3D images of sample surfaces by scanning a focused electron beam (5–50 nm in diameter) across the surface. SEM does not transmit electrons through the sample but instead collects secondary and backscattered electrons emitted from the surface, providing insights into surface texture, morphology, and particle distribution.

To prevent charging effects in non-conductive silica films, samples were coated with a thin conductive layer (e.g., gold or carbon).

Differences of TEM and SEM techniques :

- TEM reveals internal structure at near-atomic resolution, requires ultrathin samples, and provides 2D projections of internal features.
- SEM excels in surface imaging and 3D morphology but has lower resolution and cannot visualize internal features unless the sample is fractured or etched.

Similarities of TEM and SEM techniques :

- Both use high-energy electron beams and electromagnetic lenses for image formation.
- Both require high-vacuum environments and careful sample preparation.

• Both are essential tools for nanoscale characterization of hybrid porous materials.

Together, TEM and SEM provided complementary information. TEM was used to confirm the presence and arrangement of mesopores, while SEM revealed surface morphology, homogeneity, and macroscopic features of the thin films and SBA-15 silica grains.

Transmission electron microscopy imaging was performed using a JEOL JEM-3010 high-resolution transmission electron microscope (JEOL Ltd., Tokyo, Japan) operated at acceleration voltage of 300 kV. The microscope was equipped with a LaB6 electron emission source and Gatan 2k×2k Orius^{TM} 833 SC200D CCD camera (Gatan Inc., Pleasanton, CA, USA). The sample preparation for TEM analysis involved dispersing a small amount of powder sample in isopropanol to form a well-diluted suspension. In order to prepare the suspension, the powder samples did not require any treatment, while thin layers had to be scraped off the substrate. A few drops of the suspension were placed on a carbon-coated copper TEM grid and left to dry at room temperature before imaging.

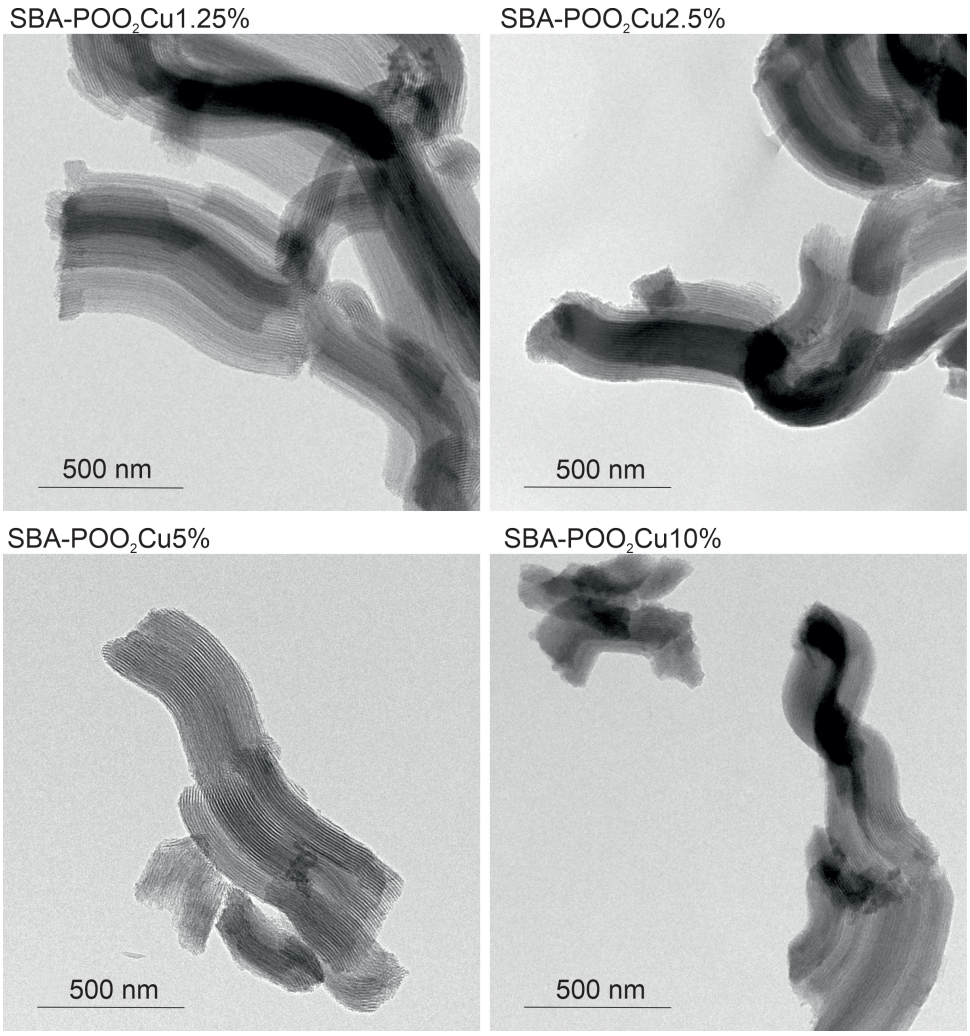


Fig. 5.2. TEM images of SBA-POO_2Cu1.25%, SBA-POO_2Cu2.5% , SBA-POO_2Cu5%, and SBA-POO_2Cu10%.

Transmission Electron Microscopy of both powder and dip-coated thin film samples revealed a well-organized hexagonal mesoporous structure (Figure 5.2 and Figure 5.3), characteristic of SBA-15-type silica. This demonstrates the successful formation of a long-range periodic framework with well-defined 2D packing. While such structural order is commonly observed in powders, achieving similar organization in dip-coated thin films is more challenging due to substrate interactions and drying-related constraints. However, our method proved to be effective, as illustrated in Figure 5.3. At all concentrations, mesopores were arranged in a well-defined hexagonal pattern oriented parallel to the glass substrate. Mesochannel alignment is visible in all TEM images, demonstrating the effectiveness of our controlled dip-coating and humidity-assisted drying approach in directing mesostructural order at the film-substrate interface.

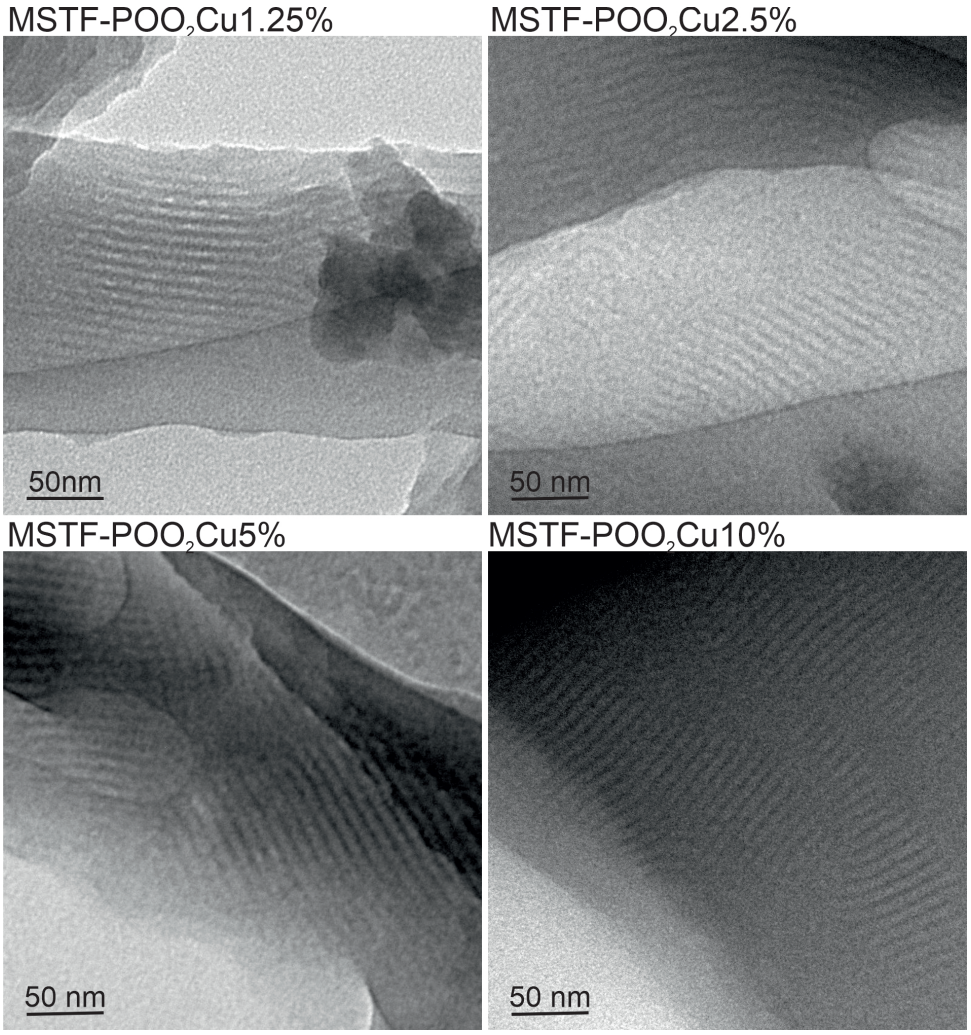


Fig. 5.3. TEM images of MSTF-POO_2Cu1.25%, MSTF-POO_2Cu2.5%, MSTF-POO_2Cu5%, and MSTF-POO_2Cu10%.

The surface morphology of the samples at different concentrations was examined using the scanning electron microscope (Tescan Vega 3, Brno, Czech Republic), while the cross-

section of the thin films was examined by SEM (JEOL JSM-IT 500 HR) at the LCPME facility.

Before imaging, the samples were sputter-coated with a thin layer of gold to enhance their electrical conductivity. Each sample was analyzed at multiple locations to assess structural homogeneity.

As depicted in Figure 5.4, the SEM images of all powder samples revealed no significant differences in the granular morphology of the SBA-15 particles, indicating a consistent and homogeneous structure across all concentrations. Increasing the concentration of the functionalizing agent did not affect the particle shape or surface texture.

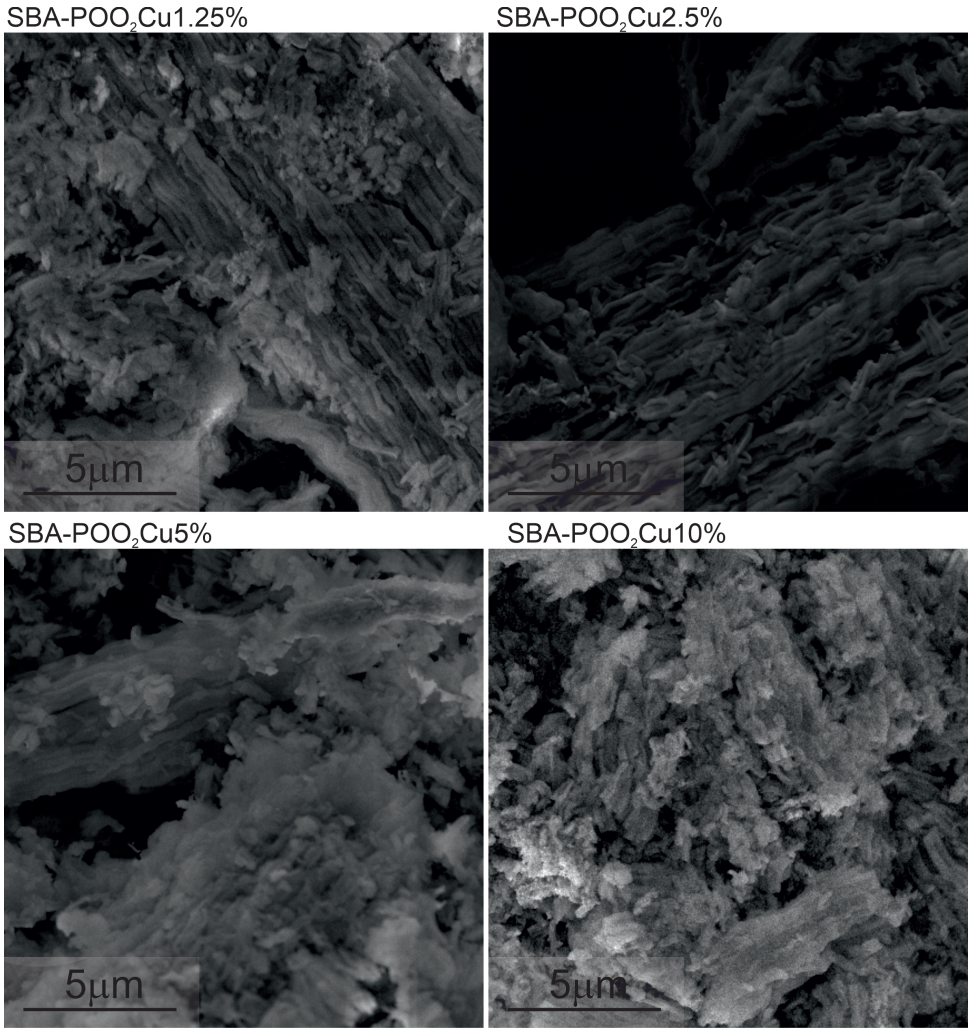


Fig. 5.4. SEM images of SBA-POO_2Cu1.25%, SBA-POO_2Cu2.5%, SBA-POO_2Cu5%, SBA-POO_2Cu10%.

Regarding thin films, Figure 5.5 presents both cross-sectional and surface SEM images of the mesoporous silica thin film. Only representative SEM images are shown, since the four thin-film samples with 1.25%, 2.5%, 5%, and 10% concentrations of the functional groups exhibited a similar morphology.

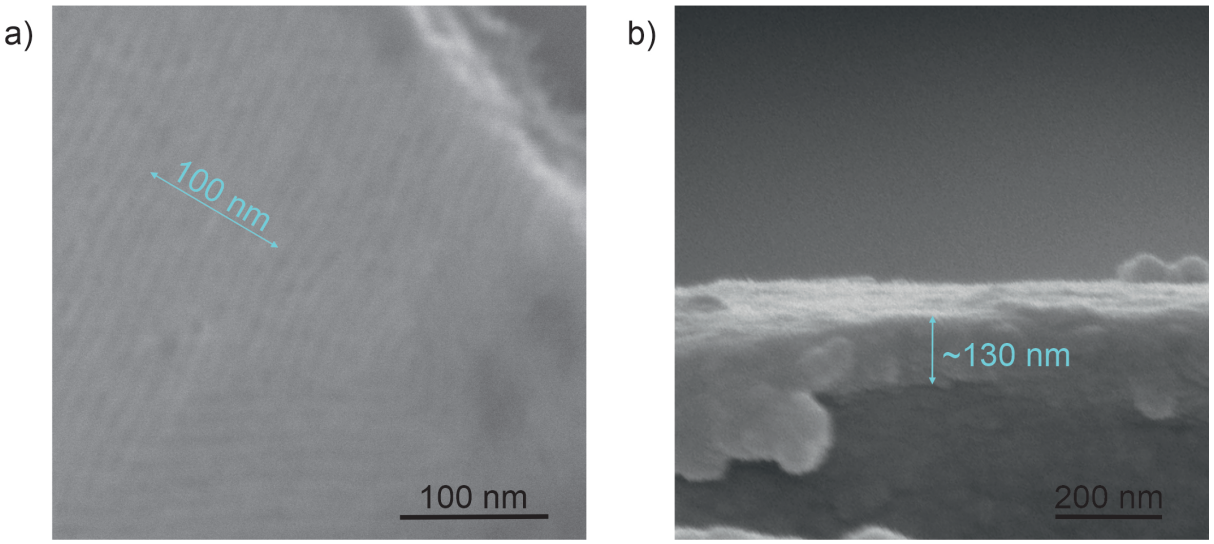


Fig. 5.5. SEM images of mesoporous silica thin film MSTF-$POO_2Cu5\%$ surface (a), and cross section (b).

The images confirm a well-defined two-dimensional pore arrangement, with mesopores oriented parallel to the substrate surface. The film thickness was measured to be approximately 130 nm. No signs of structural deformation were observed on the film surface or at the film–substrate interface, suggesting good adhesion. Moreover, no silica sphere aggregates were detected on the film surface, which are often observed in films prepared by electrochemical-assisted self-assembly (EASA), as reported, for example, by Moehl et al. [152].

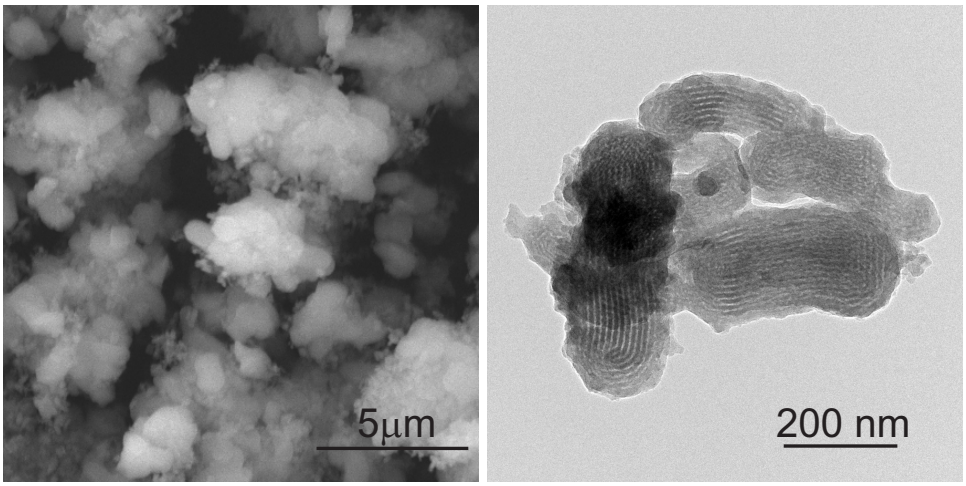


Fig. 5.6. SEM and TEM images of SBA-$POO_2Cu20\%$

The samples presented above with four different concentrations of functional groups were not the only ones prepared as part of this work. In order to test the upper limit of the concentration of functional groups at which the sample still retains its intended

properties, a sample in powder form with a concentration of 20% was prepared. The SEM and TEM images (Fig. 5.6) of sample SBA-POO_2Cu20% with the highest concentration of functional groups showed significant differences in the morphology of silica grains. In comparison to the samples with lower concentrations of functional groups, the silica grains are smaller and not very well defined. A detailed characterization of the sample SBA-POO_2Cu20% showed that an excessive concentration of precursors with functional groups disrupts the self-assembly of the silica network around the supramolecular template during the co-condensation process and causes the material obtained to differ from other samples with lower concentrations. This was the reason why thin layers with a 20% concentration of functional groups were not prepared.

TEM analysis confirmed the internal pore ordering of the SBA-15 nanostructured material in all of the tested samples, including thin films. Up to a functional group loading of 10%, the highly ordered mesoporous structure with parallel pore channels in the thin films remained unaffected by silica matrix functionalization. Beyond this concentration, the powder samples showed slight pore shrinkage, so preparing thin films with a 20% functional group loading was unnecessary.

SEM, on the other hand, provided detailed insights into surface morphology, demonstrating that up to 10% loading, the samples maintained similar structural and morphological features, with no significant variation in film thickness or grain morphology. Overall, this study shows that thin films and powders have similar morphological and structural properties within the functionalization range studied.

5.2 Energy-Dispersive X-Ray Spectrometry (EDS)

Energy-dispersive X-ray spectroscopy (EDS) is an analytical technique widely used in conjunction with scanning electron microscopy (SEM) or transmission electron microscopy (TEM) for elemental composition analysis of solid materials. Its operating principle is based on the detection of characteristic X-rays emitted by a sample when it is irradiated with a focused high-energy electron beam. These interactions provide valuable qualitative and quantitative information about the chemical elements present in the analyzed region.

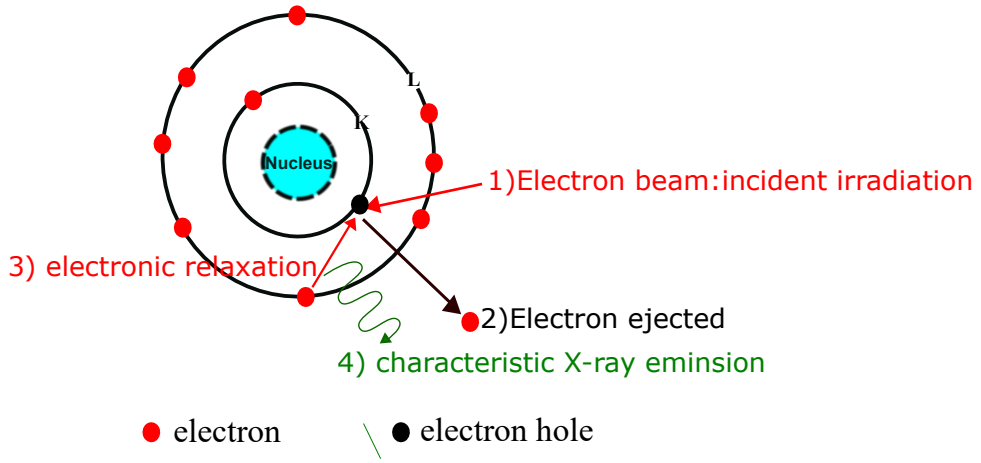


Fig. 5.7. EDS principle based on characteristic X-ray emission resulting from electron irradiation.

As illustrated in Figure 5.7, the EDS principle involves a sequence of fundamental physical processes. When the incident electron beam interacts with atoms in the sample, it can eject electrons from the inner shells, creating electronic vacancies. To restore electronic equilibrium, electrons from higher energy levels transition into these lower energy vacancies. This relaxation process results in the emission of X-ray photons with energies characteristic of the specific elements involved. These characteristic X-rays are then detected and analyzed by an energy-dispersive spectrometer, allowing the identification and quantification of the elements present in the sample.

Energy-dispersive X-ray spectroscopy also offers elemental mapping capabilities that enable the selection of specific regions within the imaged sample to generate spatial distribution maps of individual elements. This technique provides insight into the composition, distribution, and homogeneity of specific elements in the selected area, helping to determine where and how particular elements are spatially localized within the sample. This spatially resolved information is especially valuable in studies of heterogeneous materials, composite systems, or functionalized surfaces, where the presence, segregation, or

clustering of elements can significantly affect the properties of the material [153].

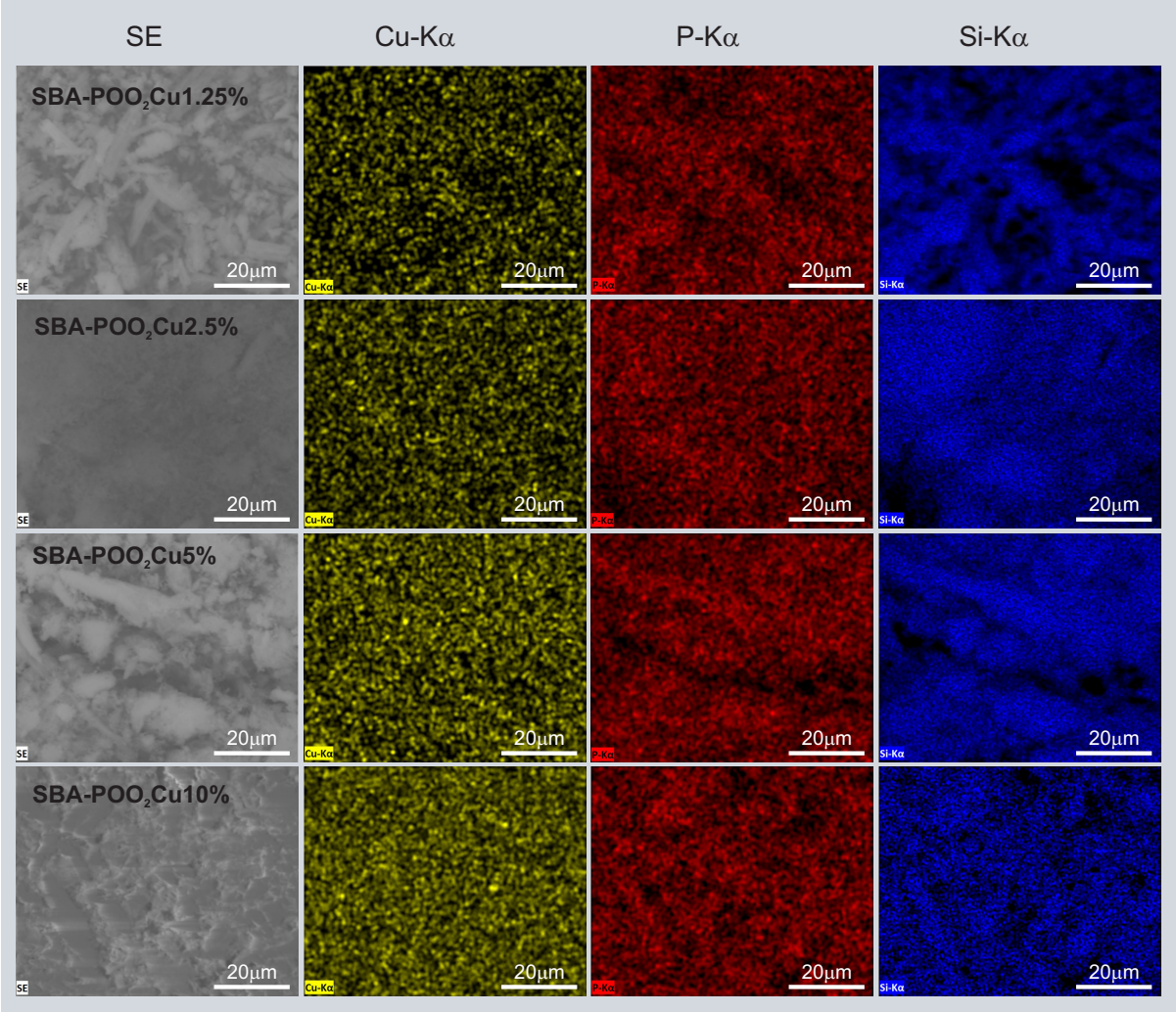


Fig. 5.8. SEM images and EDS maps of SBA-POO_2Cu powder samples with different concentrations of functional groups.

Figure 5.8 presents the elemental mapping results of SBA-POO_2Cu powders obtained via EDS analysis, confirming the uniform spatial distribution of copper, phosphorus, and silicon across all tested concentrations. The silicon elemental map closely reflects the morphology and grain distribution observed in the corresponding SEM images, indicating that the mapping accurately represents the silica matrix. The elemental maps reveal that copper and phosphorus are distributed uniformly across the silica grains, with no evidence of aggregation or phase separation. This suggests that the functional groups were well-dispersed within the porous matrix and likely anchored to the internal pore surfaces of the SBA-15 structure.

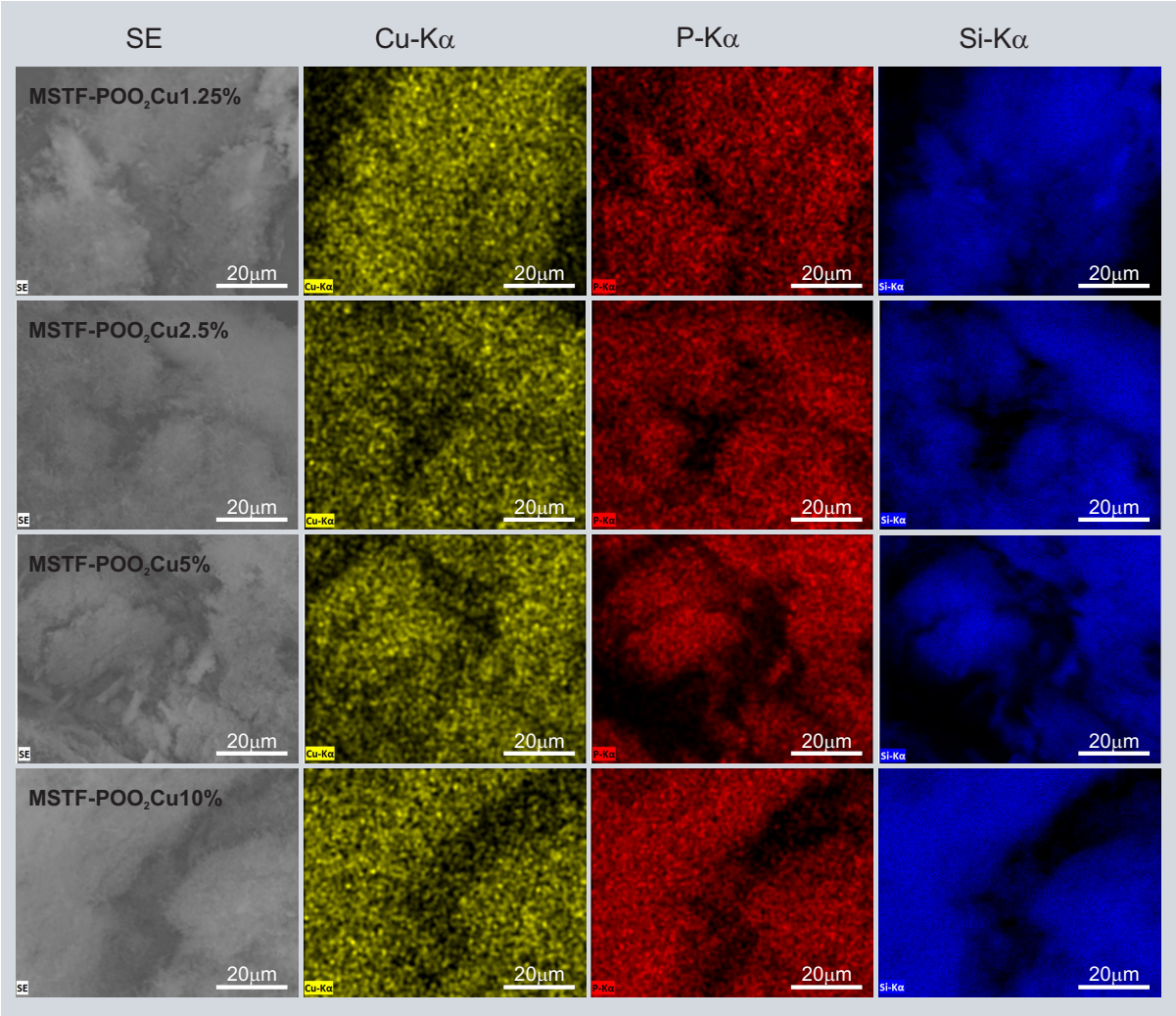


Fig. 5.9. SEM images and EDS maps of MSTF-POO_2Cu thin films with different concentrations of functional groups.

Similarly, Figure 5.9 shows the elemental distribution maps for the mesoporous silica thin films functionalized with copper-phosphonate groups. Due to the low thickness of the tested layers and the presence of a thick glass substrate, direct analysis of the material was difficult. Therefore, before measurement, the silica layer was carefully scraped off the glass substrate and placed on carbon adhesive tape. The elemental distribution in the thin films shows a similarly homogeneous presence of copper and phosphorus, aligned with the silicon framework. This confirms that the functionalization approach used in the dip-coating process resulted in spatially homogeneous incorporation of functional moieties across the film, preserving the structural uniformity. This study further confirms the reproducibility and effectiveness of the synthetic strategy for both powders and thin films of SBA-15-based materials.

Following the confirmation of elemental homogeneity through EDS mapping, quantitative EDS analysis was performed to evaluate the elemental composition of the SBA-

POO_2Cu powder samples. The EDS spectra of four representative samples with functional group concentration ranging from 1.25% to 10% are presented in Figure 5.10. These spectra confirm the presence of expected elements such as silicon, phosphorus, and copper in the investigated samples. For higher concentrations (10%, 5%, 2.5%) of functional groups, the maxima are well defined, while for the lowest concentration (1.25%), the amount of copper is at the detection limit.

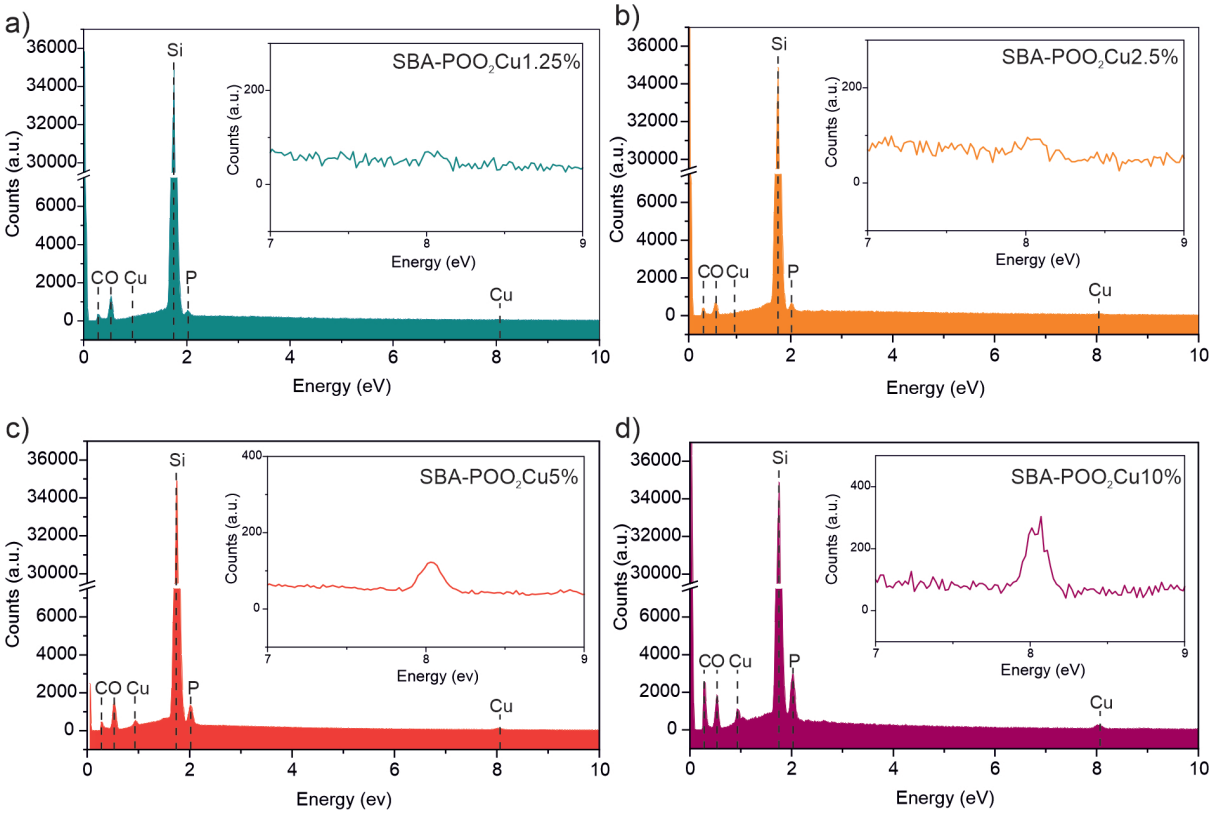


Fig. 5.10. EDS spectrum of a) SBA-POO_2Cu1.25%, b) SBA-POO_2Cu2.5%, c) SBA-POO_2Cu5%, d) SBA-POO_2Cu10%.

Quantitative EDS analysis enabled the estimation of the atomic percentage of copper, phosphorus, and silicon in the sample. Specifically, the Si:P and P:Cu atomic ratios were analyzed to assess the effectiveness of the synthesis and functionalization steps.

The Si:P ratio serves as an indicator of the incorporation efficiency of -$PO(OH)_2$ functional groups into the silica framework. As the concentration of propyl-copper-phosphonate increased from 1.25% to 10%, a systematic decrease in the Si:P ratio was observed, reflecting a greater presence of phosphorus relative to silicon. This trend confirms that the degree of functional group incorporation increased in accordance with the targeted precursor ratios.

Tab. 5.1. EDS elemental analysis results of SBA-POO_2Cu samples with functional groups concentration varying form 1.25% to 20%.

	Element content (At. %)			
	Si:P		P:Cu	
Sample	Si	P	P	Cu
SBA-POO_2Cu1.25%	98.7	1.3	46.7	53.3
SBA-POO_2Cu2.5%	97.7	2.3	48.9	51.1
SBA-POO_2Cu5%	95.0	5.0	50.9	49.1
SBA-POO_2Cu10%	87.9	12.1	50.0	50.0
SBA-POO_2Cu20%	81.9	18.1	63.0	37.0

In parallel, the P:Cu ratio provides insight into the stoichiometry of copper coordination. Since each -POO_2Cu group ideally contains one phosphorus and one copper atom, a P:Cu atomic ratio close to 1:1 was expected across all samples. The results obtained from EDS quantification are in good agreement with this theoretical ratio, confirming that copper was successfully coordinated to the phosphonate groups during post-synthetic modification. All EDS-derived atomic percentages are summarized in Table 5.1.

As part of the conducted research on the functionalization of SBA-15 powder samples, a material with a 20% loading of propyl-copper-phosphonate groups was also synthesized and characterized. Figure 5.11 presents both the EDS elemental maps and the corresponding spectrum for the SBA-POO_2Cu20% sample. The mapping confirms a homogeneous spatial distribution of silicon, phosphorus, and copper throughout the analyzed region, indicating uniform surface coverage at the microscale. However, quantitative EDS analysis revealed a deviation from the expected elemental ratios. While the Si:P and P:Cu atomic ratios in lower-concentration samples closely matched the theoretical values, the SBA-POO_2Cu20% sample exhibited a P:Cu ratio significantly above 1:1, suggesting that not every phosphonic acid group bound a copper ion (see Table 5.1). A more detailed discussion of this copper deficiency can be found in reference [150]. Because stoichiometric control could not be maintained and a consistent incorporation of copper ions was not achieved at the 20% loading level, this concentration was omitted from the analysis of the thin-film materials.

Similarly, in the case of thin film samples (MSTF-POO_2Cu), EDS spectral analysis was carried out to assess the elemental composition at various functional group concen-

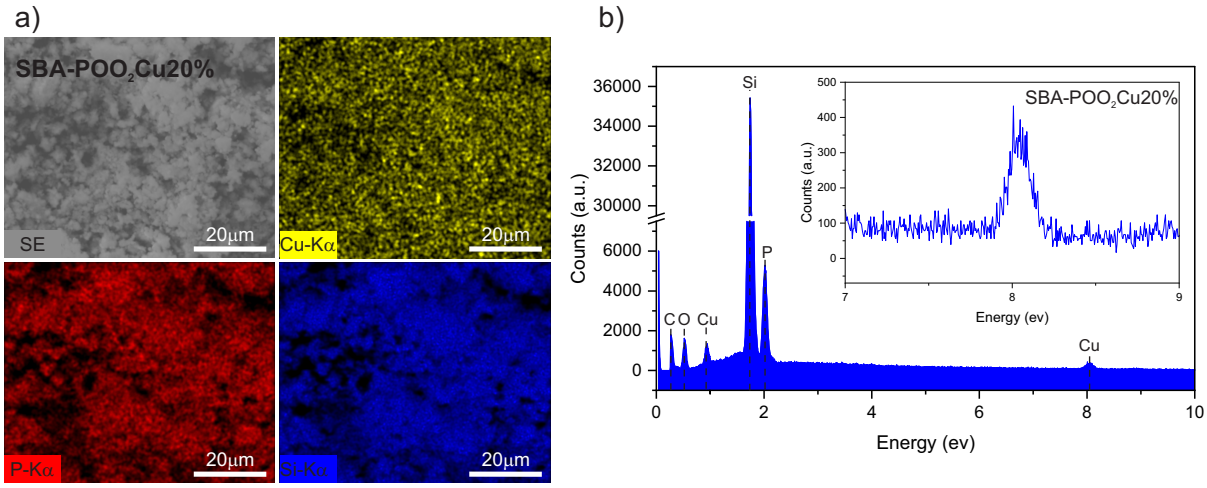


Fig. 5.11. SEM image and EDS maps (a), and spectrum (b) of SBA-POO_2Cu20%.

trations. Due to the limited thickness of the films and the relatively low sensitivity of EDS, direct analysis of the material on the glass substrate proved challenging. To improve signal clarity, the silica layer was carefully scraped off the substrate before measurement. This approach enabled more accurate detection of elemental peaks and estimation of atomic concentrations, as reported in Table 5.2.

Each of the spectra presented in Figure 5.12 shows variations in the intensity of characteristic peaks associated with the elements introduced through functionalization. The copper and phosphorus signals, are clearly visible in the spectra of the samples with the highest functional group concentrations. At lower loadings (2.5% and 1.25%), the peaks are noticeably less intense but still detectable, and the resulting atomic percentages remain reasonably consistent with expected values. In this context, EDS provides qualitative confirmation of the presence of functional elements, while the quantitative results, although somewhat limited by signal intensity, offer supportive evidence for successful modification.

The EDS quantification results closely match the expected theoretical values, indicating that copper was effectively coordinated with the phosphonate groups during the post-synthetic modification process. The atomic percentages obtained from EDS analysis are presented in Table 5.2.

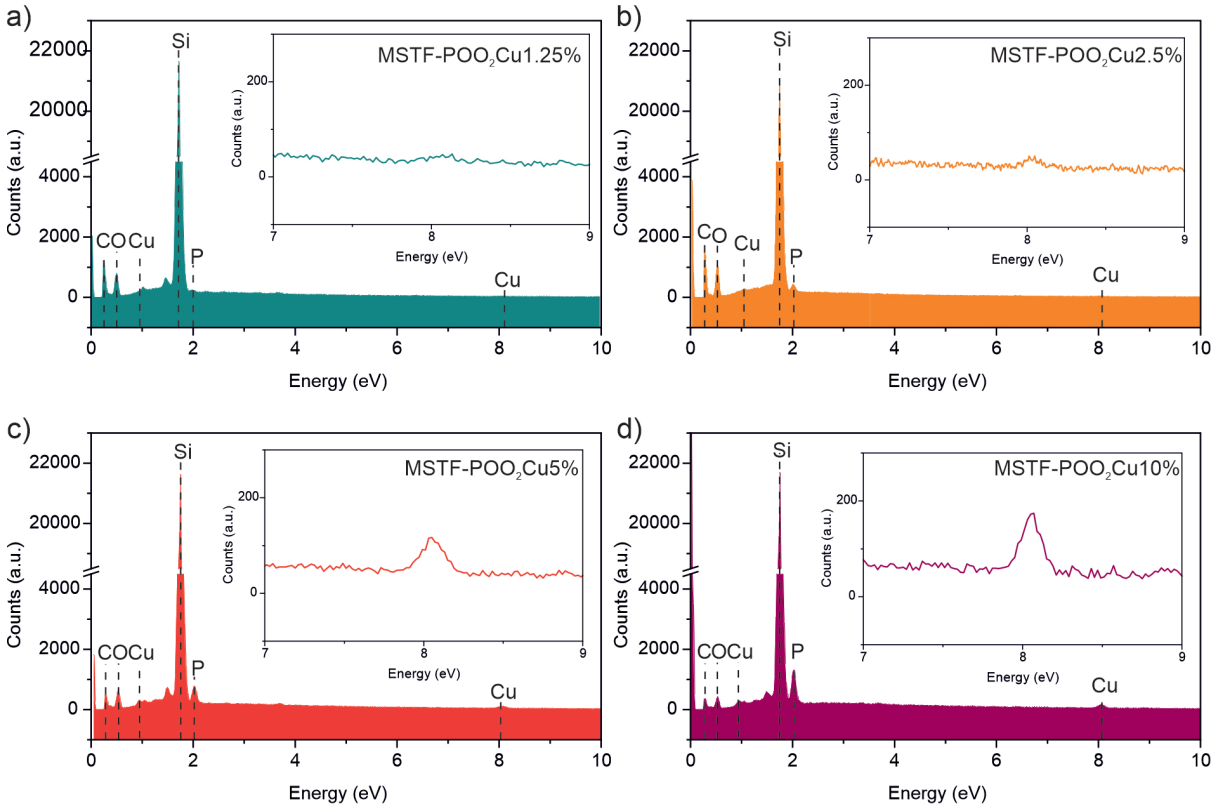


Fig. 5.12. EDS spectra of a) MSTF-POO_2Cu1.25%, b) MSTF-POO_2Cu2.5%, c) MSTF-POO_2Cu5%, and d) MSTF-POO_2Cu10%.

Tab. 5.2. EDS elemental analysis results of MSTF-POO_2Cu samples with functional groups concentration varying form 1.25% to 10%.

	Element content (At. %)			
	Si:P		P:Cu	
Sample	Si	P	P	Cu
MSTF-POO_2Cu1.25%	99.3	0.7	40.0	60.0
MSTF-POO_2Cu2.5%	96.6	3.4	48.9	51.1
MSTF-POO_2Cu5%	95.0	5.0	50.8	49.2
MSTF-POO_2Cu10%	91.2	8.8	56.7	43.3

In conclusion, EDS analysis confirmed a uniform and consistent elemental distribution within the mesoporous silica. The homogeneity of the copper–phosphonate configuration was maintained up to a functional group loading of 10%. Beyond this concentration, the ratio P: Cu changed from 1:1 to 1.7:1, indicating a possible change in the coordination

environment, with either two phosphonate groups coordinating a single copper ion, or the presence of less accessible phosphonate centers for copper ions in a less organized material. More importantly, the precursor concentrations assumed prior to synthesis corresponded to the final elemental compositions found in both powders and thin films. This consistency demonstrates the successful synthesis of thin films similar to their powder counterparts.

5.3 Nitrogen physisorption

When a porous solid sample is exposed to a gas such as nitrogen, commonly used because of its chemical inertness and well characterized behavior, the gas molecules move freely and collide with the internal surfaces of the pores. Upon contact with the surface, a gas molecule may either rebound into the gas phase or become temporarily adsorbed onto the surface.

This adsorption occurs due to weak intermolecular forces, specifically van der Waals interactions, between the adsorbate (gas molecule) and the adsorbent (solid surface). Because these forces are weak, the process is classified as physisorption (or physical adsorption), in contrast to chemisorption, which involves stronger chemical bonding. The enthalpy of physisorption is relatively low (typically less than 20 kJ/mol), meaning that gas molecules remain adsorbed for only a short period before desorbing.

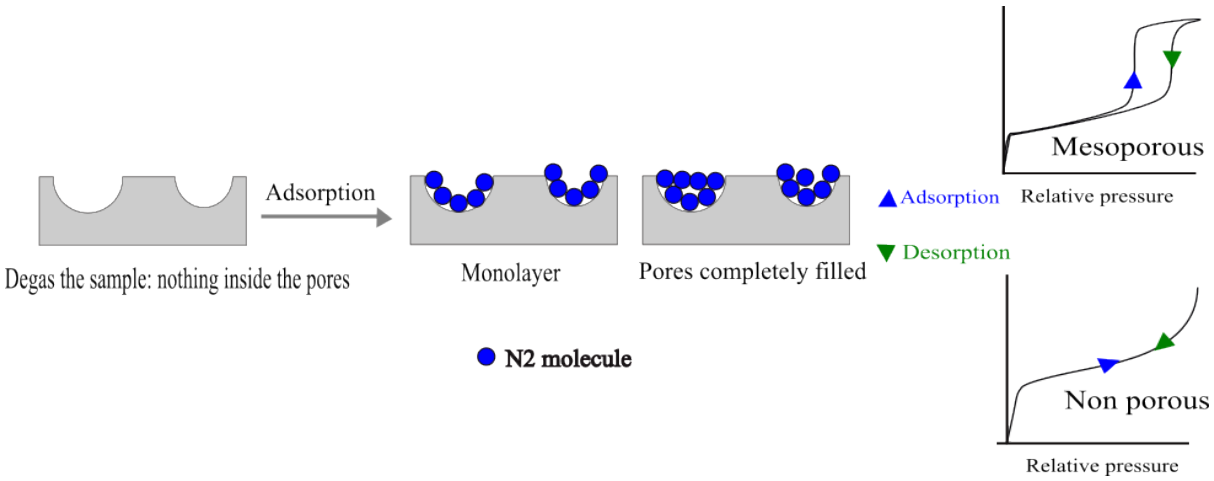


Fig. 5.13. Principles of Nitrogen Physisorption.

Desorption may occur spontaneously due to thermal motion, or as a result of an incoming gas molecule colliding with an already adsorbed molecule, displacing it from the surface. At any given pressure and temperature, a dynamic equilibrium is established between adsorbed and free gas molecules.

Early models, such as the Langmuir isotherm, were developed under the assumption of monolayer adsorption, where a single layer of gas molecules forms on the surface. While

conceptually useful, this model oversimplifies the behavior of physisorption in porous solids. In practice, multilayer adsorption occurs, especially at higher relative pressures and is more accurately described by the Brunauer–Emmett–Teller (BET) theory. The principle of nitrogen physisorption is illustrated in Figure 5.13.

In porous materials with a distribution of pore sizes, the adsorption process also involves capillary condensation in mesopores. It gives rise to a characteristic hysteresis between the adsorption and desorption branches of the isotherm. These features make nitrogen physisorption a powerful technique for probing the surface area, pore volume, and pore size distribution of porous materials.

According to the International Union of Pure and Applied Chemistry (IUPAC), hysteresis observed in nitrogen adsorption-desorption isotherms can be attributed to adsorption metastability and network effects. In materials with complex pore structures, desorption is often delayed due to pore blocking, especially in pores with narrow openings, such as those shaped like ink bottles. The geometry of the pores and their connectivity determine the shape of the hysteresis loop. Each type of pore network is associated with a characteristic loop shape, which can serve as a fingerprint for identifying the porosity of unknown materials. These loops provide valuable information about the size, shape, and internal architecture of pores [154].

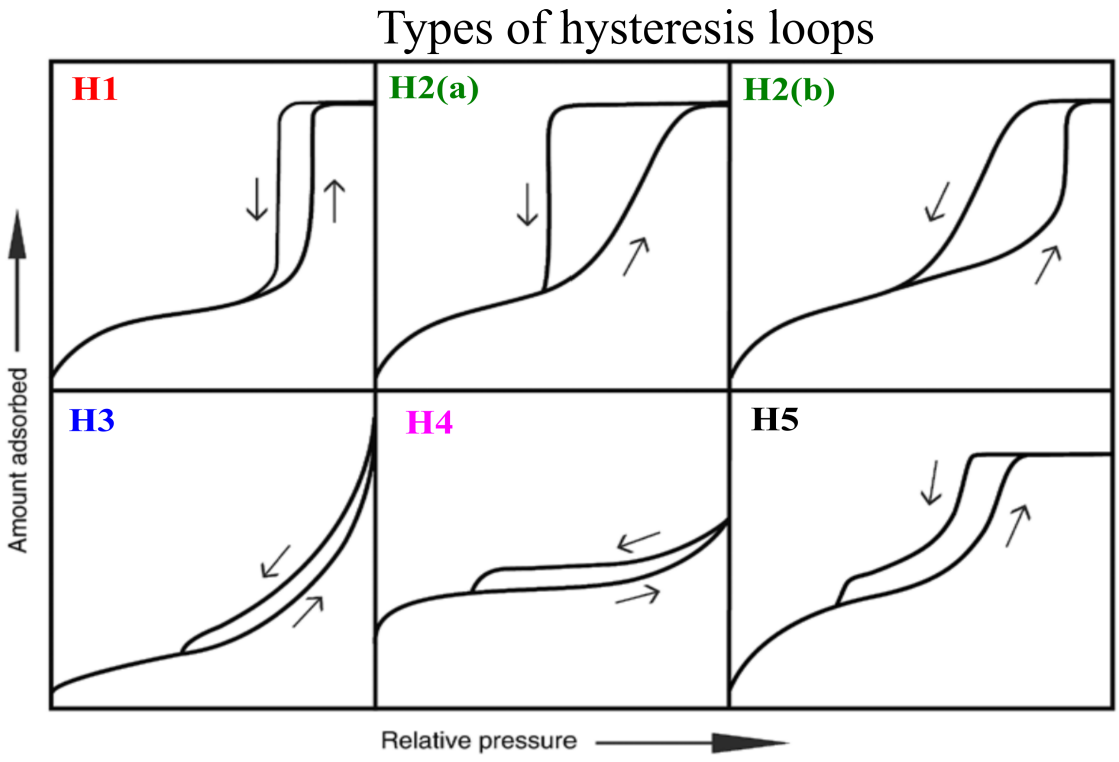


Fig. 5.14. Classification of hysteresis loops according to the IUPAC

According to IUPAC, hysteresis loops are categorized into five primary types (H1–H5),

each reflecting a distinct pore geometry or connectivity (Figure 5.14):

- H1: Typically observed in materials with well-ordered, uniform cylindrical mesopores, such as SBA-15 and MCM-41. The loop is steep and nearly vertical, reflecting the presence of highly regular pore channels with minimal pore connectivity complexity.
- H2: Associated with materials exhibiting complex pore networks.
  - H2(a) Indicates significant pore blocking or cavitation effects, typically observed in materials like silica gels, Vycor glass, and SBA-16.
  - H2(b) Reflects a broader distribution of pore neck sizes and higher structural disorder, seen in materials such as mesocellular foams or hydrothermally treated mesoporous silicas.
- H3: Characteristic of materials composed of non-rigid aggregates of plate-like particles or systems with slit-shaped macropores that do not fully fill with adsorbate. The isotherm typically resembles Type II and exhibits cavitation during desorption.
- H4: Similar in shape to H3 but also shows significant micropore filling at low relative pressures. This type is commonly found in micro-porous materials, such as zeolites and activated carbons.
- H5: A less common loop type associated with materials containing both open and partially blocked mesopores, for example, plugged hexagonal templated silicas.

In physisorption analysis, aside from the classification of hysteresis loops, an equally important concept is that of adsorption isotherms. An adsorption isotherm represents the relationship between the amount of gas adsorbed on a solid surface and the relative pressure (p/p_0) at constant temperature. In this context, p denotes the equilibrium pressure of the adsorbate, while p_0 refers to its saturation vapor pressure at the measurement temperature, which is typically 77 K for nitrogen. The shape of the isotherm offers important information about the type of porosity present in the material, indicating whether it is microporous, mesoporous, or macroporous, and also helps determine its surface area and the dominant adsorption mechanism.

Adsorption isotherms, which describe how gas molecules interact with solid surfaces at constant temperature, are classified by IUPAC into six main types (Types I–VI), each corresponding to a specific pore structure and adsorption mechanism. Type I isotherms are characteristic of microporous materials with pore widths smaller than 2 nm, where adsorption occurs rapidly at low relative pressures and reaches a plateau, indicating micropore saturation. Types II and III are generally associated with nonporous or macroporous materials, where gas molecules adsorb freely, without the influence of pore confinement. In contrast, Types IV and V are observed in mesoporous materials and are marked by multilayer adsorption followed by capillary condensation, often accompanied by a hysteresis loop. Type VI isotherms, rarely encountered, display stepwise multilayer adsorption

on highly uniform surfaces.

To investigate the sorption properties of SBA-15 samples functionalized with copper phosphonate at various concentrations, nitrogen physisorption experiments were conducted. Prior to measurements, the samples were degassed under vacuum at 110°C for 14 hours to remove adsorbed impurities. Nitrogen adsorption-desorption isotherms were recorded at 77 K using a Quantachrome Autosorb iQ automated gas sorption system to analyze the textural properties of the materials. The Brunauer–Emmett–Teller (BET) method was used to determine the specific surface area, while the Barrett–Joyner–Halenda (BJH) method was applied to calculate the mesopore size distribution. All data were analyzed using the ASiQwin software.

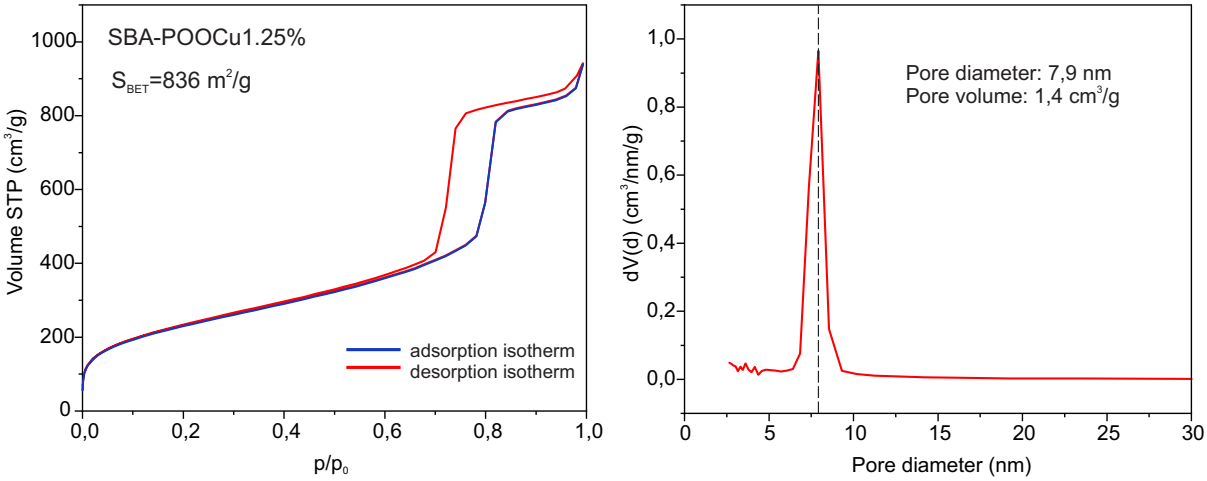


Fig. 5.15. Nitrogen adsorption–desorption isotherms of SBA–POO_2Cu1.25% and corresponding BJH pore size distribution plot.

In this study, SBA-15 was used as a mesoporous silica material characterized by a highly ordered hexagonal array of cylindrical mesopores with diameters ranging from 5 to 10 nm. During nitrogen physisorption at 77 K, SBA-15 typically displays a Type IV isotherm with an H1-type hysteresis loop, marked by steep and nearly vertical adsorption and desorption branches. This behavior is indicative of uniform cylindrical mesopores and open, unobstructed pore structures.

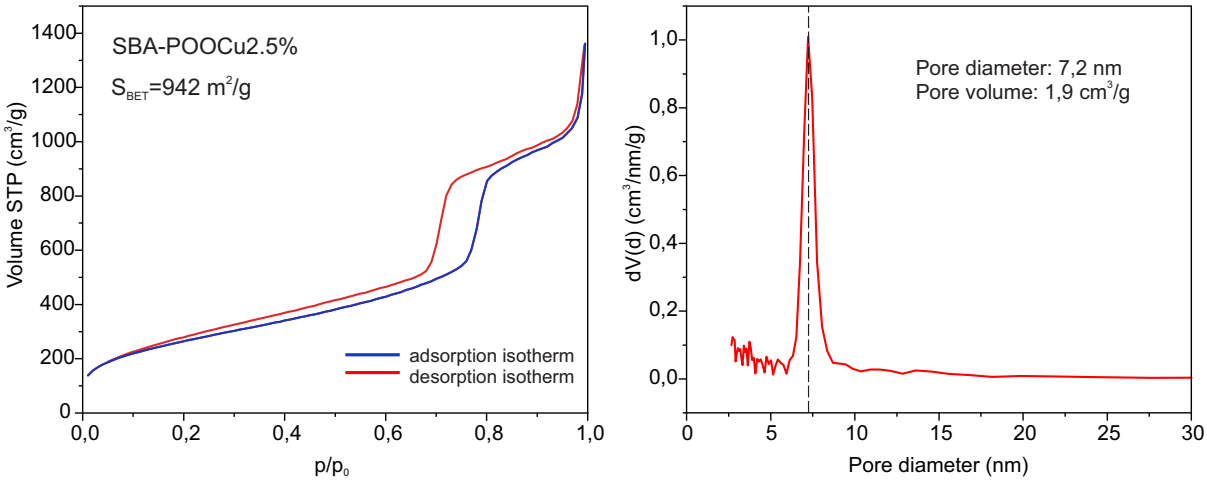


Fig. 5.16. Nitrogen adsorption–desorption isotherms of SBA–POO_2Cu2.5% and corresponding BJH pore size distribution plot.

The key variable among the studied samples is the concentration of copper phosphonate functional groups incorporated into the SBA-15 framework. Both the Brunauer–Emmett–Teller (BET) surface area and the pore volume distribution are influenced by the extent of functionalization.

The sample with the lowest copper phosphonate content (1.25%), shown in Figure 5.15, exhibits a specific surface area of approximately 836 m^2/g, a narrow pore size distribution with a maximum at 7.9 nm, and a total pore volume of 1.4 cm^3/g. Interestingly, this is not the lowest pore volume among the series. Upon increasing the functional group concentration to 2.5%, the specific surface area increases to 942 m^2/g, and the total pore volume rises to 1.9 cm^3/g. This trend may initially appear counterintuitive, as a higher concentration of functional groups is typically expected to reduce pore volume and surface accessibility due to pore blockage. However, at this moderate loading level, it is likely that the copper phosphonate moieties adopt a more extended conformation along the pore walls, enabling a more uniform coating without significantly obstructing the mesopore network. Consequently, nitrogen molecules retain access to the internal surfaces, resulting in an apparent increase in BET surface area. The slight reduction in average pore diameter at this stage reflects partial pore filling rather than complete blockage. Variations in experimental conditions, such as differences in degassing efficiency, may also contribute to the observed differences in textural parameters.

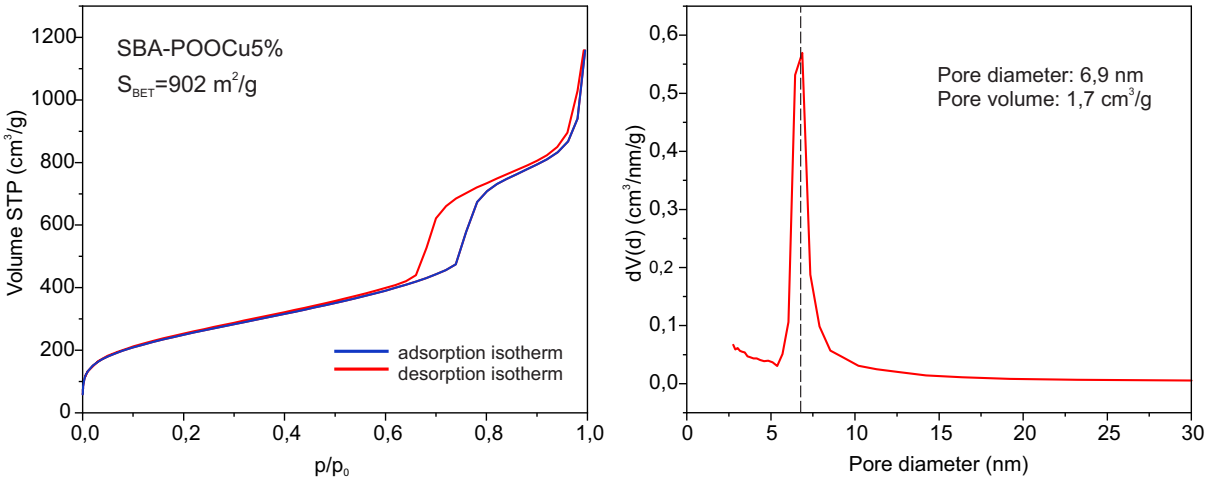


Fig. 5.17. Nitrogen adsorption–desorption isotherms of SBA–$POO_2Cu5\%$ and corresponding BJH pore size distribution plot.

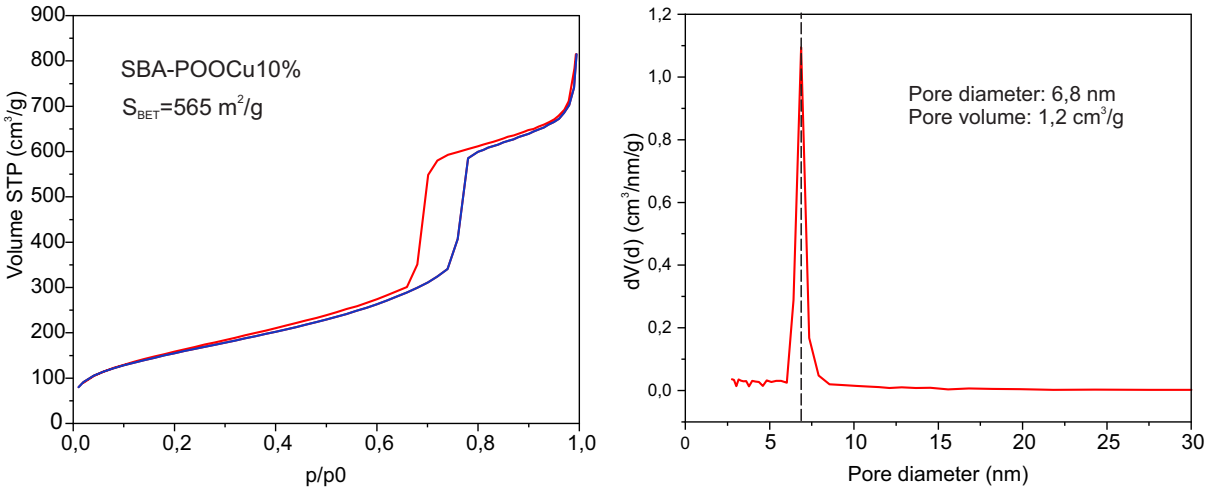


Fig. 5.18. Nitrogen adsorption–desorption isotherms of SBA–$POO_2Cu10\%$ and corresponding BJH pore size distribution plot.

With further increases in functional group concentration to 5%, 10%, and 20% (Figures 5.17 - 5.19), a more conventional trend emerges. A gradual decrease in both specific surface area and average pore diameter is observed, which can be attributed to denser packing of the functional groups within the mesopores. This leads to a reduction in accessible surface area and effective pore size, as the copper phosphonate species increasingly occupy the internal pore volume. The progressive physical filling and partial obstruction of the pore network limits nitrogen diffusion, thus diminishing the overall adsorption capacity.

The sample with the highest degree of functionalization (20%), shown in Figure 5.19, exhibits a notably steep desorption branch in its isotherm, suggesting the onset of complex porosity effects, possibly due to pore blocking and/or less ordered mesoporous material.

The average pore diameter in this sample decreases substantially to 3.8 nm, compared to 7.9 nm in the minimally functionalized material.

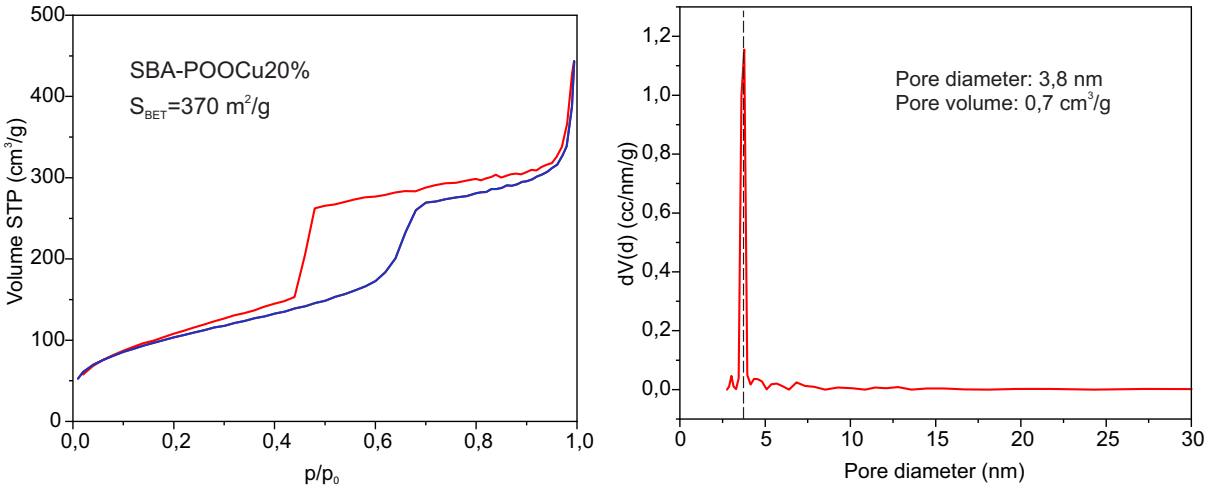


Fig. 5.19. Isotherms of Nitrogen adsorption-desorption of SBA–$POO_2Cu20\%$

It is important to note that nitrogen physisorption measurements were conducted exclusively on powdered samples. Due to the limited quantity of material deposited on the substrates, it was not feasible to recover sufficient sample mass from the thin films for analysis. Nevertheless, a similar trend in textural changes as a function of functional group loading is anticipated for the thin films, given the consistent use of precursor materials and synthesis conditions.

To conclude, N_2 physisorption experiments confirmed the expected mesoporosity, as indicated by the characteristic shape of the hysteresis loop. Increasing the propyl–copper phosphonate loading resulted in a consistent trend in surface area, pore volume, and pore diameter variations. As the functional group density increases, the intermolecular distance between adjacent groups decreases, reducing the accessibility of N_2 molecules to the silica walls.

Up to a loading of 2.5%, the intermolecular distance remains sufficiently large to allow efficient N_2 adsorption. However, a transition in surface area is observed when the concentration reaches 5%, accompanied by a noticeable narrowing of the pore diameter. As the concentration continues to increase beyond this point, the same trend of reduced surface area and pore narrowing persists.

5.4 Small-Angle X-ray Scattering (SAXS) and Grazing-Incidence Small-Angle X-ray Scattering (GISAXS)

While X-ray diffraction (XRD) has traditionally been used for well-ordered crystalline materials to determine crystal structures and identify phase compositions—typically by scanning over large incident angles—advancements such as small-angle X-ray scattering (SAXS) have extended structural characterization capabilities. However, this technique still exhibits limitations in analyzing thin films, interfaces, and low-scattering-volume systems due to the minimal volume of material and the high background scattering of the substrate [155]. This limitation has been addressed by grazing incidence small-angle X-ray scattering (GISAXS), which introduces a grazing incident angle to improve surface sensitivity. GISAXS has become an essential tool for studying nanoscale organization in thin films, self-assembled structures, and periodic surface morphologies.

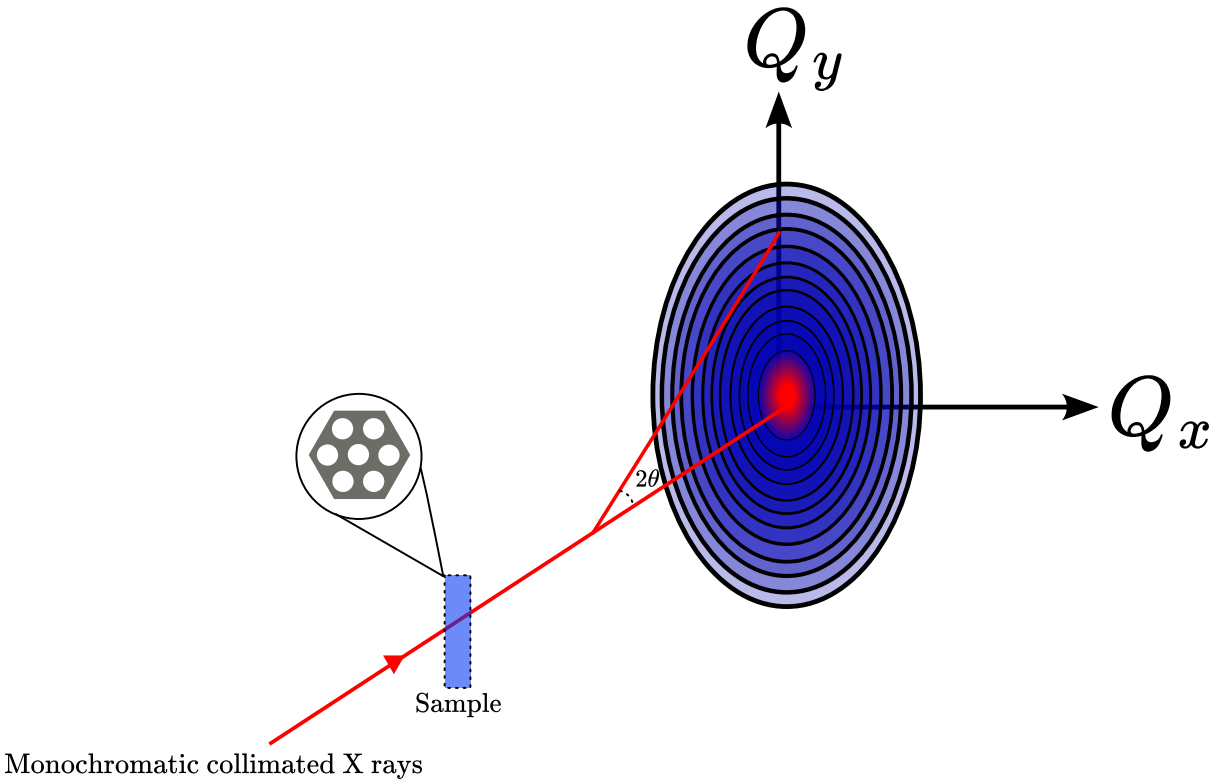


Fig. 5.20. Principle of SAXS.

First of all, small-angle X-ray scattering (SAXS) can be considered a zoomed-in version of conventional X-ray diffraction (XRD), allowing access to structural information at the nano- and mesoscale. Figure 5.20 illustrates the basic setup of a SAXS measurement, where a highly collimated beam of monochromatic X-rays with wavelengths between 0.2 and 0.7 nm is used. The X-ray beam passes through the sample and is scattered onto a detector, which contains a beam stop at its center to block the direct beam and monitor

the incident intensity.

The scattering angle, denoted 2θ, is measured at very small values, typically in the range of 0.1° to 1°.

The scattering angle θ is related to the scattering vector q (also known as the momentum transfer) by:

$$q = \frac{4\pi \sin\theta}{\lambda} \tag{5.5}$$

where λ is the X-ray wavelength.

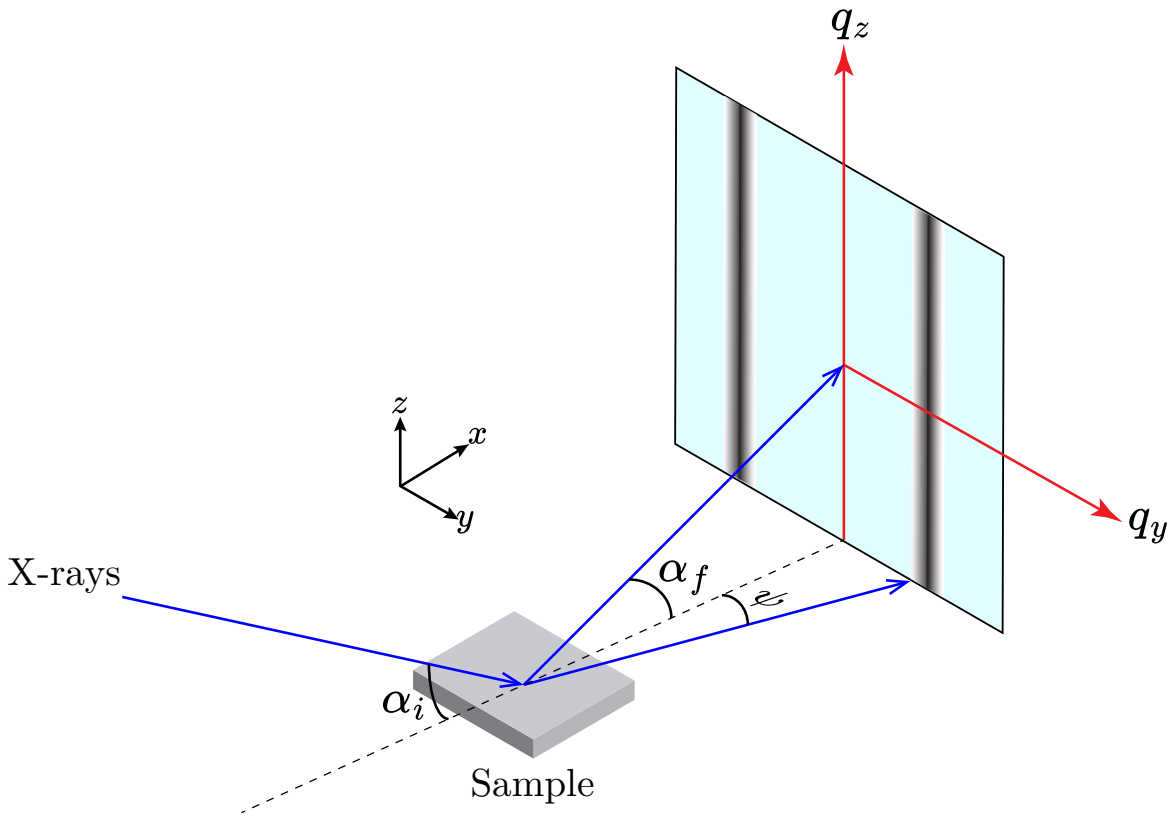


Fig. 5.21. Principle of GISAXS.

On the other hand, GISAXS is a reflection-mode version of SAXS that is used to determine the structural parameters of mesostructured silica thin films and to study the alignment order of oriented pores.

Figure 5.21 illustrates the experimental geometry of the GISAXS setup. The sample is inclined at a small incident angle (α_i) relative to the incoming X-ray beam ($\mathbf{k}_i$), and the scattered intensity is recorded by a two-dimensional detector as a function of the exit angles α_f and ψ.

The scattering wavevector $\vec{q}$ coincides with a reciprocal lattice point under constructive interference [156].

$$\vec{q} = \vec{k}_f - \vec{k}_i = \begin{pmatrix} q_x \\ q_y \\ q_z \end{pmatrix} = \frac{2\pi}{\lambda} \begin{pmatrix} cos(\alpha_f)cos(\psi) - cos(\alpha_i) \\ cos(\alpha_f)sin(\psi) \\ sin(\alpha_i) + sin(\alpha_f) \end{pmatrix} \tag{5.6}$$

The thin film samples under investigation is assumed to consist of cylindrical mesopores arranged in a two-dimensional hexagonal structure, with the pore channels oriented parallel to the substrate surface. Scattering occurs when the Bragg condition is satisfied, when the path difference between scattered waves equals an integer multiple of the X-ray wavelength.

Table 5.3 provides a comparative overview of the SAXS and GISAXS techniques, highlighting their main advantages and limitations.

Tab. 5.3. Comparison of SAXS and GISAXS techniques.

Technique	**Advantages**	**Limitations**
Small-Angle X-ray Scattering (SAXS)	Probes nanoscale structure in bulk materials, colloids, polymers, and solutions. Used for determining particle size, shape, and distribution.	Not surface-sensitive; provides averaged information over the sample volume. Less effective for thin films or layered structures.
Grazing Incidence Small-Angle X-ray Scattering (GISAXS)	Probes surface and near-surface nanostructures in thin films and patterned surfaces. Suitable for studying self-assembled structures and interfacial morphology.	Requires grazing incidence alignment; data analysis is more complex due to 2D scattering and interference effects.

SAXS and GISAXS measurements were carried out on a SAXSpace Anton Paar instrument. This instrument is attached to an ID 3003 laboratory X-Ray generator (General Electric) equipped with a sealed X-ray tube (PANalytical, $\lambda_{\mathrm{CuK}\alpha} = 0.1542$ nm) operating at 40 kV and 50 mA.

SAXS was used to analyze the nanostructure of powder samples, whereas GISAXS was employed to probe the surface morphology and ordering in thin films.

For the SAXS measurements, the samples were introduced into a “Special Glass” capillary with a diameter of 2 mm, subsequently sealed, before being placed at 25°C, inside

an evacuated sample chamber equipped with a temperature-controlled sample holder unit, and exposed to an X-Ray beam for about 30 min. Scattering of the X-Ray beam was recorded by a 1D detector (Mythen 2 with strip of 50μm x 8mm) placed at 317 mm distance from the sample. Scattering intensities I(q) were provided as a function of the magnitude of the scattering vector $q = \frac{4\pi}{\lambda}\sin(\theta)$, where 2θ is the total scattering angle. Thanks to a translucent beamstop allowing the measurement of an attenuated primary beam at q = 0, all measured intensities can be calibrated by normalizing the attenuated primary intensity. The data were collected in a q-range from 0.13 to 7.7 nm^{-1} and then corrected for the background scattering, from the empty capillary and for slit-smearing effects by a desmearing procedure, using the Lake method. After correction, obtained intensities are scaled into absolute units using water as a reference material. GISAXS measurements of the thin film samples were done by the use of a GISAXS module using a point collimation beam. The Samples were introduced on the GiSAXS deck inside an evacuated sample chamber and exposed to X-Ray beam for about 50 minutes. The scattering of X-Ray beam was recorded by a CCD detector 2D (Princeton Instruments SCX-TE 4300K/2 CCD 2084×2084 pixels array with 24×24 μm^2 pixel size) placed at 299 mm distance from the sample.

Small angle X-ray scattering (SAXS) technique was performed on the prepared powders at various concentrations by identifying the presence of scattering planes (100), (110), and (200) characteristics of 2D hexagonal ordering of mesopores.

Figure 5.22 shows the SAXS diffractograms of SBA-15 hybrid mesoporous powders with concentrations of 1.25%, 2.5%, 5%, 10%, and 20% respectively. All diffractograms exhibit three intense diffraction peaks, indexable as (100), (110), and (200) reflections with slightly different intensities and peak positions, except for SBA-POO_2Cu20%, which contains the highest concentration of copper functional groups (20%). These peaks are typical of a highly ordered two-dimensional hexagonal structure of cylindrical pores, with space group *P6mm*, characteristic of SBA-15.

The interplanar spacing (d_{hkl}), estimated according to Bragg's equation ($n\lambda = 2d\sin\theta$) or directly from the scattering vector as $q = \frac{2\pi}{d}$, and the lattice parameter (a_{hkl}) values were calculated from those d_{hkl} values using the following relationships:

$$a_{100} = \frac{2d_{100}}{\sqrt{3}}, \quad a_{110} = 2d_{110}, \quad a_{200} = \frac{4d_{200}}{\sqrt{3}}$$

with $\lambda_{Cu(K\alpha)} = 0.1542$ nm.

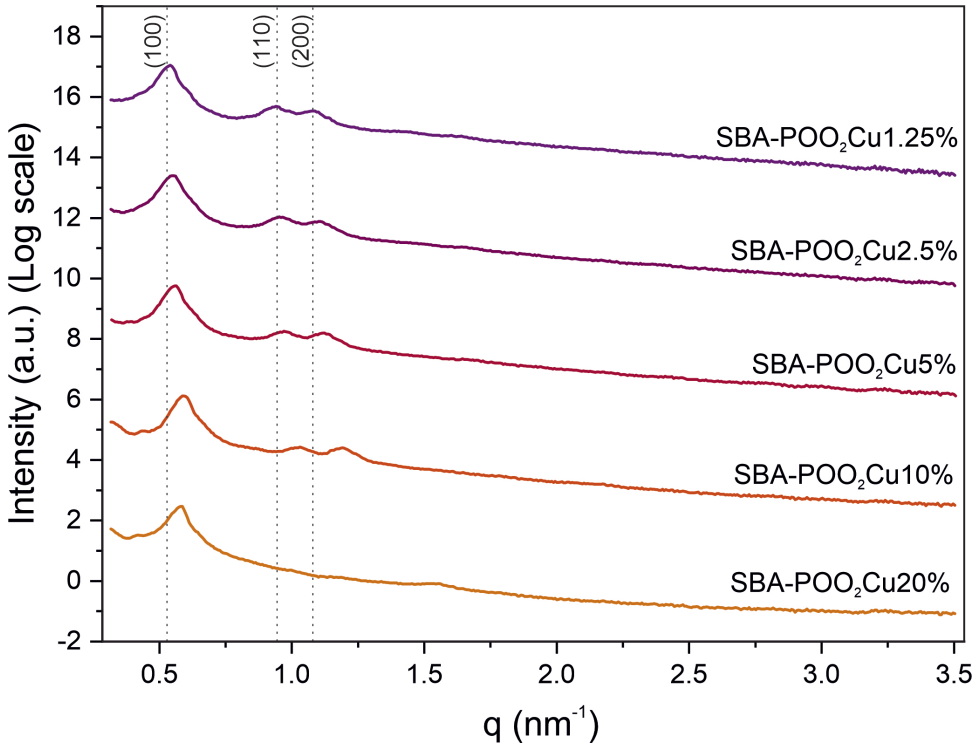


Fig. 5.22. SAXS diffractograms of silica SBA-15 containing propyl-copper-phosphonate units with different concentrations.

Tab. 5.4. Interplanar spacings and lattice parameters of SBA-POO_2Cu samples with different functional group concentrations. Mean a_0 and standard deviation are calculated from the available a_{hkl} values.

Samples	d_{100} (nm)	d_{110} (nm)	d_{200} (nm)	a_{100} (nm)	a_{110} (nm)	a_{200} (nm)	Mean a_0 (nm)	Std. dev. (nm)
SBA-POO_2Cu1.25%	11.64	6.75	5.77	13.44	13.50	13.31	13.42	0.097
SBA-POO_2Cu2.5%	11.36	6.54	5.72	13.11	13.08	13.21	13.13	0.068
SBA-POO_2Cu5%	11.24	6.48	5.62	12.97	12.96	12.96	12.96	0.006
SBA-POO_2Cu10%	10.66	6.15	5.33	12.31	12.30	12.33	12.31	0.015
SBA-POO_2Cu20%	10.85	–	–	12.53	–	–	–	–

In all cases, the lattice parameters derived from different reflections are consistent within less than 1% deviation, which can be attributed to experimental uncertainties such as peak broadening, instrumental calibration, or slight sample heterogeneity. One can observe that the interplanar distances decrease as the loading of functional groups

increases, which suggests a shrinkage behavior of the material. This phenomenon can be attributed, in part, to the hydrolysis of phosphonic acid ester groups into phosphonic acid groups. As the concentration of these groups increases on the silica surface, adjacent phosphonic acid groups may interact and form intermolecular bridges, potentially via coordination with copper ions, which can lead to structural contraction.

Another possible explanation for the decrease in interplanar distances with increasing functionalization is the formation of micropores within the silica matrix. This can occur during synthesis, where the presence of functional group precursors may promote deeper penetration of the hydrophilic PEO chains of the P123 template into the silica walls. Upon removal of the template, these regions may leave behind micropores, contributing to overall shrinkage of the structure [15, 21].

Furthermore, it has been observed that overloading SBA-15 with 20% copper phosphonate leads to significant disruption in the periodicity and uniformity of the pores, resulting in a loss of long-range order in the highly concentrated sample.

Figure 5.23 shows the 2D GISAXS pattern of the prepared dip-coated films. Each GISAXS image displays well-defined Bragg spots and exhibits the (01) and (10) equivalent reflections of the p6m space group, suggesting a highly ordered structure. This pattern is characteristic of mesoporous silica films with a two-dimensional (2D) hexagonal arrangement of pores [157, 158].

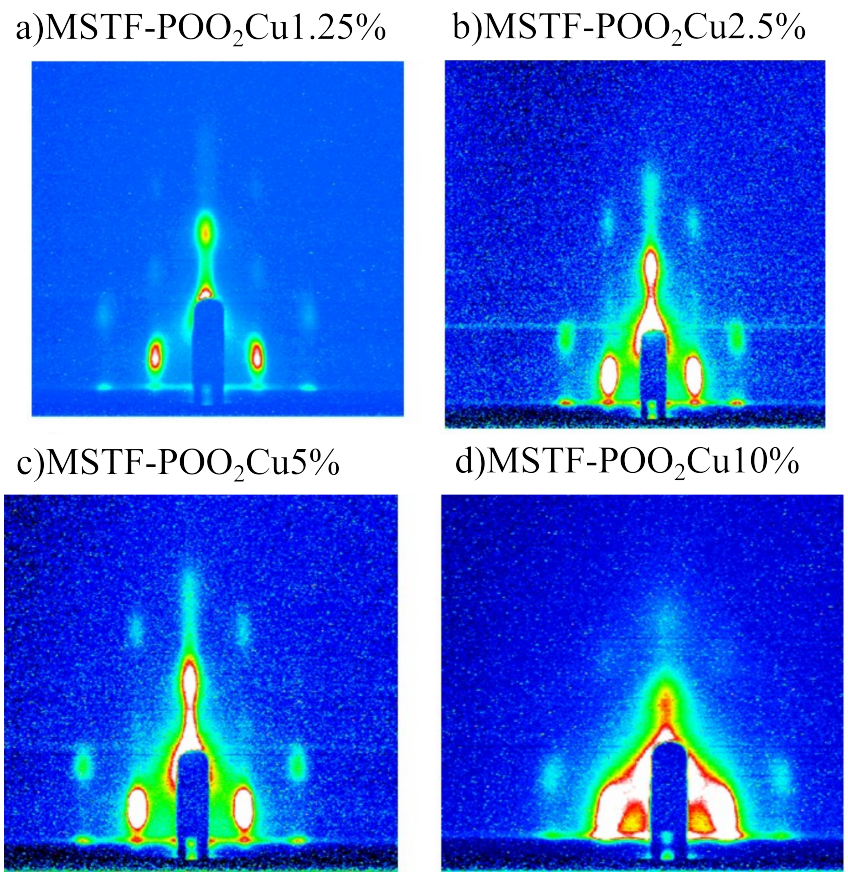


Fig. 5.23. GISAXS pattern of the dip-coated films prepared with different concentrations.

In conclusion, SAXS measurements on functionalized powders revealed the preservation of nanostructural order, whereas GISAXS measurements on dip-coated thin films revealed well-defined hexagonal mesostructures parallel to the substrate surface. Both systems demonstrated a threshold concentration of functional groups above which the porosity's structural arrangement was disturbed.

5.5 Raman spectroscopy

The interaction of light and matter is the fundamental starting point for all spectroscopic techniques. The specific nature of this interaction, and particularly the type of signal that is chosen for analysis, determines the spectroscopic method employed. When light interacts with a material, incident photons may be absorbed, reflected, transmitted, or scattered. Each of these processes can provide different types of information depending on the spectroscopic technique applied.

In the context of Raman spectroscopy, the focus is on light scattering. Scattering can be elastic, such as Rayleigh scattering, where no energy exchange occurs between light and matter, or inelastic, where energy is transferred between the photons and the

molecular system. The Raman effect arises from this inelastic scattering and enables direct probing of vibrational and rotational-vibrational states in molecules and materials [159, 160]. The Raman effect was first experimentally observed by C.V. Raman and K.S. Krishnan in 1928 [161]. It remains a widely used technique for investigating molecular vibrations, offering insights into the structure, symmetry, electronic environment, and bonding characteristics of molecules [162].

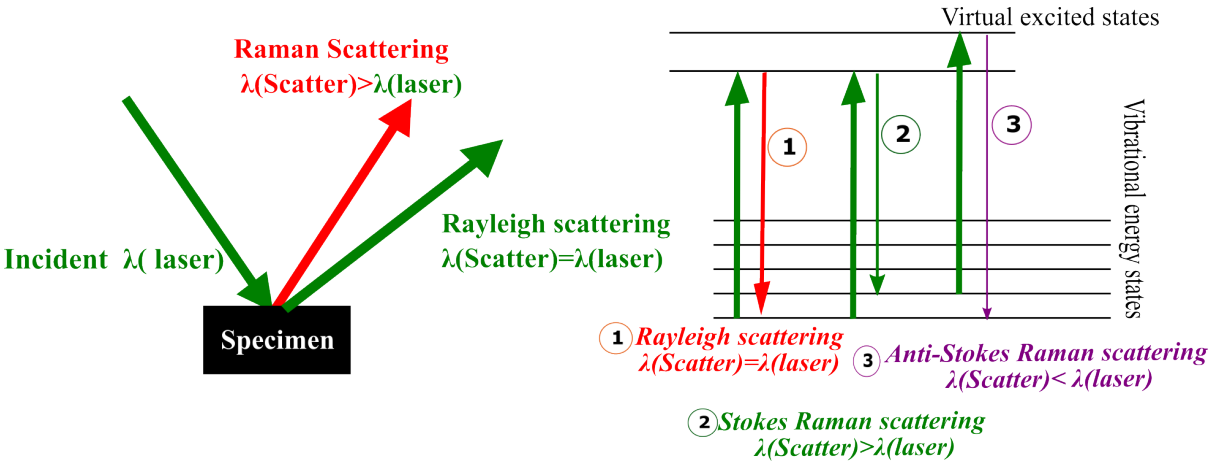


Fig. 5.24. Basic principle of Raman scattering and types of scattering with Vibrational energy level diagram showing Rayleigh and Raman Stokes and anti-Stokes scattering.

Figure 5.24 illustrates the two types of scattering: elastic (Rayleigh) and inelastic (Raman). In Raman scattering, the energy of the scattered light changes due to interaction with vibrational energy levels of molecules. While atomic systems are typically described by transitions between ground and excited electronic states, molecular systems exhibit additional sub-levels associated with vibrational and rotational modes. If the scattered photon gains energy, it results in anti-Stokes Raman scattering; if it loses energy, it results in Stokes Raman scattering. Different vibrational modes, such as stretching, bending, or twisting of chemical bonds, contribute distinct spectral features to the Raman spectrum, collectively shaping its overall profile and enabling detailed insights into molecular structure.

This is why Raman spectroscopy is a powerful analytical technique that provides detailed information about the molecular structure and chemical composition of a material. By measuring the inelastic scattering of monochromatic light, Raman spectroscopy detects vibrational, rotational, and other low-frequency modes of the molecules. These modes are highly specific to the molecular structure and bonding environment, making Raman spectra uniquely characteristic of individual compounds, essentially serving as a molecular fingerprint. This technique enables precise identification and differentiation of materials, even those with very similar compositions, and allows for the monitoring of

structural changes, phase transitions, or interactions within complex systems.

The spectra of the materials discussed in this work were recorded using a WITec alpha 300R confocal Raman microscope (Oxford Instruments, Abingdon, UK) equipped with a $\lambda = 532$ nm laser. The microscope setup consisted of a high-performance low-dark current CCD camera (ANDOR iVac DR-316B-LDC-DD-35B, Oxford Instruments, Abingdon, UK), a Zeiss EC Epiplan-Neofluar Dic 100x/0.9 objective (Jena, Germany). A UHTS300 SMFC VIS-NIR spectrometer (Oxford Instruments, Abingdon, UK) with a 300 mm focal length operated using a 600 grooves/mm grating with blaze wavelength (BLZ) of 500 nm. The spectra were accumulated over 50 scans with a 5-second integration time per scan. The laser power ranged from 10 to 20 mW, depending on the sample. All spectra were baseline-corrected and normalized to the intensity of the peak at 495 cm^{-1}, which is characteristic of silica.

Accurate band assignment for the analyzed materials was based on a combination of literature data and spectroscopic analysis of reference samples. This approach required measurements of a series of reference samples, which were materials obtained at various stages of the synthesis process, but also prepared separately solely for the purpose of collecting the spectrum of certain parts of the analysed material. The spectra of the reference samples are shown in Figure 5.25.

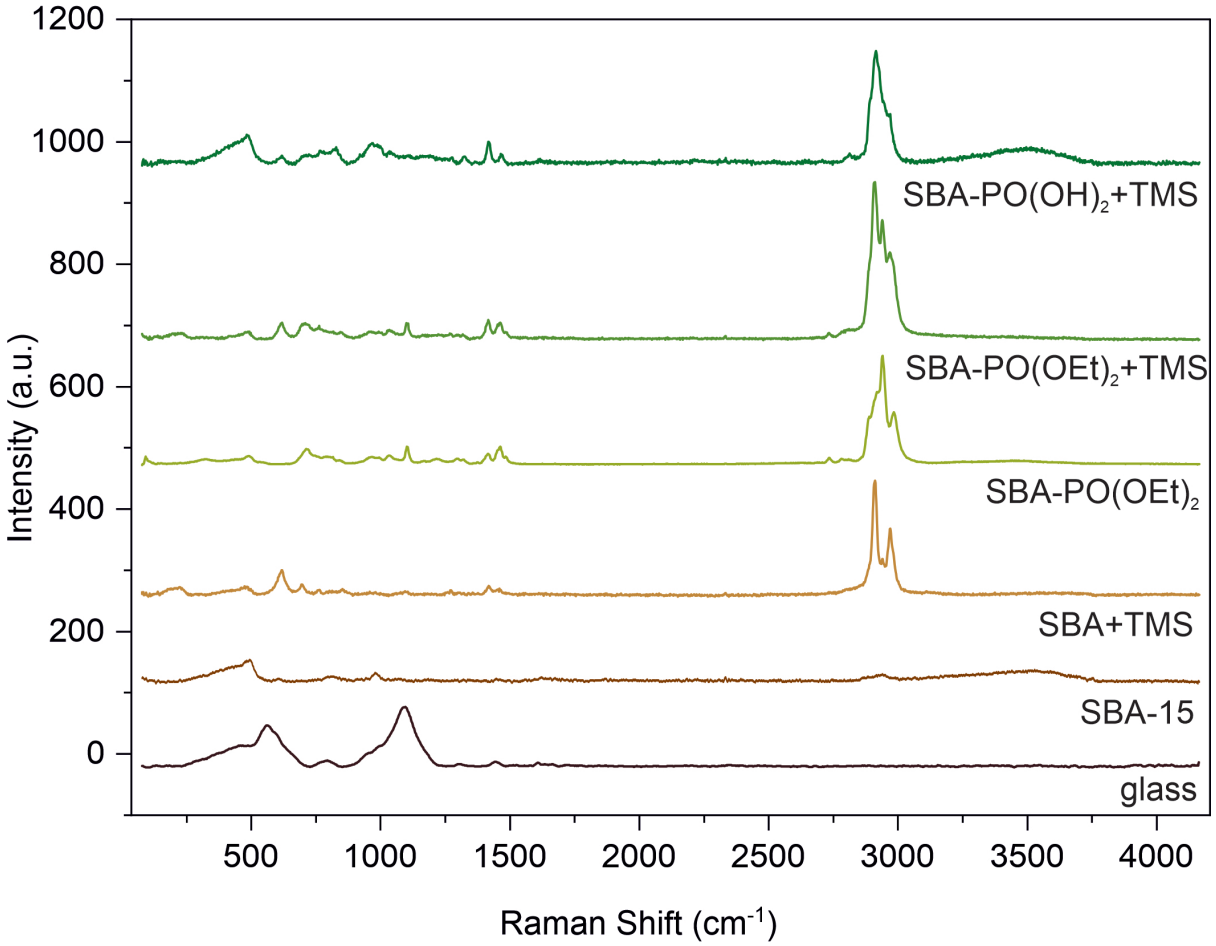


Fig. 5.25. Raman spectra of reference samples.

The following reference samples were used: (1) bare glass used as a substrate for mesoporous silica thin films, (2) bare SBA-15 silica with surface silanol groups (SBA-15), (3) SBA-15 after silylation process in which silanol groups have been replaced by trimethylsilane groups (SBA-15+TMS), (4) SBA-15 with propyl diethyl phosphonate groups it is a sample prepared in functionalization procedure before silylation and hydrolysis (SBA-$PO(OEt)_2$10%), (5) silica with both propyl diethyl phosphonate groups and TMS groups it is a sample prepared in functionalization procedure after silylation but before hydrolysis (SBA-$PO(OEt)_2$10%+TMS), (6) silica with propyl phosphonic acid groups and TMS (SBA-$PO(OH)_2$10%+TMS). All of these samples were used to identify bands characteristic to individual functional groups introduced on the silica surface. It was particularly important in this case because the functional groups are located inside the mesopores of silica and their vibrational modes may undergo certain modifications due to this spatial confinement. All bands identified using reference samples were subsequently verified for correctness through comparison with literature data.

Complete spectra of SBA-POO_2Cu powder samples with various concentrations of functional groups ranging from 1.25% to 20% and two of reference samples are presented

in Figure 5.26.

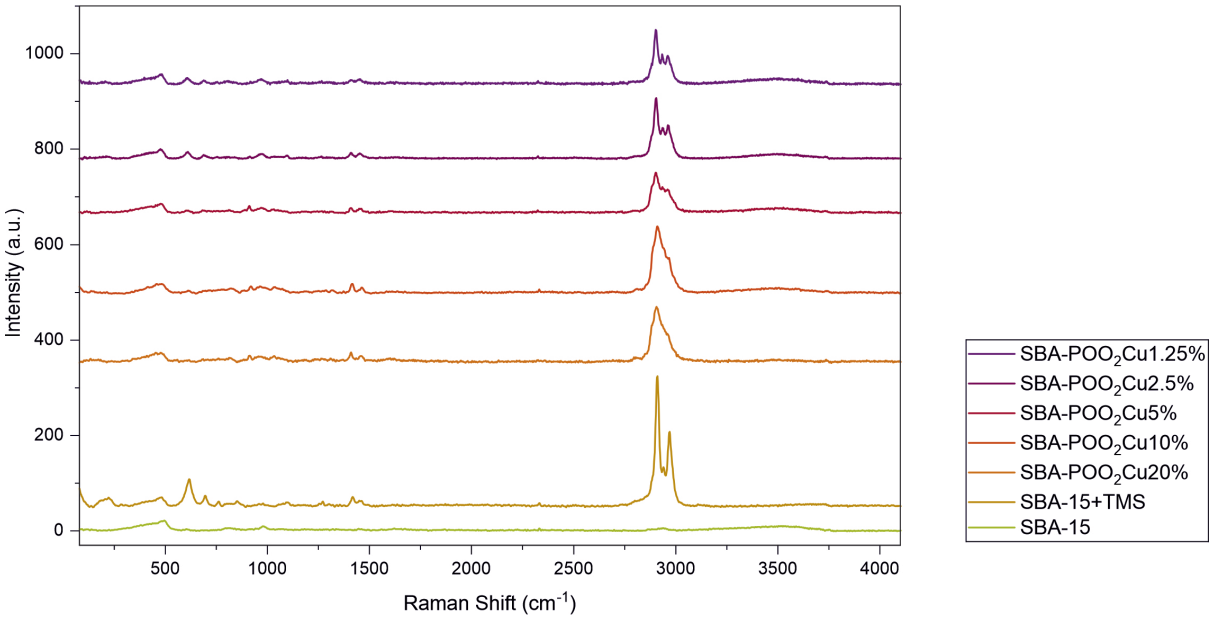


Fig. 5.26. Raman spectra of SBA-POO_2Cu powder samples with contentration ranging from 1.25 to 20% and two reference samples SBA-15 and SBA-15+TMS.

A comparison of the analysed spectra with the spectra of reference samples of pure silica (SBA-15) and silica after silylation (SBA-15+TMS), in which the silanol groups have been replaced by trimethylsilane groups, allows for easy visualisation of the source of the bands observed in the spectra of the analysed samples. In addition, this comparison leads to the conclusion that two significant spectral regions can be distinguished in these spectra. The first region, between 400 and 1600 cm^{-1}, contains several bands originating from both silica and functional groups and is the most important for describing the molecular structure of the analyzed materials. The second region ranging from 2700 to 3200 cm^{-1}, originates mostly from organic moieties such as methyl and methylene groups. In this area, bands associated with vibrations of water molecules or silanol groups may also be observed, although they are less expected.

To take a closer look at these regions, they are shown separately in Figure 5.27 a and b.

Starting with the reference samples, the low frequency region of the pure, non-functionalized SBA-15 exhibits several Raman features that are characteristic of the silica framework. In amorphous SiO_2 systems, a broad peak around 430 cm^{-1} indicates the presence of six-membered siloxane rings in the silica network. Furthermore, the features observed at 492 cm^{-1} and 605 cm^{-1} are assigned to the symmetric bending vibrations of O-Si-O of vibrationally isolated four-membered rings of SiO_4 tetrahedra, and the breathing modes of three-membered rings of SiO_4 units, respectively [163].

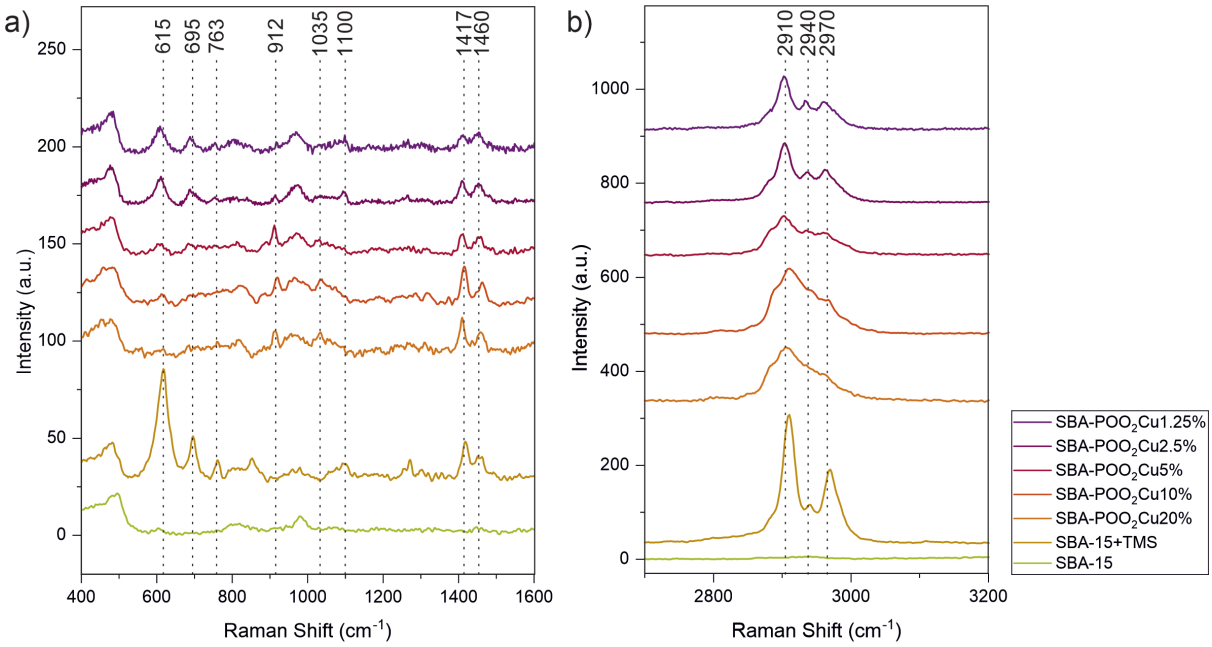


Fig. 5.27. Raman spectra of SBA-POO_2Cu powder samples with contentration ranging from 1.25 to 20% and reference sample in two magnified regions: 400-1600 cm^{-1} (a), 2700-3200 cm^{-1} (b).

The SBA-15+TMS sample shows additional peaks that were absent in bare SBA-15 spectrum, which is expected because trimethylsilyl -$Si(CH_3)_3$ groups on the silica surface. These bands appear at 615, 695, 763, 1100, 1270, 1417, and 1460 cm^{-1} in the SBA-15+TMS spectrum. Additionally, three distinct bands originating from methyl -CH_3 in TMS groups are observed in high-frequency region at 2910, 2940, and 2970 cm^{-1} [164,165]. Since the intensity of Raman bands is strongly influenced by the concentration of specific functional groups in the sample, spectral analysis reveals trends in band intensities that correspond to changes in the amount of these groups. This is observed in the case of TMS and copper-phosphonate groups when their relationships change. In samples with low concentrations of copper-phosphonate groups, TMS groups dominate. However, as the concentration of -POO_2Cu groups increases, the number of TMS groups decreases, which is reflected by a reduction in the intensity of their characteristic bands, particularly those at 615 and 695 cm^{-1}. For other bands, this effect is less pronounced due to overlap with vibrations from methylene (-CH_2) groups present in the propyl chain of the copper-phosphonate moiety.

The presence of copper-phosphonate functional groups incorporated in the silica matrix was confirmed by the presence of specific Raman bands that correspond to the vibrational modes of bonds within the -POO_2Cu group or the propyl chain connecting this moiety to the silica wall. The modes related to the methylene -CH_2 groups present in propyl chains can be observe at 1320 and 1460 cm^{-1}, and the high-frequency region

between 2910-2970 cm^{-1} [166, 167]. Additionally, bands at 820, 1035, 1324, and 1417 cm^{-1} increases in intensity as functional group concentrations increases because these bands are associated to deformations within the -POO_2Cu fragment. This implies that the band originates from a vibrational mode associated with a component that becomes more prominent upon increased functionalization [168]. All of these bands, except for the one at 820 cm^{-1}, also appear in the reference sample SBA-$PO(OEt)_2$10%, which contains only -$PO(OEt)_2$ groups and no TMS groups. This confirms that these features are more likely related to the phosphonate moiety rather than to Cu–O vibrations. There are only two characteristic bands that are absent in the spectra of the reference samples SBA-$PO(OEt)_2$10%+TMS and SBA-$PO(OH)_2$10%+TMS, but are present exclusively in the spectra of the copper-containing samples. Therefore, it can be concluded that these bands are associated with vibrational modes of functional groups involving copper. These bands are observed at 820, and 912 cm^{-1}, and their intensities increase with increasing concentration of copper-phosphonate functional groups [168].

In the high-frequency region (Fig. 5.27 b), four bands are observed at 2888, 2910, 2940, and 2970 cm^{-1}. All of them are present in the spectra of reference samples, except for pure SBA-15 silica, which shows no significant bands in this region. Their presence indicates the incorporation of both TMS groups and propyl-copper-phosphonate groups into the silica matrix. Moreover, changes in their relative intensities depend on the amount of functional groups present on the surface. Notably, the bands at 2888 and 2940 cm^{-1} decrease in intensity as the concentration of functional groups decreases across all five samples, suggesting that these bands originate from the propyl chain that links the copper-phosphonate group to the silica wall.

A similar analysis can be applied to the Raman spectra of the thin films. The main difference in the spectra of the thin film samples is the presence of very intense bands originating from the glass substrate. Figure 5.28 shows the complete spectra of mesoporous thin films containing 1.25 to 10% of propyl-copper-phosphonate groups, along with a spectrum of bare glass for comparison.

As in the case of powder samples, the spectra can be divided into two areas containing bands characteristic of the structure under investigation. The spectral region from 450 to 1800 cm^{-1}, shown in Figure 5.29a, contains numerous broad and intense bands originating from the glass, which overlap most of the features characteristic of the functional groups. Only two of them, at 1417 and 1460 cm^{-1} are clearly visible and may serve as evidence of the successful synthesis of the studied thin films, indicating the formation of a molecular structure similar to that of the powder samples and consistent with the synthesis assumptions. Moreover, the decrease in the intensity of the 1417 cm^{-1} band with decreasing concentration of the functional groups supports the successful function-

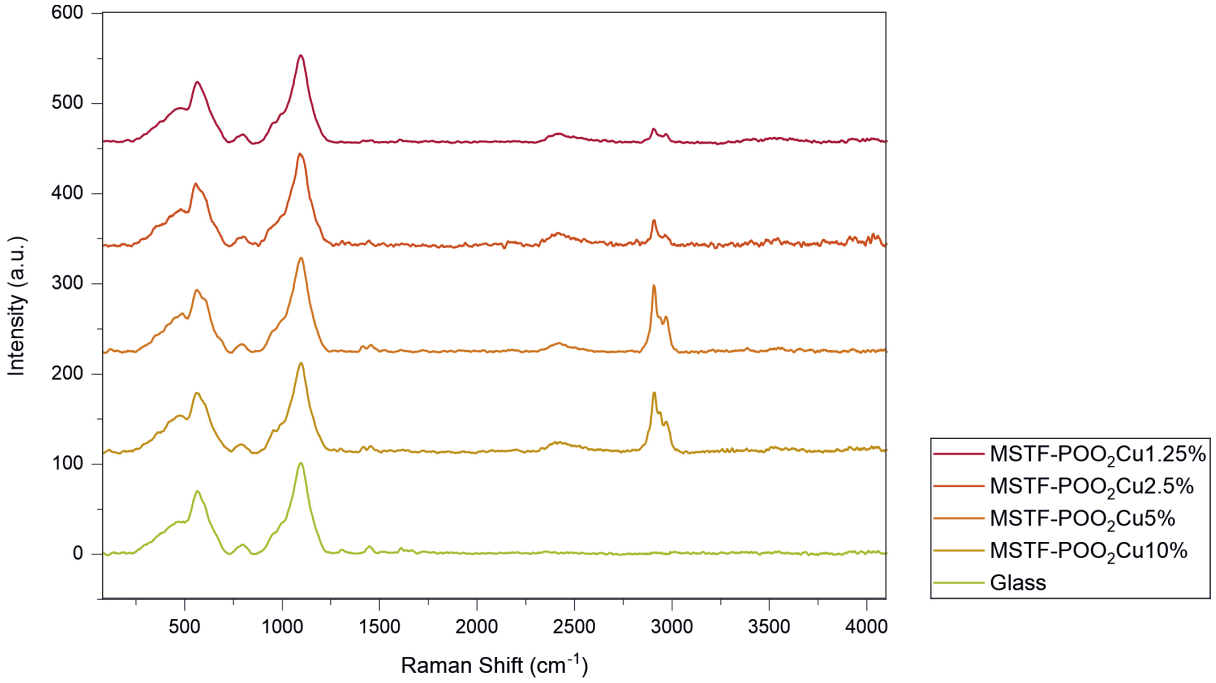


Fig. 5.28. Raman spectra of propyl-copper phosphonate functionalized mesoporous silica thin films at different concentrations of functional groups, as well as the spectrum of the glass substrate for reference.

alization of the films.

The second spectral region, from 2700 to 3300 cm^{-1} (Fig. 5.29b), contains bands originating mainly from methyl and methylene moieties present in both TMS and propyl-copper-phosphonate groups. Additionally, bands corresponding to silanol vibrations are observed in the spectrum of the glass reference sample and contribute to the features detected in the region. Since the bands partially overlap, it is difficult to distinguish individual changes in intensity. However, relative intensity variations are clearly visible, suggesting modifications in the molecular structure of the samples corresponding to changes in the concentration of -POO_2Cu groups. As in the case of powder samples, the thin films exhibit a decrease in the intensity of the 2940 cm^{-1} band, as well as similar relative changes in the intensities of the bands at 2910, 2940, and 2970 cm^{-1}. This may confirm the formation of a molecular structure comparable to that observed in the powder samples.

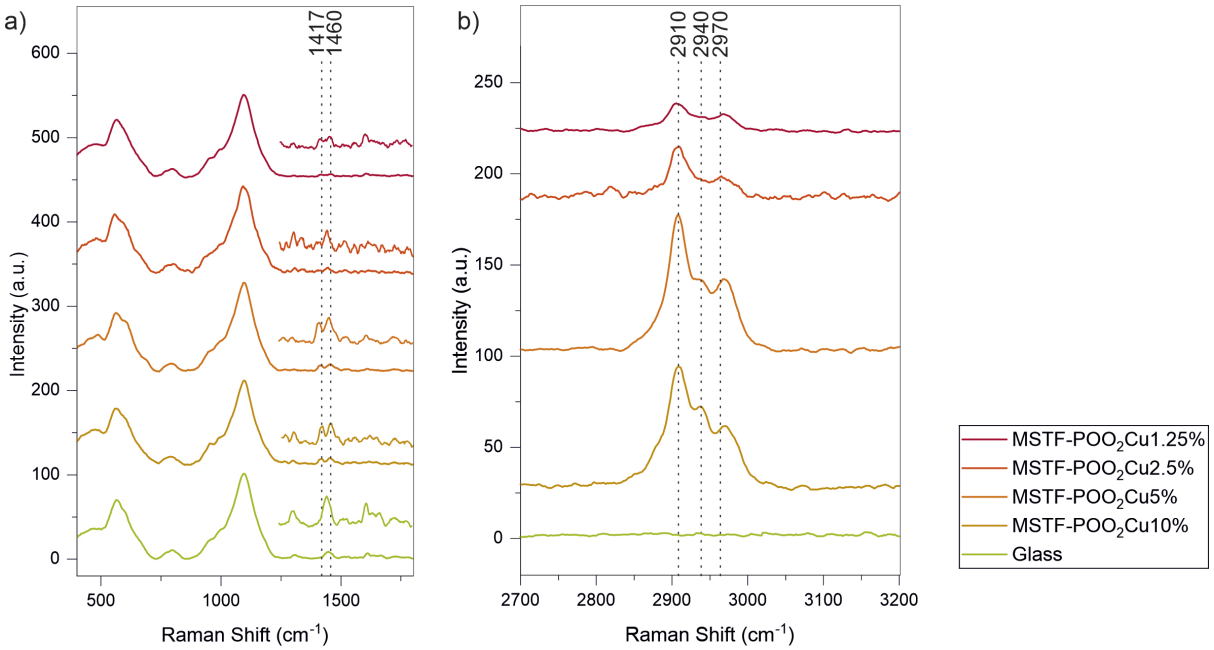


Fig. 5.29. Raman spectra of MSTF-POO_2Cu thin film samples with contentration ranging from 1.25 to 10% and reference sample in two magnified regions: 450-1800 cm^{-1} (a), 2700-3200 cm^{-1} (b).

In summary, all analyzed samples, both in powder and thin film form, exhibit a similar molecular structure, as evidenced by the comparable shape of the Raman spectra. However, a more detailed analysis reveals subtle differences in the intensities of specific bands, which are consistent with the results of the EDS study, indicating changes in the amounts of copper and phosphorus in accordance with the synthesis design. Moreover, the positions of the observed bands confirm the successful incorporation of TMS and propyl-copper-phosphonate groups in the silica structure.

6 Experimental study for resolving the copper phosphonate functional groups structure using X-Ray absorption fine structure spectroscopy (XAFS)

6.1 Introduction

It is necessary to first describe the workflow and rationale for the results and analysis presented in this chapter. In the preceding chapter, we conducted a thorough experimental investigation into the structural, morphological, and chemical properties of the investigated materials. Prepared samples with concentrations of functional groups from 1.25 to 10% showed very good agreement of the synthesis results with their assumptions. Only the highest-concentration sample (SBA-POO_2Cu 20%) showed significant structural deviations, including pore shrinkage and loss of long-range order, as measured by nitrogen sorption and SAXS. As well as the change of the copper amount that switches from 1:1 (Cu: P) to 1:1.7 (Cu: P). Even though this sample deviated slightly from the assumptions of the synthesis, it made an important contribution to the understanding of the molecular structure of the materials in question because it was the only one that contained a high enough concentration of copper to perform XAS in transmission mode, while the other samples, due to the limited amount of copper, were subjected to XAS in fluorescence mode. Measurement in transmission mode provided superior signal-to-noise for both XANES and EXAFS analysis enabling accurately determine the environment of copper ions in the silica matrix.

In this chapter, I will discuss the fundamental principles of X-ray absorption spectroscopy (XAS), including the types of information that can be extracted—such as oxidation state, local coordination environment, and bonding geometry—as well as the key challenges of data analysis and interpretation. The theoretical overview will be followed by a the analysis of the Cu K-edge XANES and EXAFS data for the highest-loaded sample, SBA-POO_2Cu20%, measured in transmission mode. The motivation for extending the EXAFS fitting to include copper's second coordination shell will be highlighted,

as will the importance of computationally assisted data analysis in interpreting local structure.

Following that, data collected in fluorescence mode for samples with lower copper phosphonate concentrations, both powders and thin films, will be qualitatively analyzed at the Cu and P K-edges and compared with structural insights from literature and the 20% sample serving as a reference point.

6.2 Short introduction to X-Ray Absorption Near-Edge Spectroscopy (XANES)

XANES is a versatile technique used in a wide range of research domains to probe the local atomic environment and electronic structure, including the oxidation state of a specific element. A XANES spectrum is the lower energy part of the overall X-ray Absorption Fine Structure (XAFS) spectrum, extending up to 50 eV above the absorption edge.

XANES' physical processes are similar to those of Extended X-ray Absorption Fine Structure (EXAFS). However, the key distinction lies in the kinetic energy of the outgoing photoelectrons: in the XANES region, lower-energy photoelectrons undergo multiple scattering events, which frequently involve strong interactions with the valence electrons of the neighboring atoms. On the other hand, in the EXAFS region the photoelectron gains more kenetic energy (see equation 6.1) and primarily undergoes single scattering, allowing structural information to be extracted over longer distances by fitting the EXAFS equation 6.5.

The kinetic energy of a photoelectron ejected during X-ray absorption is related to the energy of the incident photon and the electron's binding energy. However, in an XAFS spectrum, we report the incident photon energy on the X-axis [169].

$$KE = h\nu - E_{\mathrm{B}} \tag{6.1}$$

where:

- KE is the kinetic energy of the emitted photoelectron,
- $h\nu$ is the energy of the incident X-ray photon,
- E_{B} is the binding energy of the core-level electron.

When a sample is exposed to a monochromatic X-ray beam, it absorbs photons and emits photoelectrons of varying kinetic energies as the energy of the X-ray probe is chinging. The emitted photoelectrons are analysed to obtain structural and electronic data about the material. While the underlying photon-matter interaction is similar to many other spectroscopic techniques, X-ray absorption spectroscopy is distinguished by the specific way in which the signal is analyzed and detected following the interaction.

An intuitive approach to understanding the absorption process is through Beer-Lambert's law, which describes how the intensity of transmitted X-rays decreases as they pass through an absorbing medium. This principle explains how XAFS spectra are measured at a synchrotron beamline, where the change in transmitted (or Fluorescence) intensity is monitored as a function of the incident photon energy (Figure 6.1) [169, 170].

$$I(E) = I_0(E)e^{-\mu(E)t} \tag{6.2}$$

where:

- $I(E)$ is the transmitted intensity at energy E,
- $I_0(E)$ is the initial intensity,
- $\mu(E)$ is the absorption coefficient,
- t is the sample thickness.

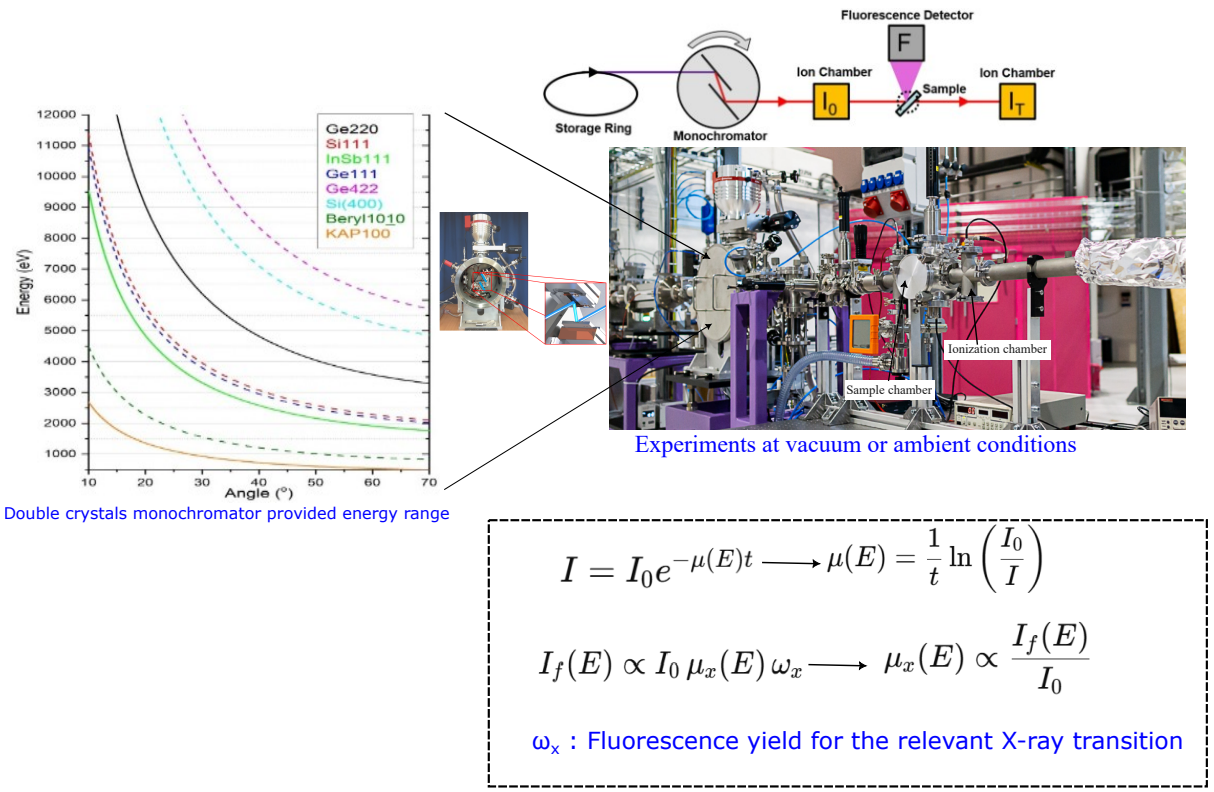


Fig. 6.1. Tender X-Ray absorption spectroscopy ASTRA Beam line station [169].

Every bending magnet in a synchrotron facility delivers a wide range of X-ray energies, resulting in polychromatic X-rays. In order to select a specific X-ray energy, a monochromator must be used. In our study, we did all measurements at the ASTRA bean line (see Figure 6.1), which uses a double-crystal monochromator to tune the energy range of interest. For example, to probe the copper element, we started at an energy of 20 eV below the copper absorption edge, which is around 8979 eV, and scanned 100

eV above it, using germanium Ge(220) monochromator crystals under vacuum to select the appropriate energy range.

The X-ray beam is first directed through a first ionization chamber, where the incident intensity I_0 is measured. This measurement serves as a reference for the incoming photon flux. The beam then interacts with the sample, and the transmitted X-rays are detected by a second ionization chamber . The transmitted photons ionise the gas inside this chamber, producing a signal that corresponds to the transmitted intensity I.

This configuration enables the calculation of the absorption coefficient $\mu(E)$ using the Beer–Lambert law in eq.6.2 [169]:

$$\mu(E) = \frac{1}{t} \ln\left(\frac{I_0}{I}\right) \tag{6.3}$$

When transmission measurements are not possible, such as for highly absorbing or dilute samples, a fluorescence detector is placed at 90° to the incident beam, above the sample. This detector detects the element-specific fluorescence emitted after X-ray absorption, allowing for data acquisition in fluorescence mode.

Another capability of XAFS (X-ray Absorption Fine Structure) measurement is that various types of samples can be analyzed, including powders, liquids, and gases. These measurements can be performed in three different modes: Transmission Mode – Best suited for highly concentrated samples. Fluorescence Mode – Suitable for diluted samples, where the absorber (the element of interest) is present in low concentrations. Electron Yield Mode – Provides surface-sensitive information. It is important to note that XAFS is a bulk-sensitive technique, meaning it provides information from the bulk of the material, unlike X-ray Photoelectron Spectroscopy (XPS), which is a surface-sensitive technique.

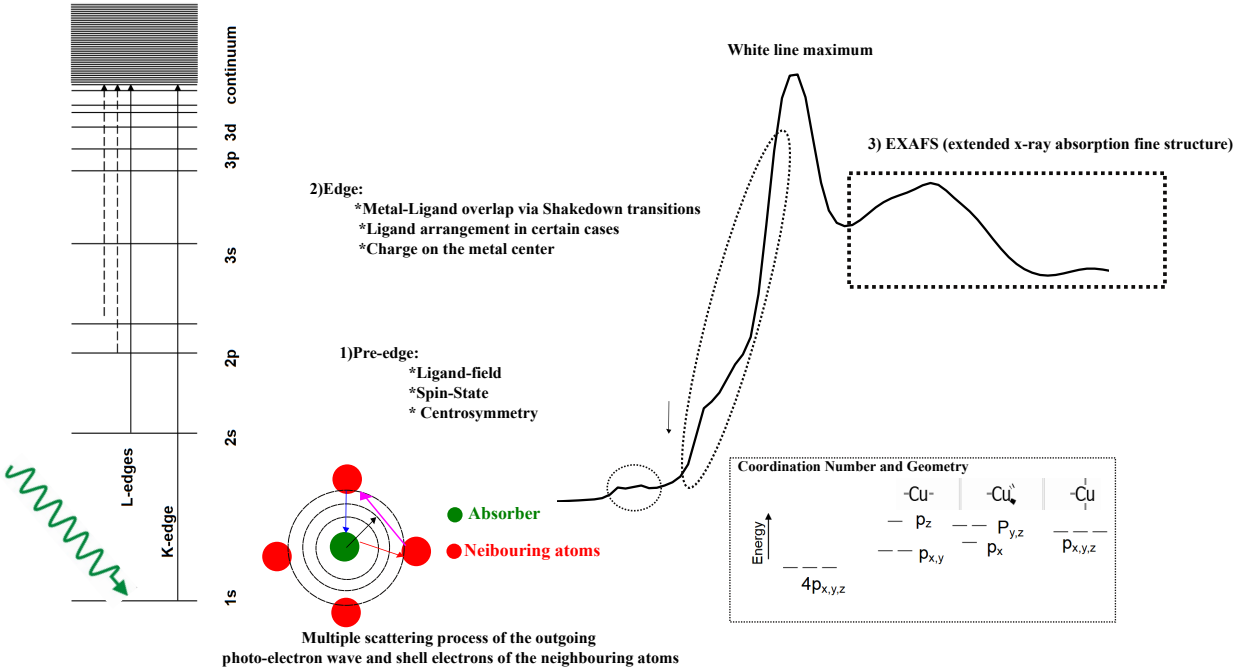


Fig. 6.2. The three main regions of XAS data and the physical process behind the scattering of an ejected photoelectron by its neighbors.

Different electronic energy levels can be accessed using X-ray photons in the process of X-ray Absorption Fine Structure (XAFS). When a photoelectron is ejected from the 1s energy level of the absorbing atom, we say that we are measuring the K-edge of that specific element (see Figure 6.2). This process occurs when the energy of the incident X-ray matches or exceeds the binding energy required to emit a photoelectron. At this point, an electron leaves its shell, causing a sudden increase (or jump) in the absorption coefficient, usually referred to as a white line or absorbing edge. The emitted photoelectron then undergoes several scattering mechanisms. In the X-ray Absorption Near Edge Structure (XANES) region, which extends a few eV above the absorption edge, the photoelectron primarily undergoes multiple scattering interactions with the valence electrons of surrounding atoms.

Theoretically, the physics of the absorption process can be described using Fermi's Golden Rule, which defines the probability of interaction between electromagnetic waves and atoms. This principle states that the absorption process is proportional to the probability of an electron transitioning from an initial state to a final state (see equation 6.4) [171].

$$\mu_{i\to f} \approx \Sigma|\langle f|H'|i\rangle|^2\rho(E - E_f + E_i) \tag{6.4}$$

where: $\mu_{i\to f}$ is the absorption coefissient probability per unit time, H' is the perturbation Hamiltonian (interaction with the electromagnetic wave), $|i\rangle$ and $|f\rangle$ are the initial and final electronic states, and $\rho(E - E_f + E_i)$ is the density of final states respecting

the conservation of energy.

This probabilistic description provides key insights, such as that XANES is purely governed by electronic transitions that are highly sensitive to the local symmetry of ligands (coordination number). Due to this, the equation cannot be analyzed quantitatively, which gives the XANES region its qualitative nature, making it an interesting tool for speciation analysis. By comparing the spectra of well-defined chemical species as standards, we can model the spectrum of a new sample [172].

It is well known that the position of the K-edge depends on several factors: the oxidation state of the absorbing ion, the stereochemistry, and the covalency of the bonding. A straightforward way to determine the oxidation state of a sample is by analyzing the chemical shift in the XANES spectrum. The chemical shift refers to the shift to higher energies in the XANES spectrum as a result of oxidation.

This shift occurs because when an atom transitions from a neutral state to an ionic state, the oxidation of the absorbing atom creates an imbalance in charge distribution. The loss of electrons leads to an increased effective nuclear charge, meaning that the remaining electrons experience a stronger attraction to the nucleus. Consequently, the 1s electrons are drawn closer to the nucleus, requiring more energy for excitation, which shifts the absorption edge to higher energy [173].

6.3 Short introduction to Extended X-ray Absorption Fine Structure (EXAFS)

Extended X-ray Absorption Fine Structure (EXAFS), unlike XANES, is treated separately, even though both belong to the same absorption spectrum. By simply extending the energy range further above the absorption edge, we observe a different spectral shape.

In the EXAFS region, the absorption coefficient decreases, and characteristic wiggles or oscillations appear in the spectrum. These oscillations arise due to constructive and destructive interference of the emitted photoelectron wave as it scatters off neighboring atoms (see Figure 6.2).

This process is primarily dominated by single-electron scattering, where the photoelectron emitted from the absorbing atom interacts with the core-shell electrons of surrounding atoms. This single-scattering regime gives EXAFS its quantitative nature, allowing us to extract crucial structural information, such as: the type and number of coordinating ligands, and the bond lengths between the absorbing atom and its neighbors.

By measuring the spectrum up to 1000 eV above the absorption edge, we can extract the background of the XAFS spectrum to isolate the chi function $\chi(k)$, which is described by the EXAFS equation. Each single-scattering path of the emitted photoelectron can

be modeled using the EXAFS equation below [174]:

$$\chi(k) = \sum_i \frac{(S_0^2\, N_i)\, F_i(k)}{k\, R_i^2} \sin\left(2kR_i + \delta_i(k)\right) e^{-2\sigma_i^2 k^2}\, e^{-\frac{2R_i}{\lambda(k)}} \tag{6.5}$$

where the N_i is the coordination number (number of atoms in the i^{th} shell), R_i is the interatomic distance between the central atom (absorber) and i^{th} neighbor, $F_\mathrm{i}(k)$ is the scattering amplitude, $\delta_\mathrm{i}(k)$ is the phase shift, $\lambda(k)$ is the mean free path of the photoelectron, σ_i is the Debye-Waller factor, S_0^2 is the many-body amplitude reduction factor which is a chemically transferable property of chemical bonds.

By determining the parameters of this equation, we obtain detailed information about the local coordination environment of the absorbing atom, including:

- The type and number of neighboring atoms;
- Interatomic distances;
- Structural disorder around the absorber.

XAFS measurements were performed at the SOLARIS National Synchrotron Radiation Center (Krakow, Poland) at ASTRA beamline (Figure 6.1). The beamline utilized a double-bend achromatic 1.3 Tesla bending magnet to generate the incident photon beam with an energy range from 1 to 15 keV.

For Cu K-edge and P K-edge data acquisition, the incident photon beam was monochromatized using a Lemonnier-type double-crystal monochromator (DCM) equipped with Ge(220) and InSb(111) crystals, respectively. Energy calibration was performed using a copper metal foil for the Cu K-edge and $FePO_4$ for the P K-edge, aligning the maximum of the first derivative of the absorption spectrum to 8979 eV and 2145.5 eV, respectively.

6.4 Copper K-edge XAFS transmission data analysis of SBA-POO$_2$Cu20%

6.4.1 XANES data analysis of SBA-POO$_2$Cu20%

Initially, the Cu K-edge of SBA-POO_2Cu20% was measured separately to verify the local coordination environment in the highly concentrated sample. The goal was to determine which conformer the copper phosphonate complex adopts and to confirm the assumption based on SEM-EDS analysis, which was that at low functional group concentrations, one copper ion was proposed to be linked to a single phosphorus-containing group, whereas at higher concentrations, a single copper ion coordinates with two phosphorus-containing groups. Other conformations may also occur, such as two copper ions coordinated by two phosphonate groups, especially when the pore diameter shrinks, as the nitrogen sorption

and SAXS showed, pushing two adjacent functional groups to overlap. This configuration is strictly not present at lower concentrations (See Figure 6.3).

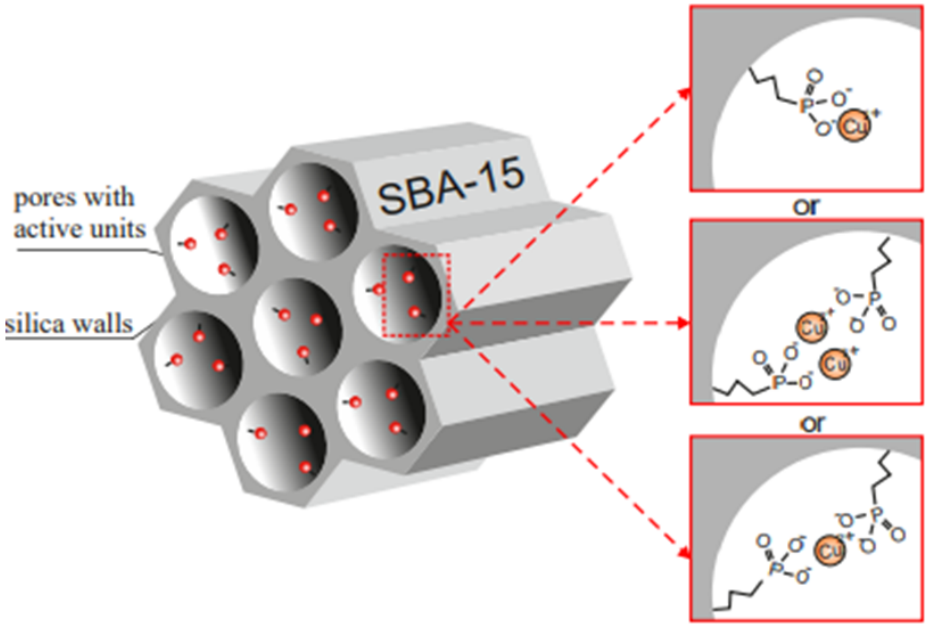


Fig. 6.3. Schematic representation of the possible copper-phosphonate conformers within the silica mesopores

The highest concentration sample was analyzed separately because its high copper absorber content allowed the acquisition of a transmission-mode XAFS spectrum. This mode enables more reliable quantitative analysis, as transmission XAFS measurements give better information than fluorescence XAFS does [175]. Moreover, it is not always straightforward to obtain noise-free fluorescence spectra at high k-values, which are essential for fitting the EXAFS equation 6.5.

The Cu K-edge spectrum of the sample SBA-POO_2Cu20% was measured in transmission mode with ionization chambers and a sample chamber filled with argon gas at a pressure of 52 Torr. The sample of interest was prepared by pressing the powder sample inside a rectangular sample holder folded between a Kapton tape, which resulted in a 300 μm of the sample's thickness. The reference powder samples were ground with a mortar and pestle and spread on the Kapton tape, which was checked before the measurement to make sure that the tape doesn't contain Cu species. All spectra were collected at room temperature.

The sample of interest (SBA-POO_2Cu20%) and copper-containing references (copper foil, CuO, Cu_2O) were measured in the above-described conditions. The reference samples were used for rough estimating of the copper oxidation state and to get more insights about the coordination geometry of the copper ions in the sample of interest, see Figure

6.4.

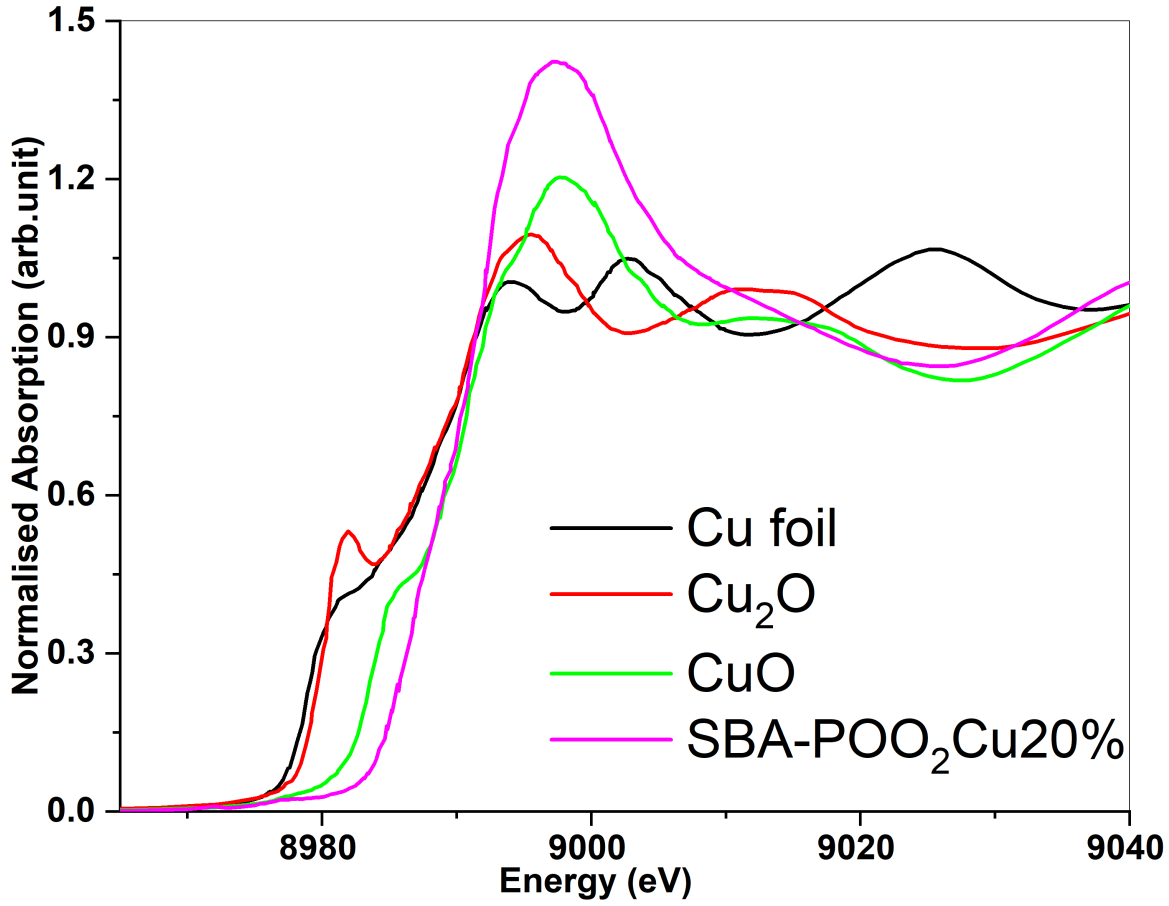


Fig. 6.4. XANES spectra of Cu K-edge of SBA-POO_2Cu20% compared to the standard samples with different oxidation states of copper.

By comparing (fingerprint analysis) the XANES spectrum of the SBA-POO_2Cu20% sample with the spectra of well-known copper standards, such as metallic copper, Cu^{2+} oxide, and Cu^{+} oxide (Figure 6.4), we can determine the degree of copper oxidation inside the mesoporous silica matrix. For Cu^{2+} species, the white line position is typically found between 8986 and 8993 eV, and the position of the first inflection point of SBA-POO_2Cu20% is found on 8986.99 which confirms the 2+ Cu $^{2+}$oxidation state of copper ions in the SBA-POO_2Cu20% sample, but it is worth mentioning that depending on the specific chemical environment and ligands around the Cu atom, the exact location of the white line can change [176, 177].

6.4.2 EXAFS data analysis of SBA-POO_2Cu20%

The Extended X-ray Absorption Fine Structure (EXAFS) analysis provides quantitative information about the absorbing atom's local coordination environment.

Herein, as mentioned earlier, measuring the extended spectrum for all samples was challenging, and only the EXAFS data of the most concentrated sample were collected.

As depicted in Figure 6.5 a, the post-edge region of the X-ray absorption spectrum exhibits characteristic oscillations beyond the absorption edge. These oscillations arise from interference between the outgoing photoelectron wave emitted by the absorbing atom and the waves scattered back from neighboring atoms. The amplitude of these oscillations is more pronounced just above the edge but gradually diminishes with increasing photon energy due to inelastic losses and the decreasing scattering efficiency of the photoelectron [178].

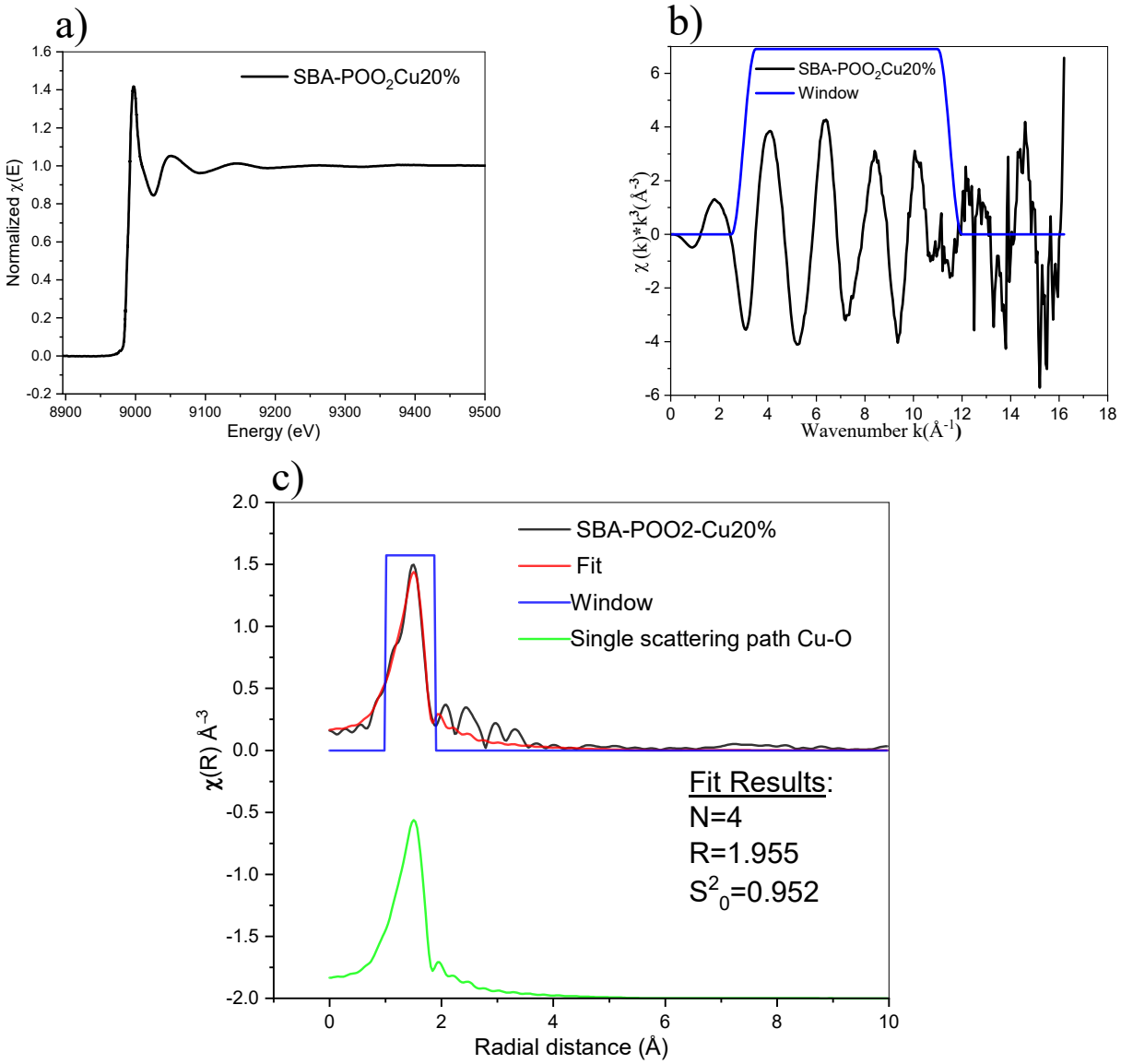


Fig. 6.5. Experimental EXAFS spectrum of SBA-POO_2Cu 20% displayed as: (a) absorption as a function of photon energy, (b) EXAFS oscillations in k-space, and (c) the magnitude of the Fourier-transformed EXAFS signal in R-space, along with the fit to the first coordination shell.

To better analyze and interpret this fine structure, the data is typically transformed from energy space to photoelectron wavevector space (k-space). This transformation is based on the de Broglie relation for the photoelectron, where the wavevector k is related to its kinetic energy by [169]:

$$k = \sqrt{\frac{2m_e(E - E_0)}{\hbar^2}} \tag{6.6}$$

and :

$$k = \frac{2\pi}{\lambda} \tag{6.7}$$

where E is the photon energy, E_0 is the absorption edge energy, and λ is the wavelength of the photoelectron. In this transformed representation (see Figure 6.5b), the oscillatory structure becomes clearer and more suitable for Fourier analysis and quantitative fitting of the local coordination environment.

Athena software [179] was used to process the raw data (calibration, normalization, background subtraction) and to extract the EXAFS signal that was analyzed by Artemis software [180].

The Artemis package uses the standard EXAFS equation to analyze the EXAFS signal, which can be formulated in EXAFS equation 6.5 [174, 181]:

$$\chi(k) = \sum_i \frac{S_0^2\, N_i\, F_i(k)}{k\, R_i^2} \sin\big(2kR_i + \delta_i(k)\big)\, e^{-2\sigma_i^2 k^2}\, e^{-\frac{2R_i}{\lambda(k)}}$$

where the N_i is the coordination number (number of atoms in the i^{th} shell), R_i is the interatomic distance between the central atom and i^{th} neighbor, $F_\mathrm{i}(k)$ is the scattering amplitude, $\delta_\mathrm{i}(k)$ is the phase shift, $\lambda(k)$ is the mean free path of the photoelectron, σ_i is the Debye-Waller factor, S_0^2 is the many-body amplitude reduction factor which is a chemically transferable property of chemical bonds, that's why it was calculated by fitting the FT $\chi(k)$ signal of Cu foil, to deduce that S_0^2=0.952.

The recorded EXAFS spectra were processed as follows:

- The spectra were normalized by subtracting a linear pre-edge and post-edge background; this step is necessary to eliminate the effect of the sample thickness on the rising edge,
- The $\chi(k)$ function (defined by the Equation, 6.5) was extracted from the raw data by subtracting the atomic background using piece-wise splines to approximate a smooth background function,
- Data were Fourier transformed (FT) to isolate individual frequencies in the $\chi(k)$ spectra (k range for FT was (3 – 11.6 A^{-1}).

The EXAFS fitting approach is based on calculating a set of photoelectron scattering paths and adding their contributions to reproduce the experimental spectrum. Each

scattering path represents a specific photoelectron interaction with neighboring atoms, which is typically classified as a single, double, or multiple scattering. These paths are derived from a structural model and correspond to various atom pairs or geometries in the absorber's surroundings. To improve the visibility of oscillatory features in the EXAFS signal, the raw $\chi(k)$ function is often multiplied by a weighting factor such as k^2 or k^3, which amplifies the higher-k components. Although the k-weighted representation improves subtle features, it is not immediately intuitive from a structural point of view. To extract structural information more clearly, a Fourier transform (FT) of the k-weighted EXAFS function is performed over a selected k (defined by a window function). This transformation converts the data from momentum space to real space, resulting in a radial distribution function that represents the average distance between the absorber and neighboring atoms. Figure 6.5c depicts the resulting FT magnitude, denoted by $\chi(R)$. Each peak in the Fourier-transformed spectrum corresponds to a shell of neighboring atoms, though the positions are frequently shifted due to phase effects and do not represent exact interatomic distances without additional fitting. Fitting the magnitude of the Fourier-transformed EXAFS signal in R-space allows for the extraction of meaningful structural parameters such as coordination number, bond distance, and disorder factor for each shell. The results of the first-shell fit are shown in Figure 6.5c. We can cautiously conclude that the nearest coordination shell around copper consists of four oxygen atoms located at a distance of 1.955 Å$\pm$0.02 Å. However, this does not imply a rigid four-fold or square-planar geometry. The second shell appears intense in the Fourier-transformed data, and its inability to fit at this point does not imply that it lacks structural relevance.

The inability to accurately fit the second coordination shell is due to the limited resolution in R-space, which is determined by the available k-range. Resolution is defined as [169, 182]:

$$R = \frac{\pi}{2\Delta k} \tag{6.8}$$

For the SBA-POO_2Cu20% , with a Δk range of approximately 8.6 Å^{-1}, the resolution is about 0.18 Å. This value represents the smallest difference in metal-ligand distances at which two scattering paths from atoms of the same element can be distinguished. Insufficient k-range reduces the ability to resolve overlapping contributions from the second shell, especially when they are close to the first shell. To improve resolution, the data's k-range needs to be extended. Furthermore, statistical constraints, commonly expressed as the Nyquist criterion, limit the number of independent parameters that can be varied during EXAFS fitting [169].

$$N_{\text{ind}} = \frac{2\Delta k \Delta R}{\pi} \tag{6.9}$$

The data ranges in k- and R-space are represented by Δk and ΔR, respectively. This relationship imposes a practical limit on the number of parameters that can be

meaningfully extracted from the data. Exceeding this limit increases the risk of overfitting and introduces nonphysical results. As a result, the fitting must be done with careful consideration of the data range and the model complexity.

Nonetheless, the first-shell fit serves as a solid foundation for developing molecular models that can be used to extend the fitting to include the second coordination shell and better describe the local environment surrounding copper.

6.5 Copper K-edge XANES data analysis of SBA-POO_2Cu1.25%, 2.5%, 5%, and 10% powders and MSTF-POO_2Cu2.5%, 5%, and 10% thin films

This section presents the results of XANES at the Cu K-edges for four different SBA-15 powder samples, each with varying amounts of propyl-copper phosphonate incorporated onto the pore surfaces. All measurements were performed in fluorescence mode.

For functionalized mesoporous silica thin films (MSTFs), it was particularly challenging to obtain noise-free spectra. Increasing the number of scans did not significantly improve the spectral quality, and the lowest-concentration film could not be measured at all due to its extremely diluted absorber and small thickness. Therefore, only MSTFs with loading of 2.5%, 5%, and 10% were successfully measured.

It is essential to reiterate that working with amorphous silica materials and low absorber concentrations (copper in this case) makes EXAFS data acquisition particularly challenging. Since XANES signals are much stronger and easier to collect than EXAFS and can be obtained at relatively lower concentrations [183], most of the data were collected at the XANES level.

The main goal of this analysis is to qualitatively interpret the XANES spectra and compare the spectral features of functionalized SBA-15 powders and mesoporous silica thin films at different functional group concentrations. This helps identify similarities in electronic structure and local coordination around the metallic center between the two forms, which will be further explored through computational analysis in the next chapter

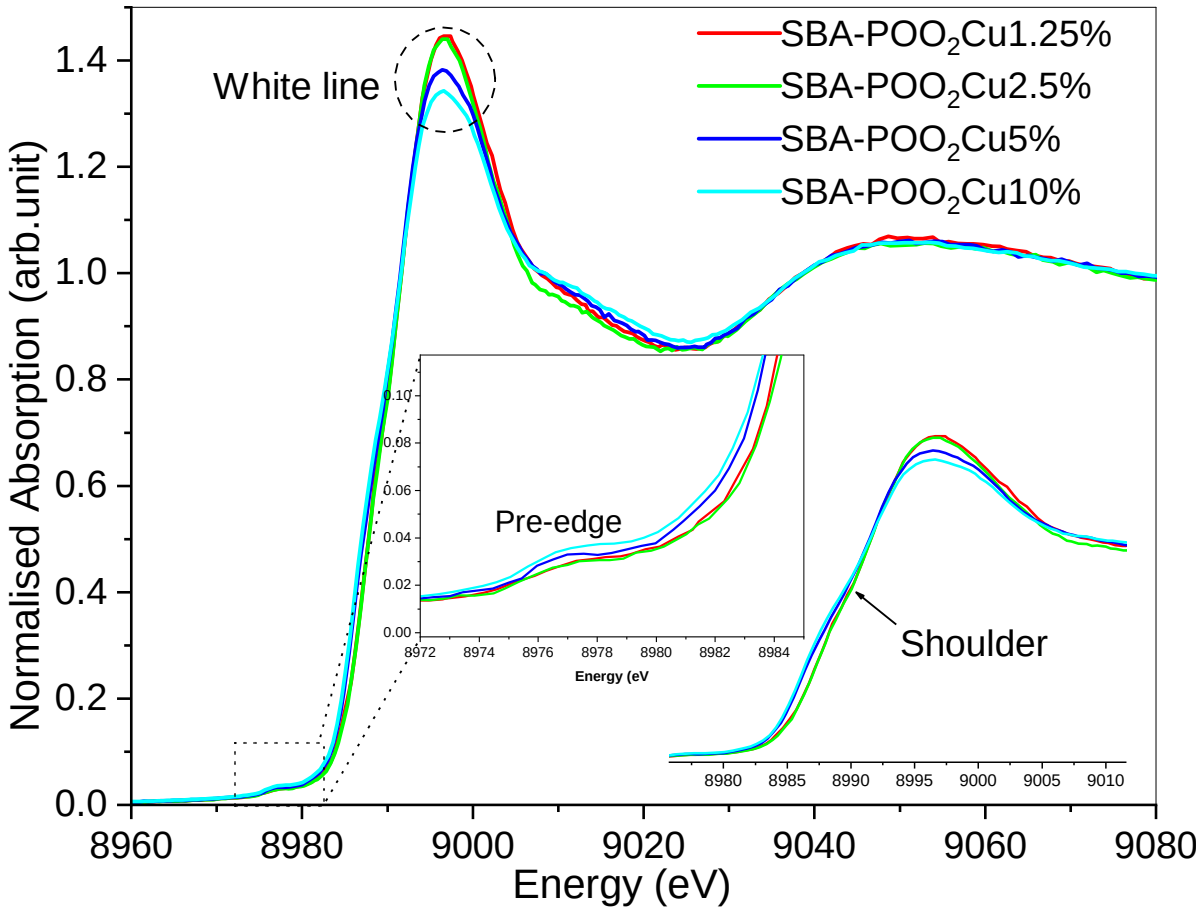


Fig. 6.6. Normalized Cu K-edge absorption coefficient for SBA-POO_2Cu samples with 1.25%,2.5%,5% and 10 % copper-phosphonate concentration.

In the XANES region, the pre-edge peak (shown in Figure 6.2) is an important feature for analysis. This pre-edge can provide insights into electron transitions to unoccupied states, particularly those governed by the dipole and quadrupole selection rules. For transition metals, the pre-edge peak arises from 1s $\rightarrow$ 3d quadrupole transition regardless of the symmetry [184]; each electron transition is associated with a unique shape and intensity of the pre-edge peak, making it an effective diagnostic tool, particularly when studying transition metals like copper [173, 185, 186].

These pre-edge features correspond to 1s $\rightarrow$ 3d transitions that are quadrupole-allowed ($\Delta l = +2$) and thus typically have low intensity compared to the main edge peak. Their intensity and presence are highly dependent on the type of ligand environment, as well as the symmetry of the metal center (copper in this case), both of which influence the number of 3d holes available [186]. Transitions like these are frequently seen in d^9 metal systems, such as Cu^{2+} at around 8977 eV [187]. Sano et al. demonstrated that the intensity of the pre-edge peak increases with the increase in the dihedral angle between the two L-Cu-L planes [188]. Also, it has been shown that the pre-edge peak intensity

decreases in the Cu^{2+} ions in the octahedral geometry as the axial bond distance increases, which we refer to as the octahedron being tetrahedrally distorted (Figure 6.7) [189–191]. Sometimes, despite the filled $3d^{10}$ electron configuration of Cu(I), a pre-edge peak can still be observed. For example, in Cu(I) complexes such as Cu(I)-(styrene) or Cu^{+} coordinated to H_2O or NH_3, a pre-edge feature appears [177, 192]. However, in these cases, the pre-edge peak occurs at a slightly higher energy around 8983eV. This enhancement is attributed not to the $1s \rightarrow 3d$ transition (which is forbidden due togeneral the fully occupied d-orbitals), but rather to a $1s \rightarrow 4p$ transition, which becomes allowed due to the asymmetric coordination environment around the Cu(I) center. Therefore, the presence or absence of a pre-edge should not be used to determine oxidation state, but rather as a probe of local symmetry.

When the SBA-POO_2Cu20% sample was analyzed separately, the pre-edge appeared glitched, which is why this feature was initially overlooked [168]. However, as shown in Figure 6.6, the experimental SBA-POO_2Cu spectra exhibit a well-defined weak pre-edge absorption peak at 8977 eV, which becomes more intense as the concentration of copper-functionalized groups increases. Surprisingly, the pre-edge evolution appears to follow a pattern: Group 1 (G1) for low-concentration samples, and Group 2 (G2) for highly concentrated samples. This behaviour is consistent with patterns observed through other experimental analyses. This observation supports the hypothesis that variations in intermolecular spacing cause a transition or modification in the electronic structure of the functional groups. All of this indicates that the copper absorber in all samples has a +2 oxidation state, as the position of the pre-edge suggests, while each of the investigated samples has a slightly different ligand symmetry environment, as evidenced by the pre-edge peak intensities. The intensity of the pre-edge increases with distortion from a tetragonal symmetry due to enhanced mixing between the Cu 3d and O 2p orbitals.

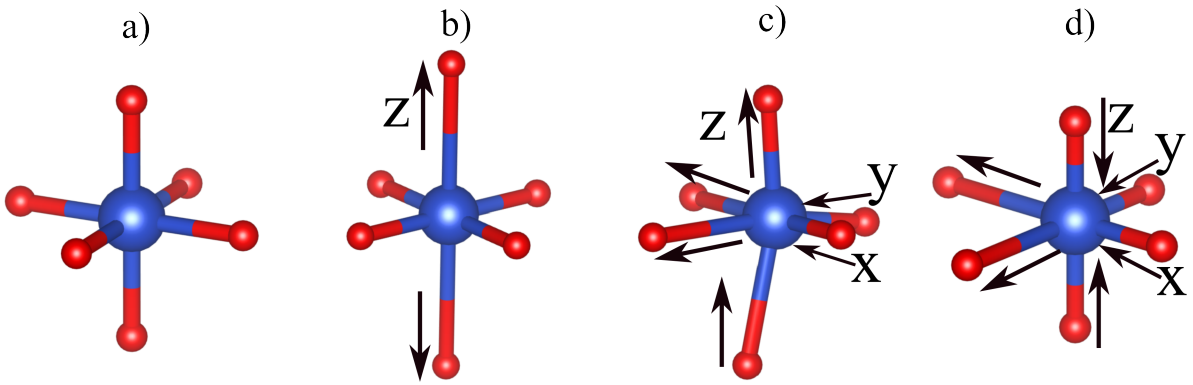


Fig. 6.7. Different types of octahedral packing (a) no distortion,(b) tetragonal-distortion(c) trigonal distortion (d) orthorhombic-like distortion [193].

Furthermore, in our XANES spectra we can expect another type of 1s→4p transitions, called shakedown transitions, which are most likely manifested by the presence of a shoulder at halfway of the rising edge. The value of energy dividing 1s → 4p (shakedown) and 1s → 4p (main) is used to assess the covalency of the metal-ligands bonds [194, 195]. It is difficult to observe the shoulder in the main edge region. However, it is clearly visible in the first derivative of all spectra of SBA-POO_2Cu (see: Figure 6.8).

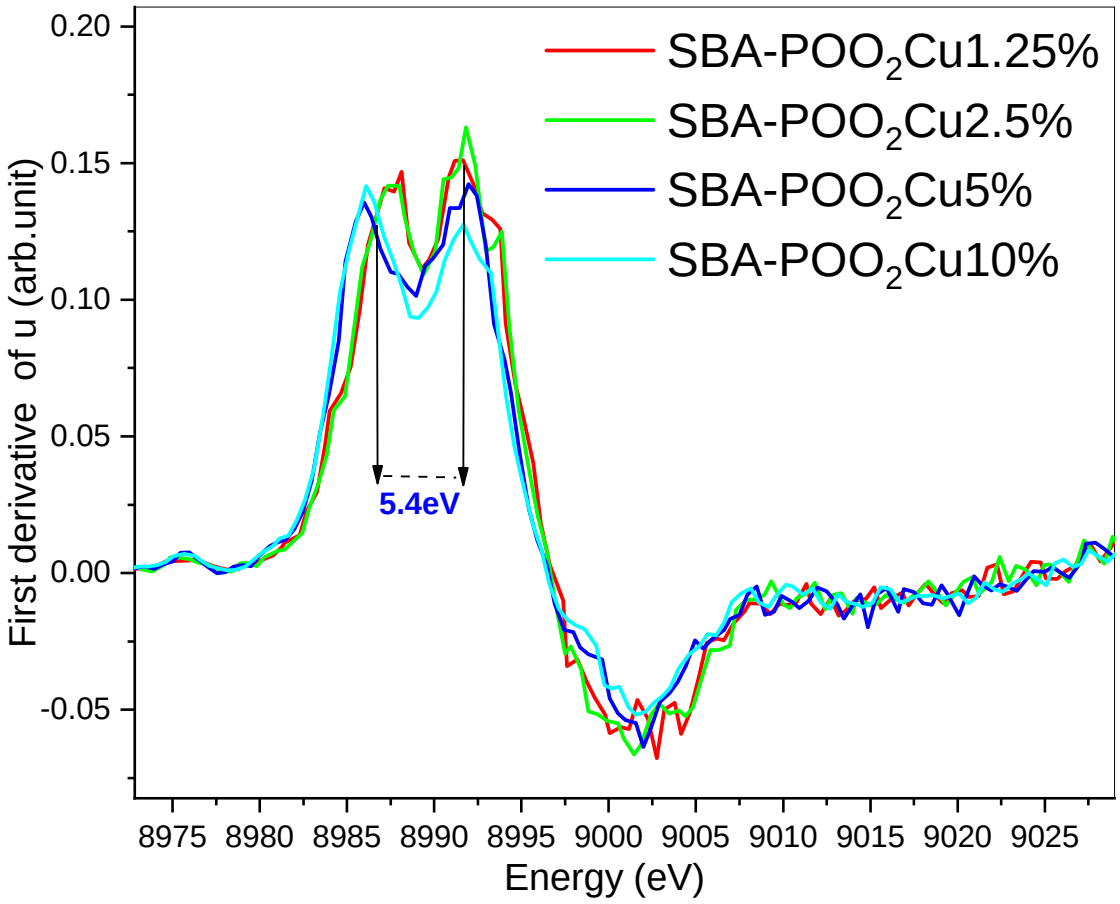


Fig. 6.8. First derivatives of the copper K-edge experimental spectra, $\mu(E)$, for propyl-POO_2Cu-functionalized mesoporous silica powder samples at different functional group concentrations.

SBA-POO_2Cu samples all have the same shoulder feature at a similar energy position around 8986 eV, with an estimated energy separation of 5.4 eV between the two peaks of the shoulder. This energy difference may indicate an increase in the covalent character of the equatorial bonds, caused by charge transfer from the oxygen ligands' 2p orbitals to the copper centres' 3d orbitals. [196, 197]. Palladino et al. [189] observed a similar split in a slightly tetragonally-distorted Cu^{2+}-ATP complex, which is usually attributed to the Jahn-Teller effect observed in hydrated copper complexes. In another study, authors have reported the XANES spectrum of Cu^{2+} in a tetragonally-distorted octahedral

coordination environment, which is similar to the shape of our SBA-POO_2Cu XANES spectra, and it is in accordance with our previous explanation [198].

The white line, which represents the intensity of the main peak at approximately 8997 eV, varies slightly between samples. Notably, the lowest-concentration samples have the highest intensity. This suggests a shift in the Fermi level or a lower energy of the unoccupied 4p orbitals, increasing the likelihood of the 1s $\rightarrow$ 4p transition.

The XANES spectra of the (MSTFs) are not significantly different from those of their powder counterparts, as expected (Figure 6.9). Although the data for the thin films appear to be noisy, there is a noticeable shakedown shoulder at the main absorption edge for the MSTF-POO_2Cu 2.5% sample. While it is difficult to make a precise assessment because of the noise, the overall electronic structure and local geometry around the copper centers embedded in the pores of the thin films are expected to resemble those observed in powder samples.

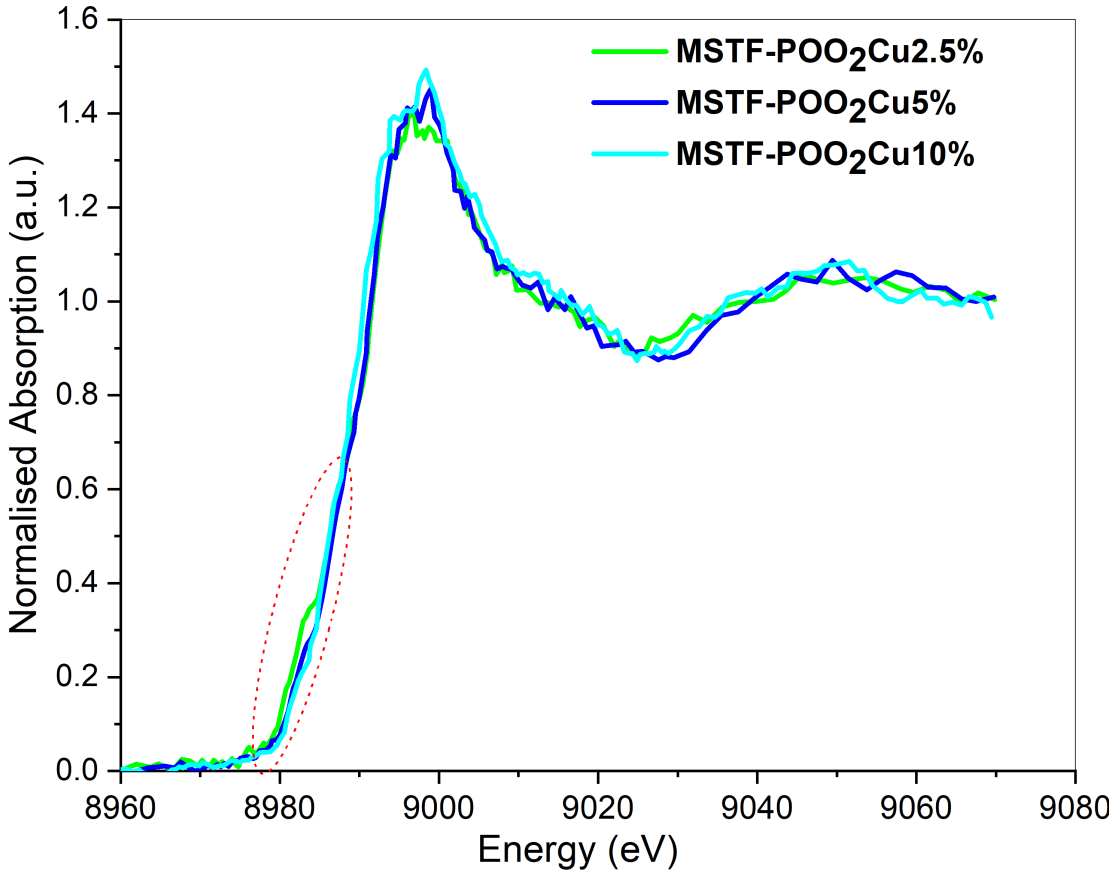


Fig. 6.9. Copper K-edge XANES of thin films with three concentrations of functional groups.

At this stage, it is worth mentioning that the preliminary analysis presented above is

the starting point for comparing the obtained spectra with numerical models to determine the exact coordination environment of the copper centers that are part of functional groups. It is challenging to accurately read the geometry of the copper environment only on the basis of literature data comparison, all the more so, taking into account the limitations in the resolution of the measuring apparatus.

To conclude the qualitative analysis of the copper K-edge, the XANES spectra reveal three key features:

1. Pre-edge feature (8976 eV): The low-intensity peak corresponds to the quadrupole-allowed 1s $\rightarrow$ 3d transition. Its intensity can be quantified by calculating the area under the pre-edge peak and is influenced by 3d–4p orbital mixing [199, 200]. Interestingly, the two lower-concentration samples (1.25% and 2.5%) show similar pre-edge intensities, suggesting a comparable degree of 3d–4p mixing. Likewise, the two higher-concentration samples (5% and 10%) exhibit increased pre-edge intensity, indicative of greater distortion and enhanced 4p orbital contribution.

2. Shoulder on the rising edge: A shoulder feature appears in the middle of the rising edge, corresponding to the dipole-allowed 1s $\rightarrow$ 4p transition. The increasing intensity of this feature, observed in the first-derivative spectra, supports a trend of increasing tetragonal distortion with higher copper-functional group concentrations [199].

3. White line (8997 eV): The intense peak near 8997 eV is attributed to 1s $\rightarrow$ continuum transitions, primarily into unoccupied 4p states. First-derivative spectra reveal that the rising edge shifts to higher energy for the lower-concentration samples. These same samples also exhibit higher white line intensity. This behavior suggests a shift in the Fermi level and possible delocalization effects of the Cu 4p orbitals. In contrast, for the higher-concentration samples (5% and 10%), the white line is less intense and shifted to lower energy, indicating a change in the local electronic structure and possibly more localized unoccupied 4p states.

4. The postedge region appears consistent across all samples. This part of the XAFS signal arises from multiple-scattering effects, potentially involving the same water solvation shell. A more detailed analysis of the post-edge features will be presented later.

6.6 Phosphorus K-edge XANES data analysis of SBA-POO_2Cu1.25%, 2.5%, 5%, and 10% powders and MSTF-POO_2Cu2.5%, 5%, and 10% thin films

The SBA–POO_2Cu samples are analyzed by comparison with their reference counterparts, SBA–$PO(OH)_2$ (propyl-phosphonic acid units before copper immobilization), to highlight the changes induced by copper on the electronic structure of the phosphorus ligands.

At first glance, the P K-edge XANES spectra of the investigated SBA-$PO(OH)_2$ and SBA-POO_2Cu samples at various concentrations (Figure 6.10) reveal only subtle differences among the eight measured samples. This is not unusual, as it is common for light elements such as phosphorus (P), carbon (C), and oxygen (O) to exhibit relatively minor spectral variations, even when their chemical environments differ.

Phosphorus plays a crucial role in biological and mineralogical speciation [201], making it a widely studied element across disciplines. However, it has been argued that phosphorus XAS offers limited advantages, particularly due to the subtlety of its spectral features and the experimental challenges connected with soft X-ray measurements, as George [202] pointed out. These limitations are reflected in the relatively limited number of studies focusing on soft X-ray XAS of phosphorus-containing systems as compared to metallic absorbers such as Cu. Hence, the interpretation of these data has to be done with care, not to overinterpret some spectral features. Importantly, there has long been an effort to understand how changes to phosphorus ligands affect the electronic structure and reactivity of transition metal complexes, especially for catalytic purposes [203]. In the copper phosphonate system investigated here, there is no direct Cu-P bond. Instead, copper is coordinated through the oxygen atoms of the phosphonic acid group. While prior knowledge predicted this binding mode, the P K-edge XANES data provide additional support. Notably, the absence of a pre-edge peak, which is typically associated with metal-to-ligand charge transfer or the mixing of metal d-orbitals with phosphorus p-orbitals in metal-phosphorus bonding, provides spectroscopic evidence that such orbital mixing does not occur here. This re-validates that copper is located outside of the nearest coordination environment of phosphorus. The phosphorus atoms in the functionalized silica, either bearing propyl phosphonic acid groups or propyl copper phosphonate groups, are located at the center of a distorted tetrahedral environment. This geometry consists of one double-bonded oxygen atom (P=O), two hydroxyl groups (P–OH), and one carbon atom from the propyl chain (P–C). As a result, the hybridization of the phosphorus atom is sp^3.

The trend of the white line is another feature of the P K-edge spectra that is noticeable at first glance. Surprisingly, samples with the lowest concentrations of functional groups

show the most intense white line features, and vice versa. One should note that XANES spectra are normalized per absorbing atom, meaning the white line height is not directly proportional to the total phosphorus concentration, but rather reflects the electronic structure around each absorber.

While this trend may appear counterintuitive at first, it can be explained by several factors. The first relates to the effect of intermolecular distances as the surface concentration of phosphorus-containing functional groups changes. In low-concentration samples, these groups are expected to be more isolated, and the phosphorus atoms are farther apart. These spatially separated sites tend to exhibit more localized electronic environments and are less perturbed by neighboring phosphorus centers, resulting in sharper and more intense white line features [204].

The second contributing factor may be the loss of degeneracy in the unoccupied electronic states due to symmetry breaking upon deprotonation. As discussed by Wibowo et al. [205], such structural changes can significantly influence the distribution and energy of unoccupied states probed by XANES, thereby altering the intensity and shape of the white line.

Following this general overview of the obvious spectral features in the P K-edge spectra, a closer look at each experimental spectrum was done on the light that the overall line shape is similiar across all samples.

However, distinct spectral features can still be identified and classified as regions A, B, C, D, and E. These regions correspond to specific transitions or structural motifs in the phosphorus coordination environment and are used to guide the comparison of samples, see Figure 6.10.

Region A, the rising edge corresponds to the 1s $\rightarrow$ p orbital transition and shows a noticeable shift of the absorption edge (K-edge) towards higher energies as the concentration of phosphonic acid units increases. Region B, the white line intensity at the edge. Region C highlights an asymmetry in the white line peak, which becomes more pronounced with concentration changes. Region D, the valley following the white line peak, also shows a trend, becoming deeper or shallower depending on the concentration.

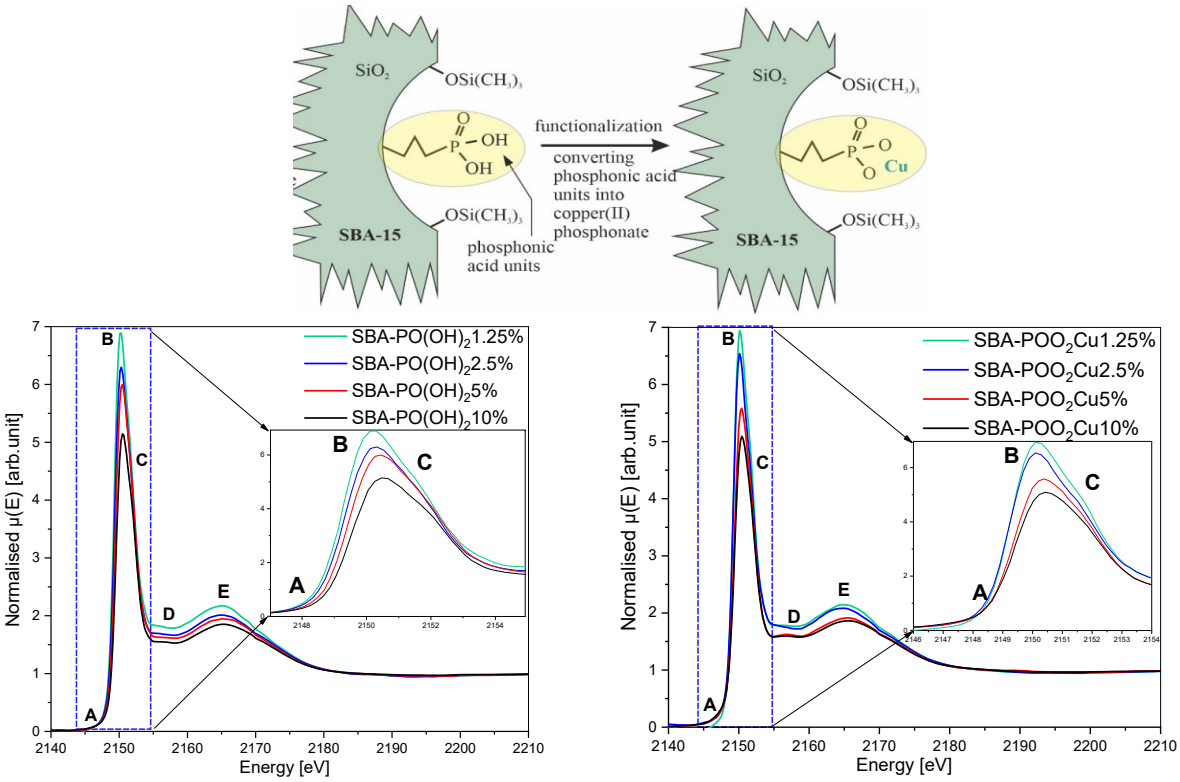


Fig. 6.10. Normalized P K-edge absorption coefficient for SBA-$PO(OH)_2$ and SBA-POO_2Cu samples with 1.25%, 2.5%, 5%, and 10 % copper-phosphonate concentration.

Finally, the post-edge region (E) displays an increase in intensity as the concentration of phosphonic acid units decreases, in a similar trend to the white line peak (B).

- (A) The rising edge, estimated from the first inflection point of the first derivative of the XANES spectrum, appears at approximately 2148.2 eV, corresponding to phosphorus in the +5 oxidation state. The zoomed-in spectra in Figure 6.10 show clear differences in rising edge position. The SBA-$PO(OH)_2$ series exhibits a progressive shift toward higher energies by 0.1 eV as the surface concentration of phosphonic acid functional groups increases. This trend produces well-separated spectra for various concentration levels, indicating changes in the local electronic structure around the phosphorus atoms. The SBA-POO_2Cu series exhibits the grouping trend that was observed for other experimental results. Higher-concentration samples (5% and 10%) exhibit a noticeable shift toward higher energies, despite clustering around a similar rising edge energy. Lower-concentration samples (1.25% and 2.5%) also show overlapping rising edge positions, indicating less significant changes in the phosphorus coordination environment with lower copper loading. This is a very interesting observation as it's in great agreement with the previous experimental conclusion showing that the copper indeed is well incorporated, and it has a critical role in determining the electronic

structure of the entire functional group.

- (B) The white line intensity and position can be used as sensitive probes of the local ligand field surrounding the absorbing atom. The white line intensity decreases with increasing functional groups concentration ($PO(OH)_2$ and POO_2Cu), indicating changes in the local electronic environment and the coordination of phosphorus atoms. A similar trend has been observed in aqueous and solid phosphonic acid at different molar concentrations, although it has not been thoroughly discussed. The authors of that study suggested the effect could be due to self-absorption, as their measurements were performed using the electron yield mode [206]. However, observing the same trend in our study (fluorescence yield) suggests that it could be due high coordination environment that is simply related to the moisture effect, where more water molecules can enter between the functional groups at low concentration as the intermolecular distances are wider. As for the position of the white line maximum, the SBA-$PO(OH)_2$ series shows a slight shift towards higher energies as the concentration of phosphonic acid units increases. Interestingly, the addition of copper causes a distinct grouping trend in the white line maximum of the spectra, indicating systematic changes in the local electronic structure following copper coordination.
- (C) The right part of the main peak shoulder, which is illustrated as a split in the negative lobe of the first derivative presented in Figure 6.11.

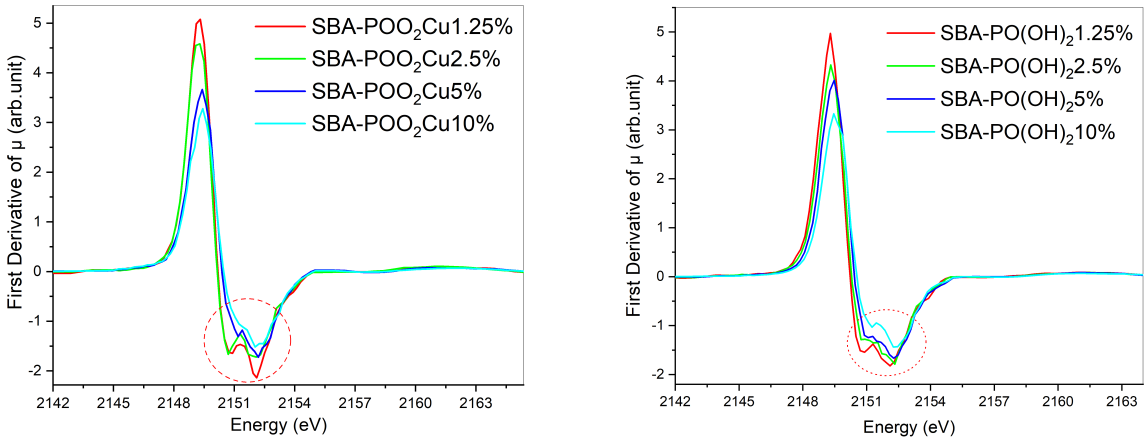


Fig. 6.11. The first derivative of the absorption coefficient function, $\mu(E)$, for propyl-POO_2Cu and propyl-$PO(OH)_2$ functionalized mesoporous silica powders at the phosphorus K-edge

The shoulder splits appear at (2151–2152.1 eV), and it is more prominent at low concentrations of phosphonic acid units and copper-phosphonate. This suggests first that this feature is not connected with the copper electronic cloud but with the nearest phosphorus neighbors, and secondly that at lower concentrations, the phosphorus

environment is more ordered, allowing distinct unoccupied electronic states to be resolved. A. Rouf et al. assign this peak to molecular orbitals with primarily O(2p) character [207].

In contrast, increased concentration likely reduces the average distance between anchored groups, introducing steric interactions and geometrical distortions. These changes broaden the electronic transitions, smearing the spectral features and reducing the derivative intensity of feature C [204, 208].

- (D) The valley feature shows a similar grouping trend when the copper is introduced, a small bump barely visible for the highest concentration of SBA-POO_2Cu; its origin is unclear at this stage.
- (E) The post edge feature usually assigned to multiple scattering resonances or shape Resonances. When the photoelectron scattered waves interfere constructively, this enhances the absorption signal at certain energies (resonance). This resonance can involve a delocalised many-body final state, which reflects the extended coordination environment around the absorbing atom [204].

In order to investigate the effect of copper coordination on the electronic structure of phosphorus, each concentration of functional groups was plotted separately in Figure 6.12. A clear shift in the P K-edge is observed, along with a slight increase in the white line intensity for the sample with 2.5% loading.

This analysis highlights the significant influence of intermolecular distances between functional groups on the molecular orbitals and the overall electronic structure. The P K-edge spectra provide compelling evidence of this, as shown by the distinct spectral grouping patterns. These groupings suggest that key properties of the system—such as electronic behavior or NLO response are governed primarily by the spatial arrangement and intermolecular distances between the copper phosphonate functional groups.

As for the mesoporous silica thin films depicted in Figure 6.13, a similar lineshape and spectral pattern are observed. The same interpretation and analysis described above for the powder samples can therefore be extended to the thin film system.

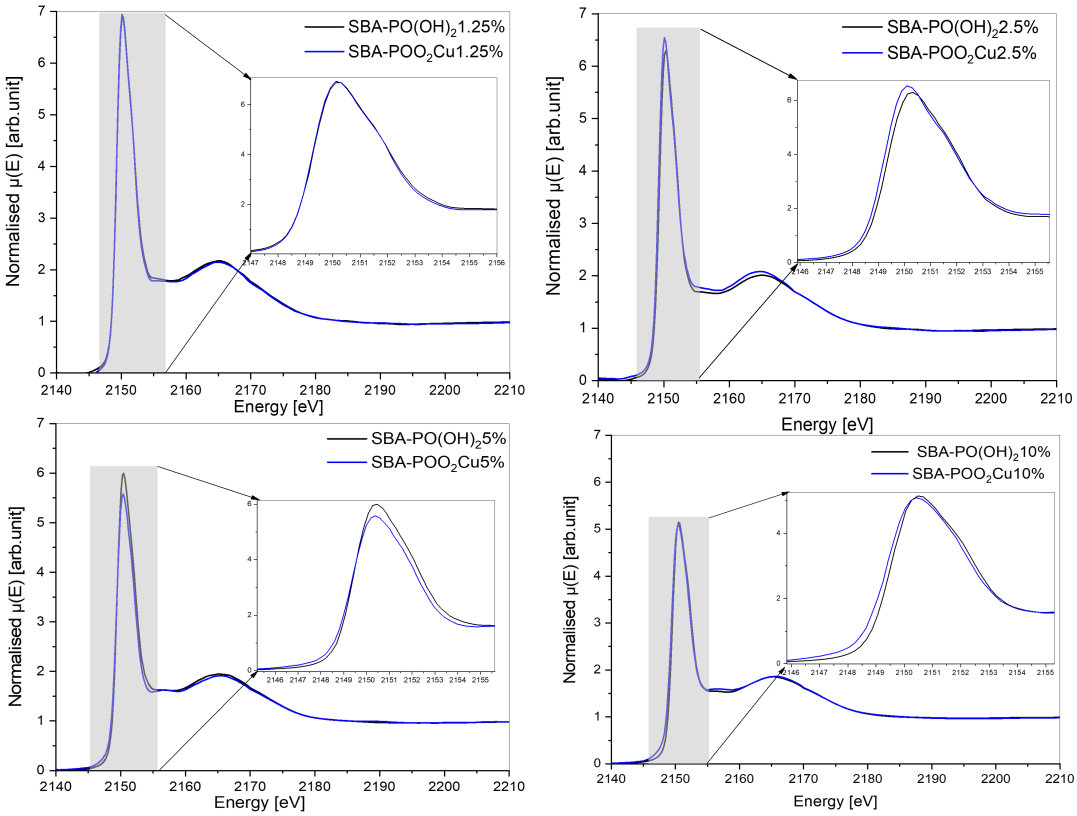


Fig. 6.12. A comparative plot of normalized P K-edge absorption coefficient for SBA-$PO(OH)_2$ and SBA-POO_2Cu samples with 1.25%,2.5%,5% and 10 % copper-phosphonate concentration.

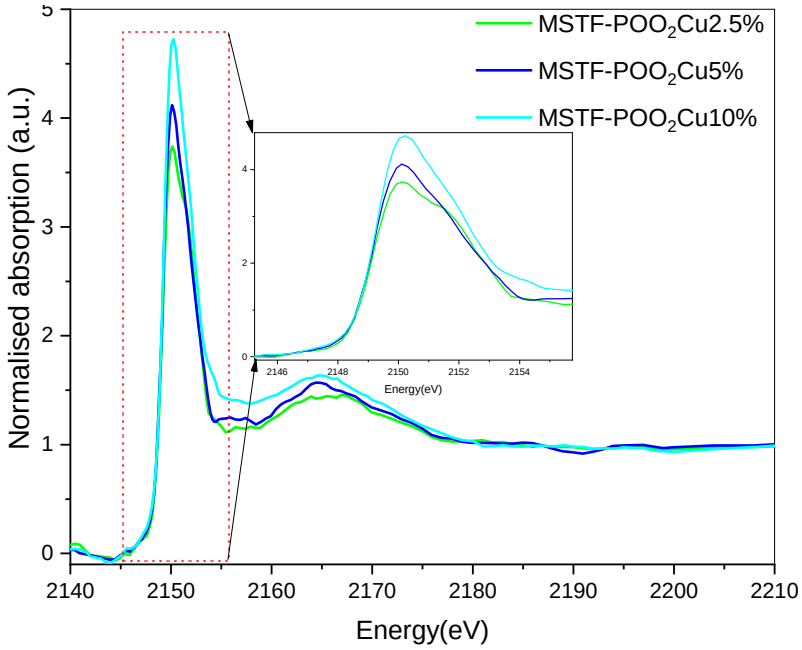


Fig. 6.13. Normalized P K-edge absorption coefficient for MSTF-POO2Cu samples with 2.5%,5% and 10 copper-phosphonate concentration

7 Computational approach of resolving the copper phosphonate functional groups structure using XANES simulation

7.1 Introduction

While EXAFS fitting can provide detailed structural information such as bond distances and coordination numbers, its accuracy is highly dependent on the quality of the experimental data. Noise levels and a limited k-range can have a significant impact on fit reliability. Furthermore, EXAFS requires precise theoretical scattering paths, making it less suitable for highly disordered or heterogeneous systems with poorly defined local structures.

In such cases, XANES fitting, for instance using Linear Combination Fitting (LCF), can be an effective solution when experimental reference spectra are available. This method is particularly useful for deconvoluting mixed-valence or multi-component systems because it provides fractional compositions of the various species present without extracting structural parameters. But, if appropriate references are not available, theoretical spectra can be computed instead using real-space multiple-scattering codes (such as FEFF) [209]. However, one should proceed with caution because the quality and interpretability of theoretical XANES spectra are influenced by the input structural model, core-hole potentials, potential types, and cluster size. So by keeping the input calculation parameters constant and only changing one specific structural parameter of the molecular model, structural changes, such as bond lengths, bond angles, and coordination environments, can be directly linked to variations in the XANES spectral features.

Especially, with the recent advancements, such as the use of AI tools, have greatly simplified the large dataset analysis, making it easier to investigate various potential structures. Models developed from complementary experimental techniques (for example, FTIR, Raman) were used to simulate theoretical XANES spectra with FEFF [168]. These models, which had already been tuned to resemble the real system, served as the foundation for matching and interpreting the XANES experimental spectra. While this approach is not new, it remains highly effective for studying the local structure and

electronic configuration, especially in novel material systems where suitable reference materials are not available.

7.2 Theoretical description of the absorption coefficient

7.2.1 FEFF10 theoretical overview

In this section, I aim to redefine the way XANES spectra are calculated using the real-space Green's function code FEFF, moving beyond the conventional description. In the previous section, I introduced the absorption coefficient, which encodes, within its expression, both the density of the material and the scattering cross section of its constituent atoms. This formulation highlights how the interaction of light with matter depends on the number of available scatterers and their individual ability to interact with incoming photons.

It is well known that the XANES region of the absorption spectrum is dominated by multiple scattering effects. Upon photon absorption, the generated photoelectron undergoes a series of scatterings by the shallow electrons of neighboring atoms. It is important to note that this behavior is the main reason why XANES and EXAFS are analyzed differently, even though they are parts of the same spectrum. The energy of the incoming photon directly influences the kinetic energy of the outgoing photoelectron, as described by the equation:

$$E_{\mathrm{ph}} = \mathrm{KE}_{\mathrm{photoelectron}} + E_0 \tag{7.1}$$

where E_{ph} is the energy of the incident photon, $\mathrm{KE}_{\mathrm{photoelectron}}$ is the kinetic energy of the emitted photoelectron, and E_0 is the binding energy of the core electron.

As the energy of the incident photons increases, the photoelectron acquires more kinetic energy, allowing it to travel further and probe deeper into neighboring atoms, as typically observed in EXAFS. In contrast, low kinetic energy photoelectrons, typical in the XANES region, have longer wavelengths ($\lambda \propto 1/\sqrt{E}$) and exhibit pronounced wave-like behaviour. Due to their long wavelengths, these photoelectrons are easily scattered by nearby atoms, leading to strong multiple scattering contributions. Multiple scattering paths are extremely sensitive to the three-dimensional arrangement of atoms (bond lengths and angles), making the fine structure observed in XANES a powerful probe of the local stereochemistry [210, 211].

Throughout the years, researchers have developed a quantitative and well-established model for analyzing the Extended X-ray Absorption Fine Structure (EXAFS), commonly referred to as the EXAFS equation. This approach allows for detailed structural information to be extracted, such as interatomic distances, coordination numbers, and disorder.

However, a similarly universal and simple analytical model has not been achieved for the X-ray Absorption Near Edge Structure (XANES) region, due to its more complex and dense spectral features, which are sensitive to both local geometry and electronic structure. It is at this point that real-space multiple scattering (RSMS) theory becomes essential [212, 213]. XANES requires a full multiple scattering description to capture the rich interference patterns and strong final-state effects near the absorption edge.

RSMS operates directly in real space, making it suitable for disordered, aperiodic, or molecular systems. Real-Space Multiple Scattering (RSMS) theory starts by calculating a photoelectron's scattering paths, atom by atom, beginning with the absorbing atom and extending outward into its local environment. The method uses the Muffin-Tin approximation to simplify the complex potential landscape by assuming spherical atomic potentials centred on each atom (see Figure 7.1). Then the entire formalism is based on the use of Green's functions, which provide an efficient way to model photoelectron propagation and account for all possible scattering events, including complex multiple scattering paths.

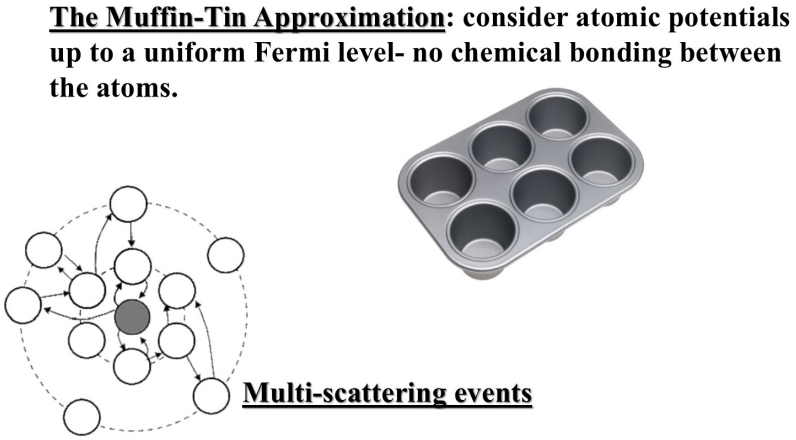


Fig. 7.1. Muffin-tin approximation.

The single-particle Green's function used in XANES calculations is given by [214]:

$$G(E) = (E + i\Gamma - H)^{-1} \tag{7.2}$$

where:

- E is the energy of the photoelectron relative to the Fermi level,
- Γ is a small imaginary broadening term accounting for core-hole lifetime and inelastic losses,
- H is the effective one-electron Hamiltonian, typically within the muffin-tin approximation.

The Green's function can also be expanded into a series of multiple scattering events [215]:

$$G(E) = G^0(E) + G^0(E)tG^0(E) + G^0(E)tG^0(E)tG^0(E) + \cdots \tag{7.3}$$

where:

- $G^0(E)$ is the free-electron propagator,
- t is the scattering matrix (t-matrix) of an atom,

The terms in equation 7.3 represent single, double, triple, etc., scattering paths. The Green's function approach allows, under certain conditions, the absorption coefficient to be expressed as a sum over an infinite series of terms, each corresponding to a specific scattering path [212].

$$\mu(\omega) \propto \mathrm{Im} \sum_c \langle c|d^\dagger G(\omega + E_c)d|c\rangle \, \theta_\Gamma(\omega + E_c + E_{\mathrm{Fermi}}) \tag{7.4}$$

where d, $d^\dagger$ are single particle dipole operator and its Hermitian conjugate while θ_Γ is broadened step function.

This expansion allows XANES to capture the complex interference patterns resulting from multiple scattering, which are essential for interpreting near-edge fine structure [214].

7.2.2 FEFF10 Software Graphical User Interface (GUI)

Despite the complex theoretical framework behind the `FEFF` code, its Graphical User Interface (GUI) is remarkably straightforward and user-friendly. As shown in Figure 7.2, the main components of the interface are divided into four major control panels, each highlighted in a colored box [216].

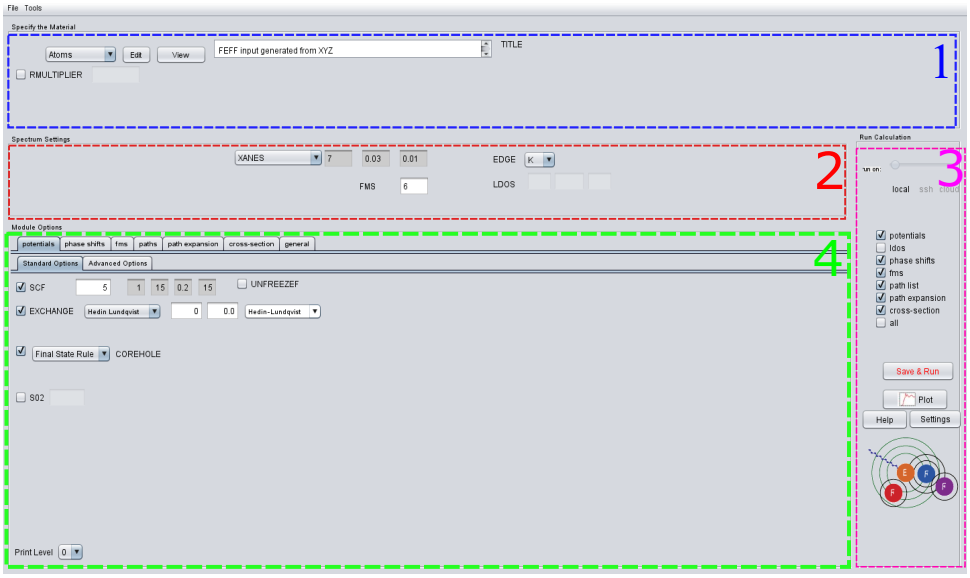


Fig. 7.2. GUI interface of FEFF10 Code.

1. **Material Dashboard**: This is the first control card, where users can specify the system under study. Loading a simple `feff.inp` file, as shown in Figure 7.3, allows viewing and editing the atomic structure's Cartesian coordinates. Users can also select the absorber atom, inspect the uploaded structure, and make adjustments as needed.

```
TITLE Molecule-1
COREHOLE FSR
EDGE K
CONTROL 1 1 1 1 1 1
FMS 4 1
XANES 7 0.03 0.1
EGRID
e_grid  -20  80.0  0.1
SCF 3 1 15 0.2 20
EXCHANGE 0   0
RGRID
POTENTIALS
0 15 P
1 8 O
2 1 H
3 6 C
4 29 Cu
ATOMS
  7.14200    1.33260    1.07500    3 C
  6.34470    1.89240    1.56040    2 H
  0.00000    0.00000    0.00000    0 P
  0.27960    1.59190   -0.23750    1 O
  2.88370   -1.14730   -0.09880    4 Cu
END
```

Title of the system

ipot , ixsph, ifms, ipaths, igenfmt, iff2x.
Full multiple scattering
The output k values for the XANES calculation

The output energy grid of XANES

Self-consistent potential calculations
The energy dependent exchange correlation potential
The radial grid used for the potential and phase shift calculation

Potential indices of each atom in the system :
0 is always assigned the absorber.

Cartesian coordinates (in Ångstroms)

Fig. 7.3. Overview of a typical FEFF input.

2. **Spectroscopy Dashboard**: The second card allows the user to select the type of spectroscopy being simulated (e.g., XANES or EXAFS) and specify parameters such as the absorption edge (e.g., K-edge) and the scattering path length, which determines how far neighboring atoms are considered in the calculation.

3. **Control or calculation Dashboard**: This section manages the simulation run's parameters, plots the calculated spectrum, and includes additional modules that can be activated and run concurrently, such as the local density of state ldos.

4. **Modules Dashboard**: This card allows access to various computational modules within FEFF, including full multiple scattering, self-consistent field (SCF) iterations, and potential analysis.

The FEFF guide manual provides a detailed description of each card and module.

7.3 Geometry optimization of structural models using Gaussian16

Density Functional Theory (DFT) is a computational method that uses the time-independent Schrödinger equation to calculate the eigenvalues (energy levels) and eigenstates (wavefunctions) of a quantum mechanical system. However, it is difficult to solve this equation precisely for systems containing more than one electron at a time. Even for relatively simple systems such as the hydrogen atom, analytical solutions are nontrivial, and as the number of electrons increases (for molecules) the complexity of electron-electron interactions makes an exact solution nearly impossible. This is where approximations are required. DFT avoids the need to solve the many-body wavefunction directly by focusing on electron density, which is a function of only three spatial coordinates, regardless of the number of electrons. This simplification, combined with well-established approximations to the exchange-correlation energy, makes DFT a powerful and widely used tool for studying molecular and solid-state systems, with reasonably accurate results that are often in close agreement with experimental data.

Instead of solving directly for the many-electron wavefunction, we can reformulate the quantum mechanical problem by focusing on the electron density $\rho(\mathbf{r})$. This is the fundamental idea behind Density Functional Theory (DFT). An electronic system's total energy is treated as a function of electron density, $E[\rho(\mathbf{r})]$, rather than the many-electron wavefunction.

The electron density is calculated using the Kohn-Sham orbitals $\psi_i(\mathbf{r})$, which are solutions to the effective one-electron Kohn-Sham equations. The definition is as follows

[217]:

$$\rho(\mathbf{r}) = \sum_{i=1}^{N} \psi_i(\mathbf{r})^2 \tag{7.5}$$

with N is the number of electrons.

The first step in the DFT calculation workflow would be building or proposing a molecular system that represents, at best, the atomic or molecular motifs present in the real system under study. Making a molecular model usually consists of building a molecule that is thought to represent the material under investigation. This rudimentary model is guided by preliminary experimental results and chemical intuition of the synthesis process, which includes knowledge of bonding preferences, coordination environments, and possible geometries. After placing the atoms and connecting them with chemical bonds, a geometry optimization is performed. Geometry optimization is done to minimize the internal energy of a molecular system by adjusting the chemical bonds and angles to find the most stable conformers of a molecule. Most modern (gradient) optimization procedures require calculation of the Hessian (H) or its inverse, the individual diagonal elements of H are identified as bond-stretching and bond-bending force constants [218].

From the first-shell fit of the EXAFS experimental SBA-POO_2Cu20% data (four oxygen atoms around the copper Figure 6.5) and literature reports, particularly on Jahn–Teller distortions in Cu(II) [177, 219–222], a set of DFT-structural models was built for reliable (guided by experimental analysis) XANES fitting and computational model generation. SBA-15 silica rings [223] were excluded from the conformer models, as they are computationally expensive and unnecessary for XANES, which is a local probe.

DFT modeling in this research was guided by experimental results. The coordination environment was shown to depend on the concentration of functional groups—shifting from one phosphonic unit binding a copper ion at low concentrations to two phosphonic units coordinating copper at higher concentrations (see Figure 6.3). Models were thus developed to represent the molecular structure of SBA-15 silica functionalized with 20% groups. This sample exhibited a reduced copper-to-phosphorus ratio (EDS) alongside structural changes such as pore narrowing (SAXS) and decreased specific surface area (N_2 sorption). For samples with lower functional group concentrations, additional model sets were prepared to fit XANES data, consistent with their experimental EDS, SAXS, and N_2 sorption results.

7.3.1 Set (S1): Models representing the conformer at highest functional group concentration

The first set (S1) includes models with a double functional group consisting of two $CH_3PO_3H^-$ groups, one copper ion (Cu^{2+}), and two water molecules, as well as models with a double

functional group consisting of two $CH_3PO_3H^-$ groups, one copper ion (Cu^{2+}), and four water molecules.

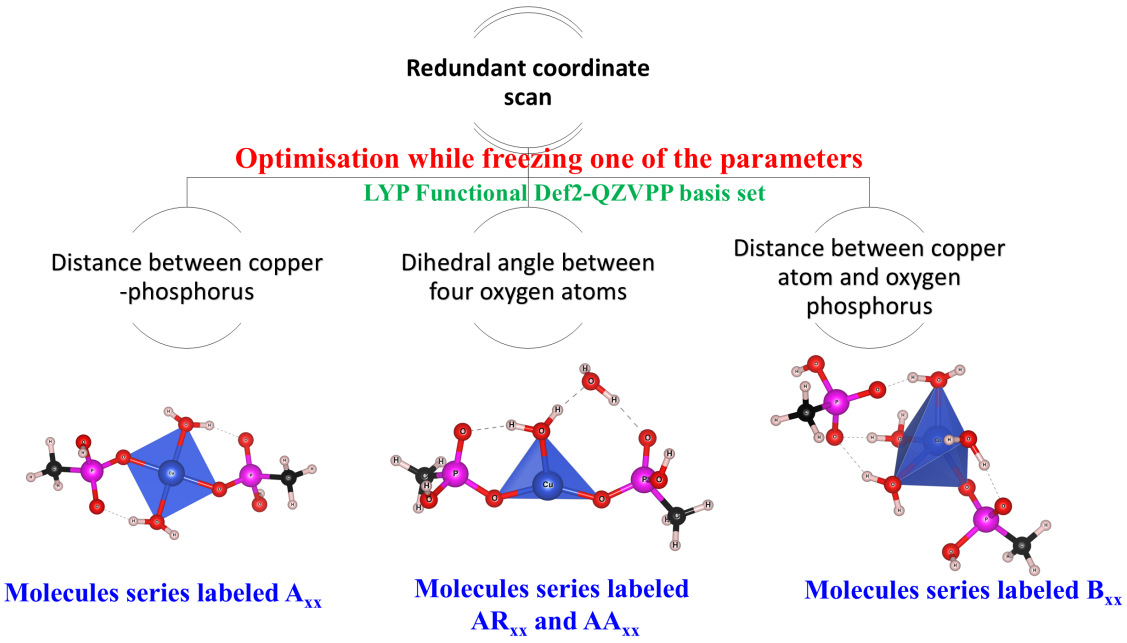


Fig. 7.4. Redundant coordinate scan workflow.

These models were deformed by changing and freezing one of the parameters. These parameters were as follows: the distance between copper and phosphorus atoms (models named Axx), the dihedral angle between four oxygen atoms (models named ARxx and AAxx), and the distance between the copper atom and oxygen phosphorus group P=O (models named Bxx). This allowed us to explore different plausible configurations without relying on a single optimized geometry (Figure 9.9). based on these models, the results of the XAFS analysis for this material were presented in the publication [168]. A total of 64 models were created and used to find the most probable molecular structure of the sample SBA-POO_2Cu20%. Figure 7.5 shows all 64 models of double functional groups named set 1. These models were used to analyze the XAS study whose results were published in the [168].

The constrained optimizations were performed at the DFT level using the Becke 3-parameter hybrid functional (B3) [224] with the Lee-Yang-Parr (LYP) [225] correlation functional [226] with the standard basis set of bases def2-QZVPP [227].

The Relaxed scanned models generated around 64 conformers that range between distorted trigonal planar, T-shaped, tetrahedral, square planar, seesaw, trigonal bipyramid and octahedral.

Figure 7.6 shows a relaxed scan along the P-Cu bond distance in 23 steps of 0.1 Å, ranging from 3.13 Å to 5.72 Å. At each step, the molecule's geometry was optimized while

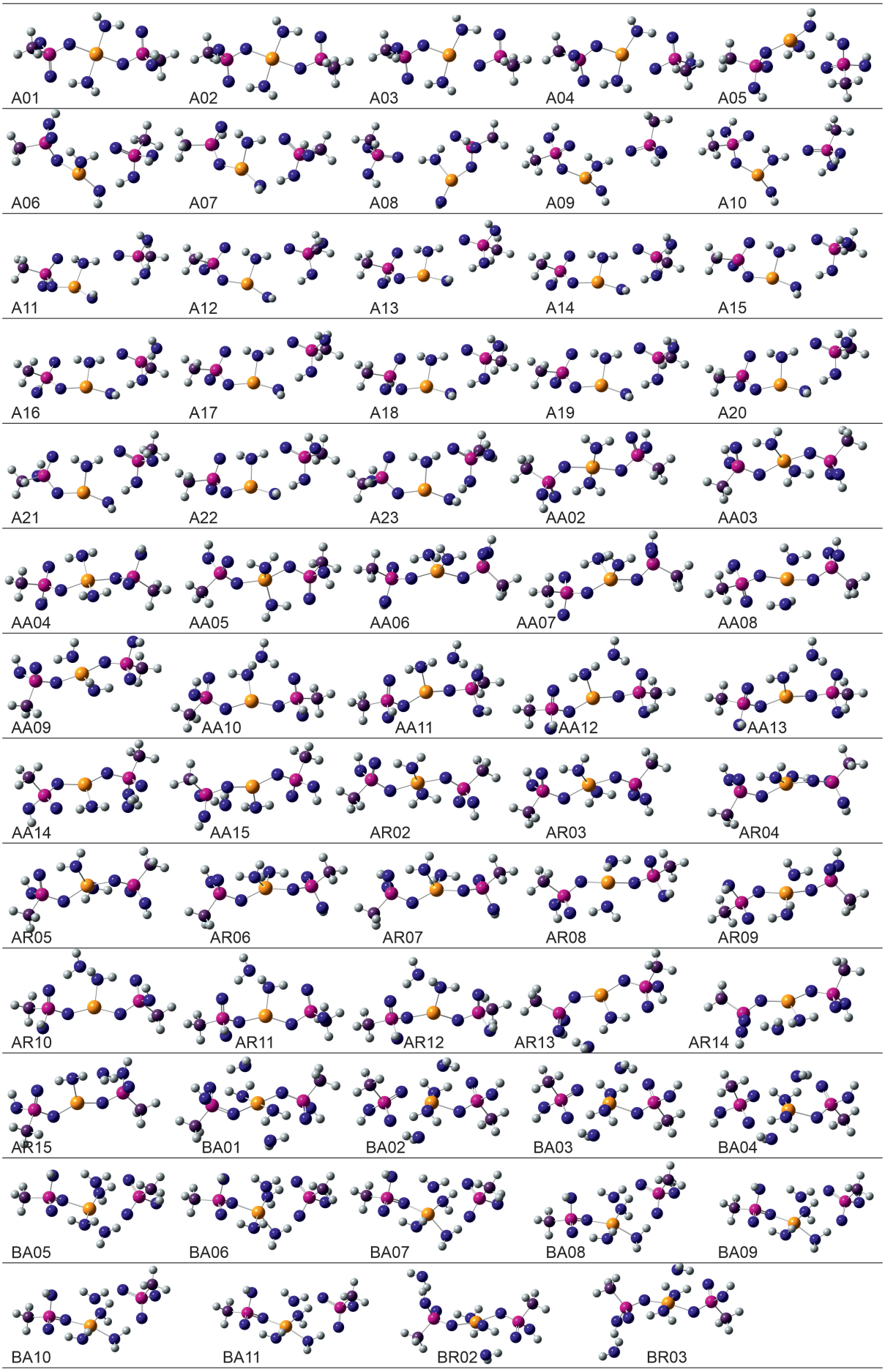


Fig. 7.5. The 64 models of double functional group - set 1.

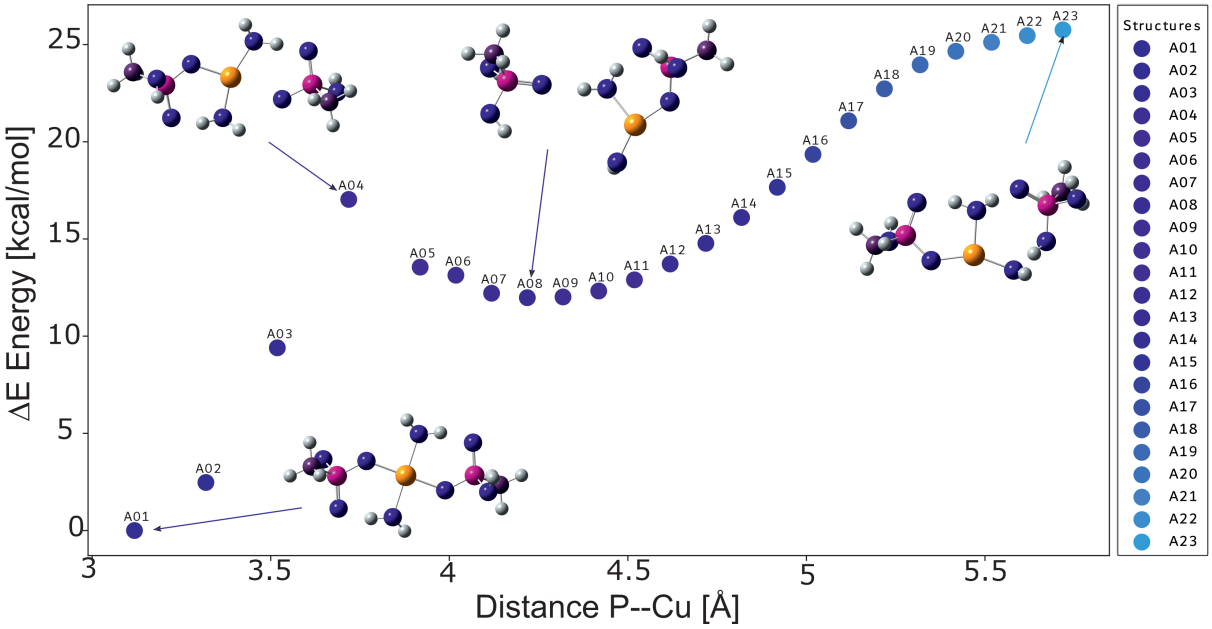


Fig. 7.6. Relaxed scan energy curves varying changing distance between one copper and phosphorus atoms. ΔE values (in kcal/mol) with respect to the lowest minimum energy structure (A01) are plotted [168].

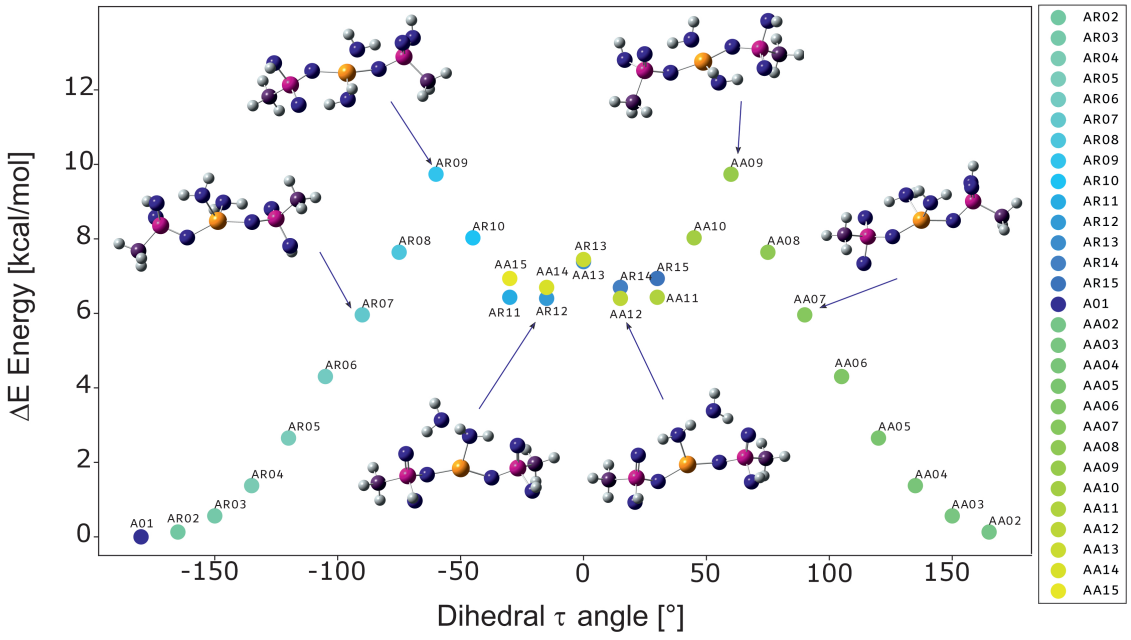


Fig. 7.7. Relaxed scan energy curves varying torsion angle. ΔE values (in kcal/mol) with respect to the lowest minimum energy structure (A01) are plotted [168].

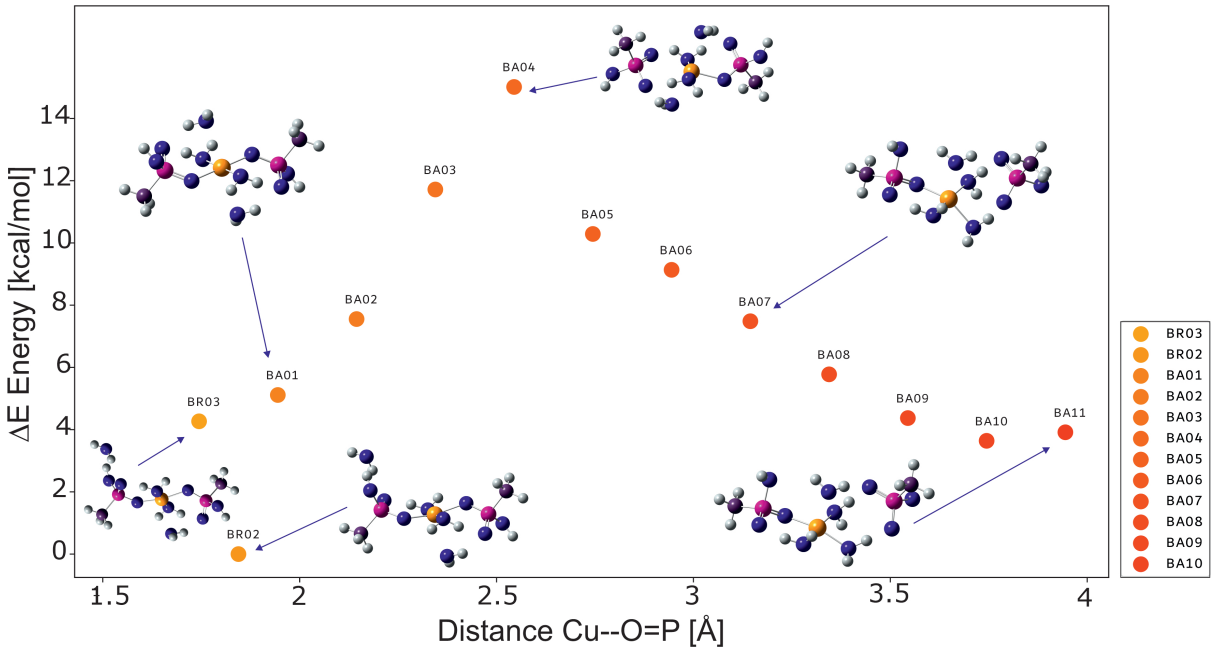


Fig. 7.8. Relaxed scan energy curves varying distance between oxygen from P=O group and copper atom. ΔE values (in kcal/mol) with respect to the lowest minimum energy structure (BRO2) are plotted.

the P-Cu distance remained constant. The findings indicate that as the P-Cu distance increases, the molecular geometry gradually shifts from a square planar configuration to a more trigonal configuration. This structural distortion is accompanied by a moderate increase in the system's internal energy, which is still within physically acceptable limits. In the second scan, starting from the same square planar model (A01), the dihedral angle defined by the four coordinating oxygen atoms was constrained to vary in 15° increments in both positive and negative directions (see Figure 7.7). For this set of constrained optimizations, a lower internal energy minimum was found compared to the bond distance scan, indicating that dihedral flexibility in the ligand environment is more important in stabilizing the copper coordination geometry. As for the third category of scans (Figure 7.8) we aimed to expand the square planar coordination environment into five- and six-coordinate geometries by adding more water molecules to the initial model. The distance between the copper atom and the oxygen atom of the phosphoryl group (O=P) was the key geometric parameter examined in this set. By systematically changing the Cu-(O=P) distance, we were able to see how the coordination geometry evolved and how the internal energy responded to this geometric change.

As shown in Figure 7.6, Figure 7.7, and Figure 7.8, each structural conformer was at an energy minimum, ensuring the stability of these configurations and the correctness of the computational models.

7.3.2 Set (S2) and (S3): Models representing the conformer at lower functional group concentration, with and without copper

In order to analyze the XAFS results for samples with lower concentrations of functional groups, additional models were prepared. In this case, the models of a single functional group were built. It was two sets of numerical models. First of them (S2) include systems containing one phosphonate group ($CH_3CH_2PO_2^{3-}$), one copper atom (Cu^{2+}), and n water molecules (n=0...6). Moreover, these models take into account the ionic forms formed after the detachment of a proton or the addition of an OH^- group. These models are visualized in Figure 9.12.

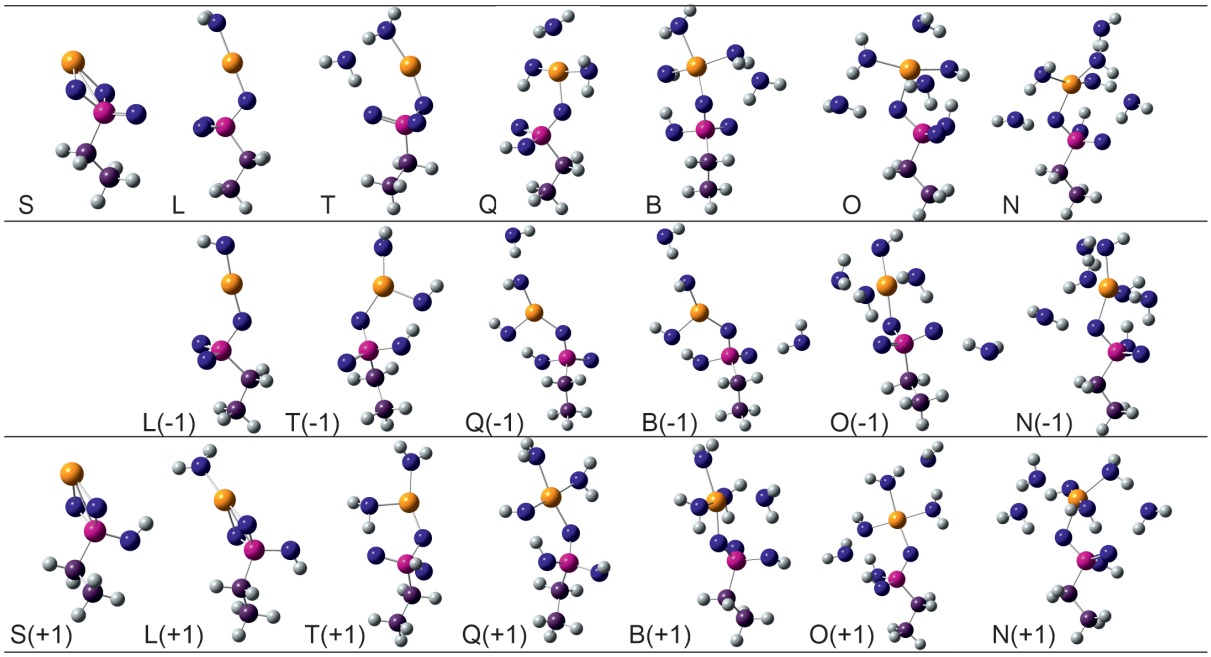


Fig. 7.9. The 20 models of single functional group - set 2 (S2).

The second set of numerical models (S3) include systems containing one propyl phosphonate group ($CH_3CH_2PO_2^{3-}$), and n water molecules (n=0...6). These models without a copper atom were used to verify XAFS data collected at the phosphorus K-edge. These models are visualized in Figure 7.10. In total, both sets contain 32 numerical models of individual functional groups.

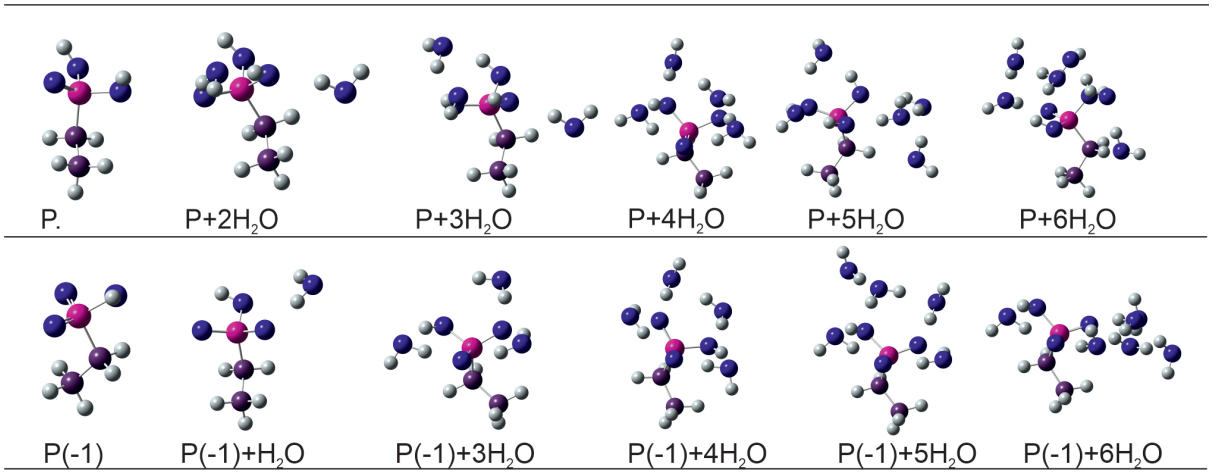


Fig. 7.10. The 12 models of single functional group - set 3 (S3).

7.4 XANES analysis on the basis of numerical simulations

Once the computationally optimized structural models were obtained, they were used as input for calculating the XANES spectra at the copper K-edge using the FEFF10 code [216].

The input parameters we use as following: the wave vector range of `kmax` = 7 Å^{-1}, `kstep` = 0.03 Å^{-1}, and `Estep` = 0.01 eV. The FMS was set to 6 Å, and the self-consistent potential (SCF) loop was defined with the following parameters: `rfms` = 5 Å, `lfms` = 1, `nscmt` = 15, `ca` = 0.2, and `nmix` = 15.

- `rfms` is the radius of the cluster used for full multiple scattering during the self-consistency loop,
- `lfms` = 1 specifies that the FMS sphere is centered on the absorbing atom,
- `nscmt` defines the maximum number of self-consistent iterations,
- `ca` is the convergence acceleration factor,
- `nmix` is the number of mixing steps per iteration.

The default exchange-correlation potential was Hedin-Lundqvist, and the final state rule with a core-hole was applied, corrections card has been used to adjust the energy edge shift and the peak broadening. Unless otherwise stated, all other parameters were left at their default. Spectral convergence was confirmed by gradually increasing the FMS radius, ensuring that the resulting spectrum was consistent across this increase.

To systematically organize the obtained models into well-defined coordination geometries, all spatial analyses were carried out with the copper position as the reference. In addition, a distance matrix between the nearest oxygen atoms was used to capture the spatial arrangement of ligands around the copper center, a Gaussian function was superimposed to the atoms' spatial position, see Figure 7.11. The models BA are not

shown in the figure, but the same procedure was applied without excluding any model. These supplementary analyses can be found in the Supplementary Information of the our publication [168].

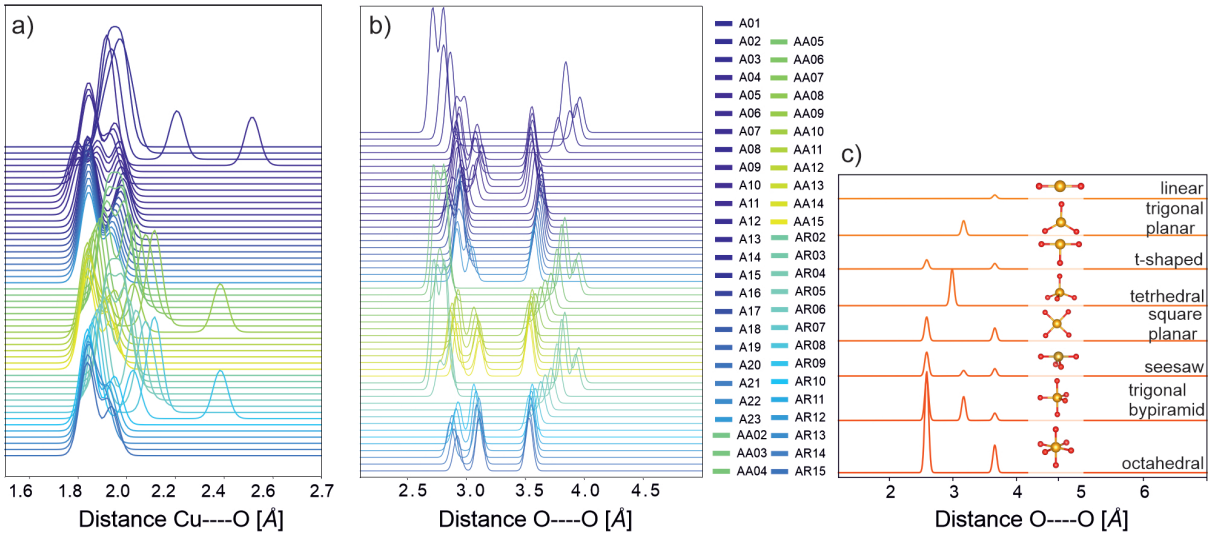


Fig. 7.11. Spectrogram of distance distribution between (a) oxygen and copper (Cu–O),and (b) oxygen and oxygen (O–O) located in the nearest sphere of the copper atom. Model of potential shapes of the copper environment (c). Gaussian functions were applied to each distance value [168].

Cluster analysis was then applied to quantify the similarity of copper atom environments in the functional groups, and the models were sorted into related clusters accordingly. This routine analysis led to groups of models labeled as following [168]:

- pseudo t-shape: Group1 (models: A13, A14, A15, A16, A17 and A18); Group2 (models: A12, A19, A20, and A21);
- pseudo t-shape-triangle: Group1 (models: A07, A10, AA11, AR10, A05, A06, AA10, A22, A11, and A23); Group2 (models:AA12, AA14, AA13, AR13, AR15, AR12, AR14, AR11, AA15, A08, A09);
- pseudo seesaw (models: AA05, AR05, AA07, AR07, AA06, and AR06);
- pseudo tetragonal (models: AA09, AR09, AA08, and AR08);
- pseudo square Group1 (models: A03, AA04, AR04, A02, AA03, AR03, A01, AA02, and AR02); Group2 (model A04); Group3 (models: BRO2 and BR03);
- pseudo trigonal bipyramid (models: BA05, BA06, BA07, BA08, BA09, BA10, BA11);
- pseudo octahedral (models: BA01, BA02, BA03, and BA04);
- pseudo square, pseudo trigonal bipyramid, and pseudo octahedra (B-labeled models).

Now, statistically speaking, before deciding on the best statistical data analysis method for each dataset, careful thought is required depending on the type of the data set. Linear Combination Fitting (LCF) and Principal Component Analysis (PCA) are two widely

used methods for analyzing XANES data beside other advanced techniques such as: multivariate curve resolution - alternate least squares (MCR-ALS) [228], the reverse Monte Carlo method [229], and machine learning analysis [230]. When analyzing mixtures of known reference compounds, LCF is typically preferred in speciation studies [231]. It allows for the quantification of the relative concentrations of these known components by fitting the experimental spectrum as a weighted sum of their respective spectra. When the number and identity of pure components are unknown, PCA serves as an exploratory tool. PCA reduces the dataset's dimensionality, allowing the discovery of underlying components and clustering of similar spectral features. PCA is a powerful method for unsupervised, data-driven analysis in complex systems [232, 233].

In general, the PCA was used to find the optimal position of the spectrum with respect to the experimental spectrum on the energy axis, and then a neural network was built to find the appropriate weights.

Figure 9.10a shows the XANES stacked plotting spectra of the experimental Cu K-edge XANES spectrum of propyl-copper phosphonate-functionalized mesoporous silica powder at a 20% functional group concentration, along with the computaionaly calculated specra of the DFT models, while Figures 9.10b-d show the results of a PCA analysis on the computed dataset.

The shift between the simulated and experimental XANES data is expected, as the FEFF10 code calculates the photoabsorption cross-sections of molecules and atomic clusters for X-ray photons using the real-space Green's function (RSGF) formalism. Additionally, DFT-optimized models contain distortions that may not fully capture the experimental system's local geometry, which contributes to the observed shift.

To determine the optimal energy shift between theoretical and experimental XANES spectra, we applied principal component analysis (PCA) to the 65 simulated spectra in the 8968–9067 eV range (Figure 9.10a). Spectra were normalized (mean = 0, Standard deviation = 1) before PCA. The first three principal components (PCs) captured 95% of the variance, and up to PC7 captured 99%.

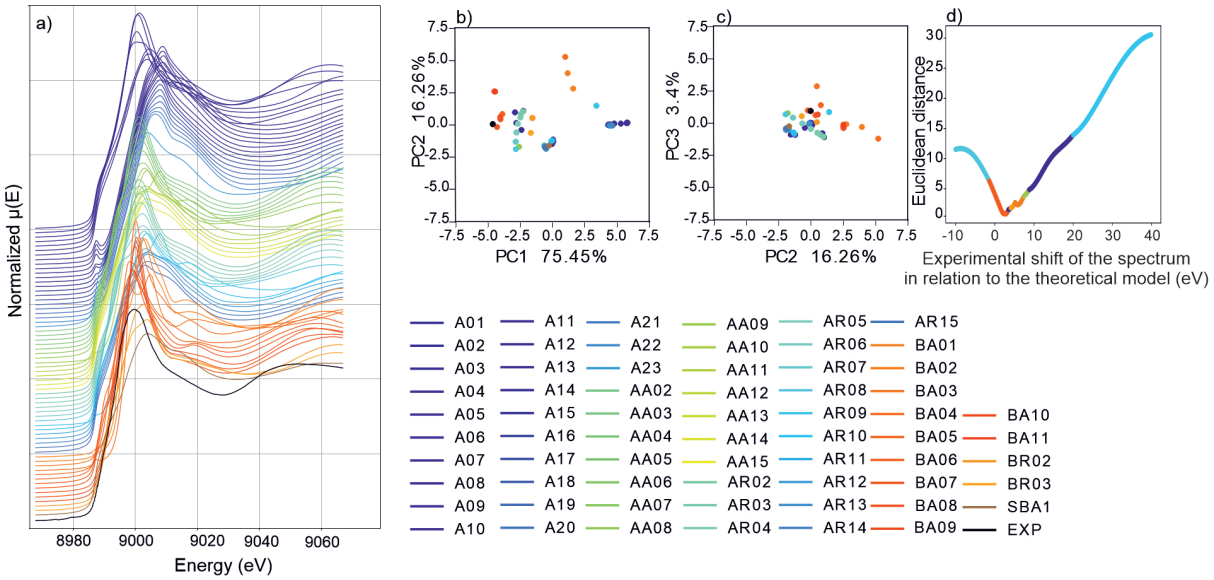


Fig. 7.12. A juxtaposition of XANES spectra for the molecules forming the PCA model and the experimental spectrum shifted by 2.3 eV relative to the measurement (a). The PCA score plot PC1-PC2 (b), PC2-PC3 (c) with nearest neighbor marked. The Euclidean distance between experimental spectra and nearest neighbor simulated spectra in 7-dimensional space to the nearest neighbor (d). Color points corresponds to structures presented in Figures 7.6, 7.7, and 7.8 [168].

The experimental spectrum was shifted from -10 eV to +40 eV in 0.1 eV increments, and for each step, the Euclidean distance in PC space (PC1-PC3 and PC1-PC7) was calculated to identify the closest match (Figure 9.10d). The best match was model BA06 with a 2.3 eV shift (Figure 9.11), followed by BA09 and BA05, corresponding to a deformed trigonal bipyramidal copper environment. The results indicate the coexistence of several similar copper–phosphonate environments within the silica matrix (Figure 9.11).

In Figure 9.11 the theoretically computed spectra have been shifted by 2.3 eV to align the white lines of all the spectra together. This shift in the edge is expected as the FEFF10 always doesn't estimate the real Fermi level of the molecular structure accurately, hence the corrections are needed. The models BA06, BA09, and BA05 models, were chosen as the most representative components, producing the best fit to the experimental spectrum, which means that the best description of the copper geometry in the SBA-POO_2Cu20% powder samples would be a deformed trigonal bipyramid.

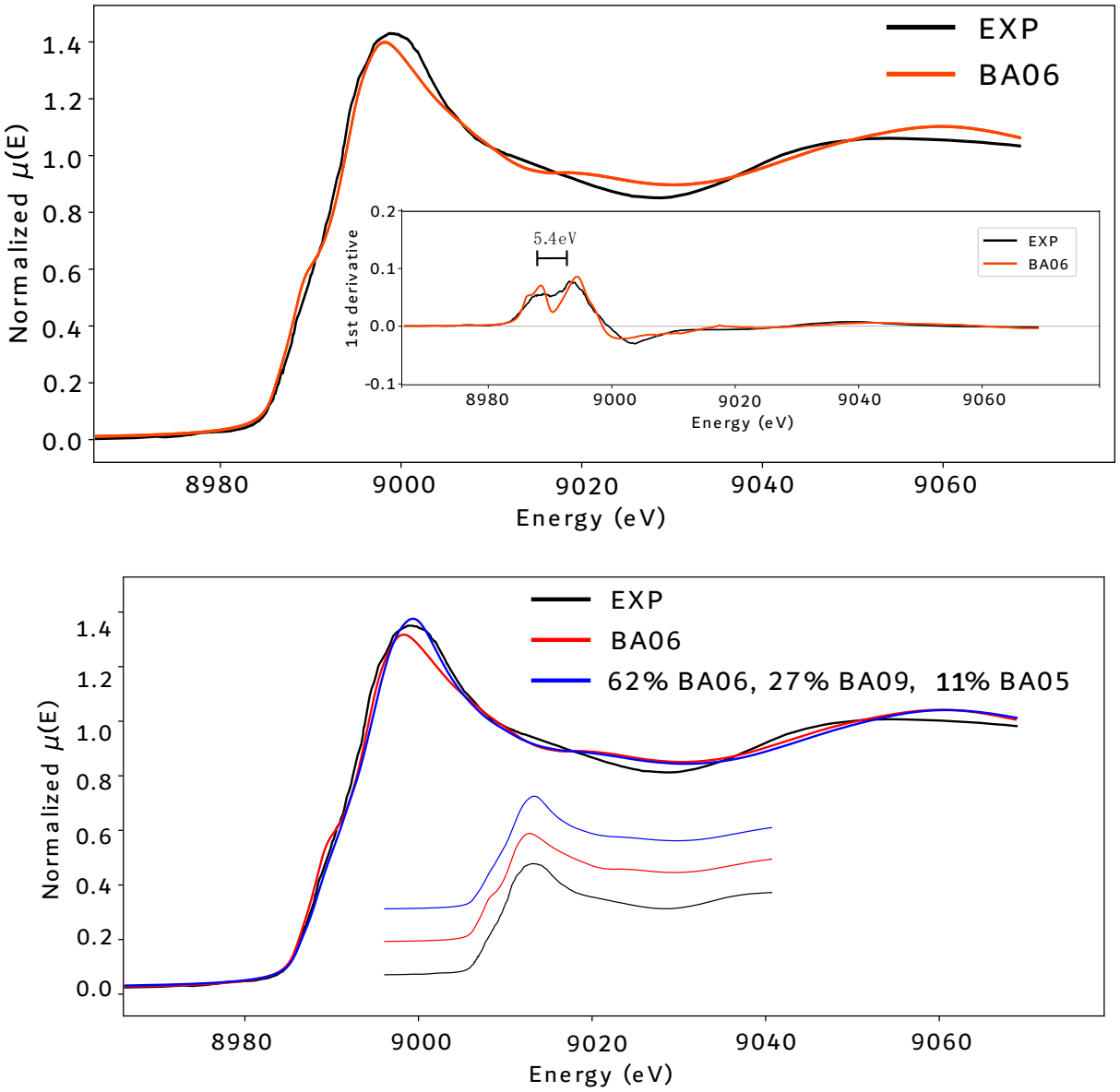


Fig. 7.13. Comparison of experimental spectrum with BA06 and their first derivatives (top). Machine learning decomposition (bottom) showing 62% BA06, 27% BA09, and 11% BA05, with component stack plot. Theoretical spectra are shifted by 2.3 eV [168].

7.4.1 Verification of structural models: Extended second-shell EXAFS fitting based on simulation results

The Extended X-ray Absorption Fine Structure (EXAFS) analysis provides quantitative information about the local coordination environment of the absorbing atom, including the type and number of neighboring atoms, as well as their radial distances. The EXAFS data of the highest concentrated samples were used to validate and extend conclusions drawn from the XANES region by delving deeper into the second and third coordination shells. This is especially important in our system, where the third coor-

dination shell is thought to contain phosphorus. EXAFS analysis was carried out on the SBA-POO_2Cu20% sample, with models derived from the most likely coordination environments identified in the XANES fits. Given the limited number of independent data points (governed by the Nyquist criterion), we chose only two theoretical models for fitting. These were selected for their spectral relevance and contribution to the XANES spectrum. Although additional structural motifs could be plausible, incorporating more than two would have introduced unnecessary complexity without significantly improving the fit, as EXAFS is generally insensitive to subtle variations in bond lengths and geometries [234].

Figure 7.14 demonstrates that this reductionist approach was computationally efficient and produced high-quality fit results. Both selected models produced consistent results with minimal statistical uncertainty, confirming the fitting strategy's validity. Table 7.1 summarizes the refined EXAFS parameters such as bond lengths, Debye-Waller factors, and coordination numbers.

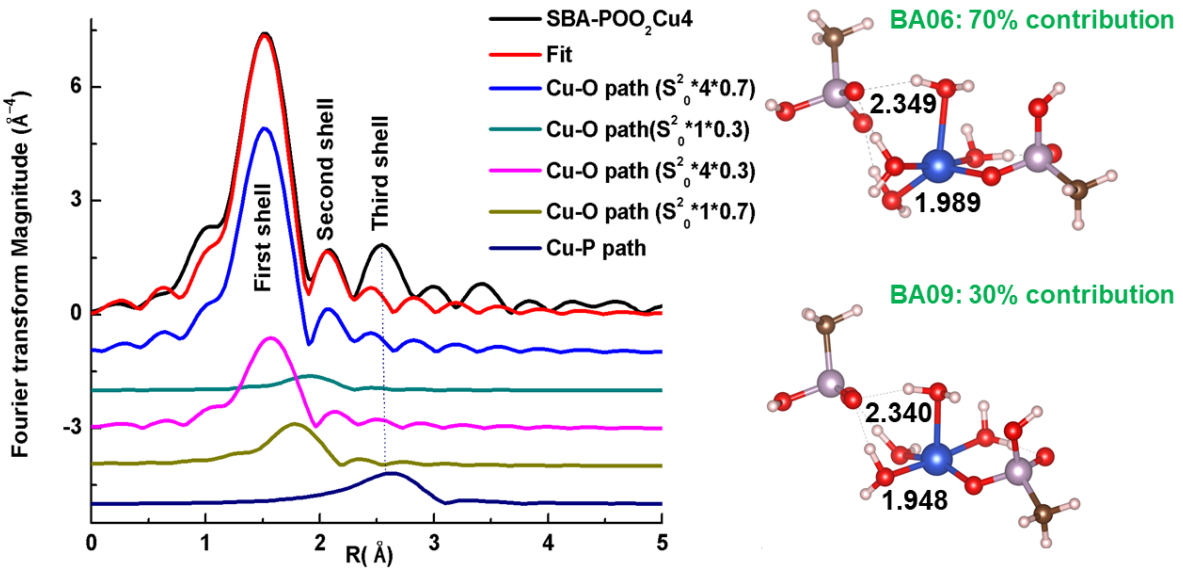


Fig. 7.14. Magnitude of Fourier transform of the EXAFS plotted vs radial distance of the central copper atom to other elements (R). The presented experimental spectrum was juxtaposed with the theoretical fit draw based on two theoretical models (presented at the right) with the assumed contribution. Also, the signals typical for the assumed paths were presented below the main plot.

For fitting the theoretical model to the experimental data of SBA-POO_2Cu20%, a single value of ΔE has been defined for all the paths, but different values of ΔR have

been defined for different paths. Debye–Waller factor values have been defined for each type of scattering path. The input parameter Rbkg was set to 1.1Å. The fitting has been performed in the R-space in the range of 1–2.3Å (Table 7.1).

The best fit of the SBA-$POO_2Cu20\%$ experimental data was obtained using the BA06 and BA09 models, derived from XANES analysis. It is worth mentioning that using only one model to refine the experimental EXAFS spectrum was enough to get a good fit, but when we set up the amplitude factor in the EXAFS equation to $S_0^2 \cdot 0.7 \cdot 4$ for the fourth nearest neighbors and $S_0^2 \cdot 0.7 \cdot 1$ for the farthest fifth oxygen neighbor, using the BA06 model with an input of 0.7 and doing the same with the BA09 model for the contribution of 0.3. This led to an even better fit with lower reduced chi-square and R-squared values in the refinement.

In the EXAFS refinement, the number of statistically independent points is N_{ind}=6.27 with five variables to be found (four values of the Cu-O paths' distances and one value of energy shift). The DW factors were set according to the literature [220].

Attempting to add a phosphor scattering path to match the third shell significantly degrades the fit. However, it is important to realize that phosphorus contributes strongly to the spectrum of the real shell (blue spectrum in fig 7.14). This confirms that our proposed models are quite reliable, Cu^{2+} ions are coordinated by five oxygen atoms, and the local environment of all copper atoms inside the silica matrix is slightly different for all five copper sites, which is in good agreement with the above XANES analysis.

Tab. 7.1. Structural parameters achieved from best fitting of the EXAFS spectrum, R-factor=0.004, Reduced chi-square= 672.91.

Bond type	**N**	**R(Å)**	**DW factor**	**ΔE**
Cu–O	$4 \cdot 0.7$	1.961 ± 0.008	0.0046	3.006 ± 1.77
Cu–O	$4 \cdot 0.3$	1.920 ± 0.008	0.0046	3.006 ± 1.77
Cu–O	$1 \cdot 0.7$	2.238 ± 0.040	0.0056	3.006 ± 1.77
Cu–O	$1 \cdot 0.3$	2.039 ± 0.077	0.0050	3.006 ± 1.77

7.5 Analysis of Cu K-edge XANES spectra of SBA-POO_2Cu powders and MSTF-POO_2Cu thin films based on numerical models

The subtle differences in XANES spectra (Figure 6.6) of lower-concentration samples necessitate interpretation using XANES simulations. These simulations were found to be

useful in determining the plausible local structure of the copper coordination environment. For the highest loaded sample, 20%, a model with two phosphonate ligands coordinated to a single copper ion was adopted and verified to nicely fit experimental data.

As the analysis proceeds to lower concentrations, the numerical model should be updated. As previous studies (EDS) have shown, in samples with lower concentrations of functional groups, the copper to phosphorus ratio is 1:1, so the samples contain a configuration with one copper atom per phosphonate unit.

The previous analysis of SBA-POO_2Cu20% based on simulation concluded that the experimental spectrum may represent a superposition of several structural configurations present in the sample or an intermediate configuration between the closest-matching theoretical models [168]. To investigate how the coordination environment of copper changes with decreasing functional group concentration, a new series of numerical models was used for the analysis, which was created to represent these lower concentrations. These models (shown in Figure 9.12 as S2) contain copper atoms coordinated by a single phosphonate group.

It should be mentioned that, in preparing the models, we paid particular attention to a model in which Cu^{2+} ion is surrounded by oxygen atoms in a deformed trigonal bipyramid system. This resulted from the analysis of literature data. In this context, a set of copper and chloride complexes from the work of Uchikoshi et al. [235] was selected for analysis. No good fit was obtained for any type of copper environment other than the one mentioned above, so we consider it the most likely.

Spectral fitting was carried out for the experimental XANES spectra at the copper K-edge. This approach is justified by certain simplifications applied in the preparation of the numerical models. Specifically, the propyl chain was shortened by one carbon atom, and this terminal carbon was not connected to the silica surface. Such a modification was introduced to considerably reduce the simulation time. Importantly, the immediate copper coordination sphere—critical for assessing NLO properties—remained intact and was reproduced with high accuracy in the model. In contrast, for phosphorus, it cannot be guaranteed that its local environment would remain unaffected by the motion of the unattached and relatively unstable carbon chain.

Moreover, the FEFF10 software package used for spectrum generation was developed with particular focus on accurately modeling the spectra of transition metals only [216]. As a result, XANES spectra obtained from numerical models at the copper K-edge are expected to more reliably represent the actual atomic arrangement in the investigated materials than those generated at the phosphorus edge, and thus these spectra were selected for the fitting procedure.

For this purpose, XANES spectra corresponding to all numerical models were gen-

erated and then fitted to the experimental spectra obtained. A complete database of models was used, but the fitting was carried out in several stages. The first stage aimed to reduce the size of the model database by excluding those that were highly unlikely. This was done based on an analysis of the results of the first fit from the complete model database, followed by an analysis of models with very low fit indices. This analysis was performed based on previously obtained XANES results, indicating what types of structures may be present in the material. After the first matching stage, the following models were retained in the database: S, L, T, B, O, and N, as shown in Figure 9.13.

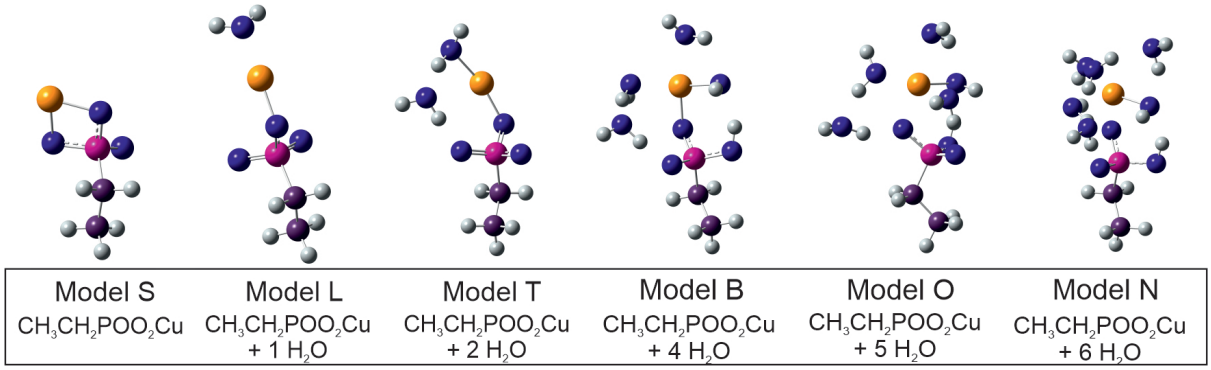


Fig. 7.15. The most suitable 6 models chosen from Set-2 to the second stage of fitting.

This combination of methods was used to improve the match between the measured spectra and those in a reference database. The procedure produced a very high person correlation coefficient (>0.996) [236], indicating that the overall shape of the matched spectra was similar to the experimental ones.

However, the detailed agreement was not perfect, particularly in the shoulder regions. These mismatches demonstrate how even advanced algorithms can produce ambiguous or misleading results when the training database is limited. Furthermore, the system's complexity, which most likely lacks long-range order, makes it difficult for the used models to accurately capture all spectral features.

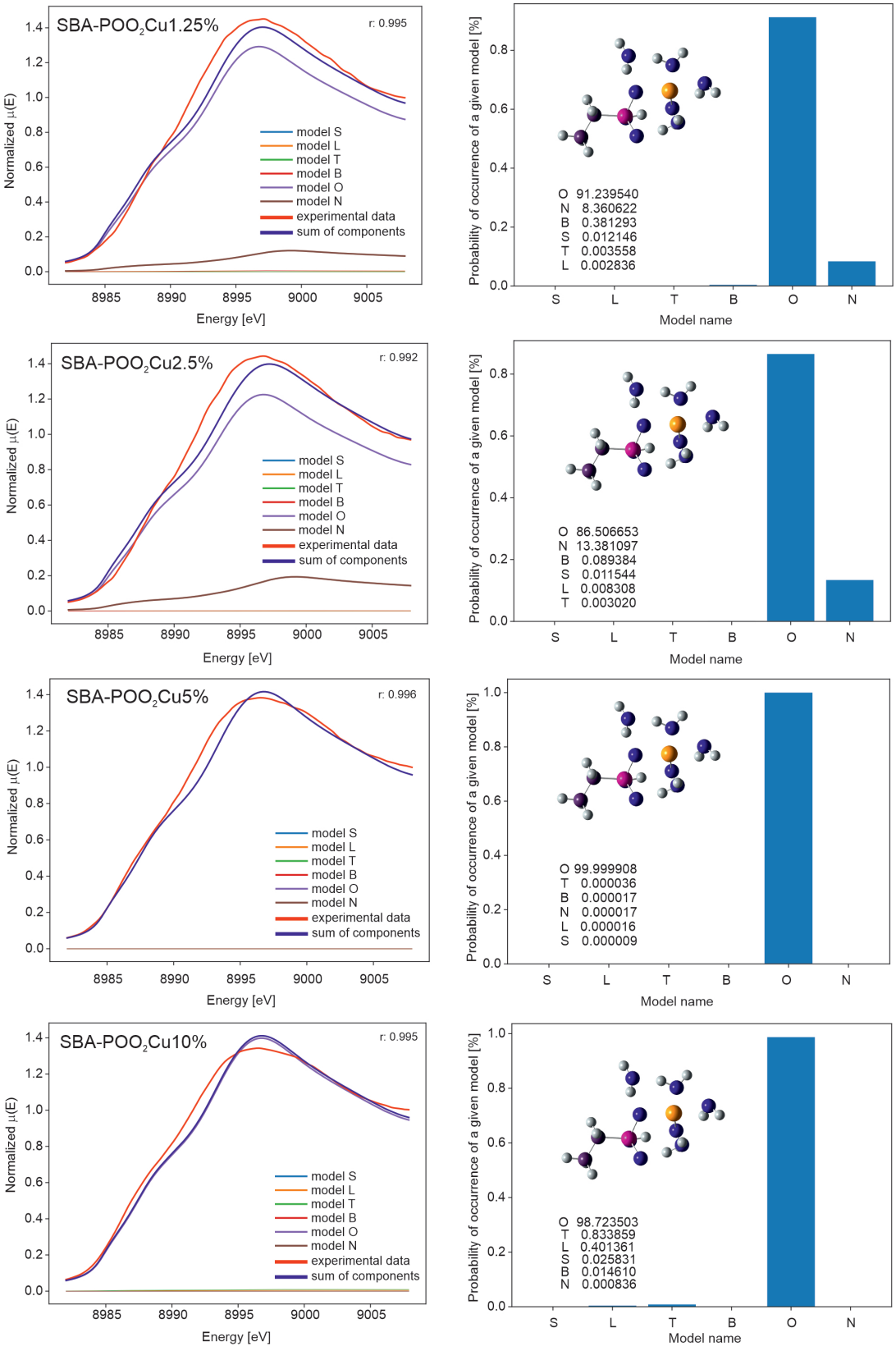


Fig. 7.16. Fitting results for each concentration of SBA–POO_2Cu at lower concentrations, showing the percentage match of theoretical models in Figure 7.15 to the XANES experimental spectra, along with a visualization of the most likely model.

7.6 Analysis of P K-edge XANES spectra of SBA-POO_2Cu powders and MSTF-POO_2Cu thin films based on numerical models

In order to compare experimental spectra of XANES at phosphorus K-edge with theoretical models, we simulated spectra for each model (S1, S2, S3). For models containing two phosphorus atoms, spectra were calculated separately for each phosphorus atom. The fitting results showed that the shape of the theoretical spectrum only roughly corresponds to the shape of the experimental results. As it was mentioned earlier, the most likely reason for the low match agreement is the use of an overly simplified functional group model containing only two carbons from the propyl chain and the lack of adequate immobilization of the chain, which resulted in the phosphorus environment not being well represented in this model. Another significant reason for the poor match between the theoretical spectra and the experiment may be problems with the FEFF10 software, which was designed for transition atoms such as copper rather than phosphorus [216]. For this reason, we decided not to use the XANES K-edge results for phosphorus as support in selecting the most appropriate model for further analysis.

In summary, Chapter 6 presented a computational approach for determining the structure of copper phosphonate functional groups through XANES simulations. The analysis indicated that the configuration most representative of the functional groups in the investigated materials corresponds to model O, shown in Figure 9.13 (inset, right plot). In this model, the functional group adopts a degenerate trigonal bipyramidal geometry, with five water molecules coordinated around the copper center. This arrangement is fully consistent with the structural assumptions derived from the XANES spectra. Contributions from alternative structures are minimal; however, the N model is also present to a limited extent, particularly in the SBA-POO_2Cu2.5% sample. The N model closely resembles the O model, differing only by the presence of an additional water molecule located beyond the primary copper solvation sphere. Based on these findings, models O and N were selected for subsequent analysis of NLO properties as they most accurately represent the functional group structure in the investigated materials.

8 Characterization of nonlinear optical (NLO) properties

This chapter presents the results of an investigation into the nonlinear optical (NLO) properties of silica-based materials functionalized with copper-phosphonate groups. Second harmonic generation (SHG) and third harmonic generation (THG) measurements were performed on mesoporous silica materials in the form of powders and thin films, prepared with varying concentrations of functional groups ranging from 1.25% to 10%. For the powdered samples, an additional material with 20% functional group concentration was also prepared to assess the effect of higher surface loading. The experimental setup was designed to evaluate the nonlinear optical response as a function of incident laser intensity. By systematically varying the concentration of copper-phosphonate groups in the samples, the relationship between functional group density and NLO efficiency was established. The results of this study revealed the existence of a distinct optimal concentration of functional groups at which the second and third harmonic generation efficiencies reach their maximum. This behavior is attributed to the intrinsic nonlinear optical properties of the copper-phosphonate moieties acting as chromophores, as well as to their intermolecular interactions, which influence the overall NLO response through local field effects and spatial arrangement.

8.1 Experimental setup for SHG and THG measurements

The measurement system used to study second and third harmonic generation (SHG and THG) in copper-phosphonate functionalized mesoporous silica materials is shown in Figure 8.1. The fundamental radiation source was an 8-nanosecond pulsed Nd: YAG laser with a wavelength of 1064 nm and a repetition frequency of 10 Hz. The power of the incident fundamental laser wavelength was tuned by Glan's polarizer with a laser damage power density of 4 GW/cm^2. The laser beam profile diameter was equal to about 8 mm. The value of the fundamental laser energy signal was evaluated by the germanium photodetector, and its second harmonic signal by a Hamamatsu photomultiplier with an installed interferometer filter at 532 nm and 355 nm with a spectral width of about

5 nm, which transmits electromagnetic radiation with a wavelength at 532 nm or 355 nm. The studied samples were placed on a rotating table in a special cover. Levels of obtained fundamental and second harmonic signals were measured using a Tektronix MSO 3054 oscilloscope with a sampling of 2.5 GS. The oscilloscope and the rotary table digit signals were input to the two channels of the oscilloscope, connected to the PC. The entire measuring stand was placed under the box, eliminating the influence of external undesirable light scattering [237].

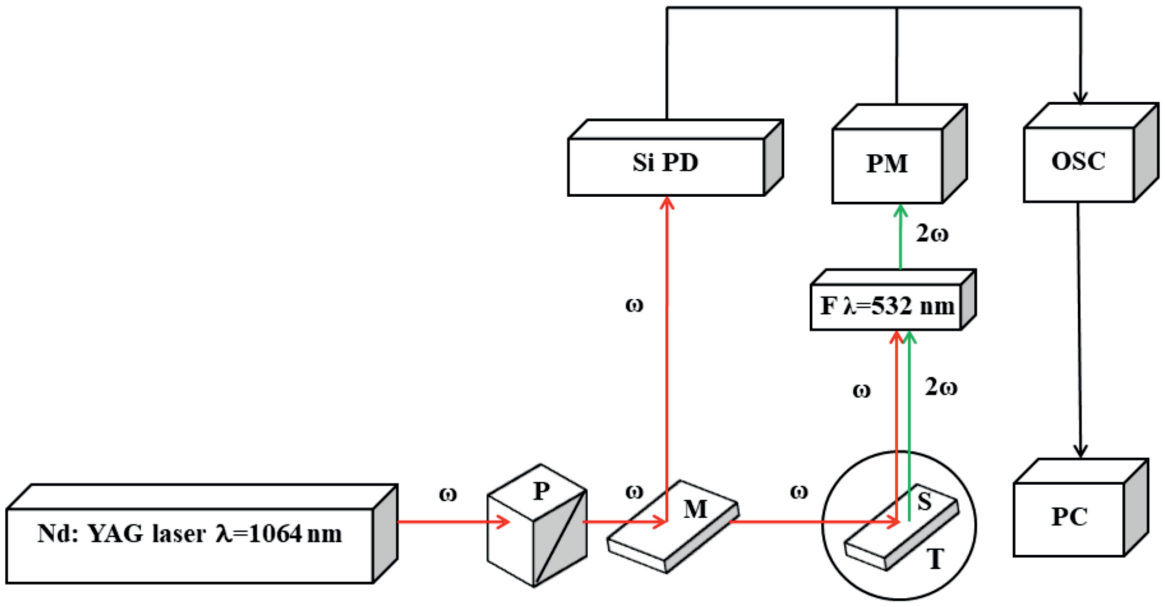


Fig. 8.1. Schematic of the experimental setup for SHG and THG measurements: Nd:YAG laser (8 ns, 1064 nm); Glan's polarizer (P) for power density control; beam splitter (M) and optical filters (F) for beam handling; silicon photodetector (Si PD) and photomultiplier (PM) for signal detection; oscilloscope (OSC) for signal readout.

All measurements were made in a reflected light regime, which makes the thickness of the samples not an influential parameter in the NLO-response. A Barium Borate single crystal was used as a reference for the SHG and THG runs. The results of the SHG/THG dependence versus the fundamental energy densities are presented in the following section. To collect this data, the incident energy density (E_d) on the sample surface was adjusted by rotating a Glan-type polarizer in the laser beam path. The transmission of the fundamental 1064 nm laser beam followed Malus' Law [238], where the transmitted intensity $I(\theta) = I_0 \cos^2(\theta)$, with I_0 is the initial intensity and (θ) is the angle between the laser polarization direction and the polarizer's axis. Using this relationship, the sample's energy per pulse per unit area (energy density) was calculated. At a 360° polariser angle, full transmission resulted in a maximum energy density of

99.5 J/m^2. The energy density at other polarizer angles was calculated using the cosine-squared dependency, allowing for controlled variation of incident intensity in nonlinear optical measurements [238].

8.2 Nonlinear optical properties of the copper-phosphonate functionalized mesoporous silica

The hybrid materials under investigation were expected to exhibit nonlinear optical activity because they contain polar functional groups. Their incorporation within a confined nanospace could further enhance this response. Moreover, synthesizing them with precisely controlled concentrations, by adjusting the intermolecular distance between adjacent functional groups, was expected to induce changes in molecular conformation, which directly influences the dipole moment of these functional groups. Hence, resulting in a different NLO activity.

The SHG and THG responses of five samples of copper-phosphonate functionalized SBA-15 powders, as well as four copper-phosphonate functionalized mesoporous silica thin films each, containing a specific concentration of functional groups. The measurements were performed as a function of excitation energy density, with the maximum value reaching 100 J/m^2. The laser-stimulated second harmonic generation (SHG) response is shown in Figure 8.2 and Figure 8.3, which depict the dependence of SHG intensity on the fundamental energy density of the incident laser for functionalized mesoporous silica powders and thin films. The data are referenced to BBO as a standard and bare mesoporous silica. BBO was selected as a reference material because of its well-established role as a benchmark in both second and third harmonic generation studies, owing to its high nonlinear optical coefficients, broad transparency range, and extensively characterized harmonic generation efficiency.

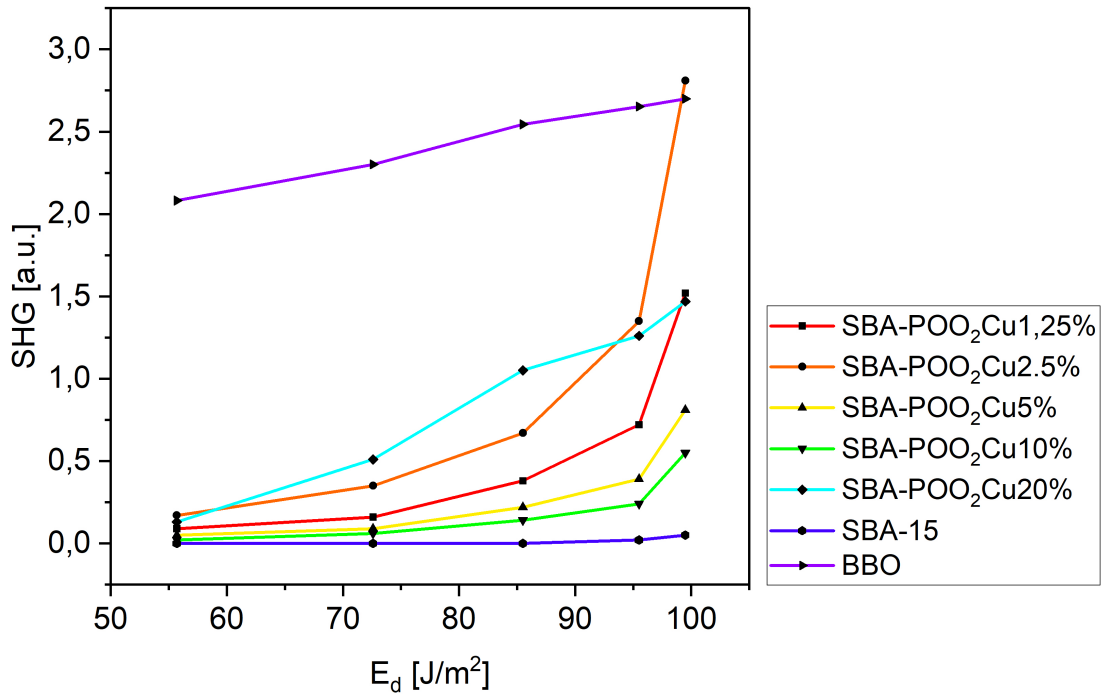


Fig. 8.2. Dependence of SHG intensity on the fundamental beam energy per unit area E_d for powder samples with concentrations ranging from 1.25% to 10%, along with two reference samples: a bare mesoporous silica thin film and a barium borate (BBO) standard.

The results obtained for the bare silica matrix confirm that the light conversion comes directly from the copper phosphonate chromophores, as pure silica exhibits very weak NLO properties. For all samples, we can observe an increase in the SHG response with increasing laser energy density, which is expected due to an increase in the polarization of the medium. However, each sample with a different chromophore concentration exhibits a distinct SHG response. The highest SHG response at the maximum fundamental beam energy density was observed for the sample with a 2.5% concentration of functional groups. For the other concentrations, the SHG efficiency was significantly lower. The material with a concentration of 20% stands out from the other samples. The observed differences in the upward trend of the SHG signal with increasing laser energy density can be attributed to the different molecular structure of this material and, consequently, to different phenomena responsible for the generation of the second harmonic.

It is worth noting that for a sample with a concentration of 2.5%, the observed maximum SHG intensity value is similar to that observed for BBO crystal and is 1.9 times greater than the result for a sample with a concentration of 1.25%. The lowest SHG intensity value at a laser energy density of 100 J/m^2 is observed for a sample with a

concentration of 10%, while sample with a concentration of 5% exhibits slightly higher intensity. The maximum SHG intensities recorded for these samples are respectivelly 5.1 and 3.5 times lower than the maximum intensity observed for a concentration of 2.5Similar results were obtained for samples in the form of thin films. Figure 8.3 shows that the dependence of SHG intensity on the fundamental beam energy per unit area E_d follows the same trend observed for powder samples.

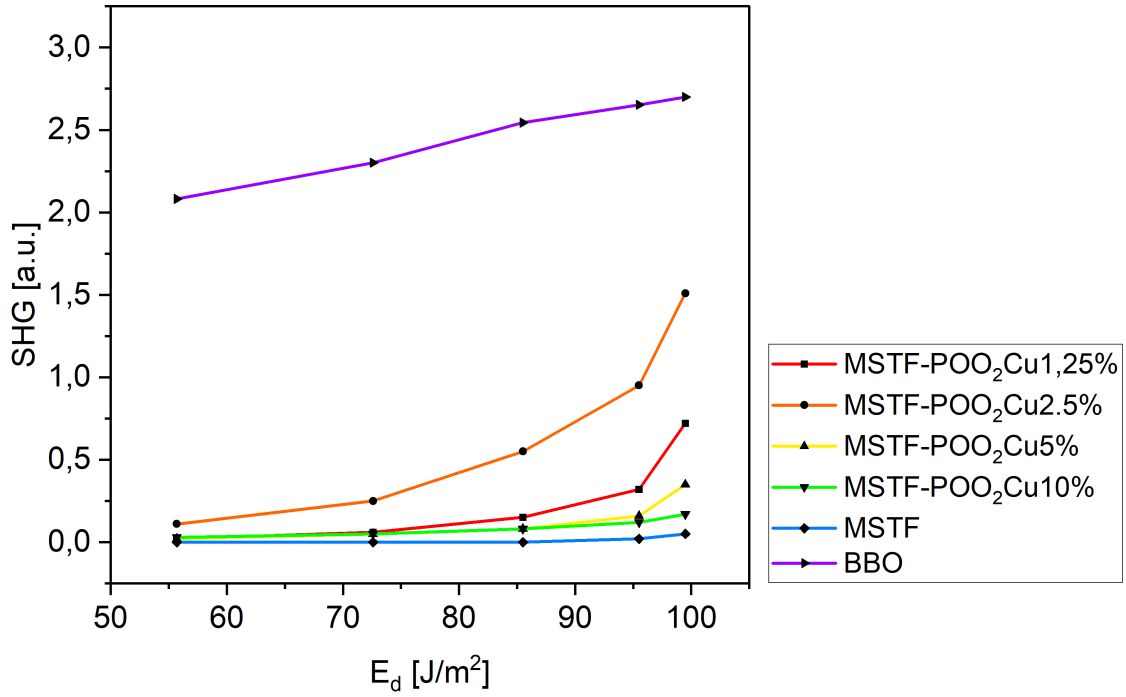


Fig. 8.3. Dependence of SHG intensity on the fundamental beam energy per unit area E_d for thin film samples with concentrations ranging from 1.25% to 10%, along with two reference samples: a bare mesoporous silica thin film and a barium borate (BBO) standard.

Although the measurements were performed in reflection mode to minimize the influence of sample thickness, the SHG signals observed for thin films with a thickness of approximately 130 nm were significantly weaker. This reduction is likely due to the limited optical interaction volume, as the thickness of the film is smaller than the penetration depth of the incident laser beam, thereby reducing the effective nonlinear response. However, when comparing powders and thin films, concentration changes play an important role. The material with a functional group concentration of 2.5% in the form of a thin layer also exhibits the highest SHG intensity. For thin layers, increasing the concentration from 1.25% to 2.5% results in a 2.1-fold increase in the maximum SHG response. Once

again, materials with concentrations of 5 and 10% show the weakest SHG response, with slightly better results for concentration of 5%.

Following the SHG analysis, third-harmonic generation (THG) measurements were performed to further evaluate the nonlinear optical properties of the investigated materials. Figure 8.4 shows the results of THG obtained for powder samples.

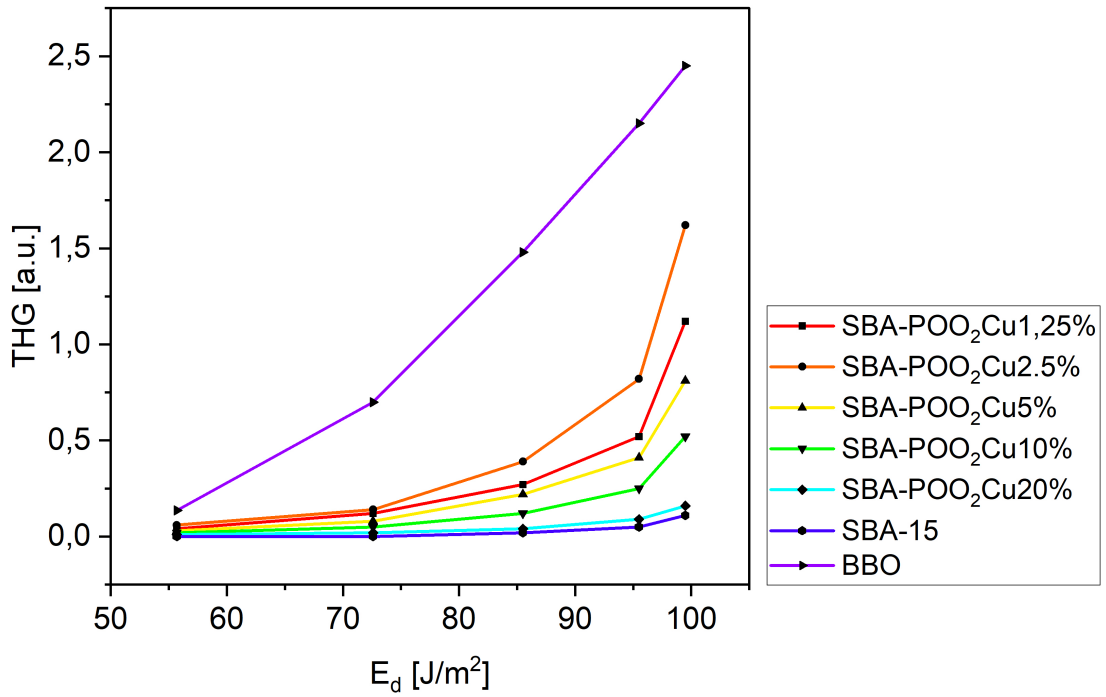


Fig. 8.4. Dependence of THG intensity on the fundamental beam energy per unit area E_d for thin film samples with concentrations ranging from 1.25% to 10%, along with two reference samples: a bare mesoporous silica thin film and a barium borate (BBO) standard.

Using the same BBO reference, the THG response of all the functionalized samples was also evaluated in a similar manner to the SHG measurements. Similarly, the samples with 2.5% functional groups concentration also exhibited an enhanced THG response relative to other concentrations. The THG results show a clear correlation between the maximum THG intensity (value obtained at an energy density of 100 J/m^2) and the concentration of functional groups. In this case, the maximal intensity recorded for the sample SBA-POO_2Cu2.5% is 1.4 times greater than the maximal intensity observed for the sample SBA-POO_2Cu1.25% and 3.1 times greater than the highest intensity generated of sample SBA-POO_2Cu10%. As in the case of the second harmonic generation, also in the sase of third harmonic generation powder samples showed that the highest intensity is observed

for a 2.5% concentration, but now its value did not match the THG intensity observed for BBO. The intensity observed at 100 J/m^2 energy density for BBO is 1.5 times higher than for the best silica sample.

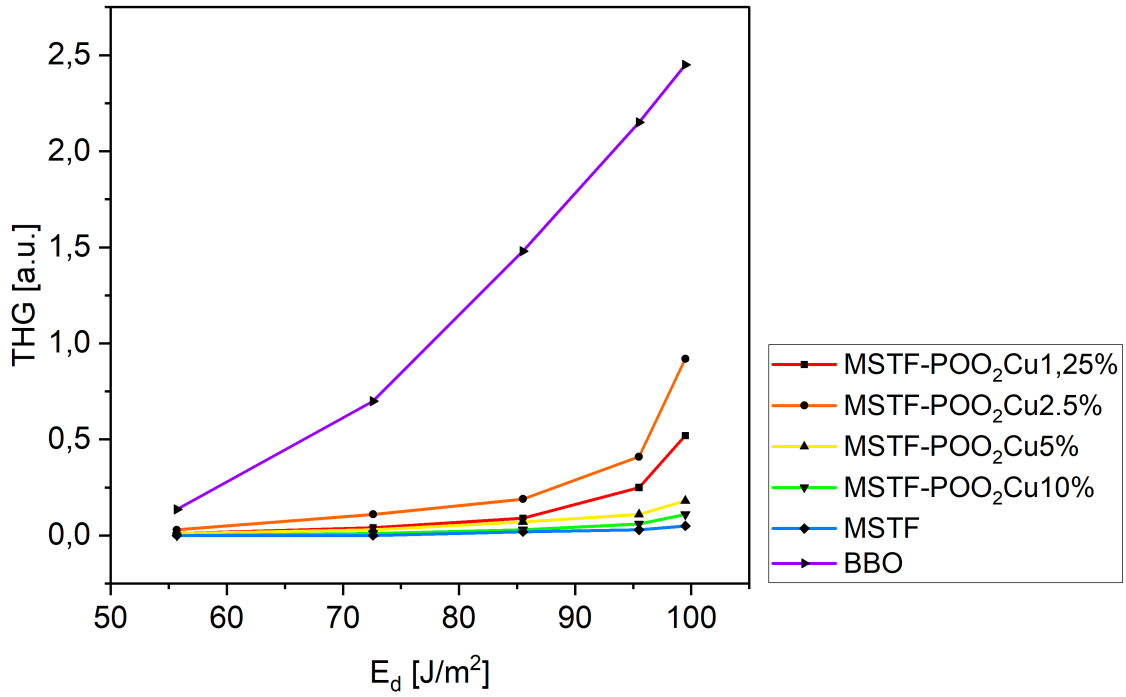


Fig. 8.5. Dependence of THG intensity on the fundamental beam energy per unit area E_d for thin film samples with concentrations ranging from 1.25% to 10%, along with two reference samples: a bare mesoporous silica thin film and a barium borate (BBO) standard.

The dependence of THG intensity on the fundamental beam energy per unit area E_d for thin film samples shows the same trend as in the case of powders, but the intensities observed are significantly lower. For thin film samples, the highest intensity was again observed for the sample with a concentration of 2.5% and the lowest for 10%.

In summary, SHG and THG intensities increase with the laser's energy density. This expected behavior is due to the increased electric polarization of the material; higher intensities lead to greater distortion of the electronic distribution within the medium, which enhances the nonlinear optical response. However, in this work, we focus on how the concentration of functional groups affects the SHG and THG responses at a fixed laser energy density. Interestingly, while varying the concentration of the functionalized silica in both powder and thin film form, we observed that the nonlinear response does not follow an increasingly proportional trend with the concentration of the copper-phosphonate

functional groups (Figure 8.6). Instead, the highest SHG and THG intensities were consistently recorded at a concentration of 2.5%.

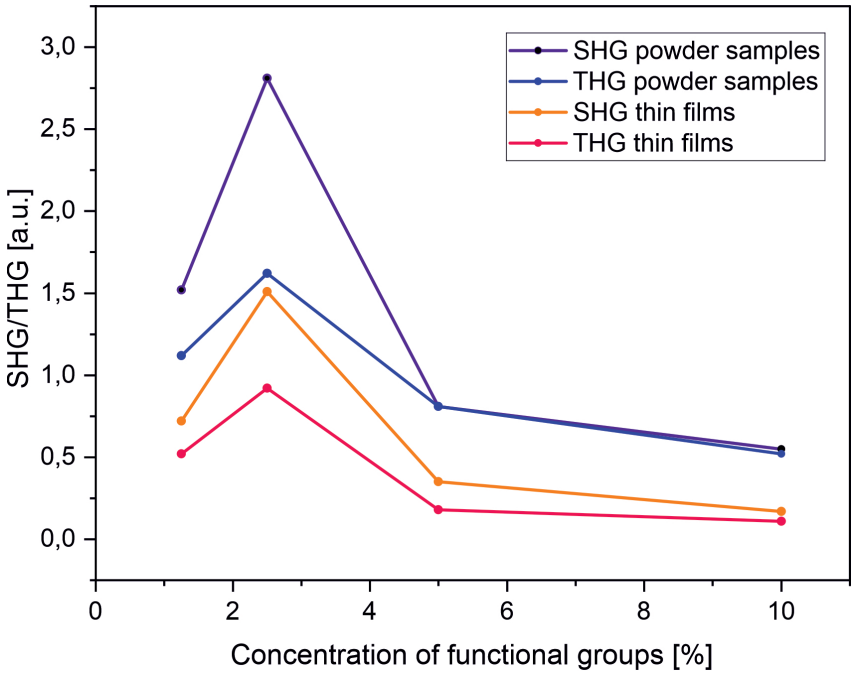


Fig. 8.6. Dependence of SHG and THG signals on maximum fundamental intensity as a function of functional group content.

It is also notable to compare the nonlinear optical (NLO) behaviour of vertically oriented copper-phosphonate functionalized mesoporous silica thin films prepared via the electro-assisted self-assembly (EASA) technique, where the NLO behaviour follow similar trend and the optimal SHG efficiency was reported at a higher functional group concentration of 5% [46].

This variance in the optimal functional group content between the dip-coated and EASA-derived thin films—despite containing the same functional groups—is likely attributed to differences in pore size, orientation, and the density of the silica matrix.

This observations suggests that the nonlinear response is not solely determined by the number of functional groups as a simple additive effect, where more functional groups lead to proportionally higher SHG or THG. In fact, beyond the concentration of 2.5%, the non-linear signal decreases. A plausible explanation could be related to the spatial distribution or local packing density of the functional groups. Although a higher concentration could, in principle, increase the nonlinear response, it might also lead to effects such as dipole-dipole interactions or steric hindrance that reduce the overall efficiency of harmonic generation. Importantly, our previous structural characterization confirmed the absence of centrosymmetric aggregation or crystallization of the functional groups, which rules out centrosymmetry as the cause of signal suppression. Our interpretation is that at low

concentrations, the functional molecular moieties are likely to be well-isolated within the silica matrix, resulting in minimal inter-group interactions. This isolation helps preserve their non-centrosymmetric alignment, thereby maintaining or enhancing their nonlinear optical (NLO) activity.

8.3 Effect of intermolecular distances on nonlinear optical properties

Chapter 6 presented an analysis of the experimental XANES results, which revealed that the most likely molecular configuration around the copper center is a five-fold coordination geometry represented by numerical model O for all the materials studied. According to the fitting results also a small population of model N is possible in the samples. Having selected models corresponding to the actual conformations of functional groups in silica, we applied DFT methods to investigate NLO-related parameters, such as HOMO-LUMO energy gap, dipole moment (μ), and first hyperpolarizability (β) which provide insight into the observed NLO behavior. These parameters are shown in Table 8.1.

Tab. 8.1. Key electronic parameters dependent on harmonic generation corresponding to the numerical models analysed: hyperpolarizability (β_{total}), dipole moment (μ), and energy gap between HOMO and LUMO levels (E_g).

Model:	β_{total} [a.u]	μ [D]	E_g [eV]
O	542.4	5.80	3.826
N	459.3	2.67	3.819

The electronic properties calculated for both structures enabled better understanding of their role in observed SHG and THG phenomena. Figure 8.7 shows models O an N with a visualisation of their electrostatic potentials and the HOMO and LUMO orbitals.

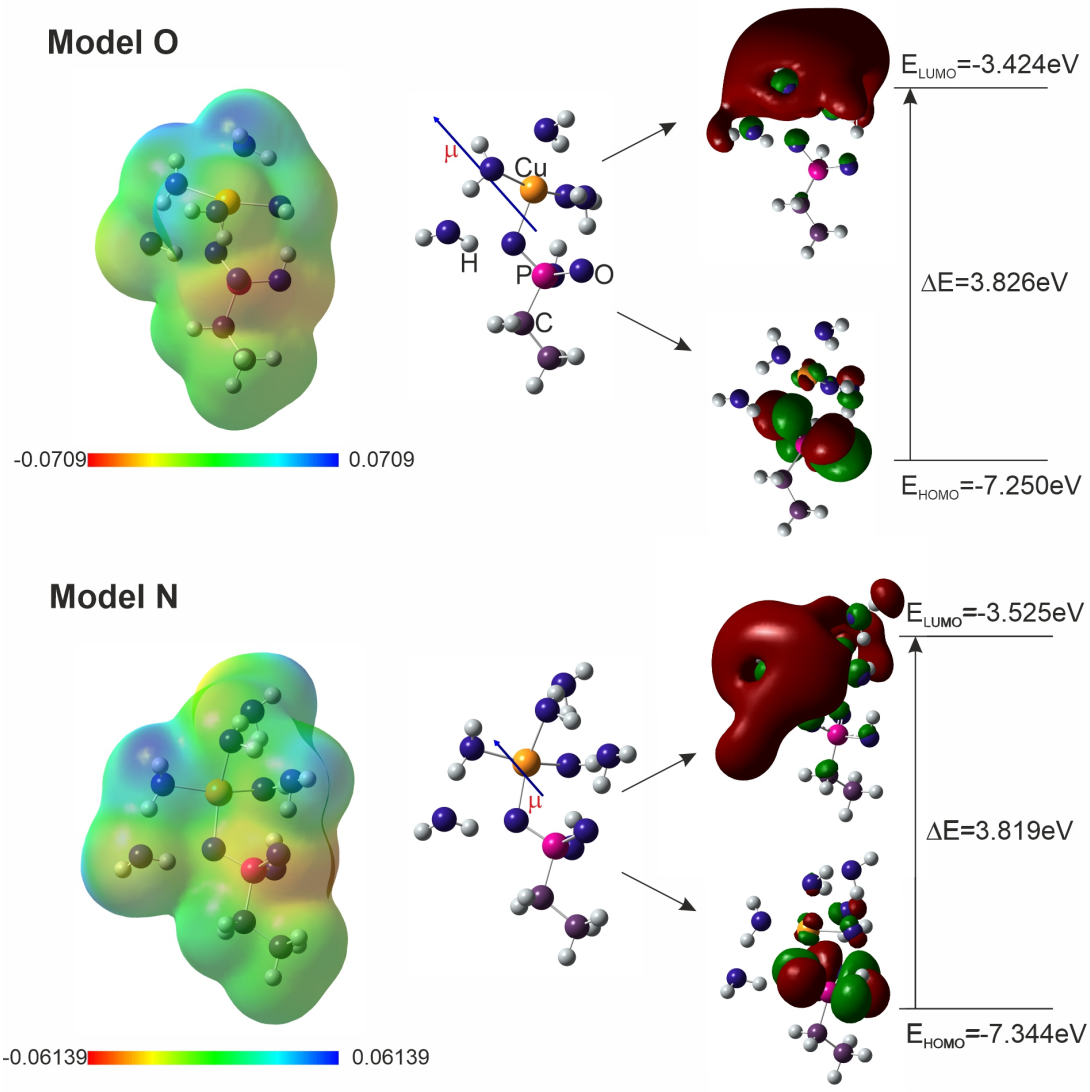


Fig. 8.7. Visualisation of the models with the most significant contribution to the population of functional group structures in the materials studied (model selected on the basis of fitting to XANES theoretical spectra to experimental spectra).

As shown, the two models exhibit quite similar potential nonlinear optical properties. In both cases, the acentrosymmetric charge distribution is clearly evident. The hyperpolarizability and energy gap values are comparable. Moreover, a HOMO–LUMO energy gap of approximately 3.8 eV suggests moderate chemical stability, balancing resistance to spontaneous excitation with the capacity for efficient charge transfer under strong optical fields. This combination of traits is typical for effective NLO chromophores, which require both high polarizability and sufficient stability for practical applications [239, 240].

Although investigated materials are inorganic, these compounds differ fundamentally from conventional inorganic chromophores. While traditional inorganic NLO chromophores are generally derive their optical properties primarily from collective solid-state

phenomena, including crystal lattice structure, ion arrangement, and domain orientation effects [241], rather than from individual molecular characteristics presented here propyl-copper-phosphonate functional groups are of a completely different nature. For these material, the nonlinear optical behavior originates intrinsically from the molecular structure itself, representing a paradigm shift in how inorganic chromophores are understood and designed.

Moreover, as it was shown in this Chapter 7, the second- and third-harmonic generation (SHG and THG) responses strongly depend on the concentration of functional groups in the silica mtrix. It should be emphasized that the concentration of functional groups on the silica surface determines their mutual distances and as it was observed in experiments with second and third harmonic generation affects NLO properties of the material. Therefore, in order to explain why a decrease in SGH and TGH intensity is observed for concentrations above 2.5%, the influence of the mutual distances between functional groups on NLO parameters was analysed. To do this, it was necessary to estimate the statistical distances between groups for samples with different concentrations and prepare numerical models corresponding to the respective sample concentrations.

8.3.1 Estimation of the average intermolecular distance between two adjacent functional groups

The functional groups described above were introduced onto the surface of mesoporous SBA-15 silica and randomly distributed in varying amounts. By controlling the concentration of functional group precursors during synthesis, the amount of functional groups introduced onto the silica surface could be planned during synthesis and precisely controlled. The results of the synthesis were thoroughly verified in Chapter 4, in particular, the EDS study confirmed the homogeneous spatial distribution of the groups and their quantity in accordance with the assumptions. In order to analyse the impact of the spatial distribution of functional groups on their potential interactions, we estimated the number of functional groups per unit area. This was possible thanks to our knowledge of the molar mass of the material and the specific surface area of the silica on which the groups are located. The molar mass was estimated approximately, taking into account the atoms of the functional group and the simplified composition of silica as SiO_2, the multiple of which reflects the concentration of functional groups in accordance with the proportions adopted during synthesis. The number of hydrogen atoms bound to silicon atoms and TMS groups, which replaced silanol groups during synthesis, was omitted from the calculations of the molar mass of the material (it can be stated that the silica was simplified to the SiO_2 system). A summary of all the information obtained from this analysis is presented in Table 8.2.

Tab. 8.2. Approximate estimation of molar and surface parameters for SBA-POO_2CuX samples, including estimated intermolecular distances based on functional group concentration on silica walls.

Functional group concentration	20%	10%	5%	2.5%	1.25%
Molecular formula	$C_3H_6O_{13}PCuSi_5$	$C_3H_6O_{23}PCuSi_{10}$	$C_3H_6O_{43}PCuSi_{20}$	$C_3H_6O_{83}PCuSi_{40}$	$C_3H_6O_{163}PCuSi_{80}$
1 Molecule mass [g]	8.05E–22	1.30E–21	2.30E–21	4.30E–21	8.29E–21
Molar mass [g/mol]	4.85E+02	7.85E+02	1.39E+03	2.59E+03	4.99E+03
Moles in 1 g sample	2.06E–03	1.27E–03	7.22E–04	3.87E–04	2.00E–04
Functional groups in 1 g	1.24E+21	7.67E+20	4.35E+20	2.33E+20	1.21E+20
Specific surface area [m^2/g]	370	565	902	942	836
Func. groups per m^2	3.36E+18	1.36E+18	4.82E+17	2.47E+17	1.44E+17
Func. groups per μm^2	3.36E+06	1.36E+06	4.82E+05	2.47E+05	1.44E+05
Func. groups per nm^2	3.36	1.36	0.48	0.25	0.14
Surface area per group [nm^2]	0.30	0.74	2.08	4.05	6.93
Intermol. distance [nm]	0.55	0.86	1.44	2.01	2.63

- Starting from the stoichiometric molecular formula of the functional group, its molecular mass can be calculated by summing the atomic masses of its constituent atoms.
- The molar mass (in g/mol) can be used to calculate the number of moles in a given mass:

$$\text{moles} = \frac{\text{mass (g)}}{\text{molar mass (g/mol)}}$$

- One mole contains 6.022×10^{23} functional groups. Thus, the total number of functional groups is:

$$\text{number of groups} = \text{moles} \times N_A$$

- Knowing the specific surface area (m^2/g) of the silica at each concentration, and assuming that each functional group is positioned at the corner of a square (see Figure. 8.8), the number of functional groups per m^2 can be estimated.
- Converting this density into nm^2/group, the average distance between two functional groups can be deduced as the square root of the surface area per group:

$$d = \sqrt{\text{nm}^2/\text{group}}$$

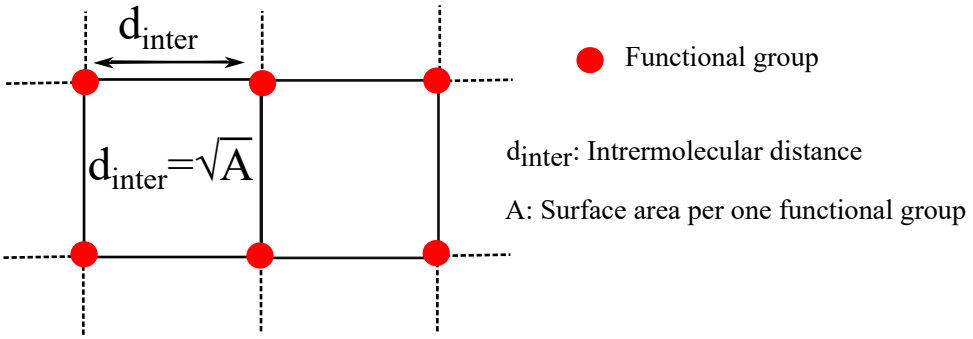


Fig. 8.8. Ideal distribution of the functional group on a square surface area.

However, in the case of real materials, we do not deal with such an ideal arrangement of functional groups, but only with their random distribution on the surface. To introduce spatial randomness in the distribution of functional groups, a simulation of random molecular placement was performed over a surface area of 1 μm^2, with a minimum distance constraint of 0.5 nm to reflect steric hindrance. Figure 8.9 shows sample simulation results for concentrations ranging from 1.25 to 10% on a surface area of 10 x 10 nm, which is a small section of the simulated surface area of 1 mm^2. However, for the sake of clarity, only a fragment is shown.

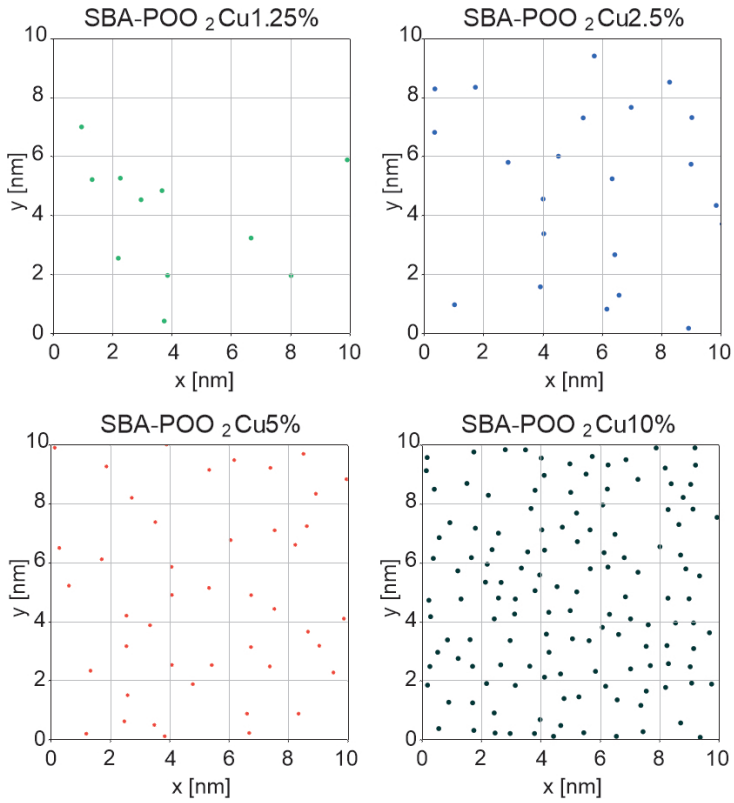


Fig. 8.9. Visualisation of the distribution of distances between functional groups in SBA-15 mesoporous silica functionalized with various concentrations of propyl-copper-phosphonate units (SBA-POO_2CuX).

By analyzing all pairwise distances and applying KDE to the resulting dataset, we obtained a smooth probability density curve that allowed us to identify the characteristic intermolecular spacings. The corresponding distribution is presented in Figure 8.10.

The simulation results allowed us to identify the most common distances between functional groups, which enabled the preparation of numerical models reflecting the dominant structures in the sample. Calculations show that the most common distance between functional groups in the sample with the lowest concentration of 1.25% is 11.86 nm, while for the sample with the highest concentration of functional groups, equal to 10%, this distance decreases to 5.70 nm. The most frequent distances between groups for all samples are presented in Table 8.3.

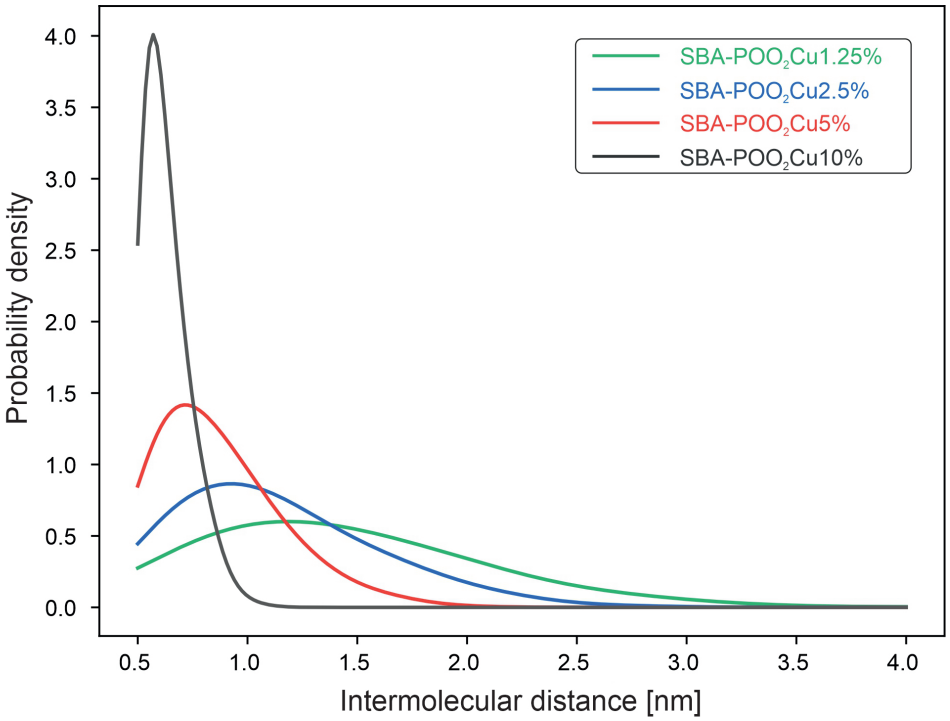


Fig. 8.10. Probability density function (PDF) of intermolecular distances in SBA-POO_2Cu materials, estimated using kernel density estimation (KDE).

Sample name	SBA-$POO_2Cu10\%$	SBA-$POO_2Cu5\%$	SBA-$POO_2Cu2.5\%$	SBA-$POO_2Cu1.25\%$
R [nm]	0.570	0.711	0.922	1.186

Tab. 8.3. Statistically most probable distances between functional groups in SBA-15 mesoporous silica functionalized with varying concentrations of propyl copper phosphonate units (SBA-POO_2CuX). R represents the most frequent intermolecular distance in the sample.

8.3.2 Effect of spatial arrangement of functional groups on nonlinear optical responses

Based on the estimated distances between functional groups, calculated as a function of their concentration within the silica matrix, numerical models were developed. To analyze the influence of the spacing between functional groups on the material's NLO properties, models consisting of two functional groups separated by defined distances were constructed. For this purpose, the O model was employed to consider how mutual distances, nd consequently intermolecular interactions, affect the nonlinear optical behavior of the material. Based on the estimated distances, models containing two func-

tional groups (model O) separated by 0.6, 0.7, 0.9, and 1.2 nm. In order to introduce the specified distance between the groups, the distance between the phosphorus atoms in both groups was frozen. The models prepared in this way were subjected to geometric optimization necessary for further calculations. Next, DFT was used to investigate NLO-related parameters, such as HOMO-LUMO energy gap, dipole moment (μ), and first hyperpolarizability (β), and correlate them with experimental NLO characterization. Table in figure 9.14 summarizes calculated parameters such as molecular group, including the hyperpolarizability (β_{total}), dipole moment (μ), and the energy gap between HOMO and LUMO levels (E_g), as well as vizualises electrostatic potentials and the electron density surfaces.

The model representing the distribution of functional groups in the SBA-POO_2Cu2.5% material exhibits the greatest potential for second harmonic generation (SHG) [242, 243]. Its electrostatic potential surface reveals pronounced charge asymmetry, which translates into exceptionally high hyperpolarizability and dipole moment, both significantly exceeding the values obtained for the other models. Additionally, the material has a relatively small energy gap (2.23 eV), notably lower than that of an isolated functional group. This combination of properties aligns well with the requirements for efficient NLO chromophores, where a low energy gap is advantageous [244, 245]. Comparable conclusions arise from evaluating the material's potential for third harmonic generation (THG). In this case, however, the dipole moment becomes the decisive factor, as centrosymmetric materials can also support THG [246, 247]. Notably, the dipole moment reaches its maximum value for SBA-POO_2Cu2.5%.

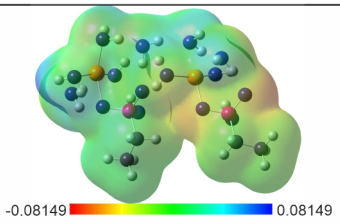
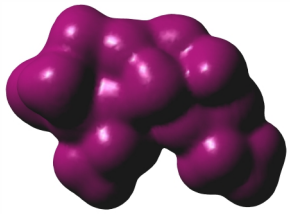
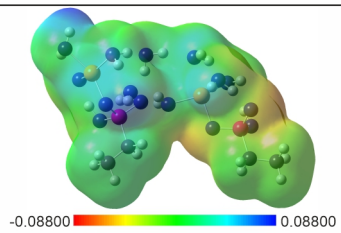
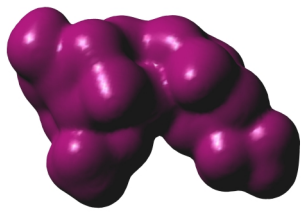
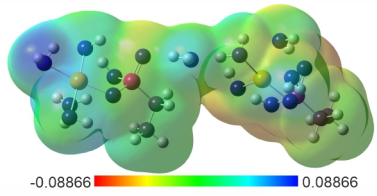
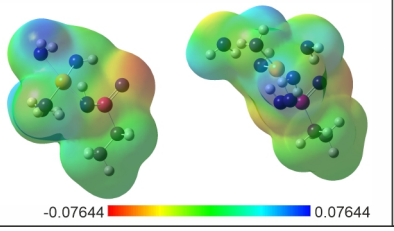
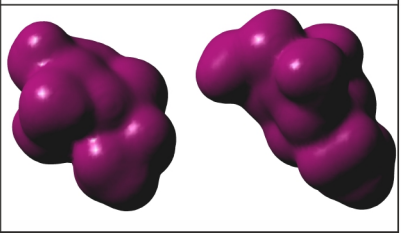
Model description	NLO parameters	Numerical model with electrostatic potential surface	Electron density surface
SBA-POO_2Cu10% Intermolecular distance: 0.6 [nm]	β=891.19 μ=8.94 D ΔE=2.49 eV		
SBA-POO_2Cu5% Intermolecular distance: 0.7 [nm]	β=884.56 μ=10.73 D ΔE=2.11 eV		
SBA-POO_2Cu2.5% Intermolecular distance: 0.9 [nm]	β=1032.95 μ=15.27 D ΔE=2.23 eV		
SBA-POO_2Cu1.25% Intermolecular distance: 1.2 [nm]	β=969.93 μ=9.55 D ΔE=3.23 eV		

Fig. 8.11. Visualisation of optimized models consisting of two functional groups separated by distances resulting from the application of the KDE method to the materials under investigation. In addition, key values for NLO properties are given for each model: hyperpolarisability (β), dipole moment (μ), and energy gap value (ΔE).

It is noteworthy to compare the plots illustrating how key NLO parameters of the developed models vary with the assumed distance between functional groups, expressed here in terms of their concentration in the samples (Figure 8.12) with the experimental results of second and third harmonic generation obtained for the investigated materials (Figure 8.6).

Examining the parameters that directly influence the intensity of second harmonic generation, namely hyperpolarizability and dipole moment (Figure 8.12), reveals that their variation with functional group concentration closely mirrors the experimentally observed dependence of second harmonic intensity on concentration (Figure 8.6).

The dependence of hyperpolarizability shows a slightly different trend, with a minimum for SBA-POO_2Cu5%. However, the differences between samples with higher concen-

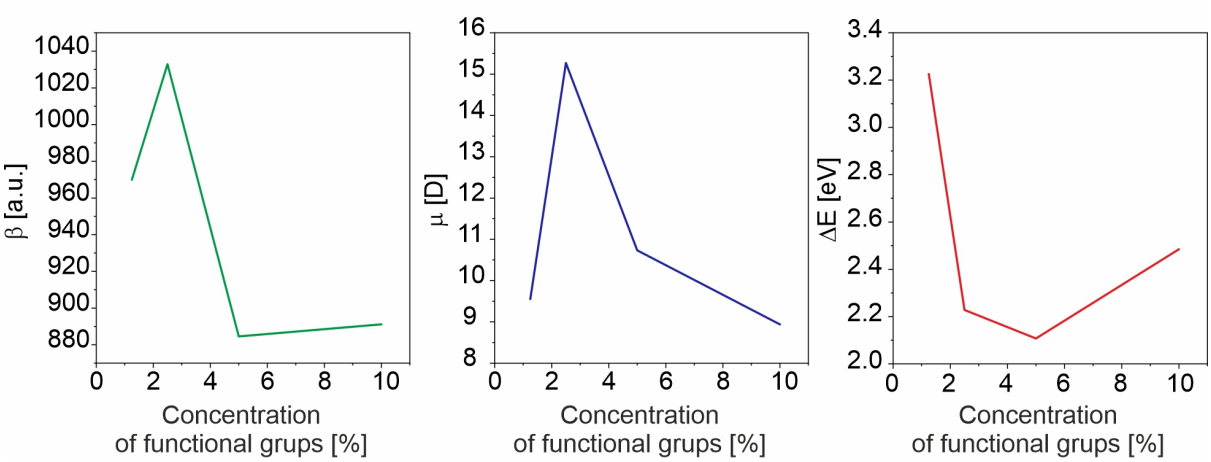


Fig. 8.12. A plot of the dependence of the key NLO property parameters: hyperpolarisability (β), dipole moment (μ), and energy gap value (ΔE), simulated for distances corresponding to given concentrations of functional groups, as a function of the concentration of functional groups in the tested materials.

trations (SBA-POO_2Cu5% and SBA-POO_2Cu10%) are relatively small and can be offset by considering the dipole moment, whose variation with concentration closely matches the experimental data. In contrast, the plot of the energy gap as a function of functional group concentration (which directly reflects the statistical distance between these groups, Figure 8.12) reveals an opposite trend to that observed experimentally. This agrees with the two-level theory describing nonlinear optical properties, according to which SHG efficiency is inversely proportional to the energy gap value [242]. The simulated value for the 5% concentration slightly deviates from this relationship, but the difference compared to SBA-POO_2Cu2.5% is small and can be compensated by the lower hyperpolarizability obtained for this concentration.

When considering third harmonic generation, hyperpolarizability should be excluded from the analysis, since THG properties are governed by a fourth-order tensor and can occur even in centrosymmetric materials [248]. For comparison with experimental results, the plots of dipole moment and energy gap versus concentration (Figure 8.12) should be examined. The dipole moment curve closely follows the experimental THG dependence on functional group concentration (Figure 8.6), while the remarks regarding the energy gap remain the same as in the SHG discussion.

In summary, the simulation results show excellent agreement with the experimental data, allowing for a precise explanation of the observed phenomena based on numerical modelling. The source of both SHG and THG signals in the studied materials is identified as NLO chromophores - propyl-copper-phosphonate functional groups. Simulations con-

sistent with the XANES findings indicate that the molecular structure and conformation of these chromophores are relatively uniform across all investigated samples. Therefore, the observed differences in NLO signal intensity are not due to variations in molecular structure, but rather to intermolecular interactions, which depend on the degree of material functionalization. Notably, there exists an optimal distance between groups at which the key parameters for NLO performance, namely high hyperpolarizability, high dipole moment, and low energy gap, reach their most favourable values. For the materials tested, this optimum distance is approximately 9 nm, corresponding to a functional group concentration of 2.5%.

The findings of this analysis make it possible to introduce an additional parameter into the design of functionalized nanomaterials for NLO applications, which is the degree of matrix functionalization with SMICs. To illustrate this approach, we carried out additional numerical simulations for binary systems, this time including SMIC–SMIC distances not covered in the initial study and extending the range up to 2.7 nm. The resulting NLO parameters, such as hyperpolarizability, dipole moment, and energy gap, are presented as plots comparable to those for the original material models in Figure 8.13.

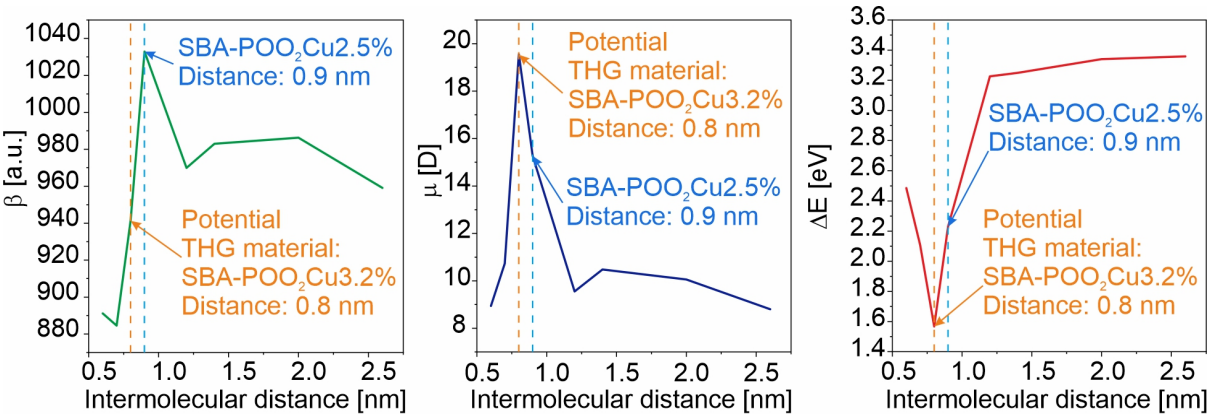


Fig. 8.13. A plot of the dependence of the key NLO property parameters: hyperpolarisability (β), dipole moment (μ), and energy gap value (ΔE), simulated for distances from 0.5 to 2.7 nm.

An examination of the complete set of data shows that the material SBA-POO_2Cu2.5% offers the most favourable conditions for second harmonic generation. Its maximum hyperpolarizability combined with a relatively low energy gap suggests that it exhibits the highest SHG intensity among the materials with varying degrees of functionalization. When considering the ability of the materials to produce third harmonic generation, a different composition, in which the functional groups are separated by 8 nm, appears to be the most effective. By applying the inverse approach to that used for determining

distances from a given concentration, it can be calculated that this optimal material for THG would correspond to an functional group concentration of 3.2% in molar ratio to the SiO_2 groups in the silica matrix.

9 General conclusions and future perspectives

In this doctoral thesis, mesoporous silica materials of SBA-15 type functionalized with copper phosphonate groups at various contents were thoroughly investigated. Although the main focus was initially intended to be on thin-film forms, the materials were also prepared as powders to enable a more detailed and comprehensive characterization. This dual approach allowed for extensive structural and optical analyses, while also demonstrating the high application potential of the developed materials, which can be easily deposited onto a variety of substrates using a simple dip-coating technique.

Firstly, the research was focused on confirming that the obtained materials met the intended synthesis objectives. Elemental composition analysis via EDS verified the presence of the expected elements as copper, phosphorus and silicon in proportions assumed during the synthesis, while elemental mapping revealed a uniform distribution of copper phosphonate groups in the silica nanochannels. Techniques such as TEM, SAXS, GISAXS, and nitrogen adsorption–desorption isotherms revealed the ordered mesoporous structure of the silica matrix, with information on specific surface area, pore diameter and pore volume enabling proper characterization of the spatial arrangement of the functional groups within the silica matrix. Additionally, using Raman spectroscopy an initial insight into the molecular structure of the studied systems was made.

Once it was confirmed that the obtained materials had the expected structure and composition, a study was initiated to determine the exact immediate vicinity of the copper atoms and to develop the numerical model that best reflected the material, which was essential for explaining the interesting non-linear optical properties observed for these materials. To this end, a study was conducted with the help of X-ray absorption spectroscopy (XAS) measurements. The XANES and EXAFS methods proved to be an excellent source of information about the closest environment of copper and phosphorus atoms, which resulted in the selection of appropriate numerical models for further analysis.

The last part of the thesis attempts to explain the influence of functional group content on the observed nonlinear optical properties of the studied materials. For this purpose, numerical models were constructed to accurately represent the molecular arrangement of functional groups as chromophores within the mesoporous silica framework. These mod-

els were parameterized based on structural data obtained from experimental techniques and subsequently used in quantum-chemical simulations. The calculations focused on determining key parameters directly related to nonlinear optical performance, namely the first hyperpolarizability, the dipole moment, and the energy gap between frontier molecular orbitals.

By systematically varying the intermolecular distances in the models—corresponding to different concentrations of functional groups in the experimental samples—it was possible to establish clear correlations between these parameters and the efficiency of second- and third-harmonic generation. The simulations revealed that the observed trends in NLO responses can be attributed not only to the intrinsic properties of the individual chromophores but also to their mutual interactions, which are strongly distance-dependent. This approach provided a consistent explanation for the non-linear dependence of the NLO signal intensity on functional group concentration, confirming that an optimal spatial arrangement of functional groups exists for maximizing the material's nonlinear optical response.

Beyond providing a fundamental understanding of the nonlinear optical behaviour, the results obtained in this work highlight the considerable application potential of SBA-15-based materials functionalized with copper phosphonate groups. Their tunable NLO response, resulting from the ability to control both the concentration and spatial arrangement of the active chromophores, opens the possibility of designing materials with properties tailored to specific photonic applications. The strong second- and third-harmonic generation efficiencies observed for optimally functionalized samples indicate their suitability for use in frequency conversion devices, optical signal processing, and laser-based sensing technologies.

An equally important advantage lies in the versatility of the deposition process. The studied materials can be easily applied as thin films on a wide variety of substrates using the dip-coating technique, which is both cost-effective and scalable. This makes them promising candidates for integration into compact photonic circuits, flexible optoelectronic devices, and sensor platforms. Furthermore, the modular nature of the synthesis allows copper phosphonate units to be replaced by other metal-organic functionalities, thereby enabling the creation of a broader family of hybrid mesoporous silica systems with tailored optical responses. Such flexibility paves the way for developing multifunctional nanomaterials that combine NLO activity with other desirable properties, such as catalytic, sensing, or light-harvesting capabilities.

Of particular significance is the fact that the developed materials exhibit multifunctionality. In addition to their exceptional nonlinear optical properties, SBA-15 mesoporous silica functionalized with copper phosphonate groups also demonstrates pro-

nounced antibacterial activity (not discussed here). This effect is not due to the release of copper ions but rather to the unique catalytic action of atomically dispersed copper sites, which promote the formation of reactive oxygen species (ROS) [249]. These highly reactive molecules are known to damage cellular components of microorganisms, leading to effective bactericidal action. The combination of strong NLO performance with intrinsic, ROS-mediated antimicrobial activity opens up entirely new avenues for applications, particularly in environments where both optical performance and biological safety are required. Potential examples include optical sensors operating in biomedical or environmental monitoring contexts, where the antibacterial properties could help maintain device cleanliness and prevent biofouling without the need for additional protective coatings. Such dual functionality significantly increases the technological value of the material, offering a unique platform for the development of advanced, multifunctional photonic devices.

List of scientific achievements

Publications

1. Agnieszka Karczmarska*; Michał Adamek; Sara El Houbbadi; Paweł Kowalczyk and Magdalena Laskowska*, Carbon-Supported Noble-Metal Nanoparticles for Catalytic Applications—A Review, MDPI, Crystals, 12, 584 (2022), MNiSW: 70, IF: 2.670.

2. Sara El Houbbadi, Magdalena Laskowska, Alain Walcarius, Marek Doskocz, Alexey Maximenko, Zbigniew Olejniczak, Łukasz Laskowski*. Revealing the molecular structure of copper phosphonate groups anchored inside SBA-15 silica channels: Theoretical and experimental study, Elsevier, Applied Surface Science, 669, 160425 (2024), MNiSW: 140, IF: 6.3.

Conferences

1. **EU INDTECH 2025 Polish Presidency of the EU Council, Innovative Ideas of Young Scientists** — 2 June 2025, Krakow, Poland. Multifunctional nanoporous materials, Flash Talk.

2. **Multiscale Phenomena in Condensed Matter MULTIS2024** — 16–19 September 2024, Krakow, Poland. Revealing the molecular structure of copper phosphonate groups anchored inside SBA-15 silica channels: theoretical and experimental study. Oral presentation.

3. **European Workshop on Innovative and Advanced Epitaxy** — 11–14 June 2024, Vilnius, Lithuania. Revealing the true configuration of copper phosphonate units inside silica pores with X-ray Absorption Spectroscopy. Oral presentation.

4. **LCPME Doctoral Day** — May 2024, Nancy, France. Nanostructured copper-functionalized silica-based materials for NLO applications: SHG nanoprobes advancing harmonic imaging in living tissue. Oral presentation.

5. **Green Light C2MP Seminar** — June 2024, Metz, France. Study of the local geometry of internal functional units' guests inside ordered mesoporous silica hosts. Poster.

6. **YOUNG MULTIS — Multiscale Phenomena in Condensed Matter (conference for young researchers)** — 3–5 July 2023, Krakow, Poland. Theoretical

and experimental XAFS studies of the atomic structure of copper-functionalized SBA-15 matrix. Oral presentation.

7. **IFJ PAN Young Scientist Seminars** — 23 November 2023, Krakow, Poland. Journey into the channels of copper-functionalized silica SBA-15: revealing the true configuration of copper phosphonate units inside silica pores using X-ray Absorption Spectroscopy. Seminar oral presentation.

8. **Multiscale Phenomena in Condensed Matter MULTIS2022** — 27–30 June 2022, Krakow, Poland. Multifunctional ordered mesoporous silica-based materials for nanotechnological applications. Poster.

9. **Joint Meeting of the Polish Synchrotron Radiation Members and SOLARIS Centre Users** — 20–23 September 2022, Krakow, Poland. Functionalized silica-based nanomaterials: unravelling the local structure at the ASTRA beamline. Poster.

10. **SYLINDA International Symposium** — 7–8 March 2024, Krakow, Poland. Investigating the correlation between copper concentration in SBA-15 and its NLO properties through X-ray Absorption Spectroscopy. Poster.

Summer Schools

1. **Jülich Centre for Neutron Science (JCNS) Laboratory Course — Neutron Scattering** — September 2024. One week of courses at the Jülich Centre for Neutron Science and one-week visit to the Garching nuclear reactor in Munich.

2. **Spectroscopies et Microscopies des Interfaces: Concepts et Couplages Méthodologiques** — 28–30 May 2024.

3. **Stanford Synchrotron Radiation Lightsource X-ray Absorption Spectroscopy and Imaging Summer School Workshop** — 25–28 October 2022, online via Zoom.

4. **XAFS 2022 Short Course on X-ray Absorption Fine Structure: Theory, Data Analysis and Modeling** — 2–4 November 2022, online via Zoom.

5. **XFELs for Beginners 2023 Workshop** — 12–13 October 2023, The Institute of Nuclear Physics Polish Academy of Sciences, Krakow.

6. **Soft Skills: Motivating and Resolving Conflicts** — December 2023. Communication skills, international experiences, trends in universities, and the impact of research.

7. **Applications de la Spectroscopie XPS à Pression Proche de l'Ambiante (Near Ambient Pressure-XPS) Webinar** — 16 May 2023.

Résumé étendu

La silice mésoporeuse ordonnée (OMS, ordered mesoporous silica) constitue une plateforme polyvalente pour la conception de matériaux hybrides organiques–inorganiques, elle se caractérise par de larges pores (2–50 nm) capables d'accueillir des motifs moléculaires de tailles et de types variés. L'architecture hautement organisée et parfois orientée de l'OMS est avantageuse pour l'optimisation des propriétés fonctionnelles des systèmes hybrides, telles que la réponse en optique non linéaire (NLO) d'ordre deux, qui provient généralement des espèces moléculaires intégrées plutôt que de la matrice de silice elle-même. L'OMS peut être synthétisée sous diverses structures et morphologies— y compris les structures hexagonales de type SBA-15 et MCM-41 ou cubiques de type SBA-16 et MCM-48, les nanoparticules, les films minces et les aérogels — avec une taille de pore, une aire spécifique et une morphologie modulables. Ces caractéristiques rendent l'OMS particulièrement attrayante pour des applications en catalyse, adsorption, filtration, optoélectronique et vectorisation de médicaments.

L'objectif de cette thèse est d'exploiter la possible synergie entre la mésostructure ordonnée, la robustesse la charpente de silice et de la nature et du caractère modulable de la teneur en groupements fonctionnels pour des applications en optique non lineair. Plus précisément, les effets de concentration du complexe formé entre le ligand propylephosphonate et les ions cuivre(II) sur la génération de seconde harmonique (SHG) et de troisième harmonique (THG) ont été systématiquement étudiés dans des poudres de SBA-15 et des films minces de silice mésoporeuse à structure hexagonale en utilisant un large éventail de techniques expérimentales complémentaires. L'objectif global était de mettre en évidence comment la configuration moléculaire et électronique de ces groupements fonctionnels gouverne les propriétés optiques non linéaires des matériaux hybrides obtenus.

Conceptuellement, l'ajustement de la concentration des unités fonctionnelles ancrées dans les mésopores de silice module la distance moyenne entre groupes adjacents. Cette variation peut induire ou empêcher de nouvelles interactions intermoléculaires qui influencent fortement l'activité NLO globale du système. Pour explorer l'origine de ces changements, une démarche systématique d'investigations expérimentales et computationnelles a été menée, en commençant par la caractérisation structurale et morphologique des échantillons fonctionnalisés en fonction de la concentration en complexe phosphonate de cuivre.

Premièrement, une silice mésoporeuse SBA-15 fonctionnalisée par liaison covalente d'entités acide propylphosphonique a été synthétisée par une méthode de Stöber modi-

fiée, avec teneurs en groupements fonctionnels de 1,25, 2,5, 5 et 10%. Ces matériaux ont ensuite été convertis en SBA-15 fonctionnalisée au complexe phosphonate de cuivre. En parallèle, des films minces du même matériau de silice ont été préparés aux concentrations identiques par la technique de trempage–retrait (*dip-coating*). Afin d'obtenir une distribution homogène et un contrôle précis des groupes moléculaires ancrés, une voie de synthèse par co-condensation a été adoptée, dans laquelle le rapport molaire entre le précurseur de silice (TEOS, tetraéthoxysilane) et le précurseur organosilane portant le groupement fonctionnel organique **R** (acide phosphonique) a été ajusté, comme illustré à la Figure 9.1(avec R = groupement fonctionnel).

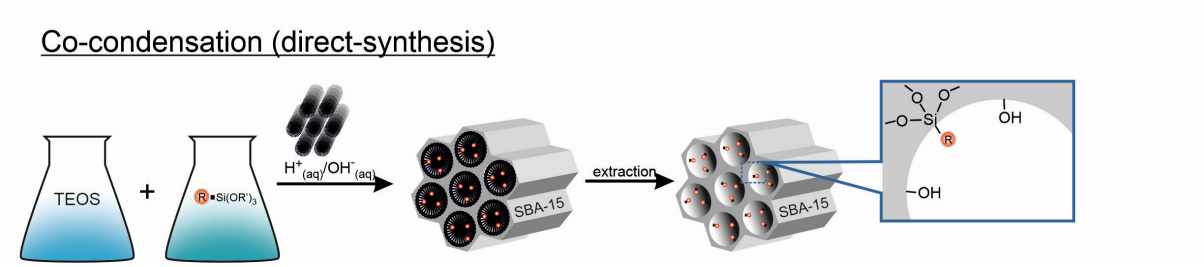


Fig. 9.1. Voie de co-condensation pour la synthèse de SBA-15 porteuse de groupements fonctionnels **R** uniformément dispersés à l'intérieur des pores de la silice mésoporeuse.

Les structures mésoporeuses ordonnées hexagonales ont d'abord été analysées par microscopie électronique à transmission (MET) et à balayage (MEB). La MET a confirmé l'arrangement hexagonal interne des pores de la porosité nanostructurée dans tous les échantillons, incluant aussi bien les poudres que les films minces. Pour des charges en groupements fonctionnels allant jusqu'à 10%, la structure mésoporeuse hautement ordonnée, avec des canaux de pores parallèles, est restée intacte, indiquant que la fonctionnalisation n'a pas perturbé la matrice de silice (voir Figure 9.2). En revanche, à des charges plus élevées, les échantillons en poudre ont montré un léger rétrécissement des pores, ce qui nous a conduit à ne pas préparer des de films minces avec 20% d'organosilane.

L'analyse MEB a fourni des informations complémentaires sur la morphologie de surface, montrant que jusqu'à 10% de charge, les échantillons conservaient des caractéristiques structurelles et morphologiques comparables, sans différences significatives en termes d'épaisseur de film ou de morphologie des grains (voir Figure 9.3).

Dans l'ensemble, ces résultats démontrent que les films minces comme les poudres préservent des caractéristiques morphologiques et structurales similaires dans l'intervalle de fonctionnalisation étudié.

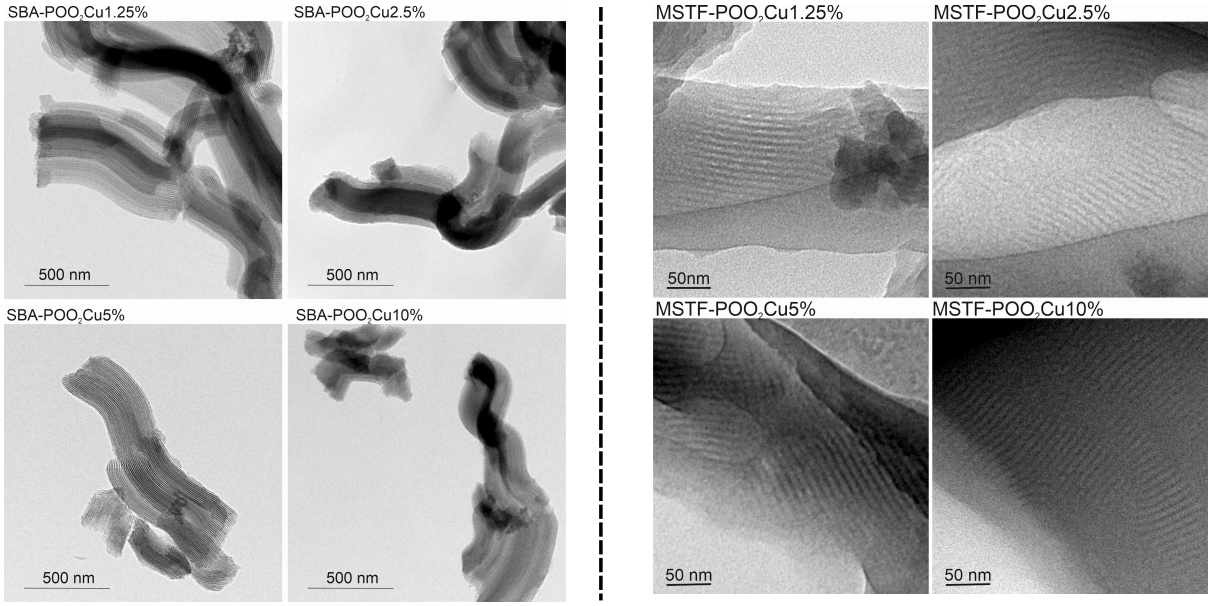


Fig. 9.2. Images MET des poudres SBA-POO_2Cu et des films minces MSTF-POO_2Cu à différentes teneurs en complexe phosphonate de cuivre..

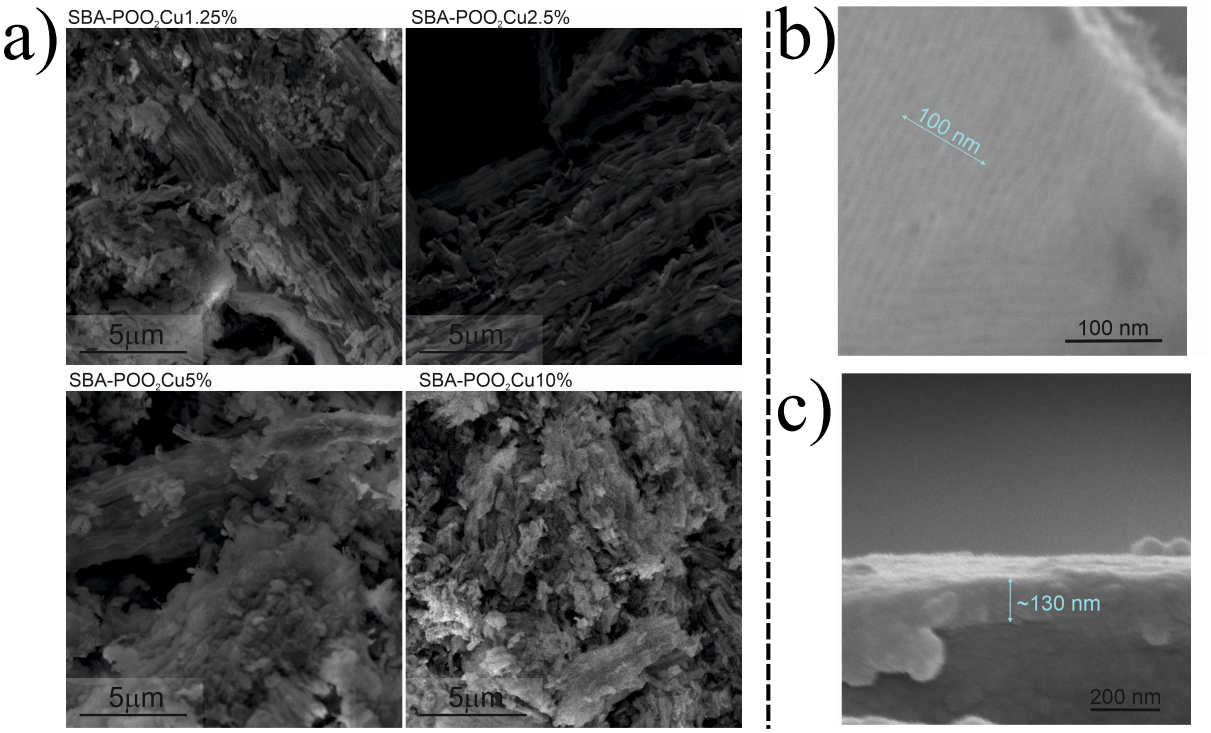


Fig. 9.3. Images MEB de la silice mésoporeuse SBA-POO_2Cu : poudres à différentes teneurs en complexe phosphonate de cuivre (a), surface du film mince (b), coupe transversale du film mince à 5 % de teneur en groupements fonctionnels(c).

De même, les mesures SAXS réalisées sur les poudres fonctionnalisées ont révélé la préservation de l'ordre nanostructural de type SBA-15 à structure hexagonale 1D, tandis

que les mesures GISAXS effectuées sur les films minces déposés par trempage–retrait (*dip-coating*) ont mis en évidence des mésostructures hexagonales bien définies, parallèles à la surface du substrat.

La cartographie élémentaire a en outre montré que les complexes phosphonate de cuivre étaient uniformément répartis sur la surface de la silice, indiquant que la stratégie de fonctionnalisation était efficace (voir Figure 9.4). .

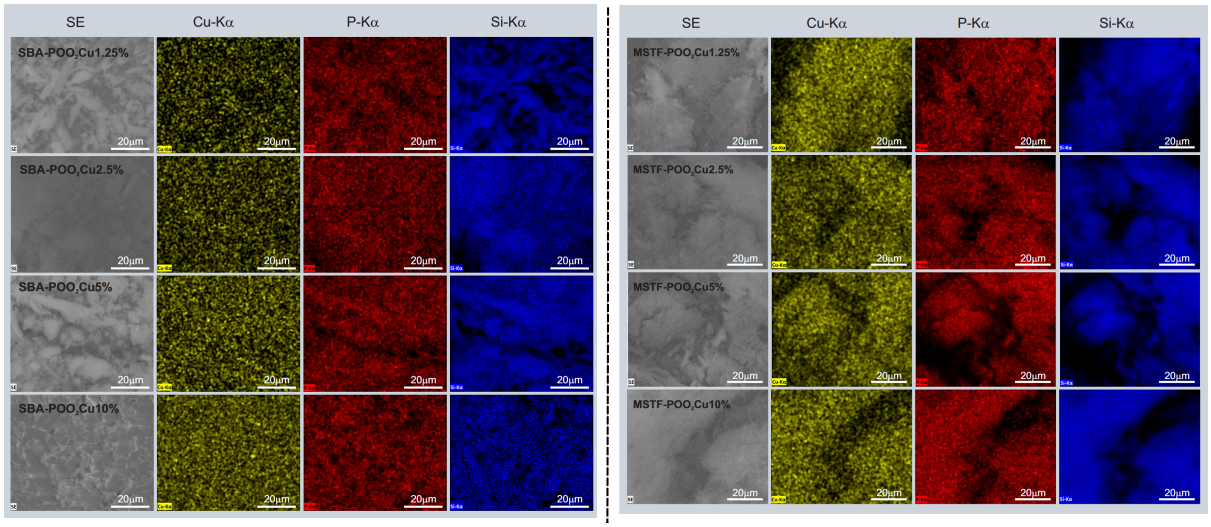
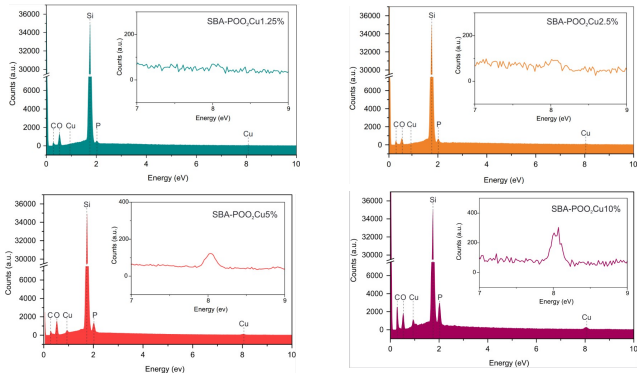


Fig. 9.4. Images MEB et cartographies EDS des poudres SBA-POO_2Cu et des films minces MSTF-POO_2Cu à différentes teneur de groupements fonctionnels.

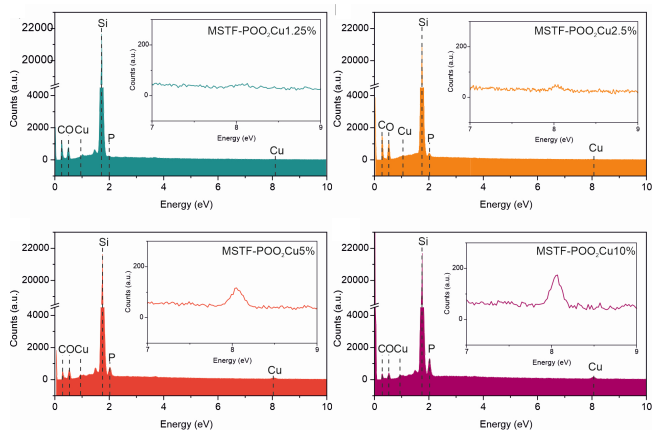
L'analyse de la composition élémentaire réalisée par spectroscopie à rayons X à dispersion d'énergie (EDS) a confirmé la présence des éléments clés — cuivre, phosphore et silicium — dans des proportions cohérentes avec conditions de synthèse utilisées. Il est particulièrement important de noter que le rapport atomique cuivre/phosphore a été maintenu à environ 1:1 pour des charges allant jusqu'à 10%, ce qui correspond à la stœchiométrie attendue du complexe cuivre–phosphonate. En revanche, à des charges plus élevées (20%), ce rapport a fortement évolué, atteignant environ 1:1,7, comme illustré à la Figure 9.5, suggérant soit une complexation 1:1 incomplète, soit la formation (partielle) de complexes 1:2.

Pour les échantillons à faible concentration, les rapports atomiques Si:P et P:Cu correspondaient étroitement aux valeurs théoriques, confirmant que la majorité des groupement phosphonate étaient effectivement coordonnés aux ions cuivre. En revanche, l'échantillon SBA-POO_2Cu20% présentait un rapport P:Cu déviant de la valeur attendue de 1:1. Cela suggère qu'à des concentrations plus élevées en groupement fonctionnels, tous les ligands acide phosphonique n'ont pas pu se lier à un ion cuivre. Une telle déviation constitue une première indication importante que la conformation moléculaire au sein des méso-canaux de silice est modifiée lorsque la teneur en groupement fonctionnels augmente, potentielle-

ment en raison d'effets stériques et de l'accessibilité à un milieu de plus en plus confiné à mesure que la teneur en ligands au sein des pores augmente.



	Element content (At. %)			
	Si:P		P:Cu	
Sample	Si	P	P	Cu
$SBA\text{-}POO_2Cu1.25\%$	98.7	1.3	46.7	53.3
$SBA\text{-}POO_2Cu2.5\%$	97.7	2.3	48.9	51.1
$SBA\text{-}POO_2Cu5\%$	95.0	5.0	50.9	49.1
$SBA\text{-}POO_2Cu10\%$	87.9	12.1	50.0	50.0
$SBA\text{-}POO_2Cu20\%$	81.9	18.1	63.0	37.0



	Element content (At. %)			
	Si:P		P:Cu	
Sample	Si	P	P	Cu
$MSTF\text{-}POO_2Cu1.25\%$	99.3	0.7	40.0	60.0
$MSTF\text{-}POO_2Cu2.5\%$	96.6	3.4	48.9	51.1
$MSTF\text{-}POO_2Cu5\%$	95.0	5.0	50.8	49.2
$MSTF\text{-}POO_2Cu10\%$	91.2	8.8	56.7	43.3

Fig. 9.5. Spectres EDS de $SBA\text{-}POO_2Cu$ (partie supérieure) et $MSTF\text{-}POO_2Cu$ (partie inférieure) à 1,25, 2,5, 5 et 10%,(l'échantillon $SBA\text{–}POO_2Cu$ à 20% a également été analysé)

Les expériences de physisorption d'azote (N_2) ont confirmé la mésoporosité attendue, comme l'indique la forme caractéristique de la boucle d'hystérèse. L'augmentation de la charge en phosphonate de cuivre a entraîné une tendance régulière dans les variations d'aire spécifique, de volume de pores et de diamètre de pores. À mesure que la densité en groupements fonctionnels augmente, la distance intermoléculaire entre complexes adjacents diminue, réduisant ainsi l'accessibilité des molécules de N_2 aux parois de silice (voir Figure 9.6).

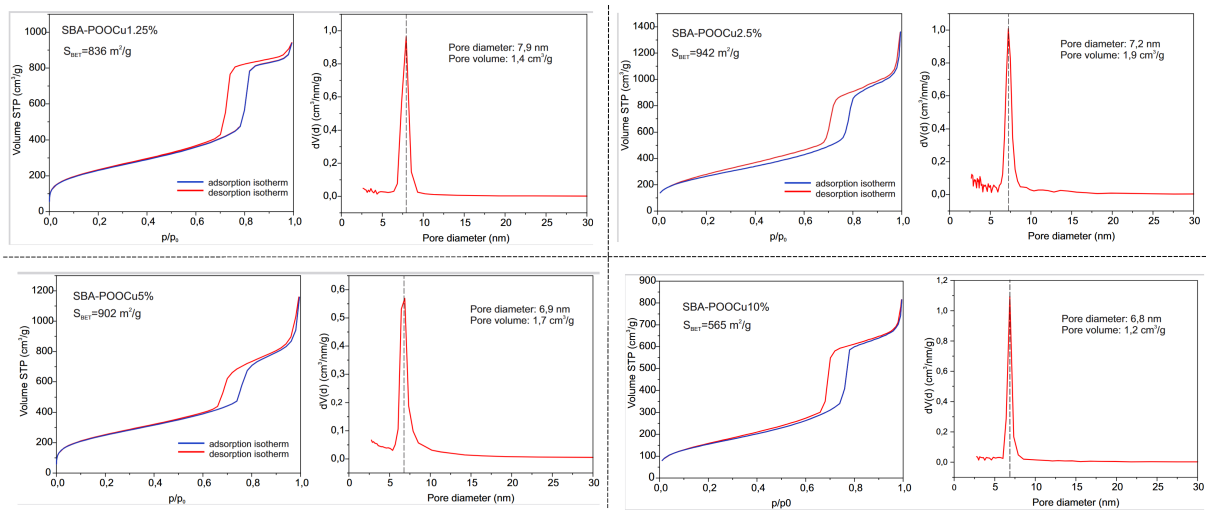


Fig. 9.6. Isothermes d'adsorption–désorption d'azote de SBA–POO_2Cu et distribution de taille des pores correspondante selon la méthode BJH à différentes teneurs en complexe phosphonate de cuivre.

Jusqu'à une charge de 2,5%, la distance intermoléculaire reste suffisamment grande pour permettre une adsorption efficace de N_2. Cependant, une transition de la surface spécifique est observée lorsque la concentration atteint 5%, accompagnée d'un rétrécissement du diamètre des pores. Lorsque la concentration continue d'augmenter au-delà de ce point, la même tendance de diminution de la surface spécifique et de rétrécissement des pores persiste.

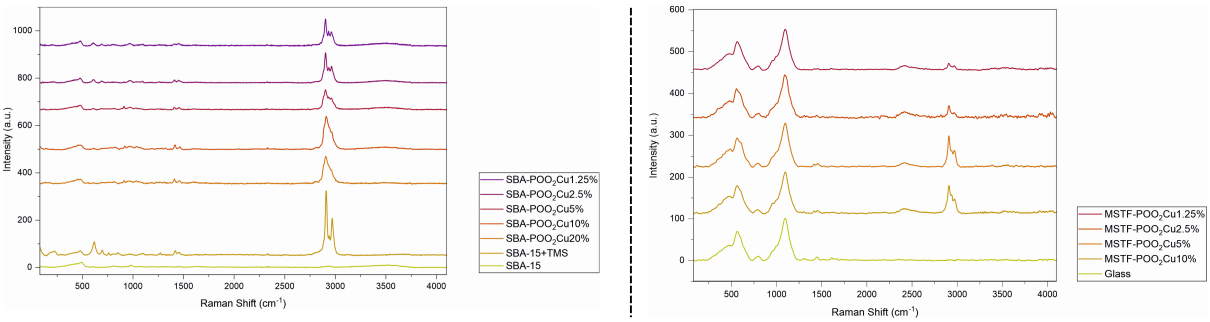


Fig. 9.7. Spectres Raman des poudres et films minces de silice mésoporeuse fonctionnalisée au phosphonate de cuivre à différentes teneurs en groupements fonctionnels.

L'analyse par spectrométrie Raman a montré que tous les échantillons étudiés, sous forme de poudre comme de film mince, présentent une structure moléculaire similaire, comme en témoigne la forme comparable des spectres Raman. Cependant, une analyse plus détaillée révèle de subtiles différences dans les intensités de certaines bandes, cohérentes avec les résultats de l'étude EDS, indiquant des variations des quantités de

cuivre et de phosphore conformément à la conception de synthèse. De plus, la position des bandes observées confirme l'incorporation réussie des groupements TMS et des complexes phosphonate de cuivre au sein de la structure de la silice (voir Figure 9.7).

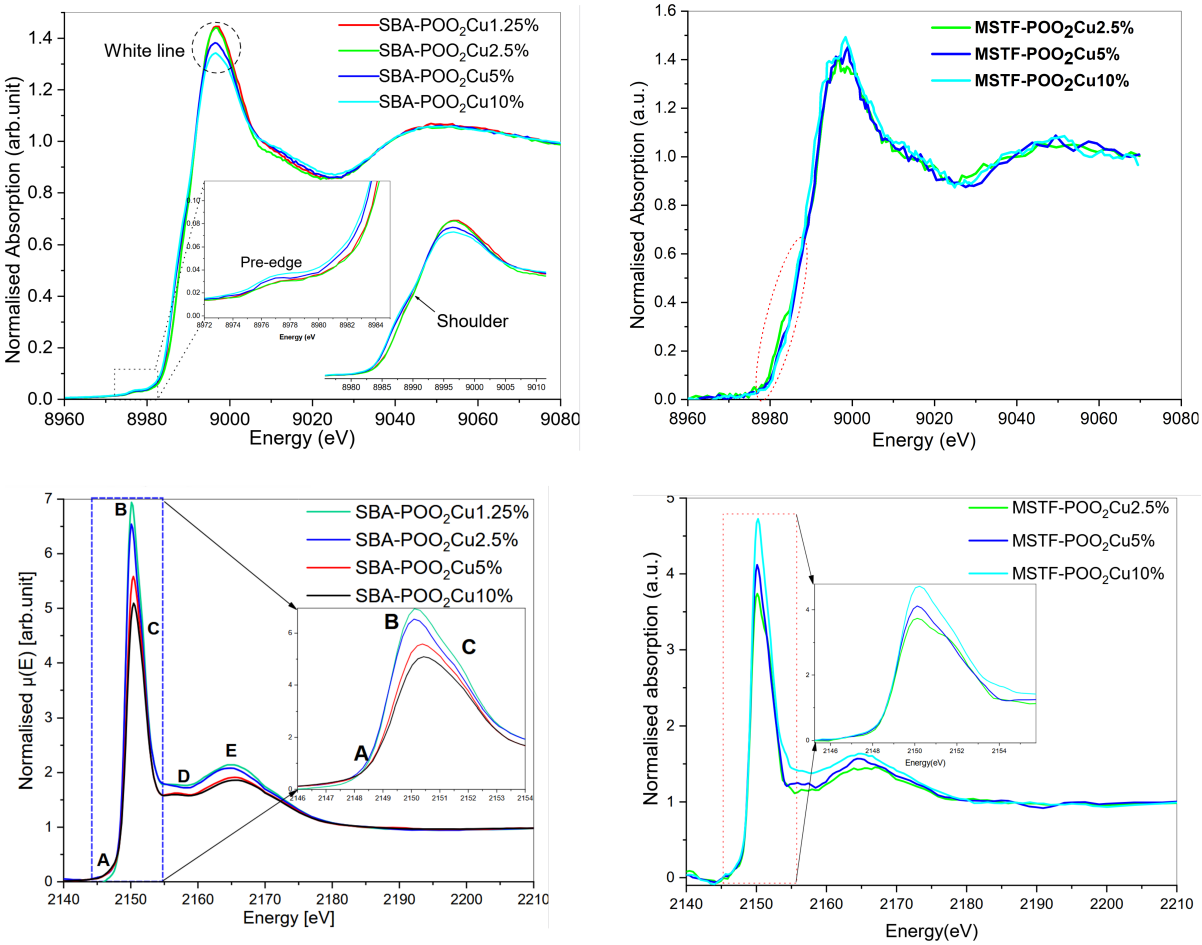


Fig. 9.8. Coefficient d'absorption normalisé aux seuils K du Cu (partie supérieure) et du P (partie inférieure) pour les poudres de silice mésoporeuse fonctionnalisée au phosphonate de cuivre SBA-POO_2Cu et les films minces MSTF-POO_2Cu à différentes teneurs en groupements fonctionnels.

Les mesures XANES aux seuils K du Cu et du P en Figure 9.8 mettent en évidence l'influence significative de la concentration en groupements fonctionnels — et donc des distances intermoléculaires entre ces groupements — sur les orbitales moléculaires et la structure électronique globale. Les spectres aux seuils K du Cu et du P apportent des preuves convaincantes par l'apparition de regroupements spectraux distincts. Ces regroupements indiquent que les propriétés clés du système, telles que son comportement électronique et sa réponse optique non linéaire (NLO), sont gouvernées principalement par l'agencement spatial et les distances intermoléculaires entre les groupes fonctionnels cuivre–phosphonate.

La modélisation DFT dans ce travail de recherche s'est appuyée sur les résultats expérimentaux. Il a été démontré par l'analyse EDS que l'environnement de coordination dépendait de la teneur en groupements fonctionnels, passant d'une unité phosphonique liant un ion cuivre à faible teneur à deux unités phosphoniques coordonnant le cuivre à des teneurs plus élevées (hypothèse selon le rapport atomique P:Cu indiqué dans la figure 9.5).

Afin d'analyser quantitativement les données expérimentales XANES, des modèles ont ainsi été développés pour représenter la structure moléculaire des fragments moléculaires de phosphonate de cuivre introduits dans la silice SBA-15 . L'échantillon contenant la plus forte teneur en groupements fonctionnels (20 %) a été analysé séparément sur la base des modèles de conformères à double coordination composés de deux groupements $CH_3PO_3H^-$, d'un ion cuivre (Cu^{2+}) et de deux molécules d'eau, ainsi que des modèles à double fonction composés de deux groupements $CH_3PO_3H^-$, d'un ion cuivre (Cu^{2+}) et de quatre molécules d'eau. Ces modèles ont été déformés en modifiant et en figeant l'un des paramètres structurels des modèles, notamment la distance entre les atomes de cuivre et de phosphore (modèles nommés Axx), l'angle dièdre entre quatre atomes d'oxygène (modèles nommés ARxx et AAxx) et la distance entre l'atome de cuivre et le groupement oxygène-phosphore P=O (modèles nommés Bxx) voir la Figure 9.9.

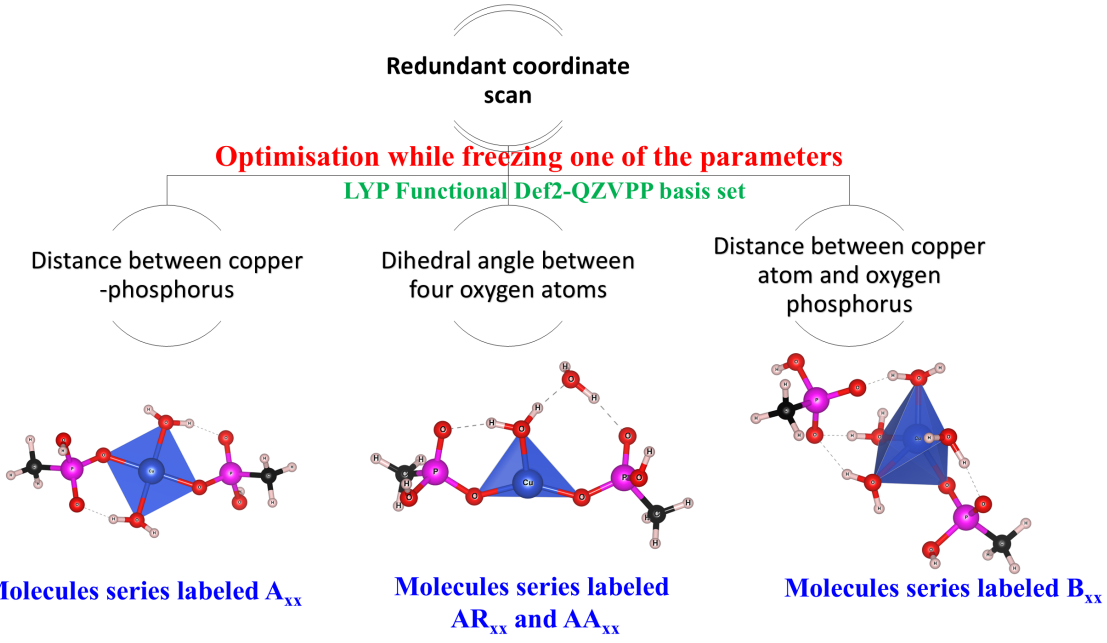


Fig. 9.9. Workflow de balayage de coordonnées redondant

Ensuite, les coordonnées cartésiennes de chaque modèle obtenu ont été utilisées pour calculer le spectre XANES à l'aide du code ab initio FEFF10. Après avoir créé une base de données composée de spectres calculés théoriquement à partir de structures moléculaires

connues, L'analyse PCA (PCA, Principal component analysis) a été utilisée pour trouver la position optimale du spectre par rapport au spectre expérimental sur l'axe d'énergie, puis un réseau neuronal a été construit pour trouver la contribution appropriée de chaque modèle structurel voire Figure 9.10.

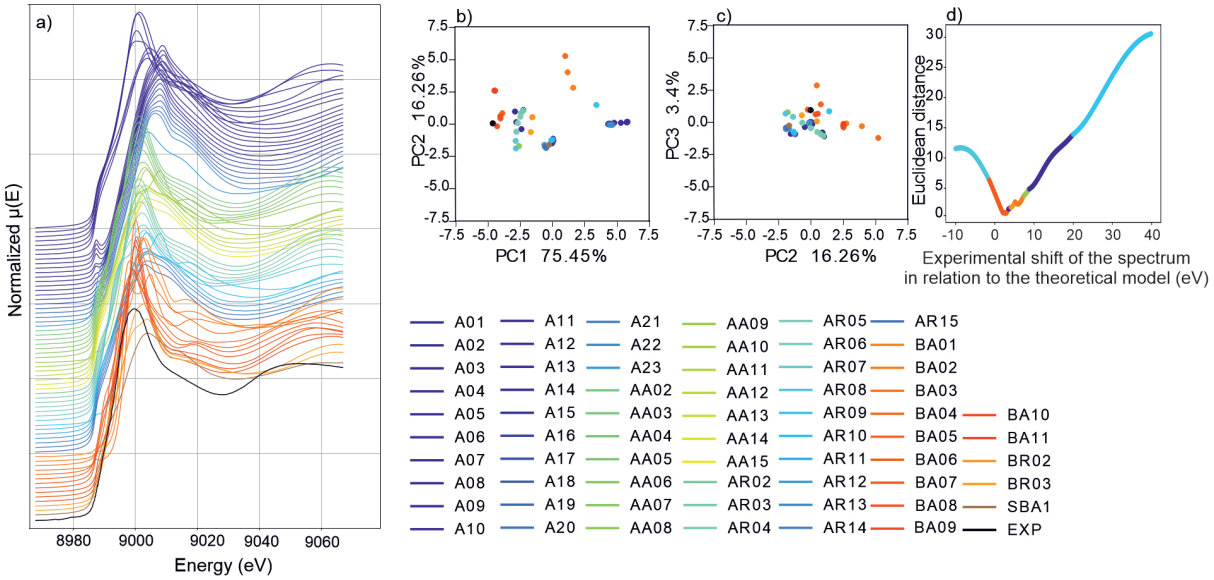


Fig. 9.10. a) Superposition du spectre XANES expérimental au seuil K du cuivre de la poudre de silice mésoporeuse fonctionnalisée au phosphonate de propyl-cuivre à une teneur de 20 % en groupements fonctionnels, avec les spectres calculés des modèles DFT. (b), (c) et (d) présentent les résultats d'une analyse PCA sur l'ensemble des données calculées.

Le spectre expérimental a été déplacé de -10 eV à +40 eV par incréments de 0,1 eV, et pour chaque étape, la distance euclidienne dans l'espace PC (PC1-PC3 et PC1-PC7) a été calculée afin d'identifier la correspondance la plus proche . La meilleure correspondance était le modèle BA06 avec un décalage de 2,3 eV, suivi des modèles BA09 et BA05, correspondant à un environnement de cuivre bipyramidal trigonal déformé. Les résultats indiquent la coexistence de plusieurs environnements de cuivre-phosphonate similaires au sein de la matrice de silice (voir Figure 9.11).

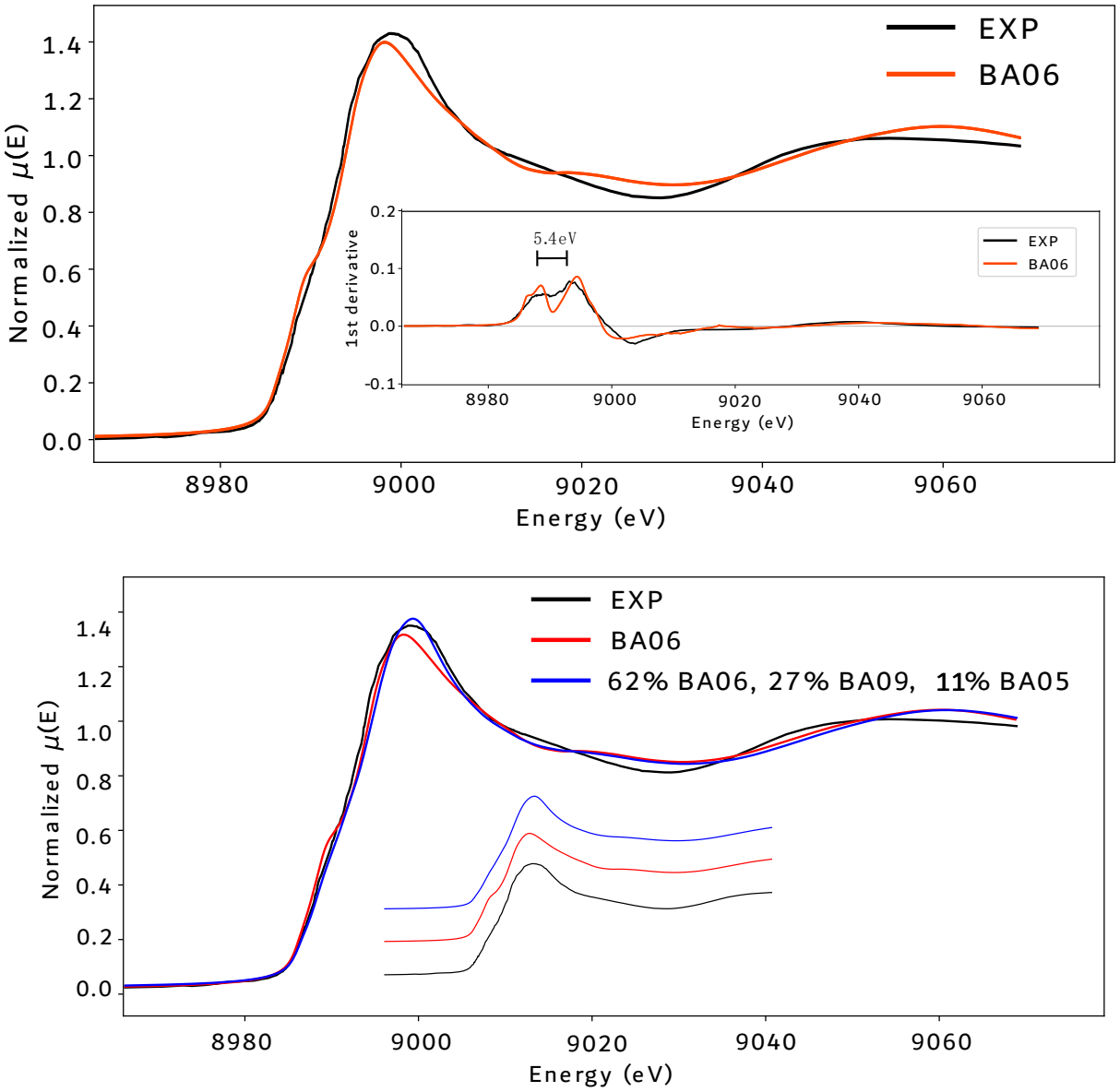


Fig. 9.11. Comparaison du spectre expérimental avec BA06 et de leurs premières dérivées (haut). Décomposition par apprentissage automatique (bas) indiquant 62% de BA06, 27% de BA09 et 11% de BA05, accompagnée du tracé empilé des composantes. Les spectres théoriques sont décalés de 2,3 eV.

En ce qui concerne l'analyse des données XANES des autres échantillons contenant des groupements fonctionnels à plus faible teneur, des modèles à groupement fonctionnel simple ont été construits, comprenant des systèmes contenant un groupement phosphonate ($CH_3CH_2PO_2^{3-}$), un atome de cuivre (Cu^{2+}) et n molécules d'eau (n=0...6) pour varier l'environnement du ligand du cuivre. De plus, ces modèles prennent en compte les formes ioniques formées après le détachement d'un proton ou l'ajout d'un groupement OH^- (voir Figure 9.12).

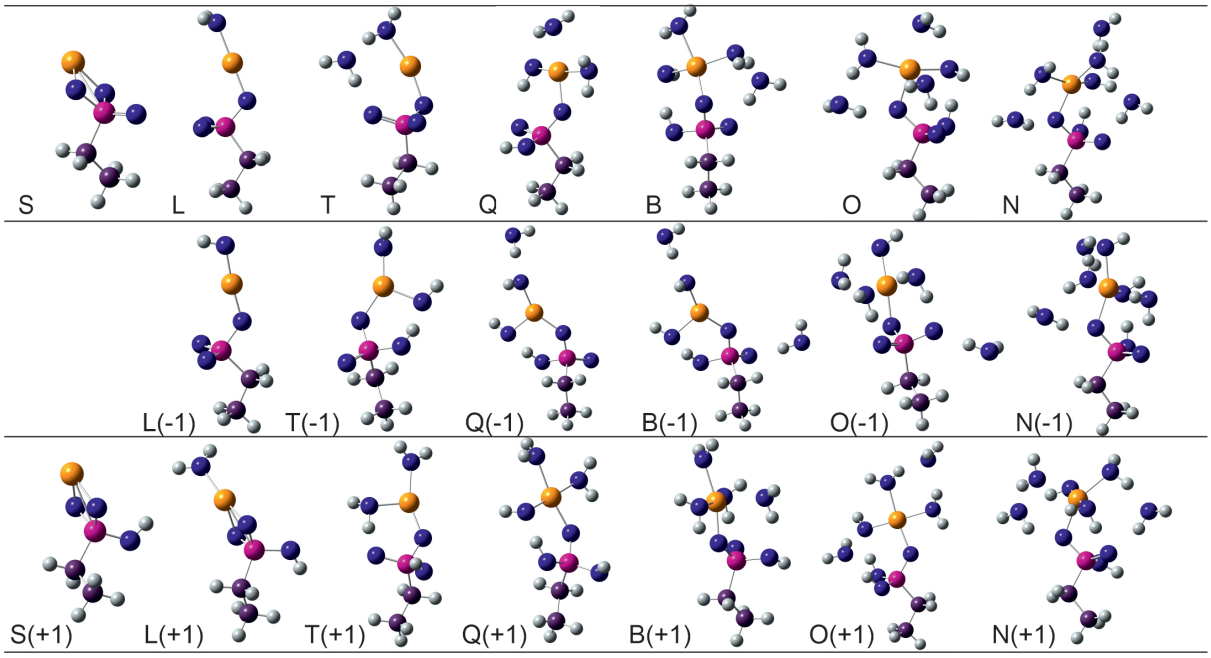


Fig. 9.12. Les 20 modèles de conformères à groupement fonctionnel unique.

De la même manière, chacun des modèles proposés dans ce nouvel ensemble a été utilisé pour ajuster les données expérimentales de la silice fonctionnalisée à faible concentration (1,25, 2,5, 5 et 10 %). Les résultats de l'ajustement sont présentés dans la Figure 9.13.

L'analyse computationnelle basée sur la DFT des spectres XANES a permis d'identifier le conformère moléculaire le plus probable, qui a ensuite été utilisé pour expliquer la relation entre la réponse optique non linéaire (NLO) et les distances intermoléculaires entre les groupements moléculaires à chaque concentration. Ceci a été réalisé en calculant les paramètres clés liés à la NLO, notamment l'hyperpolarisabilité (β_{total}), le moment dipolaire (μ) et le gap énergétique entre les niveaux HOMO et LUMO (E_g), ainsi qu'en visualisant les potentiels électrostatiques et les surfaces de densité électronique (voir Figure 9.14).

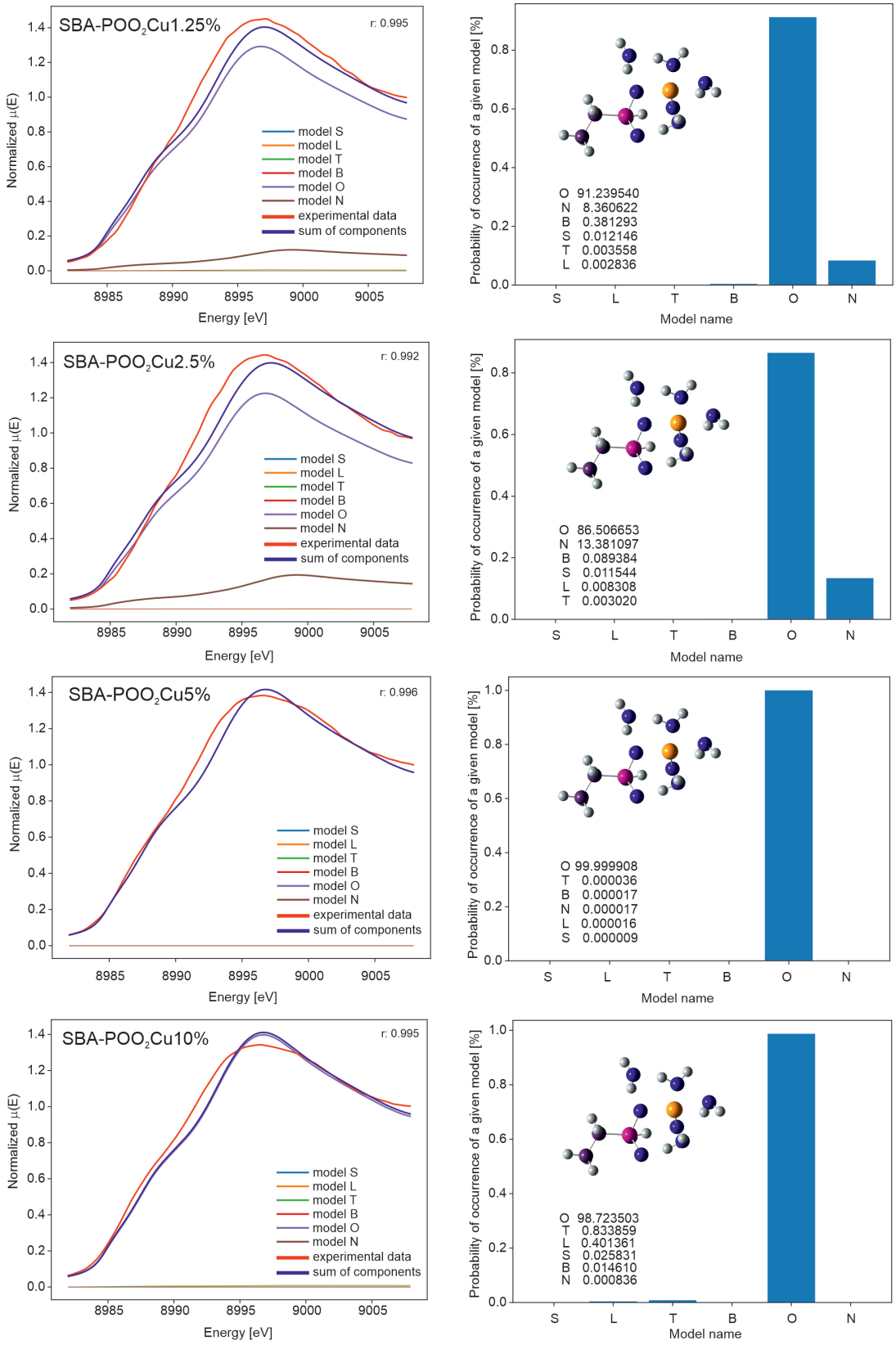


Fig. 9.13. Résultats d'ajustement pour chaque concentration de SBA–POO_2Cu à faible teneur, montrant le pourcentage de correspondance des modèles théoriques S,L,T,B,O et N avec les spectres XANES expérimentaux, ainsi qu'une visualisation du modèle le plus probable.

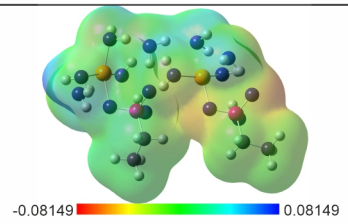
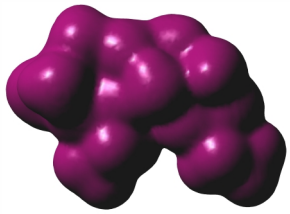
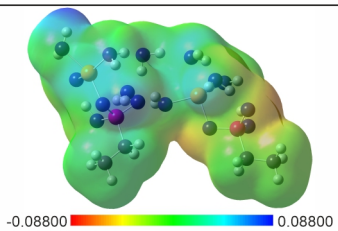
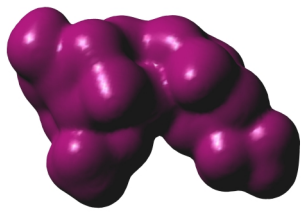
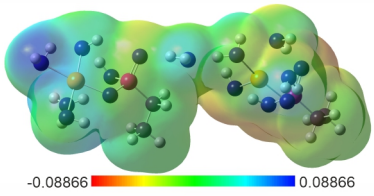
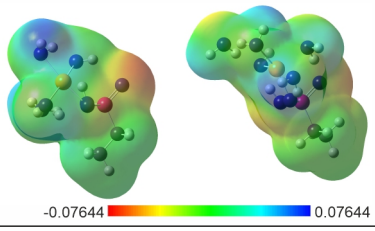
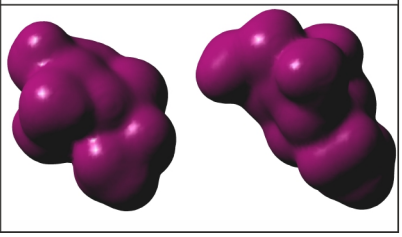
Model description	NLO parameters	Numerical model with electrostatic potential surface	Electron density surface
SBA-POO_2Cu10% Intermolecular distance: 0.6 [nm]	β=891.19 μ=8.94 D ΔE=2.49 eV		
SBA-POO_2Cu5% Intermolecular distance: 0.7 [nm]	β=884.56 μ=10.73 D ΔE=2.11 eV		
SBA-POO_2Cu2.5% Intermolecular distance: 0.9 [nm]	β=1032.95 μ=15.27 D ΔE=2.23 eV		
SBA-POO_2Cu1.25% Intermolecular distance: 1.2 [nm]	β=969.93 μ=9.55 D ΔE=3.23 eV		

Fig. 9.14. Visualisation des modèles optimisés constitués de deux groupements fonctionnels sépaeés par des distances obtenues grâce à l'application de la méthode KDE aux matériaux étudiés. De plus, les valeurs clés des propriétés NLO sont indiquées pour chaque modèle : hyperpolarisabilité (β), moment dipolaire (μ) et valeur du gap énergétique (ΔE).

Les simulations ont révélé que les tendances observées dans les réponses optiques non linéaires (NLO) peuvent être attribuées non seulement aux propriétés intrinsèques des chromophores individuels, mais également à leurs interactions mutuelles, qui dépendent fortement de la distance.

Un aspect important de cette thèse est de mettre en évidence le comportement structural, morphologique et optique de la silice de type SBA-15, tant sous forme de poudre que de film mince. La démonstration de la similitude de ces propriétés implique indirectement que les matériaux mésoporeux préparés à partir des mêmes précurseurs initiaux peuvent être attendus pour présenter des caractéristiques comparables. Cela rend l'étude des films minces plus directe, malgré les défis expérimentaux qu'ils posent, notamment

du fait qu'ils ne peuvent pas être ôtés de leur support. De plus, la polyvalence du processus de dépôt offre un avantage pratique : les matériaux étudiés peuvent être facilement appliqués sous forme de films minces sur une grande variété de substrats en utilisant la technique de trempage–retrait (*dip-coating*), qui est à la fois économique et facilement extensible à grande échelle. Ces caractéristiques en font des candidats prometteurs pour une intégration dans des circuits photoniques compacts, des dispositifs optoélectroniques flexibles et des plateformes de capteurs.

Bibliography

[1] Feynman, R. (2018) There's plenty of room at the bottom. In *Feynman and computation* pp. 63–76 CRC Press.

[2] Novoselov, K. S., Geim, A. K., Morozov, S. V., Jiang, D.-e., Zhang, Y., Dubonos, S. V., Grigorieva, I. V., and Firsov, A. A. (2004) Electric field effect in atomically thin carbon films. *science,* **306**(5696), 666–669.

[3] Binnig, G., Quate, C. F., and Gerber, C. (1986) Atomic force microscope. *Physical review letters,* **56**(9), 930.

[4] Kroto, H. W., Heath, J. R., O'Brien, S. C., Curl, R. F., and Smalley, R. E. (1985) C60: Buckminsterfullerene. *nature,* **318**(6042), 162–163.

[5] Iijima, S. (1991) Helical microtubules of graphitic carbon. *nature,* **354**(6348), 56–58.

[6] Geim, A. K. and Novoselov, K. S. (2007) The rise of graphene. *Nature materials,* **6**(3), 183–191.

[7] Zhang, F., Zhu, Y., Lin, Q., Zhang, L., Zhang, X., and Wang, H. (2021) Noble-metal single-atoms in thermocatalysis, electrocatalysis, and photocatalysis. *Energy & Environmental Science,* **14**(5), 2954–3009.

[8] Xin, Y., Yu, K., Zhang, L., Yang, Y., Yuan, H., Li, H., Wang, L., and Zeng, J. (2021) Copper-based plasmonic catalysis: recent advances and future perspectives. *Advanced Materials,* **33**(32), 2008145.

[9] Cronstedt, A. F. (1756) Rön och beskrifning om en obekant bärg art, som kallas Zeolites, , .

[10] Yan, W. and Yu, J. (2023) Our journey in zeolite science. *Microporous and Mesoporous Materials,* **358**, 112368 Avelino Corma-70.

[11] Kresge, a. C., Leonowicz, M. E., Roth, W. J., Vartuli, J., and Beck, J. (1992) Ordered mesoporous molecular sieves synthesized by a liquid-crystal template mechanism. *nature,* **359**(6397), 710–712.

[12] Costa, J. A. S., de Jesus, R. A., Santos, D. O., Mano, J. F., Romão, L. P., and Paranhos, C. M. (2020) Recent progresses in the adsorption of organic, inorganic, and gas compounds by MCM-41-based mesoporous materials. *Microporous and Mesoporous Materials,* **291**, 109698.

[13] Hunter, H. M. and Wright, P. A. (2001) Synthesis and characterisation of the mesoporous silicate SBA-2 and its performance as an acid catalyst. *Microporous and mesoporous materials,* **43**(3), 361–373.

[14] Sakamoto, Y., Díaz, I., Terasaki, O., Zhao, D., Perez-Pariente, J., Kim, J. M., and Stucky, G. D. (2002) Three-dimensional cubic mesoporous structures of SBA-12 and related materials by electron crystallography. *The Journal of Physical Chemistry B,* **106**(12), 3118–3123.

[15] Kruk, M., Jaroniec, M., Ko, C. H., and Ryoo, R. (2000) Characterization of the porous structure of SBA-15. *Chemistry of materials,* **12**(7), 1961–1968.

[16] IUPAC (1972) Manual of symbols and terminology. *Pure Appl Chem,* **31**, 578.

[17] Beck, J. S., Vartuli, J. C., Roth, W. J., Leonowicz, M. E., Kresge, C. T., Schmitt, K. D., Chu, C. T., Olson, D. H., Sheppard, E. W., McCullen, S. B., et al. (1992) A new family of mesoporous molecular sieves prepared with liquid crystal templates. *Journal of the American Chemical society,* **114**(27), 10834–10843.

[18] Zhao, D., Huo, Q., Feng, J., Chmelka, B. F., and Stucky, G. D. (1998) Nonionic triblock and star diblock copolymer and oligomeric surfactant syntheses of highly ordered, hydrothermally stable, mesoporous silica structures. *Journal of the American Chemical Society,* **120**(24), 6024–6036.

[19] Shinde, P. S., Suryawanshi, P. S., Patil, K. K., Belekar, V. M., Sankpal, S. A., Delekar, S. D., and Jadhav, S. A. (2021) A brief overview of recent progress in porous silica as catalyst supports. *Journal of Composites Science,* **5**(3), 75.

[20] Bacariza, M., Graça, I., Bebiano, S., Lopes, J., and Henriques, C. (2018) Micro- and mesoporous supports for CO2 methanation catalysts: A comparison between SBA-15, MCM-41 and USY zeolite. *Chemical Engineering Science,* **175**, 72–83.

[21] Zienkiewicz-Strzałka, M., Skibińska, M., and Pikus, S. (2017) Small-angle X-ray scattering (SAXS) studies of the structure of mesoporous silicas. *Nuclear Instruments and Methods in Physics Research Section B: Beam Interactions with Materials and Atoms,* **411**, 72–77 The 13th International School and Symposium on Synchrotron Radiation in Natural Science (ISSRNS'2016).

[22] Schulz-Ekloff, G., Rathouský, J., and Zukal, A. (1999) Controlling of morphology and characterization of pore structure of ordered mesoporous silicas. *Microporous and Mesoporous Materials,* **27**(2), 273–285.

[23] Bjork, E. M., Soderlind, F., and Oden, M. (2013) Tuning the shape of mesoporous silica particles by alterations in parameter space: from rods to platelets. *Langmuir,* **29**(44), 13551–13561.

[24] Lin, H.-P. and Mou, C.-Y. (2002) Structural and morphological control of cationic surfactant-templated mesoporous silica. *Accounts of Chemical Research,* **35**(11), 927–935.

[25] Qiao, Z.-A., Zhang, L., Guo, M., Liu, Y., and Huo, Q. (2009) Synthesis of mesoporous silica nanoparticles via controlled hydrolysis and condensation of silicon alkoxide. *Chemistry of Materials,* **21**(16), 3823–3829.

[26] Cihlář, J. (1993) Hydrolysis and polycondensation of ethyl silicates. 1. Effect of pH and catalyst on the hydrolysis and polycondensation of tetraethoxysilane (TEOS). *Colloids and Surfaces A: Physicochemical and Engineering Aspects,* **70**(3), 239–251.

[27] Brinker, C. J. (1988) Hydrolysis and condensation of silicates: effects on structure. *Journal of non-crystalline solids,* **100**(1-3), 31–50.

[28] Schubert, U. (2015) The Sol–Gel Handbook: Synthesis, Characterization, and Applications. *de Chemistry and Fundamentals of the Sol–Gel Process, VCH-Wiley Verlag,*.

[29] Emrie, D. B. (2024) Sol–Gel Synthesis of Nanostructured Mesoporous Silica Powder and Thin Films. *Journal of Nanomaterials,* **2024**(1), 6109770.

[30] Kim, J.-K. and Lawler, D. F. (2005) Characteristics of zeta potential distribution in silica particles. *Bulletin of the Korean Chemical Society,* **26**(7), 1083–1089.

[31] Wan, Y. and Zhao, N. (2007) On the controllable soft-templating approach to mesoporous silicates. *Chemical reviews,* **107**(7), 2821–2860.

[32] Pal, N. and Bhaumik, A. (2013) Soft templating strategies for the synthesis of mesoporous materials: Inorganic, organic–inorganic hybrid and purely organic solids. *Advances in Colloid and Interface Science,* **189-190**, 21–41.

[33] Hoffmann, F., Cornelius, M., Morell, J., and Fröba, M. (2006) Silica-based mesoporous organic–inorganic hybrid materials. *Angewandte Chemie International Edition,* **45**(20), 3216–3251.

[34] Hatton, B., Landskron, K., Whitnall, W., Perovic, D., and Ozin, G. A. (2005) Past, present, and future of periodic mesoporous organosilicas the PMOs. *Accounts of chemical research,* **38**(4), 305–312.

[35] Shigeno, T., Nagao, M., Kimura, T., and Kuroda, K. (2002) Direct silylation of a mesostructured precursor for novel mesoporous silica KSW-2. *Langmuir,* **18**(21), 8102–8107.

[36] Goubert-Renaudin, S., Etienne, M., Brandès, S., Meyer, M., Denat, F., Lebeau, B., and Walcarius, A. (2009) Factors affecting copper (II) binding to multiarmed cyclam-grafted mesoporous silica in aqueous solution. *Langmuir,* **25**(17), 9804–9813.

[37] Goubert-Renaudin, S., Etienne, M., Rousselin, Y., Denat, F., Lebeau, B., and Walcarius, A. (2009) Cyclam-Functionalized Silica-Modified Electrodes for Selective Determination of Cu (II). *Electroanalysis: An International Journal Devoted to Fundamental and Practical Aspects of Electroanalysis,* **21**(3-5), 280–289.

[38] Sharma, V., Agrawal, A., Singh, O., Goyal, R., Sarkar, B., Gopinathan, N., and Gumfekar, S. P. (2022) A comprehensive review on the synthesis techniques of porous materials for gas separation and catalysis. *The Canadian Journal of Chemical Engineering,* **100**(9), 2653–2681.

[39] Danks, A. E., Hall, S. R., and Schnepp, Z. (2016) The evolution of 'sol–gel'chemistry as a technique for materials synthesis. *Materials Horizons,* **3**(2), 91–112.

[40] Trewyn, B. G., Slowing, I. I., Giri, S., Chen, H.-T., and Lin, V. S.-Y. (2007) Synthesis and functionalization of a mesoporous silica nanoparticle based on the sol–gel process and applications in controlled release. *Accounts of chemical research,* **40**(9), 846–853.

[41] Kleitz, F., Marlow, F., Stucky, G. D., and Schüth, F. (2001) Mesoporous silica fibers: Synthesis, internal structure, and growth kinetics. *Chemistry of Materials,* **13**(10), 3587–3595.

[42] Yang, P., Zhao, D., Chmelka, B. F., and Stucky, G. D. (1998) Triblock-copolymer-directed syntheses of large-pore mesoporous silica fibers. *Chemistry of Materials,* **10**(8), 2033–2036.

[43] Vossen, D. L., de Dood, M. J., van Dillen, T., Zijlstra, T., van der Drift, E., Polman, A., and van Blaaderen, A. (2000) Novel method for solution growth of thin silica films from tetraethoxysilane. *Advanced Materials,* **12**(19), 1434–1437.

[44] Walcarius, A., Sibottier, E., Etienne, M., and Ghanbaja, a. (2007) Electrochemically assisted self-assembly of mesoporous silica thin films. *Nature materials,* **6**(8), 602–608.

[45] Innocenzi, P., Martucci, A., Guglielmi, M., Bearzotti, A., and Traversa, E. (2001) Electrical and structural characterisation of mesoporous silica thin films as humidity sensors. *Sensors and Actuators B: Chemical,* **76**(1-3), 299–303.

[46] Laskowska, M., Kityk, I., Dulski, M., Jędryka, J., Wojciechowski, A., Jelonkiewicz, J., Wojtyniak, M., and Laskowski, Ł. (2017) Functionalized mesoporous silica thin films as a tunable nonlinear optical material. *Nanoscale,* **9**(33), 12110–12123.

[47] Benamor, T., Vidal, L., Lebeau, B., and Marichal, C. (2012) Influence of synthesis parameters on the physico-chemical characteristics of SBA-15 type ordered mesoporous silica. *Microporous and mesoporous materials,* **153**, 100–114.

[48] Tripathi, N., Pérez-Sánchez, G., Schaeffer, N., Ray, D., Aswal, V. K., Kuperkar, K., Coutinho, J. A., and Bahadur, P. (2025) Self-Associated Engineering in P123 Micelles Rationalizing the Role of Other Pluronics with Varying Hydrophilicity as a Mixed System. *Langmuir,* **41**(15), 9967–9988.

[49] Chao, M.-C., Chang, C.-H., Lin, H.-P., Tang, C.-Y., and Lin, C.-Y. (2009) Morphological control on SBA-15 mesoporous silicas via a slow self-assembling rate. *Journal of materials science,* **44**, 6453–6462.

[50] Pirez, C., Morin, J.-C., Manayil, J. C., Lee, A. F., and Wilson, K. (2018) Sol-gel synthesis of SBA-15: Impact of HCl on surface chemistry. *Microporous and Mesoporous Materials,* **271**, 196–202.

[51] Wan, Y., Shi, Y., and Zhao, D. (2007) Designed synthesis of mesoporous solids via nonionic-surfactant-templating approach. *Chemical Communications,* (9), 897–926.

[52] Benamor, T., Vidal, L., Lebeau, B., and Marichal, C. (2012) Influence of synthesis parameters on the physico-chemical characteristics of SBA-15 type ordered mesoporous silica. *Microporous and Mesoporous Materials,* **153**, 100–114.

[53] Zhao, D., Feng, J., Huo, Q., Melosh, N., Fredrickson, G. H., Chmelka, B. F., and Stucky, G. D. (1998) Triblock copolymer syntheses of mesoporous silica with periodic 50 to 300 angstrom pores. *science,* **279**(5350), 548–552.

[54] Grosso, D., Balkenende, A., Albouy, P., Ayral, A., Amenitsch, H., and Babonneau, F. (2001) Two-dimensional hexagonal mesoporous silica thin films prepared from

block copolymers: Detailed characterization and formation mechanism. *Chemistry of Materials,* **13**(5), 1848–1856.

[55] de AA Soler-Illia, G. J., Crepaldi, E. L., Grosso, D., and Sanchez, C. (2003) Block copolymer-templated mesoporous oxides. *Current Opinion in Colloid & Interface Science,* **8**(1), 109–126.

[56] Grosso, D., Babonneau, F., Albouy, P.-A., Amenitsch, H., Balkenende, A., Brunet-Bruneau, A., and Rivory, J. (2002) An in situ study of mesostructured CTAB- silica film formation during dip coating using time-resolved SAXS and interferometry measurements. *Chemistry of Materials,* **14**(2), 931–939.

[57] Grosso, D., Cagnol, F., Soler-Illia, G. d. A., Crepaldi, E. L., Amenitsch, H., Brunet-Bruneau, A., Bourgeois, A., and Sanchez, C. (2004) Fundamentals of mesostructuring through evaporation-induced self-assembly. *Advanced Functional Materials,* **14**(4), 309–322.

[58] Cagnol, F., Grosso, D., de AA Soler-Illia, G. J., Crepaldi, E. L., Babonneau, F., Amenitsch, H., and Sanchez, C. (2003) Humidity-controlled mesostructuration in CTAB-templated silica thin film processing. The existence of a modulable steady state. *Journal of Materials Chemistry,* **13**(1), 61–66.

[59] Alberius, P. C., Frindell, K. L., Hayward, R. C., Kramer, E. J., Stucky, G. D., and Chmelka, B. F. (2002) General predictive syntheses of cubic, hexagonal, and lamellar silica and titania mesostructured thin films. *Chemistry of Materials,* **14**(8), 3284–3294.

[60] Lee, J. E., Lee, N., Kim, T., Kim, J., and Hyeon, T. (2011) Multifunctional mesoporous silica nanocomposite nanoparticles for theranostic applications. *Accounts of chemical research,* **44**(10), 893–902.

[61] Xu, B., Li, S., Shi, R., and Liu, H. (2023) Multifunctional mesoporous silica nanoparticles for biomedical applications. *Signal transduction and targeted therapy,* **8**(1), 435.

[62] Bharti, C., Nagaich, U., Pal, A. K., and Gulati, N. (2015) Mesoporous silica nanoparticles in target drug delivery system: A review. *International journal of pharmaceutical investigation,* **5**(3), 124.

[63] Xue, K., Mo, Y., Long, B., Wei, W., Shan, C., Guo, S., and Niu, L. (2022) Single-atom catalysts supported on ordered porous materials: Synthetic strategies and applications. *InfoMat,* **4**(6), e12296.

[64] Yu, X. and Williams, C. T. (2022) Recent advances in the applications of mesoporous silica in heterogeneous catalysis. *Catalysis science & technology,* **12**(19), 5765–5794.

[65] Li, C. M., Wang, X. P., Jiao, Z. H., Zhang, Y. S., Yin, X. B., Cui, X. M., and Wei, Y. Z. (2019) Functionalized porous silica-based nano/micro particles for environmental remediation of hazard ions. *Nanomaterials,* **9**(2), 247.

[66] Scott, B. J., Wirnsberger, G., and Stucky, G. D. (2001) Mesoporous and mesostructured materials for optical applications. *Chemistry of materials,* **13**(10), 3140–3150.

[67] Laskowski, Ł., Laskowska, M., Vila, N., Schabikowski, M., and Walcarius, A. (2019) Mesoporous silica-based materials for electronics-oriented applications. *Molecules,* **24**(13), 2395.

[68] Lakowicz, J. R. and Lakowicz, J. R. (1999) Introduction to fluorescence. *Principles of fluorescence spectroscopy,* pp. 1–23.

[69] Stokes, G. G. (1852) XXX. On the change of refrangibility of light. *Philosophical transactions of the Royal Society of London,* (142), 463–562.

[70] BLOEMBERGEN, N. (2023) Nonlinear optics and spectroscopy. *PHYSIOLOGY OR MEDICINE LITERATURE PEACE ECONOMIC SCIENCES,* p. 12.

[71] Duboisset, J., Boulanger, B., Brasselet, S., Segonds, P., and Zyss, J. (2025) Nonlinear Optics Through the Field Tensor Formalism. *Laser & Photonics Reviews,* **19**(2), 2400411.

[72] Franken, e. P., Hill, A. E., Peters, C., and Weinreich, G. (1961) Generation of optical harmonics. *Physical review letters,* **7**(4), 118.

[73] Boyd, R. W. (2008) Chapter 1 - The Nonlinear Optical Susceptibility. In Boyd, R. W., (ed.), *Nonlinear Optics (Third Edition)*, pp. 1–67 Academic Press Burlington third edition edition.

[74] Boyd, R. W. (2020) Chapter 1 - The Nonlinear Optical Susceptibility. In Boyd, R. W., (ed.), *Nonlinear Optics (Fourth Edition)*, pp. 1–64 Academic Press fourth edition edition.

[75] Morozov, B. and Aĭ Optical rectification effect and its applications.

[76] Boyd, R. W., Gaeta, A. L., and Giese, E. (2008) Nonlinear optics. In *Springer Handbook of Atomic, Molecular, and Optical Physics* pp. 1097–1110 Springer.

[77] Polanik, M. and Hirlinger-Alexander, J. (2016) Generation of ultraviolet laser light by frequency tripling of a high-power infrared optically pumped semiconductor disk laser. *Annual Report (Institute of Optoelectronics, Ulm University, 2016), https://www. uni-ulm. de/fileadmin/website_ uni_ ulm/iui. inst,* **140**.

[78] Maiuri, M., Garavelli, M., and Cerullo, G. (2019) Ultrafast spectroscopy: State of the art and open challenges. *Journal of the American Chemical Society,* **142**(1), 3–15.

[79] Weigelin, B., Bakker, G.-J., and Friedl, P. (2016) Third harmonic generation microscopy of cells and tissue organization. *Journal of Cell Science,* **129**(2), 245–255.

[80] Müller, Squier, and Brakenhoff (1998) 3D microscopy of transparent objects using third-harmonic generation. *Journal of microscopy,* **191**(3), 266–274.

[81] Xu, J., Semin, S., Rasing, T., and Rowan, A. E. (2015) Organized chromophoric assemblies for nonlinear optical materials: towards (sub) wavelength scale architectures. *Small,* **11**(9-10), 1113–1129.

[82] Fan, H., Ye, N., and Luo, M. (2023) New Functional Groups Design toward High Performance Ultraviolet Nonlinear Optical Materials. *Accounts of Chemical Research,* **56**(21), 3099–3109.

[83] Chen, X. and Ok, K. M. (2020) Recent Advances in Oxide-based Nonlinear Optical Materials with Wide Infrared Transparency Beyond 6 μm. *Chemistry–An Asian Journal,* **15**(22), 3709–3716.

[84] Gallais, L. and Commandré, M. (2014) Laser-induced damage thresholds of bulk and coating optical materials at 1030 nm, 500 fs. *Applied optics,* **53**(4), A186–A196.

[85] Zhou, W. and Guo, S.-P. (2024) Rational Design of Novel Promising Infrared Nonlinear Optical Materials: Structural Chemistry and Balanced Performances. *Accounts of Chemical Research,* pp. 11540–11543.

[86] Abudurusuli, A., Li, J., and Pan, S. (2021) A review on the recently developed promising infrared nonlinear optical materials. *Dalton Transactions,* **50**(9), 3155–3160.

[87] Chen, J., Hu, C.-L., Kong, F., and Mao, J.-G. (2021) High-performance second-harmonic-generation (SHG) materials: new developments and new strategies. *Accounts of chemical research,* **54**(12), 2775–2783.

[88] Aslam, H. Z., Doane, J. T., Yeung, M. T., and Akopov, G. (2023) Advances in solid-state nonlinear optical materials: from fundamentals to applications. *ACS Applied Optical Materials,* **1**(12), 1898–1921.

[89] Marble, C. B. and Yakovlev, V. V. (2020) Biomedical optics applications of advanced lasers and nonlinear optics. *Journal of Biomedical Optics,* **25**(4), 040902–040902.

[90] Carneiro, G., Vargas, H., and Sampaio, J. (2019) Thermo-optical and structural properties of barium aluminoborate glasses. *Journal of Alloys and Compounds,* **777**, 1327–1333.

[91] Halasyamani, P. S. and Zhang, W. (2017) Viewpoint: Inorganic Materials for UV and Deep-UV Nonlinear-Optical Applications. *Inorganic Chemistry,* **56**(20), 12077–12085 PMID: 28949525.

[92] Shen, Y. (1989) Surface properties probed by second-harmonic and sum-frequency generation. *Nature,* **337**(6207), 519–525.

[93] El Ouazzani, H., Iliopoulos, K., Pranaitis, M., Krupka, O., Smokal, V., Kolendo, A., and Sahraoui, B. (2011) Second- and Third-Order Nonlinearities of Novel PushPull Azobenzene Polymers. *The Journal of Physical Chemistry B,* **115**(9), 1944–1949 PMID: 21323373.

[94] Janjua, M. R. S. A. (2017) First theoretical framework of di-substituted donor moieties of triphenylamine and carbazole for NLO properties: quantum paradigms of interactive molecular computation. *Molecular Simulation,* **43**(18), 1539–1545.

[95] Zhang, D., Chen, W., Zou, J., and Luo, J. (2021) Critical role of non-classical intermolecular hydrogen bonding in affecting the π–π stacking and nonlinear optical properties of tricyanofuran-based push–pull heptamethines. *Chemistry of Materials,* **33**(10), 3702–3711.

[96] Khan, M. U., Ibrahim, M., Khalid, M., Jamil, S., Al-Saadi, A. A., and Janjua, M. R. S. A. (2019) Quantum chemical designing of indolo [3, 2, 1-jk] carbazole-based dyes for highly efficient nonlinear optical properties. *Chemical Physics Letters,* **719**, 59–66.

[97] Muhammad, S., Kumar, S., Koh, J., Saravanabhavan, M., Ayub, K., and Chaudhary, M. (2018) Synthesis, characterisation, optical and nonlinear optical properties of thiazole and benzothiazole derivatives: a dual approach. *Molecular simulation,* **44**(15), 1191–1199.

[98] Zhang, C. (1999) Novel phenylpolyene-bridged second-order nonlinear optical chromophores and new thermally stable polyurethanes for electro-optic applications, University of Southern California, .

[99] Liu, J., Zhang, M., Gao, W., Fedorchuk, A., and Kityk, I. (2018) Synthesis and nonlinear optical properties of novel conjugated small molecules based on indole donor. *Journal of Molecular Structure,* **1165**, 223–227.

[100] Özarslan, A., Çakmaz, D., Erol, F., Şenöz, H., Seferoğlu, N., Barsella, A., and Seferoğlu, Z. (2021) Synthesis and investigation of photophysical, NLO and thermal properties of D-π-A-π-D dyes. *Journal of Molecular Structure,* **1229**, 129583.

[101] Al-Busaidi, I. J., Haque, A., Al Rasbi, N. K., and Khan, M. S. (2019) Phenothiazine-based derivatives for optoelectronic applications: A review. *Synthetic Metals,* **257**, 116189.

[102] Anandan, S., Manoharan, S., Narendran, N. S., Girisun, T. S., and Asiri, A. (2018) Donor-acceptor substituted thiophene dyes for enhanced nonlinear optical limiting. *Optical Materials,* **85**, 18–25.

[103] Wazzan, N. (2020) MP2 calculations of the effect of the -conjugation on the electronic and nonlinear optical properties of para-nitroaniline (pNA) derivatives. *Optical Materials,* **110**, 110465.

[104] Muhammad, S., Al-Sehemi, A. G., Irfan, A., and Chaudhry, A. R. (2016) Tuning the push–pull configuration for efficient second-order nonlinear optical properties in some chalcone derivatives. *Journal of Molecular Graphics and Modelling,* **68**, 95–105.

[105] Xu, L., Lin, W., Huang, B., Zhang, J., Long, X., Zhang, W., and Zhang, Q. (2021) The design strategies and applications for organic multi-branched two-photon absorption chromophores with novel cores and branches: a recent review. *Journal of Materials Chemistry C,* **9**(5), 1520–1536.

[106] Terenziani, F., Le Droumaguet, C., Mongin, O., Katan, C., and Blanchard-Desce, M. (2006) Branching of substituted push-pull polyenes for enhanced two-photon absorption.. *Nonlinear optics, quantum optics,* **35**, 69–81.

[107] Liu, S., Lin, P., Wu, M., Lan, Z.-A., Zhuzhang, H., Han, M., Fan, Y., Chen, X., Wang, X., Li, Q., et al. (2022) Organic dyes with multi-branched structures for highly efficient photocatalytic hydrogen evolution under visible-light irradiation. *Applied Catalysis B: Environmental,* **309**, 121257.

[108] Combellas, C., Petit, M. A., Thiébault, A., Froyer, G., and Bosc, D. (1992) New comb-like polymers with prospective nonlinear optical properties. *Die Makromolekulare Chemie: Macromolecular Chemistry and Physics,* **193**(9), 2445–2451.

[109] Combellas, C., Kajzar, F., Mathey, G., Petit, M. A., and Thiébault, A. (2000) Zwitterionic polymers for nonlinear optics. *Chemical Physics,* **252**(1-2), 165–177.

[110] Kay, A., Woolhouse, A., Gainsford, G., Haskell, T., Wyss, C., Giffin, S., McKinnie, I., and Barnes, T. (2001) Simple zwitterionic merocyanines as potential NLO chromophores. *Journal of materials chemistry,* **11**(9), 2271–2281.

[111] Wu, A., Gao, Y., and Zheng, L. (2019) Zwitterionic amphiphiles: their aggregation behavior and applications. *Green Chemistry,* **21**(16), 4290–4312.

[112] Pan, F., Knöpfle, G., Bosshard, C., Follonier, S., Spreiter, R., Wong, M., and Günter, P. (1996) Electro-optic properties of the organic salt 4-N, N-dimethylamino-4-N-methyl-stilbazolium tosylate. *Applied Physics Letters,* **69**(1), 13–15.

[113] Kannan, S., Sekar, A., and Sivaperuman, K. (2020) Effects of the molecular structure on the second-order nonlinear optical properties of stilbazolium derivative single crystals: a review. *Journal of Materials Chemistry C,* **8**(47), 16668–16690.

[114] Zade, S. S., Zamoshchik, N., and Bendikov, M. (2011) From short conjugated oligomers to conjugated polymers. Lessons from studies on long conjugated oligomers. *Accounts of Chemical Research,* **44**(1), 14–24.

[115] Kirtman, B. and Champagne, B. (1997) Nonlinear optical properties of quasilinear conjugated oligomers, polymers and organic molecules. *International Reviews in Physical Chemistry,* **16**(4), 389–420.

[116] Bibi, A., Muhammad, S., UrRehman, S., Bibi, S., Bashir, S., Ayub, K., Adnan, M., and Khalid, M. (2021) Chemically modified quinoidal oligothiophenes for enhanced linear and third-order nonlinear optical properties. *ACS omega,* **6**(38), 24602–24613.

[117] Aragó, J., Viruela, P. M., Gierschner, J., Ortí, E., and Milián-Medina, B. (2011) Oligothienoacenes versus oligothiophenes: impact of ring fusion on the optical properties. *Physical Chemistry Chemical Physics,* **13**(4), 1457–1465.

[118] Martin, S., Bradley, D., Lane, P., Mellor, H., and Burn, P. (1999) Linear and nonlinear optical properties of the conjugated polymers PPV and MEH-PPV. *Physical Review B,* **59**(23), 15133.

[119] Agrawal, G. P., Cojan, C., and Flytzanis, C. (1978) Nonlinear optical properties of one-dimensional semiconductors and conjugated polymers. *Physical Review B,* **17**(2), 776.

[120] Nath, S., Puthukkudi, A., Mohapatra, J., and Biswal, B. P. (2023) Covalent Organic Frameworks as Emerging Nonlinear Optical Materials. *Angewandte Chemie International Edition,* **62**(18), e202218974.

[121] Li, C., Qian, G., and Cui, Y. (2024) Metal–organic frameworks for nonlinear optics and lasing. *Information & Functional Materials,* **1**(2), 125–159.

[122] Zhang, L., Li, H., Yang, Y., Yang, D., Cui, Y., and Qian, G. (2022) Aligned chromophores in a host–guest MOF crystal for switchable polarized nonlinear optical response. *Journal of Materials Chemistry C,* **10**(40), 14915–14920.

[123] Mingabudinova, L., Vinogradov, V., Milichko, V., Hey-Hawkins, E., and Vinogradov, A. (2016) Metal–organic frameworks as competitive materials for non-linear optics. *Chemical Society Reviews,* **45**(19), 5408–5431.

[124] Medishetty, R., Zaręba, J. K., Mayer, D., Samoć, M., and Fischer, R. A. (2017) Nonlinear optical properties, upconversion and lasing in metal–organic frameworks. *Chemical Society Reviews,* **46**(16), 4976–5004.

[125] Cui, Y., Qian, G., Chen, L., Wang, Z., and Wang, M. (2008) Second-order nonlinear optical properties of cross-linked silica films prepared through sol–gel process. *Thin solid films,* **516**(16), 5483–5487.

[126] Cui, Y., Li, B., Yu, C., Yu, J., Gao, J., Yan, M., Chen, G., Wang, Z., and Qian, G. (2009) Synthesis and NLO properties of hybrid inorganic–organic films containing thiophene ring. *Thin Solid Films,* **517**(17), 5075–5078.

[127] Wang, S., Zhao, L., Sun, J., Cui, Z., and Zhang, D. (2011) Preparation of stable second-order nonlinear optical films by sol–gel technique. *Polymers for Advanced Technologies,* **22**(5), 759–762.

[128] Cinteza, L.-O. and Marinescu, M. (2018) Synthesis and nonlinear studies on selected organic compounds in nanostructured thin films. In *Advanced Surface Engineering Research* pp. 1–23 IntechOpen London.

[129] Ji, S., Li, Z., Zhou, X., Cao, M., Dai, D., Zhang, R., Li, S., and Ye, C. (2003) Silica-based hybrid nonlinear optical chromophore-trapping film prepared by sol-gel polymerization. *Polymers for Advanced Technologies,* **14**(3-5), 254–259.

[130] Parola, S., Julián-López, B., Carlos, L. D., and Sanchez, C. (2016) Optical properties of hybrid organic-inorganic materials and their applications. *Advanced Functional Materials,* **26**(36), 6506–6544.

[131] Gago, S., Fonseca, I. M., and Parola, A. J. (2013) Hybrid mesoporous silica grafted with photoisomerizable 2-hydroxychalcones. *Microporous and mesoporous materials,* **180**, 40–47.

[132] Taboukhat, S., Kichou, N., Fillaut, J.-L., Alévêque, O., Waszkowska, K., Zawadzka, A., El-Ghayoury, A., Migalska-Zalas, A., and Sahraoui, B. (2020) Transition metals induce control of enhanced NLO properties of functionalized organometallic complexes under laser modulations. *Scientific reports,* **10**(1), 15292.

[133] El Karout, H., Shchur, Y., Andrushchak, A., Sahraoui, B., Wielgosz, R., Kityk, O., Jędryka, J., Slyvka, Y., and Kityk, A. V. (2023) Second harmonic generation on crystalline organic nanoclusters under extreme nanoconfinement in functionalized silica–benzil composites. *Scientific Reports,* **13**(1), 9943.

[134] S, S. N., S, R., S, S., and Ramakrishna, D. (2023) Metal-centric organic compounds: boon to third-order nonlinear optical applications. *Reviews in Inorganic Chemistry,*.

[135] Van Der Voort, P., Esquivel, D., De Canck, E., Goethals, F., Van Driessche, I., and Romero-Salguero, F. J. (2013) Periodic mesoporous organosilicas: from simple to complex bridges; a comprehensive overview of functions, morphologies and applications. *Chemical Society Reviews,* **42**(9), 3913–3955.

[136] Du, X., Li, X., Xiong, L., Zhang, X., Kleitz, F., and Qiao, S. Z. (2016) Mesoporous silica nanoparticles with organo-bridged silsesquioxane framework as innovative platforms for bioimaging and therapeutic agent delivery. *Biomaterials,* **91**, 90–127.

[137] Sanchez, C., Lebeau, B., Chaput, F., and Boilot, J.-P. (2003) Optical properties of functional hybrid organic–inorganic nanocomposites. *Advanced Materials,* **15**(23), 1969–1994.

[138] Laskowska, M., Pastukh, O., Fedorchuk, A., Schabikowski, M., Kowalczyk, P., Zalasiński, M., and Laskowski, Ł. (2020) Nanostructured Silica with Anchoring Units: The 2D Solid Solvent for Molecules and Metal Ions. *International Journal of Molecular Sciences,* **21**(21), 8137.

[139] Fedorchuk, A. and Laskowska, M. (2020) The concept of 2D solid solvents: a new view on functionalized silica-based materials. *Materials Proceedings,* **4**(1), 66.

[140] Li, Y. and Yan, B. (2010) Lanthanide (Tb3+, Eu3+) functionalized MCM-41 through modified meta-aminobenzoic acid linkage: Covalently bonding assembly, physical characterization and photoluminescence. *Microporous and Mesoporous Materials,* **128**(1), 62–70.

[141] Buso, D., Falcaro, P., Costacurta, S., Guglielmi, M., Martucci, A., Innocenzi, P., Malfatti, L., Bello, V., Mattei, G., Sada, C., et al. (2005) PbS-doped mesostructured silica films with high optical nonlinearity. *Chemistry of materials,* **17**(20), 4965–4970.

[142] Wark, M., Wellmann, H., and Rathousky, J. (2004) Homogeneously distributed CdS and CdSe nanoparticles in thin films of mesoporous silica. *Thin Solid Films,* **458**(1-2), 20–25.

[143] Winkler, H., Birkner, A., Hagen, V., Wolf, I., Schmechel, R., Seggern, H. v., and Fischer, R. A. (1999) Quantum-Confined Gallium Nitride in MCM-41. *Advanced materials,* **11**(17), 1444–1448.

[144] Lu, Q., Cui, F., Dong, C., Hua, Z., and Shi, J. (2011) Gold nanoparticles incorporated mesoporous silica thin films of varied gold contents and their well-tuned third-order optical nonlinearities. *Optical Materials,* **33**(8), 1266–1271.

[145] Riehl, D., Chaput, F., Lévy, Y., Boilot, J.-P., Kajzar, F., and Chollet, P.-A. (1995) Second-order optical nonlinearities of azo chromophores covalently attached to a sol-gel matrix. *Chemical Physics Letters,* **245**(1), 36–40.

[146] Yang, Z., Xu, C., Wu, B., Dalton, L. R., Kalluri, S., Steier, W. H., Shi, Y., and Bechtel, J. H. (1994) Anchoring both ends of chromophores into sol-gel networks for large and stable second-order optical nonlinearities. *Chemistry of materials,* **6**(10), 1899–1901.

[147] Jarmolińska, S., Feliczak-Guzik, A., and Nowak, I. (2020) Synthesis, characterization and use of mesoporous silicas of the following types SBA-1, SBA-2, HMM-1 and HMM-2. *Materials,* **13**(19), 4385.

[148] Asefa, T. and Tao, Z. (2012) Mesoporous silica and organosilica materials—Review of their synthesis and organic functionalization. *Canadian Journal of Chemistry,* **90**(12), 1015–1031.

[149] Corriu, R., Datas, L., Guari, Y., Mehdi, A., Reyé, C., and Thieuleux, C. (2001) Ordered SBA-15 mesoporous silica containing phosphonic acid groups prepared by a direct synthetic approach. *Chemical Communications,* (8), 763–764 Cited by: 94.

[150] Laskowski, L. and Laskowska, M. (2014) Functionalization of SBA-15 mesoporous silica by Cu-phosphonate units: Probing of synthesis route. *Journal of Solid State Chemistry,* **220**, 221–226.

[151] Egerton, R. (2014) Choice of operating voltage for a transmission electron microscope. *Ultramicroscopy,* **145**, 85–93 Low-Voltage Electron Microscopy.

[152] Moehl, G. E., Nasir, T., Han, Y., Noori, Y. J., Huang, R., Beanland, R., Bartlett, P. N., and Hector, A. L. (2022) AC-assisted deposition of aggregate free silica films with vertical pore structure. *Nanoscale,* **14**(14), 5404–5411.

[153] Newbury, D. E. and Ritchie, N. W. (2013) Elemental mapping of microstructures by scanning electron microscopy-energy dispersive X-ray spectrometry (SEM-EDS): extraordinary advances with the silicon drift detector (SDD). *Journal of Analytical Atomic Spectrometry,* **28**(7), 973–988.

[154] Thommes, M., Kaneko, K., Neimark, A. V., Olivier, J. P., Rodriguez-Reinoso, F., Rouquerol, J., and Sing, K. S. (2015) Physisorption of gases, with special reference to the evaluation of surface area and pore size distribution (IUPAC Technical Report). *Pure and applied chemistry,* **87**(9-10), 1051–1069.

[155] Alvarez-Fernandez, A., Reid, B., Fornerod, M. J., Taylor, A., Divitini, G., and Guldin, S. (2020) Structural characterization of mesoporous thin film architectures: a tutorial overview. *ACS applied materials & interfaces,* **12**(5), 5195–5208.

[156] Santoro, G. and Yu, S. (2017) Grazing Incidence Small Angle X-Ray Scattering as a Tool. *X-ray Scattering,* p. 29.

[157] Gibaud, A., Dourdain, S., and Vignaud, G. (2006) Analysis of mesoporous thin films by X-ray reflectivity, optical reflectivity and grazing incidence small angle X-ray scattering. *Applied Surface Science,* **253**(1), 3–11 Proceedings of the E-MRS 2005 Spring Meeting Symposium P: Current trends in optical and X-ray metrology of advanced materials for nanoscale devices.

[158] Dourdain, S., Bardeau, J.-F., Colas, M., Smarsly, B., Mehdi, A., Ocko, B. M., and Gibaud, A. (03, 2005) Determination by x-ray reflectivity and small angle x-ray scattering of the porous properties of mesoporous silica thin films. *Applied Physics Letters,* **86**(11), 113108.

[159] Jones, R. R., Hooper, D. C., Zhang, L., Wolverson, D., and Valev, V. K. (2019) Raman techniques: fundamentals and frontiers. *Nanoscale research letters,* **14**, 1–34.

[160] Wolverson, D. (2008) Raman spectroscopy. In *Characterization of semiconductor heterostructures and nanostructures* pp. 249–288 Elsevier.

[161] Raman, C. V. and Krishnan, K. S. (1928) A new type of secondary radiation. *Nature,* **121**(3048), 501–502.

[162] Andrews, D. H. (1930) The relation between the Raman spectra and the structure of organic molecules. *Physical Review,* **36**(3), 544.

[163] Borodko, Y., Ager, J. W., Marti, G. E., Song, H., Niesz, K., and Somorjai, G. A. (2005) Structure sensitivity of vibrational spectra of mesoporous silica SBA-15 and Pt/SBA-15. *The Journal of Physical Chemistry B,* **109**(37), 17386–17390.

[164] Montejo, M., Ureña, F. P., Márquez, F., Ignatyev, I., and González, J. L. (2005) Vibrational spectrum of methoxytrimethylsilane. *Journal of molecular structure,* **744**, 331–338.

[165] Ball, D., Goggin, P., McKean, D., and Woodward, L. (1960) Infra-red and Raman spectra of dimethyl and trimethyl silanes and some deuterated derivatives. *Spectrochimica Acta,* **16**(11-12), 1358–1367.

[166] Eshelman, E., Daly, M., Slater, G., Dietrich, P., and Gravel, J.-F. (2014) An ultraviolet Raman wavelength for the in-situ analysis of organic compounds relevant to astrobiology. *Planetary and Space Science,* **93**, 65–70.

[167] Schneider, B., Štokr, J., Schmidt, P., Mihailov, M., Dirlikov, S., and Peeva, N. (1979) Stretching and deformation vibrations of CH2, C (CH3) and O (CH3) groups of poly (methyl methacrylate). *Polymer,* **20**(6), 705–712.

[168] El Houbbadi, S., Laskowska, M., Walcarius, A., Doskocz, M., Maximenko, A., Olejniczak, Z., and Laskowski, L. (October, 2024) Revealing the molecular structure of copper phosphonate groups anchored inside SBA-15 silica channels: Theoretical and experimental study. *Applied Surface Science,* **669**, 160425.

[169] Calvin, S. (2024) XAFS for Everyone, CRC press, .

[170] Oshina, I. and Spigulis, J. (2021) Beer–Lambert law for optical tissue diagnostics: current state of the art and the main limitations. *Journal of biomedical optics,* **26**(10), 100901–100901.

[171] Ravel, B. (2005) A practical introduction to multiple scattering theory. *Journal of Alloys and compounds,* **401**(1-2), 118–126.

[172] Gaur, A. and Shrivastava, B. (2015) Speciation using X-ray absorption fine structure (XAFS). *Review Journal of Chemistry,* **5**, 361–398.

[173] Baker, M. L., Mara, M. W., Yan, J. J., Hodgson, K. O., Hedman, B., and Solomon, E. I. (2017) K-and L-edge X-ray absorption spectroscopy (XAS) and resonant inelastic X-ray scattering (RIXS) determination of differential orbital covalency (DOC) of transition metal sites. *Coordination Chemistry Reviews,* **345**, 182–208.

[174] Sayers, D. E., Stern, E. A., and Lytle, F. W. (1971) New technique for investigating noncrystalline structures: Fourier analysis of the extended x-ray—absorption fine structure. *Physical review letters,* **27**(18), 1204.

[175] Trevorah, R. M., Chantler, C. T., and Schalken, M. J. (2019) Solving self-absorption in fluorescence. *IUCrJ,* **6**(4), 586–602.

[176] Shimizu, K.-i., Maeshima, H., Yoshida, H., Satsuma, A., and Hattori, T. (2001) Ligand field effect on the chemical shift in XANES spectra of Cu (II) compounds. *Physical Chemistry Chemical Physics,* **3**(5), 862–866.

[177] Zhang, R. and McEwen, J.-S. (2018) Local environment sensitivity of the Cu k-edge XANES features in Cu-SSZ-13: analysis from first-principles. *The Journal of Physical Chemistry Letters,* **9**(11), 3035–3042.

[178] Rehr, J. J. and Albers, R. C. (2000) Theoretical approaches to x-ray absorption fine structure. *Reviews of modern physics,* **72**(3), 621.

[179] Ravel, B. and Newville, M. (2005) ATHENA and ARTEMIS: interactive graphical data analysis using IFEFFIT. *Physica Scripta,* **2005**(T115), 1007.

[180] Ravel, B. and Newville, M. (Jul, 2005) *ATHENA*, *ARTEMIS*, *HEPHAESTUS*: data analysis for X-ray absorption spectroscopy using *IFEFFIT*. *Journal of Synchrotron Radiation,* **12**(4), 537–541.

[181] Stern, E., Sayers, D., and Lytle, F. (1975) Extended x-ray-absorption fine-structure technique. III. Determination of physical parameters. *Physical Review B,* **11**(12), 4836.

[182] Ravel, B. (2016) Quantitative EXAFS analysis. *X-Ray Absorption and X-Ray Emission Spectroscopy: Theory and Applications,* pp. 281–302.

[183] Penner-Hahn, J. E. et al. (2003) X-ray absorption spectroscopy. *Comprehensive Coordination Chemistry II,* **2**, 159–186.

[184] Yamamoto, T. (2008) Assignment of pre-edge peaks in K-edge x-ray absorption spectra of 3d transition metal compounds: electric dipole or quadrupole?. *X-Ray Spectrometry: An International Journal,* **37**(6), 572–584.

[185] Sano, M., Komorita, S., and Yamatera, H. (1992) XANES spectra of copper (II) complexes: correlation of the intensity of the 1s. fwdarw. 3d transition and the shape of the complex. *Inorganic Chemistry,* **31**(3), 459–463.

[186] De Groot, F., Vankó, G., and Glatzel, P. (2009) The 1s x-ray absorption pre-edge structures in transition metal oxides. *Journal of Physics: Condensed Matter,* **21**(10), 104207.

[187] de Groot, F., Vankó, G., and Glatzel, P. (February, 2009) The 1s x-ray absorption pre-edge structures in transition metal oxides. *Journal of Physics: Condensed Matter,* **21**(10), 104207.

[188] Sano, M., Komorita, S., and Yamatera, H. (1992) XANES spectra of copper (II) complexes: correlation of the intensity of the 1s. fwdarw. 3d transition and the shape of the complex. *Inorganic Chemistry,* **31**(3), 459–463.

[189] Palladino, L., Della Longa, S., Reale, A., Belli, M., Scafati, A., Onori, G., and Santucci, A. (1993) X-ray absorption near edge structure (XANES) of Cu (II)–ATP and related compounds in solution: Quantitative determination of the distortion of the Cu site. *The Journal of Chemical Physics,* **98**(4), 2720–2726.

[190] Onori, G., Santucci, A., Belli, A. S. M., Della Longa, S., Bianconi, A., and Palladino, L. (1988) Cu K-edge XANES of Cu (II) ions in aqueous solution: a measure of the axial ligand distances. *Chemical Physics Letters,* **149**(3), 289–294.

[191] Hahn, J. E., Scott, R. A., Hodgson, K. O., Doniach, S., Desjardins, S. R., and Solomon, E. I. (1982) Observation of an electric quadrupole transition in the X-ray absorption spectrum of a Cu (II) complex. *Chemical Physics Letters,* **88**(6), 595–598.

[192] Tomson, N. C., Williams, K. D., Dai, X., Sproules, S., DeBeer, S., Warren, T. H., and Wieghardt, K. (2015) Re-evaluating the Cu K pre-edge XAS transition in complexes with covalent metal–ligand interactions. *Chemical science,* **6**(4), 2474–2487.

[193] Stoyanov, E., Langenhorst, F., and Steinle-Neumann, G. (2007) The effect of valence state and site geometry on Ti L 3, 2 and OK electron energy-loss spectra of TixOy phases. *American Mineralogist,* **92**(4), 577–586.

[194] Gaur, A., Nitin Nair, N., Shrivastava, B., Das, B., Chakrabortty, M., Jha, S., and Bhattacharyya, D. (2018) Study of distorted octahedral structure in 3d transition metal complexes using XAFS. *Chemical Physics Letters,* **692**, 382–387.

[195] Kosugi, N., Yokoyama, T., Asakura, K., and Kuroda, H. (1984) Polarized Cu K-edge XANES of square planar CuCl42- ion. Experimental and theoretical evidence for shake-down phenomena. *Chemical Physics,* **91**(2), 249–256.

[196] Shadle, S. E., Penner-Hahn, J. E., Schugar, H. J., Hedman, B., Hodgson, K. O., and Solomon, E. I. (1993) X-ray absorption spectroscopic studies of the blue copper site: metal and ligand K-edge studies to probe the origin of the EPR hyperfine splitting in plastocyanin. *Journal of the American Chemical Society,* **115**(2), 767–776.

[197] Choy, J.-H., Yoon, J.-B., and Jung, H. (2002) Polarization-dependent X-ray absorption spectroscopic study of [Cu (cyclam)] 2+-intercalated saponite. *The Journal of Physical Chemistry B,* **106**(43), 11120–11126.

[198] Garcia, J., Benfatto, M., Natoli, C., Bianconi, A., Fontaine, A., and Tolentino, H. (1989) The quantitative Jahn-Teller distortion of the Cu2+ site in aqueous solution by XANES spectroscopy. *Chemical Physics,* **132**(1-2), 295–302.

[199] Gaur, A., Klysubun, W., Joshi, S., Soni, B., Shrivastava, B., Prasad, J., and Srivastava, K. (2016) XAFS study of copper (II) diethylenetriamine complexes having different coordination geometries. In *Journal of Physics: Conference Series* IOP Publishing Vol. 712, p. 012084.

[200] Sarangi, R. (2013) X-ray absorption near-edge spectroscopy in bioinorganic chemistry: Application to M–O2 systems. *Coordination chemistry reviews,* **257**(2), 459–472.

[201] Hesterberg, D., McNulty, I., and Thieme, J. (2017) Speciation of soil phosphorus assessed by XANES spectroscopy at different spatial scales. *Journal of Environmental Quality,* **46**(6), 1190–1197.

[202] George, G. N. (1993) X-ray absorption spectroscopy of light elements in biological systems. *Current Opinion in Structural Biology,* **3**(5), 780–784.

[203] Gillespie, J. A., Dodds, D. L., and Kamer, P. C. (2010) Rational design of diphosphorus ligands–a route to superior catalysts. *Dalton Transactions,* **39**(11), 2751–2764.

[204] Tofoni, A., Tavani, F., Persson, I., and D'Angelo, P. (2023) P K-Edge XANES calculations of mineral standards: Exploring the potential of theoretical methods in the analysis of phosphorus speciation. *Inorganic Chemistry,* **62**(28), 11188–11198.

[205] Wibowo, R. E., Garcia-Diez, R., van der Merwe, M., Duarte-Ruiz, D., Ha, Y., Félix, R., Efimenko, A., Bystron, T., Prokop, M., Wilks, R. G., Bouzek, K., Yang, W., Cocchi, C., and Bär, M. (October, 2023) Core-Level Spectroscopy with Hard and Soft X-rays on Phosphorus-Containing Compounds for Energy Conversion and Storage. *The Journal of Physical Chemistry C,* **127**(42), 20582–20593.

[206] Wibowo, R. E., Garcia-Diez, R., van der Merwe, M., Duarte-Ruiz, D., Ha, Y., Félix, R., Efimenko, A., Bystron, T., Prokop, M., Wilks, R. G., et al. (2023) Core-Level Spectroscopy with Hard and Soft X-Rays on Phosphorus-Containing Compounds for Energy Conversion and Storage. *The Journal of Physical Chemistry C,* **127**(42), 20582–20593.

[207] Rouff, A. A., Rabe, S., Nachtegaal, M., and Vogel, F. (2009) X-ray absorption fine structure study of the effect of protonation on disorder and multiple scattering in phosphate solutions and solids. *The Journal of Physical Chemistry A,* **113**(25), 6895–6903.

[208] Kruse, J., Leinweber, P., Eckhardt, K.-U., Godlinski, F., Hu, Y., and Zuin, L. (2009) Phosphorus L2, 3-edge XANES: Overview of reference compounds. *Synchrotron Radiation,* **16**(2), 247–259.

[209] Kas, J. J., Vila, F. D., and Rehr, J. J. The FEFF code chapter 6.8, pp. 764–769 John Wiley Sons, Ltd (2021).

[210] Chaboy, J., Muñoz-Páez, A., Carrera, F., Merkling, P., and Marcos, E. S. (2005) Ab initio x-ray absorption study of copper K-edge XANES spectra in Cu (II) compounds. *Physical Review B—Condensed Matter and Materials Physics,* **71**(13), 134208.

[211] González Vallejo, I., Gallé, G., Arnaud, B., Scott, S. A., Lagally, M. G., Boschetto, D., Coulon, P.-E., Rizza, G., Houdellier, F., Le Bolloc'H, D., et al. (2018) Observation of large multiple scattering effects in ultrafast electron diffraction on monocrystalline silicon. *Physical Review B,* **97**(5), 054302.

[212] Natoli, C. and Benfatto, M. (1986) A unifying scheme of interpretation of X-ray absorption spectra based on the multiple scattering theory. *Le Journal de Physique Colloques,* **47**(C8), C8–11.

[213] Ravel, B. (2005) A practical introduction to multiple scattering theory. *Journal of Alloys and Compounds,* **401**(1), 118–126 7th International School and Symposium on Synchrotron Radiation in Natural Science and Proceedings of the International Conference on Experimental and Computing Methods in High Resolution Diffraction Applied for Structure Characterization of Modern Materials HREDAMM.

[214] Kas, J., Vila, F., Tan, T. S., and Rehr, J. (2022) Green's function methods for excited states and x-ray spectra of functional materials. *Electronic Structure,* **4**(3), 033001.

[215] Kas, J. Toward quantitative calculation and analysis of x-ray absorption near edge spectra PhD thesis University of Washington Seattle, WA (2009).

[216] Kas, J., Vila, F., Pemmaraju, C., Tan, T., and Rehr, J. (2021) Advanced calculations of X-ray spectroscopies with FEFF10 and Corvus. *Synchrotron Radiation,* **28**(6), 1801–1810.

[217] Kohn, W. and Sham, L. J. (1965) Self-consistent equations including exchange and correlation effects. *Physical review,* **140**(4A), A1133.

[218] Hinchliffe, A. (2003) Molecular modelling for beginners, John Wiley & Sons, .

[219] Guda, A. A., Guda, S. A., Martini, A., Kravtsova, A., Algasov, A., Bugaev, A., Kubrin, S. P., Guda, L., Šot, P., van Bokhoven, J. A., et al. (2021) Understanding X-ray absorption spectra by means of descriptors and machine learning algorithms. *npj Computational Materials,* **7**(1), 203.

[220] Frank, P., Benfatto, M., and Qayyum, M. (2018) [Cu (aq)] 2+ is structurally plastic and the axially elongated octahedron goes missing. *The Journal of Chemical Physics,* **148**(20).

[221] Frank, P., Benfatto, M., Szilagyi, R. K., D'Angelo, P., Della Longa, S., and Hodgson, K. O. (2005) The solution structure of [Cu (aq)] 2+ and its implications for rack-induced bonding in blue copper protein active sites. *Inorganic chemistry,* **44**(6), 1922–1933.

[222] Gaur, A., Klysubun, W., Soni, B., Shrivastava, B., Prasad, J., and Srivastava, K. (2016) Identification of different coordination geometries by XAFS in copper (II) complexes with trimesic acid. *Journal of Molecular Structure,* **1121**, 119–127.

[223] Wang, Z., Wang, D., Zhao, Z., Chen, Y., and Lan, J. (2011) A DFT study of the structural units in SBA-15 mesoporous molecular sieve. *Computational and Theoretical Chemistry,* **963**(2-3), 403–411.

[224] Becke, A. D. (1992) Density-functional thermochemistry. I. The effect of the exchange-only gradient correction. *The Journal of Chemical Physics,* **96**(3), 2155–2160.

[225] Lee, C., Yang, W., and Parr, R. G. (Jan, 1988) Development of the Colle-Salvetti correlation-energy formula into a functional of the electron density. *Phys. Rev. B,* **37**, 785–789.

[226] Stephens, P. J., Devlin, F. J., Chabalowski, C. F., and Frisch, M. J. (1994) Ab Initio Calculation of Vibrational Absorption and Circular Dichroism Spectra Using Density Functional Force Fields. *The Journal of Physical Chemistry,* **98**(45), 11623–11627.

[227] Weigend, F. and Ahlrichs, R. (2005) Balanced basis sets of split valence, triple zeta valence and quadruple zeta valence quality for H to Rn: Design and assessment of accuracy. *Phys. Chem. Chem. Phys.,* **7**, 3297–3305.

[228] Eveillard, F., Gervillié, C., Taviot-Guého, C., Leroux, F., Guérin, K., Sougrati, M. T., Belin, S., and Delbègue, D. (2020) Unravelling lithiation mechanisms of iron trifluoride by operando X-ray absorption spectroscopy and MCR-ALS chemometric tools. *New Journal of Chemistry,* **44**(24), 10153–10164.

[229] Khanna, A., Fábián, M., Krishna, P., Benmore, C. J., Kaur, A., Kaur, A., Shinde, A., Rajput, P., Jha, S., et al. (2018) Structural analysis of WO3-TeO2 glasses by neutron, high energy X-ray diffraction, reverse Monte Carlo simulations and XANES. *Journal of Non-Crystalline Solids,* **495**, 27–34.

[230] Martini, A., Guda, S., Guda, A., Smolentsev, G., Algasov, A., Usoltsev, O., Soldatov, M. A., Bugaev, A., Rusalev, Y., Lamberti, C., et al. (2020) PyFitit: The software for quantitative analysis of XANES spectra using machine-learning algorithms. *Computer Physics Communications,* **250**, 107064.

[231] Gustafsson, J. P., Braun, S., Tuyishime, J. M., Adediran, G. A., Warrinnier, R., and Hesterberg, D. (2020) A probabilistic approach to phosphorus speciation of soils using P K-edge XANES spectroscopy with linear combination fitting. *Soil systems,* **4**(2), 26.

[232] Beauchemin, S., Hesterberg, D., and Beauchemin, M. (2002) Principal component analysis approach for modeling sulfur K-XANES spectra of humic acids. *Soil Science Society of America Journal,* **66**(1), 83–91.

[233] Wasserman, S. (1997) The analysis of mixtures: Application of principal component analysis to XAS spectra. *Le Journal de Physique IV,* **7**(C2), C2–203.

[234] Penner-Hahn, J. (2003) 2.13 - X-ray Absorption Spectroscopy. In McCleverty, J. A. and Meyer, T. J., (eds.), *Comprehensive Coordination Chemistry II*, pp. 159–186 Pergamon Oxford.

[235] Uchikoshi, M. and Shinoda, K. (August, 2018) Determination of structures of cupric-chloro complexes in hydrochloric acid solutions by UV-Vis and X-ray absorption spectroscopy. *Structural Chemistry,* **30**(1), 61–74.

[236] Pearson, K. and Henrici, O. M. F. E. (1896) VII. Mathematical contributions to the theory of evolution.—III. Regression, heredity, and panmixia. *Philosophical Transactions of the Royal Society of London. Series A, Containing Papers of a Mathematical or Physical Character,* **187**, 253–318.

[237] Laskowska, M., Vynnyk, D., Jedryka, J., Kityk, I., Wojciechowski, A., and Kulwas, D. (2018) Some aspects of measuring nonlinear optical features of advanced vertically aligned mesoporous silica thin films activated by silver and copper ions. In *2018 IEEE 8th International Conference Nanomaterials: Application & Properties (NAP)* IEEE pp. 1–4.

[238] Fan, J.-Y., Li, H.-X., and Wu, F.-Q. (2003) A study on transmitted intensity of disturbance for air-spaced Glan-type polarizing prisms. *Optics communications,* **223**(1-3), 11–16.

[239] Mingabudinova, L., Vinogradov, V., Milichko, V., Hey-Hawkins, E., and Vinogradov, A. (2016) Metal–organic frameworks as competitive materials for non-linear optics. *Chemical Society Reviews,* **45**(19), 5408–5431.

[240] Zyss, J. (2013) Molecular nonlinear optics: materials, physics, and devices, Academic press, .

[241] Bordui, P. F. and Fejer, M. M. (1993) Inorganic crystals for nonlinear optical frequency conversion. *Annual Review of Materials Science,* **23**(1), 321–379.

[242] Oudar, J. d. (1977) Optical nonlinearities of conjugated molecules. Stilbene derivatives and highly polar aromatic compounds. *The Journal of Chemical Physics,* **67**(2), 446–457.

[243] Prasad, P. N., Williams, D. J., et al. (1991) Introduction to nonlinear optical effects in molecules and polymers, Vol. 1, Wiley New York, .

[244] Liu, F., Qin, G., Li, Z., Wang, Z., Peng, M., Wu, S., Li, C., and Yang, Y. (2021) The design and synthesis of nonlinear optical chromophores containing two short chromophores for an enhanced electro-optic activity. *Materials Advances,* **2**(2), 728–735.

[245] Ma, X., Ma, F., Zhao, Z., Song, N., and Zhang, J. (2009) Synthesis and properties of NLO chromophores with fine-tuned gradient electronic structures. *Journal of Materials Chemistry,* **19**(19), 2975–2985.

[246] Dalton, L. R., Sullivan, P. A., and Bale, D. H. (2010) Electric field poled organic electro-optic materials: state of the art and future prospects. *Chemical reviews,* **110**(1), 25–55.

[247] Marder, S. R., Kippelen, B., Jen, A. K.-Y., and Peyghambarian, N. (1997) Design and synthesis of chromophores and polymers for electro-optic and photorefractive applications. *Nature,* **388**(6645), 845–851.

[248] Yang, X.-l. and Xie, S.-w. (1995) Expression of third-order effective nonlinear susceptibility for third-harmonic generation in crystals. *Applied optics,* **34**(27), 6130–6135.

[249] Laskowska, M., Kowalczyk, P., Karczmarska, A., Pogoda, K., Zubko, M., and Laskowski, Ł. (2025) Functionalised Mesoporous Silica Thin Films as ROS-Generating Antimicrobial Coatings. *International Journal of Molecular Sciences,* **26**(15), 7154.